Biostratigraphic constraints on megathrust earthquake deformation history in south central Chile

GARRETT, EDMUND

Biostratigraphic constraints on megathrust earthquake deformation history in south central Chile

Two volumes

Volume 1: main text and references

Ed Garrett

Thesis submitted for the degree of Doctor of Philosophy

Department of Geography

Durham University

April 2013

Biostratigraphic constraints on megathrust earthquake deformation history in south central Chile

Ed Garrett

A lack of comprehensive understanding of the seismic hazards associated with a subduction zone can lead to inadequate anticipation of earthquakes and tsunami magnitudes. Four hundred and fifty years of Chilean historical documents record the effects of numerous great earthquakes; however, with recurrence intervals between the largest megathrust earthquakes approaching 300 years, seismic hazard assessment requires longer chronologies. This thesis seeks to verify and extend historical records in south central Chile using a relative sea-level approach to palaeoseismology, developed in Alaska and the Pacific Northwest.

Quantitative, diatom-based approaches to relative sea-level reconstruction are successful in reconstructing the magnitude of coseismic deformation during recent, well documented Chilean earthquakes. Disparities between my estimates and independent data highlight the possibility of shaking-induced sediment consolidation of tidal marshes. Following this encouraging confirmation of the approach, I quantify land-level changes in longer sedimentary records from the centre of the 1960 rupture zone. Here, laterally extensive marsh soils abruptly overlain by low intertidal sediments attest to the occurrence of four megathrust earthquakes. Field sites preserve evidence of the 1960 and 1575 earthquakes and Bayesian age-depth modelling constrains the timing of two predecessors to 1270 to 1410 and 1050 to 1200. The sediments and biostratigraphy lack evidence for the historically documented 1737 and 1837 earthquakes. The distribution of documented effects of these ruptures and the new palaeoseismic data presented in this thesis suggests these earthquakes were smaller in magnitude and located in the southern portion of the 1960 rupture segment, as other authors have previously inferred.

Coastal sediments record relative sea-level changes reflecting both the earthquake deformation cycle and non-seismic processes. The 1000 year record of net relative sea-level rise implied by the new records presented here differs from the mid to late Holocene relative sea-level fall inferred from previous field studies and modelling approaches.

Contents

Volume 1

Volume 2

Declaration of copyright

I confirm that no part of the material presented in this thesis has previously been submitted by me or any other person for a degree in this or any other university. In all cases, where it is relevant, material from the work of others has been acknowledged.

Acknowledgements

Thanks must first go to my supervisors Ian Shennan and Sarah Woodroffe. I am grateful for their thoughtful guidance and advice throughout the last three years. The initial idea for the project was Ian's and it was his enthusiasm that convinced me to do a PhD. Without his support and treacle-wading skills, I would not have gained as much as I have from the process. Sarah's reassuring and calming influence has been a great help. The 2010 field season benefitted enormously from her presence; barbed-wire limbo, off-roading, sewage tongue eating and all. Sarah and Ian, it has been an immense pleasure to work with you both.

My academic big sister, Natasha Barlow, has provided advice and encouragement throughout. She's been on hand to answer all of the questions I've had, on both sea level and bikes. Her understanding and encouragement, particularly over the last couple of months has been invaluable.

I'd like to thank all those who have contributed to the successes of the three immensely enjoyable field seasons in Chile. First to Marco Cisternas, the chief of Chilean palaeoseismology. His knowledge of the subject is unrivalled and I look forward to future field seasons in his entertaining company. The Americans, Tina Dura, Rob Wesson and Lisa Ely, have provided thought-provoking discussions in the field; it has been a pleasure to work with you all. Emma Watcham was a great help in 2010 and Caroline Taylor has made a remarkably good geographer, in addition to her interpreter and press officer roles, on two field seasons. Señora Mirta Villegas and numerous others allowed access to sites in Chile.

There are many other people who have contributed their time and knowledge to answer many questions that I've asked on all manner of topics. Pippa Whitehouse provided GIA data, Enrique Hauenstein Barra helped with vegetation identification and Pauline Gulliver assisted with radiocarbon dating at the NERC lab. Frank, Katheryn, Merv, Amanda, Chris, Neil, Martin and Paul in the department labs have all been a great help. I'd also like to thank my friends and colleagues in the department for insightful discussions and their enjoyable company.

This PhD would not have been possible without generous financial support from the Department of Geography at Durham University, the Royal Geographical Society (with the Institute of British Geographers), the British Society for Geomorphology, the Quaternary Research Association, the Natural Environment Research Council Radiocarbon Facility and Van Mildert College, Durham.

Jazz and Connie don't know just how much help they have been. Finally, to the one person who I really could not have done this without: Caroline. Thank you for standing beside me through the last three years. Your unfailing confidence in me has been amazing and inspiring.

For Caroline

1. Framework

1.1 Introduction

More than a third of the world's coastlines lie adjacent to active plate boundaries, where earthquakes and their consequent tsunamis constitute major hazards to a substantial proportion of the global population (Bernard *et al*., 2006; McGranahan *et al*., 2007; Bryant, 2008). Long aseismic intervals mean that coastal populations may be unfamiliar with the hazards posed by major earthquakes and, consequently, unaware of appropriate approaches to reducing vulnerability or increasing probability of survival. Their inherent unpredictability and ability to reach destructive capabilities within seconds of first sensation means major earthquakes are highly problematic for policy makers and the general public to contend with (Huppert and Sparks, 2006; Sieh, 2006).

Although several different kinds of fault nucleate earthquakes, subduction zones produce the most powerful, termed megathrust earthquakes. These interplate earthquakes result from the sudden release of strain accumulated during the subduction of one plate beneath an overriding plate. Twenty-first century examples include the Sunda megathrust series that began in 2004 with the moment magnitude (M_w) 9.1 Sumatra-Andaman earthquake (Briggs *et al*., 2006; Meltzner *et al*., 2006; Subarya *et al*., 2006) and the 2011 M_w 9.0 Tōhoku (Japan) earthquake (Ozawa *et al*., 2011; Simmons *et al*., 2011). The lack of comprehensive knowledge of the seismic hazards associated with these plate boundaries resulted in inadequate anticipation of the magnitude of the ensuing earthquakes and tsunamis (Stein and Okal, 2011). Subsequent field investigations in Japan and around the Indian Ocean have revealed evidence for predecessors unknown or underestimated from historical records (Jankaew *et al*., 2008; Sawai *et al*., 2012).

The potential for the Chilean subduction zone to produce very large earthquakes is well known. In May 1960, south central Chile experienced the largest earthquake of the 20th century, the M_w 9.5 Valdivia earthquake. Fifty years later, the 2010 M_w 8.8 Maule earthquake struck the area immediately to the north of the 1960 rupture. The 1960 and 2010 events were not without historical precedent, with documentary records commencing in the 16th century indicating that the Chilean subduction zone has generated numerous great earthquakes (Lomnitz, 1970). However, with return periods for the largest earthquakes potentially approaching 300 years (Stein *et al*., 1986; Barrientos and Ward, 1990; Cisternas *et al*., 2005), accurate assessment of the

seismic hazard requires longer records. This thesis seeks to extend the seismic catalogue for south central Chile by identifying sedimentary evidence for earthquakes in coastal environments.

1.2 Coastal palaeoseismology: rationale

A particular branch of palaeoseismology aims to investigate seismic processes primarily through the identification and analysis of sedimentological and morphological evidence for past relative sea-level change (McCalpin and Carver, 2009). The sea-level approach, developed over the last three decades primarily in subduction zone settings in the Pacific Northwest (Atwater, 1987; Long and Shennan, 1994; Nelson *et al*., 1996; 2006) and Alaska (Combellick, 1991; Shennan *et al*., 1999; Hamilton and Shennan, 2005a; b), has been used to extend historical records in these locations and along other active margins around the world (e.g. Sawai *et al*., 2002; Cisternas *et al*., 2005; Hayward *et al*., 2006; Dura *et al*., 2011).

1.2.1 Relative sea-level change

On long timescales (>10^3 years) relative sea-level changes are driven by mechanisms relating to the volume, mass and distribution of water stored in oceans and deformation of the earth's surface (Clark *et al*., 1978; Mitrovica and Peltier, 1991; Mitrovica and Milne, 2002). On tectonically active coastlines, tectonic land-level changes may impose a characteristic signal on top of other long-term trends (Bourgeois, 2006; Nelson, 2007). Following Shennan and Horton (2002) and Shennan *et al*. (2012), the following equation expresses the components of relative sea-level change:

$$\Delta\xi_{RSL}(\tau,\varphi) = \Delta\xi_{eus}(\tau,\varphi) + \Delta\xi_{iso}(\tau,\varphi) + \Delta\xi_{tect}(\tau,\varphi) + \Delta\xi_{local}(\tau,\varphi) + \Delta\xi_{unsp.}(\tau,\varphi)$$

(Equation 1.1)

Where:

$\Delta\xi_{RSL}(\tau,\varphi)$ = change in relative sea level at a given time (τ) and location (φ)

$\Delta\xi_{eus}(\tau,\varphi)$ = the time and space-dependant eustatic function (originally expressed as time-dependent only)

$\Delta\xi_{iso}(\tau,\varphi)$ = the total isostatic effect of glacial rebound processes, including both glacio-isostatic and hydro-isostatic load contributions

$\Delta\xi_{tect}(\tau,\varphi)$ = the tectonic effect

$\Delta\xi_{local}(\tau,\varphi)$ = the total effect of local processes, including tidal regime changes and post-deposition sediment consolidation

$\Delta\xi_{unsp.}(\tau,\varphi)$ = the sum of unspecified factors, either not quantified or not thought of.

The sea-level approach to palaeoseismology aims to identify sedimentary evidence for relative sea-level changes ($\Delta\xi_{RSL}(\tau, \varphi)$) resulting from tectonic land surface deformation, the $\Delta\xi_{tect}(\tau, \varphi)$ term of equation 1.1. The influence of the other forcing mechanisms complicates coastal relative sea-level records; however, disentangling changes relating to the different processes enables the use of coastal sedimentary records to provide evidence for both tectonic deformation and aseismic relative sea-level changes (cf. Bookhagen *et al*., 2006; Barlow *et al*., 2012).

1.2.2 Elastic deformation modelling and the earthquake deformation cycle

Coastlines adjacent to subduction zones may rapidly uplift or subside during earthquakes (coseismic deformation) and may more gradually deform between ruptures (interseismic deformation). A simple elastic dislocation model provides a first approximation of the spatial pattern of vertical deformation through a single cycle (Hyndman and Wang, 1993). During interseismic strain accumulation, the subducting oceanic plate and overriding continental plate remain seismogenically locked (figure 1.1a). The seaward edge of the upper plate moves downwards, with crustal shortening resulting in uplift in locations further removed from the fault (figure 1.1a). Once cumulative plate convergence exceeds the frictional strength of the fault, strain suddenly releases, with rapid consequential land-level readjustments. Uplift (relative sea-level fall) characterises the seawards edge of the upper plate, while the previously uplifted area rapidly subsides (relative sea-level rise) (figure 1.1b).

An axis of no coseismic elevation change separates areas of uplift and subsidence. The location of this hingeline and the exact pattern of uplift and subsidence are dependent on a number of factors, including the fault profile, the width of the locked area and the distribution of coseismic slip (Hyndman and Wang, 1995; Barrientos, 1996). The growth of anticlines and synclines as well as slip on additional crustal faults at the time of plate-boundary rupture may also increase the complexity of the deformation pattern (Nelson *et al*., 1996; Clague, 1997; Wang *et al*., 2007; Melnick *et al*., 2012b).

The earthquake deformation cycle expresses the repeated succession of land uplift and subsidence resulting from strain accumulation and release (Savage and Prescott, 1978; Savage, 1983; Thatcher, 1984; Shennan *et al*., 1999). Instrumental records have yet to recorded entire cycles and the complete sequence has been inferred through the compilation of geodetic observations of deformation associated with multiple subduction megathrust settings, in particular Japan and Alaska (e.g. Thatcher, 1984; Cohen and Freymueller, 2004). Two further stages may supplement the two-part cycle of interseismic and coseismic displacements:

postseismic and preseismic deformation, both at rates exceeding the interseismic readjustment rate (figure 1.2). Several decades of deformation at rates exceeding 20mm yr^{-1} followed the 1964 Alaskan earthquake (Savage and Plafker, 1991). Creep propagating along a downdip extension of the ruptured fault or viscoelastic readjustments of the lower lithosphere and upper asthenosphere may explain the rapidity of postseismic deformation (Barrientos *et al*., 1992; Piersanti, 1999). On the bases of microfossil analyses, Shennan *et al*. (1999) and Hawkes *et al*. (2005) suggest decimetre-scale preseismic deformation preceded a number of earthquakes in Alaska and Oregon. While Dragert *et al*. (2001) suggests this could relate to slip during slow earthquakes at deeper fault depths, there is a notable absence of evidence for coastal subsidence during slow slip events and a lack of consistent support for deformation before historical and recent great earthquakes (Bourgeois, 2006; Roeloffs, 2006).

The distance between the fault interface and the coastline is crucial to the pattern of relative sea-level changes recorded over the course of the earthquake deformation cycle (Barrientos, 1996). In locations to the seaward side of the axis of no coseismic displacement, relative sea-level fall will characterise interseismic periods, with a sudden relative sea-level rise recorded during megathrust earthquakes (figure 1.2a). Conversely, on the landward side of the axis of no displacement, coastal sites will experience gradual relative sea-level fall, with coseismic events marked by rapid relative sea-level rise (figure 1.2b). The pattern of relative sea-level change recorded in coastal locations over the course of a deformation cycle consists of the inverse of the tectonically driven land-level changes (figure 1.3a) in addition to any long-term aseismic trends in relative sea level resulting from isostatic, eustatic or local processes (figure 1.3b).

1.2.3 Tidal marshes as palaeoseismic recorders

Subduction megathrust earthquakes may submerge organic marsh soils in coastal locations into the intertidal zone (figure 1.4a). At this lower elevation, ensuing interseismic sedimentation will be minerogenic in character, resulting in the formation of an organic – minerogenic couplet. Tsunami deposited sediments may mantle the buried soil horizon if the earthquake is tsunamigenic (not shown in figure 1.4). This characteristic coseismic subsidence stratigraphy (figure 1.4b) occurs in many active margin settings, including Cascadia (Atwater, 1987; Long and Shennan, 1994; Nelson *et al*., 1996), Alaska (Shennan *et al*., 1999; Atwater *et al.*, 2001; Zong *et al.*, 2003) and Indonesia (Dura *et al*., 2011; Grand Pre *et al*., 2012).

If the fault location, geometry and slip conspire to produce an axis of no coseismic displacement landwards of the coastline, coseismic deformation will result in sea-level fall and a different

sedimentary sequence will arise. Organic rich peats abruptly overlying intertidal muds in eastern Hokkaido reflect coseismic uplift events along the southwestern Kuril subduction zone (Sawai, 2001; Sawai *et al*., 2002). Uplifted coastal landforms and biota may also indicate coseismic relative sea-level fall (Darwin, 1839; Bookhagen *et al*., 2006; Shennan *et al*., 2009; Farías *et al*., 2010).

While observations following 20th century earthquakes provide evidence for the seismic origin of some sedimentary couplets (Shennan *et al*., 1999; Cisternas *et al*., 2000), their presence along passive continental margins suggests that other processes can give rise to similar stratigraphies (Fletcher *et al*., 1993; Allen, 1997; Wilson *et al*., 2001). For instance, the lateral migration of tidal channels, short-lived inundation events, such as storm surges, and estuarine reconfiguration resulting from barrier breaching may all produce interbedded sequences of organic and minerogenic sediment (Long and Innes, 1993; Allen, 1997, 2000; Witter *et al*., 2001; Long *et al*., 2006; Switzer and Jones, 2008; Williams, 2009). The identification of couplets alone cannot, therefore, provide unequivocal evidence for coseismic land-level changes and the possible influence of other sedimentological, hydrographic and oceanographic processes must be assessed. For coseismically subsiding coastlines, Nelson *et al.* (1996) provide five criteria for the differentiation between couplets formed by seismic and non-seismic processes:

- Suddenness of submergence
- Amount of submergence
- Lateral extent of organic – minerogenic couplets
- Synchroneity of submergence at widely spaced sites
- Coincidence of tsunami deposits

Nelson *et al*. (1996) suggests the presence of laterally extensive buried soils, with sharp upper contacts, potentially with the flattened stems and leaves of herbaceous marsh plants still rooted in growth-position, can identify coseismic subsidence (see also Atwater and Yamaguchi, 1991; Combellick, 1991; Cisternas *et al*., 2005). Comparison of inferred pre and post-deformation elevations will suggest decimetre to metre scale relative sea-level changes over the shortest possible time-periods (Atwater, 1987; Clarke and Carver, 1992; Hamilton and Shennan, 2005a). Radiometric approaches will be unable to differentiate between the timing of submergence at multiple sites (Atwater *et al*., 1991). Although dependant on favourable conditions for preservation, thin, discontinuous, upward fining sand sheets may provide evidence for coincident tsunami deposition (Witter *et al*., 2003; Goff *et al*., 2010).

While early attempts to quantify the magnitude of coseismic subsidence relied on sediments and plant macrofossils (e.g. Atwater, 1987; Atwater and Yamaguchi, 1991; Atwater, 1992), subsequent microfossil-based approaches offer much higher levels of precision (Darienzo *et al*., 1994; Guilbault *et al*., 1995; Shennan *et al*., 1996). Transfer function methods, employing knowledge of the modern distribution of microfossil assemblages to reconstruct past changes in marsh elevation, have the potential to systematically quantify coseismic deformation, with decimetre-scale error terms (Zong *et al*., 2003; Hamilton and Shennan, 2005a, b; Hayward *et al*., 2006).

1.3 The Chilean subduction zone

The 22nd May 1960 Valdivia earthquake was and still is the largest earthquake since the inception of modern seismic recording. The M_w 9.5 event unlocked almost 1000 km of the fault that conveys the Nazca plate beneath South America (figure 1.5; Plafker and Savage, 1970; Cifuentes, 1989; Barrientos and Ward, 1990). The ensuing tsunami resulted in extensive damage in Hawaii, Japan and other locations across the Pacific (Cox and Mink, 1963; Keys, 1963; Sievers *et al*., 1963). Partially overlapping with the 1960 rupture zone, but principally releasing strain along a 500 km section immediately to the north, the 27th February 2010 M_w 8.8 Maule earthquake also caused extensive damage in Chile and a smaller, although still trans-Pacific tsunami (Farías *et al*., 2010; Fritz *et al*., 2011; Moreno *et al*., 2012).

The 1960, 2010 and numerous other historically documented and instrumentally recorded earthquakes (Lomnitz, 1970; Kelleher, 1972; Comte *et al*., 1986) suggest along-strike segmentation of the subduction zone (discussed further in section 2.2.2). This thesis focuses primarily on the Valdivia seismic segment, defined by the rupture zone of the 1960 earthquake (figure 1.5). Here, 450 years of historical records include four great earthquakes with a recurrence interval averaging 128 years (Lomnitz, 1970). Palaeoseismic data from a site in the centre of the Valdivia segment suggests a longer recurrence interval, exceeding twice the duration of the historical average (Cisternas *et al*., 2005). Assessment of the magnitude of past earthquakes in the Valdivia segment and consequently the seismic hazard in Chile and across the Pacific requires further palaeoseismic records to corroborate evidence from previous historical and stratigraphic studies.

1.4 Hypotheses and research objectives

This thesis sets out to test the central research hypothesis:

Coastal sediments preserve evidence for late Holocene earthquakes and relative sea level change in south central Chile

Testing of this hypothesis assists not only in developing improved chronologies of late Holocene earthquake occurrence, but also in constraining the poorly understood relative sea-level history of the western margin of South America. To approach this hypothesis, I investigate three contributing hypotheses:

1. Palaeoseismic evidence records historically documented megathrust earthquakes
2. Differences between historical and palaeoseismic records reflect coseismic deformation patterns
3. Evidence for relative sea-level change reflects both the earthquake deformation cycle and non-seismic processes

I define a set of objectives which outline the progression of this research:

- Characterise modern intertidal diatom distributions in south central Chilean tidal marshes
- Develop transfer function models for the purpose of reconstructing palaeomarsh surface elevation from fossil marsh sediments
- Test the performance of the approach by reconstructing coseismic deformation associated with recent, well documented Chilean earthquakes
- Interrogate coastal sediments in the Valdivia seismic segment for evidence of past earthquakes
- Reconstruct coseismic deformation associated with palaeoearthquakes
- Constrain the timing of palaeoearthquakes using a radiometric approach and compare inferred ages with historical records and other palaeoseismic investigations
- Investigate relative sea-level changes occurring over the course of multiple earthquake deformation cycles

1.5 Statement of collaboration

A NERC Urgency Grant (ref. I00503X/I, *Sediment Signatures of the 2010 Chile Mw 8.8 Earthquake*) to Professor Ian Shennan and Dr Sarah Woodroffe supported a rapid assessment of sediments deposited by the 2010 tsunami and subsequent postseismic accumulations. A survey in August

2010 recovered sediment blocks from three sites around the boundary between the 2010 and 1960 earthquakes: Río Andalién, Tubul and Río Tirua. Garrett *et al*. (accepted) describes the findings of this project, including insights into tsunami biostratigraphy and postseismic sedimentation. A copy of this publication is included as appendix 1.1. Chapter five of this thesis uses the new biostratigraphic records produced by the *Sediment Signatures* project to test the performance of the diatom-based coseismic deformation reconstruction approach.

1.6 Key terms

This thesis uses a range of terms from the sea level and palaeoseismic communities. To avoid ambiguity, I define certain key terms:

Displacement (also uplift, subsidence) is the vertical component of tectonic deformation, typically measured in metres.

Palaeomarsh surface elevation (PMSE) is the estimated elevation within a tidal marsh that a sample accumulated at. This thesis estimates PMSE from diatom assemblages, and expresses estimates in metres above mean sea level, accompanied by a one sigma error term.

Soil refers to organic-rich high intertidal or freshwater marsh deposits and is preferred to the term *peat* to maintain consistency with palaeoseismic convention (cf. Atwater, 1987; Nelson *et al*., 1996). The term ***buried soil*** denotes an organic deposit formed at the surface of a former marsh and subsequently covered by sediments of lower organic content.

Early, mid and late Holocene, following Walker *et al*. (2012), I adopt 8200 ka BP as the boundary between the early and the mid Holocene and 4200 ka BP as the boundary between the mid and the late Holocene.

1.7 Summary and thesis outline

Coastal palaeoseismology supplements and extends historical records of earthquake occurrence, leading to greater understanding of the seismic hazards associated with a particular subduction zone. I apply a method based on identifying stratigraphic and microfossil evidence for rapid changes in relative sea level to investigate evidence for past earthquakes in the Valdivia seismic segment of the Chilean subduction zone. This thesis tests whether tidal marshes are faithful palaeoseismic recorders through the development of new stratigraphic records and comparisons

with historical and other palaeoseismic records. Chapter two discusses the physical geography of the study area and introduces the specific field sites. Chapter three provides the field, laboratory, dating and statistical methodology implemented to test the hypotheses. Chapter four is concerned with the first two objectives, characterising modern diatom distributions and developing transfer functions. Chapter five tests the performance of the reconstruction approach using evidence for recent, well documented earthquakes. Chapter six investigates longer sedimentary records of earthquakes, presenting and discussing stratigraphic, microfossil and chronological data. Chapter seven discusses the three contributing hypotheses and makes suggestions for future research directions.

2. Study area

2.1 Introduction

This chapter introduces the physical geography of south central Chile and describes the sites used to test the hypotheses set out in chapter one. Section 2.2 discusses the tectonic setting, late Quaternary glacial history and consequential relative sea-level changes along the Chilean coastline. Section 2.3 introduces the field sites in south central Chile, divided into two groups: contemporary intertidal marshes and sites analysed for evidence for multiple earthquakes over the late Holocene.

2.2 Physical geography of the Chilean convergent margin

The Chilean mainland extends through 38 degrees of latitude, more than 4000 km, from the northern border with Peru at the Arica Bend to Cape Horn in the south (figure 2.1). The country is rarely more than 200 km in width, with the Pacific Ocean and the Andes forming the western and eastern margins.

2.2.1 Tectonic setting

A convergent margin runs approximately parallel with the coastline of western South America for a length of 7500 km, from Colombia in the north to Tierra del Fuego in the south (figure 2.2). The margin marks the subduction of the Nazca and Antarctic plates beneath continental South America. The subduction zone terminates in the north in a transform fault between the Nazca and Panamanian plates and in the south at the transition to an oceanic convergent margin between the Antarctic and Scotia plates (figure 2.2). A triple junction marks the subduction of an actively spreading ridge between the Nazca and Antarctic plates beneath South America at approximately 46°S. The section of the convergent margin between the marked coastal inflection of the Arica Bend near the Peru – Chile border and the Chile triple junction (hereafter referred to as the Chilean subduction zone) is characterised by plate convergence averaging 60 – 80 mm yr^{-1}, with the movement of the Nazca Plate approximately 13° north of east (DeMets *et al*., 1990; Somoza, 1998; Angermann *et al*., 1999). This reflects a substantial slowdown over the last 20ma from a

rate of approximately 120 mm yr^{-1} (Somoza, 1998). South of the triple junction the Antarctic and South American plates converge at a rate of approximately 20 mm yr^{-1}.

The South American convergent margin displays substantial along-strike variability in the angle of dip of the descending plate (Barazangi and Isacks, 1976; Cahill and Isacks, 1992; Tassara *et al*., 2006). Beneath Ecuador, northern Chile and south central to southern Chile the descending plate dips steeply at angles of between 25° and 30°. Central Peru and north central Chile are characterised by flat slab subduction. After a steep initial descent until the 100 km depth contour, dip angles in these areas reduce to approximately 10° and the Nazca plate travels horizontally for several hundred kilometres before resuming its downward descent (Gutscher *et al*., 2000; Anderson *et al*., 2007).

The descending Nazca plate exhibits a number of aseismic ridges and lithospheric transform faults or fracture zones. The Carnegie, Nazca, Iquique and Juan Fernandez ridges subduct beneath Ecuador, southern Peru, northern Chile and central Chile respectively. The fracture zones, emanating from the Nazca-Antarctic plate boundary subduct beneath Chile between 37°30'S and 49°S (figure 2.3). Aseismic ridges and fracture zones may act as both asperities and barriers to earthquake rupture propagation (Barrientos and Ward, 1990; Bilek, 2010; Sparkes *et al*., 2010).

The Andes form the most striking feature of the western margin of the overriding South American plate. This 7000 km long mountain chain formed, and continues to form, by crustal thickening, volcanism, sediment accretion and strike-slip faulting due to plate convergence (Cobbold *et al*., 2007). Corresponding with the along-strike variation in dip angle, the configuration of the Andes chain displays latitudinal variability. North of 28°S the Andes are comprised of a coastal cordillera, a central depression, a precordillera and a main cordillera; the central Chilean flat-slab region lacks the central depression and south of 34°S (including the area of interest to this project) the chain consists of a coastal cordillera and a main cordillera, separated by a central depression (Cembrano *et al*., 2007). Also corresponding with the zones of steep subduction, three sections of the Andean chain support volcanoes, which are notably absent in north central Chile (Stern *et al*., 2007).

Two important upper plate fault systems lie parallel to the convergent margin: the Atacama Fault Zone of the northern Chilean coastal cordillera and the Liquiñe-Ofqui Fault Zone of the main cordillera of southern and south central Chile. The latter is primarily a dextral intra-arc transform fault, defining the eastern edge of the Chiloé crustal sliver (figure 2.3) (Cembrano *et al*., 1996; Moreno *et al*., 2008; Rehak *et al*., 2008). Oblique subduction of the Nazca plate results in the

margin-parallel movement of this detached section of continental crust (Wang *et al*., 2007). The buttressing effect of the Arauco-Nahuelbuta block restricts the northwards displacement of the sliver (figure 2.3). Oblique thrusting along the Lanalhue fault and folding and crustal thickening, as evidenced by the uplift of the Arauco peninsula, accommodates the strain (Beck *et al*., 1993; Melnick *et al*., 2006; Moreno *et al*., 2008).

Earthquakes along the Chilean margin are associated with three distinct seismogenic zones (Barrientos, 2007):

- tensional and compressional events within the descending plate at depths of 70 – 100 km
- interplate thrust events with shallow epicentres (0 – 50 km)
- shallow upper plate seismicity (0 – 20 km) restricted to a few areas of the main cordillera

Interplate megathrust events, with foci located in the coastal region, have provided the largest historical magnitudes, including the largest event since the inception of modern seismic recording, the M_w 9.5 Valdivia earthquake (Plafker and Savage, 1970; Cifuentes, 1989; Barrientos and Ward, 1990). At least seven further Chilean events since the start of the 20th century have exceeded magnitude 8. Smaller intraplate events have also caused major damage; the 1939 Chillán earthquake, which resulted from normal faulting along a near vertical fault plane at depth within the descending Nazca plate resulted in 25,000 fatalities (Beck *et al.*, 1998). Instrumentally recorded shallow upper plate earthquakes in the main cordillera have not exceeded magnitude 7 or produced identifiable coastal deformation (Barrientos, 2007).

2.2.2 Historical records of earthquake occurrence

Historical records of megathrust earthquakes and their tsunamis (summarised by Berninghausen, 1962; Lomnitz *et al*., 1970; Kelleher, 1972; Beck *et al*., 1998; Campos *et al*., 2002; Cisternas *et al*., 2005; Cisternas *et al*., 2012) suggest along-strike segmentation of the subduction zone. The southern sector of the convergent margin, from approximately 35°S to the triple junction at 46°S, divides into two segments, each displaying different recurrence intervals, rupture lengths and earthquake magnitudes (figure 2.4). This thesis focuses on the Valdivia seismic segment, defined by the rupture zone of the 1960 Valdivia earthquake. Chapter 5 also incorporates evidence from the 2010 Maule earthquake, which ruptured the Concepción segment immediately to the north of the Valdivia segment.

The 1960 earthquake ruptured 1000 km of plate interface from the Arauco Peninsula in the north to the Taitao Peninsula in the south. Slip on the fault reached 40 m, resulting in a moment magnitude of 9.5 (Cifuentes, 1989; Linde and Silver, 1989; Barrientos and Ward, 1990). A coastal

downwarp of up to 2.4 ± 0.4 m, flanked by two upwarps characterised the coseismic deformation (Wright and Mella, 1963; Plafker and Savage, 1970; Villalobos, 2011). A 100 km wide offshore belt was uplifted by up to 5.7 ± 0.2 m (Plafker and Savage, 1970), causing a trans-Pacific tsunami that caused extensive damage in Chile and Hawaii (Atwater *et al*., 1999). Historical records attest to the occurrence of preceding megathrust earthquakes in 1837, 1737 and 1575 (Lomnitz, 1970; Cisternas *et al*., 2005).

The Concepción seismic segment extends northwards from the Arauco Peninsula to a more ambiguous northern boundary (figure 2.4). Historical rupture distributions inferred by Melnick *et al*. (2006) and Barrientos (2007) suggest a location in the vicinity of the coastal towns of Pichilemu (34.4°S) and Constitución (35.3°S), giving a segment length of between 300 and 400 km. Major ruptures occurred in 1570, 1657, 1751, 1835, 1928 (Darwin, 1839; FitzRoy, 1839; Kelleher, 1972; Beck *et al*., 1998; Campos *et al*., 2002; Melnick *et al*., 2006) and most recently on 27th February 2010 (Farías *et al*., 2010; Lay *et al*., 2010; Vigny *et al*., 2011). The rupture zone of the 2010 Maule earthquake was 500 km in length, with slip of up to 16 m contributing to a moment magnitude of 8.8 (Moreno *et al*., 2012).

The causes of segmentation of subduction zones remain equivocal, with subduction of lower plate bathymetric anomalies, trench sediment thickness and upper plate discontinuities among a number of potentially influential factors (Kelleher and McCann, 1976; Ruff, 1989; Melnick *et al*., 2009; Bilek, 2010; Sparkes *et al*., 2010). The northern boundary of the 1960 rupture and, therefore, the Valdivia segment may correspond with the edge of the detached Chiloé sliver (figure 2.3) (Wang *et al*., 2007; Melnick *et al*., 2008; Moreno *et al*., 2008), while the southern boundary is marked by either the subduction of an active spreading ridge at the Chile Triple Junction or a nearby fracture zone (Barrientos and Ward, 1990).

2.2.3 Glacial history

At the maximum extent of the last (Llanquihue) glaciation, the Patagonian Ice Sheet extended along the crest of the Andes from 38°S to 56°S (figure 2.5) (Caldenius, 1932; Denton *et al*., 1999; Hulton *et al*., 2002; Glasser *et al*., 2008). The Los Lagos region experienced an alpine style glaciation, with topographic constraint on ice extent, while the Patagonian region to the south was characterised by a more extensive ice-sheet style glaciation (e.g. Caldenius, 1932; Hulton *et al*., 2002). Piedmont glaciers originating in the main cordillera flowed into the central depression, including into lakes Puyehue, Rupanco and Llanquihue in the Los Lagos region and into the marine basins of Seno Reloncaví, Golfo de Ancud and Golfo de Corcovado between Isla de Chiloé and the

mainland (figure 2.5). Well-preserved moraine systems and outwash plains indicate that the Castro piedmont lobe overran the southern half of Isla de Chiloé, however northern Chiloé and the coastline of the Los Lagos region remained ice-free (Heusser and Flint, 1977; Denton *et al*., 1999; Hulton *et al*., 2002; García, 2012).

In response to climatic amelioration, the Patagonian piedmont glaciers rapidly retreated after 17500 – 17150 ka BP (Denton *et al*., 1999; McCulloch *et al*., 2000). In the northern sector, glaciers withdrew to within 10 km of their main cordilleran sources within 2000 years (Heusser, 1990; Denton *et al*., 1999). Modelling approaches concur, suggesting that the ice sheet lost over 80 % of its Last Glacial Maximum (LGM) volume over the same period (Hulton *et al*., 2002). Relative warmth characterised the period from 13500 to 4000 ka BP (Heusser and Streeter, 1980; Rabassa and Clapperton, 1990). Vegetation reconstructions in the Los Lagos region suggest temperatures peaked 2 °C above modern values (Heusser, 1974; Clapperton, 1990). Subsequent cooling and an increase in precipitation resulted in Neoglacial icefield expansion (Mercer, 1970; Aniya, 1996; Glasser at al., 2004; Bertrand *et al*., 2012). Based on constraining the timing of advances of various glaciers surrounding the Northern and Southern Patagonian icefields, Mercer (1968, 1970) and Aniya (1995, 1996) each propose a number of Neoglacial advances. While the advances may not be synchronous between the two studies, both chronologies may be valid as they record the advance and retreat of different outlet glaciers (Glasser *et al*., 2004). Together, however, they suggest a period of renewed late Holocene glacial activity following the relative warmth of the early to mid Holocene.

The modern extent of Patagonian ice cover is limited to three main areas: the North and South Patagonian Icefields and the smaller, discontinuous icefields of the Cordillera Darwin (figure 2.1). Together they cover an area exceeding 17000 km^2 (Aniya, 1996; Rignot *et al*., 2003). Glasser *et al*. (2011) estimate total losses of 103 ± 20.7 km^3 from the North Patagonian Icefield since the Holocene peak in 1870 and 503 ± 101.1 km^3 from the South Patagonian Icefield since 1650. Together, the contribution to sea level rise from the two icefields since has averaged 0.0052 ± 0.0008 mm/year since 1870 (Glasser *et al*., 2011), substantially less than the 0.042 ± 0.002 mm/year to 0.105 ± 0.011 mm/year inferred for the last few decades of the 20th century (Rignot *et al*., 2003).

2.2.4 Post last glacial maximum relative sea-level change

The transition from glacial to interglacial conditions has dominated relative sea-level changes over the last 20 kyr. During this time, the global melting of icesheets has resulted in a 120 to 125 m rise

in sea level (Fairbanks, 1989; Chappell and Polach, 1991; Flemming *et al*., 1998; Hanebuth *et al*., 2000). This rise was not, however, spatially uniform and other factors, particularly glacio-isostatic adjustment (GIA), have contributed to a high degree of spatial variability. GIA-induced relative sea-level changes have been greatest in the former centres of glaciation, where rebound following deglaciation -as resulted in substantial relative sea-level fall. With increasing distance from the formerly glaciated centres, eustatic rises become dominant over GIA-induced falls in relative sea level (Clark *et al*., 1978; Pirazzoli, 1991).

Substantial spatial variations are apparent in mid and late Holocene relative sea level changes (Pirazzoli, 1991). Milne *et al*. (2005) summarise evidence for former sea levels over the last six to ten thousand years from the Atlantic coast of South America and the Caribbean. While sites in Jamaica and Venezuela exhibit continual relative sea-level rises until the present day, records from Suriname, Brazil and southernmost South America suggest falling relative sea level from a highstand above present sea level (Milne *et al*., 2005 and references therein). This mid Holocene highstand and the subsequent relative sea-level fall reflect ongoing GIA processes, particularly equatorial ocean syphoning and continental levering due to local hydro-isostatic loading (Clark *et al*., 1978; Mitrovica and Peltier, 1991; Mitrovica and Milne, 2002).

Peltier's (2004) ICE5G (VM2) model suggests highstands above present and falling late Holocene relative sea level also characterise the Pacific coast of South America (figure 2.6). The elevation of this highstand exhibits latitudinal variation, increasing from less than two metres in northern Chile to over ten metres close to the former centre of the LGM Patagonian Icefield. GIA uplift rates in other plate subduction settings, however, suggest the rheological parameters employed by the VM2 earth model are not appropriate in this setting (James *et al*., 2000; Larsen *et al*., 2005). Chapter seven further investigates the implications of a low viscosity asthenosphere on relative sea-level change. Short-term deformation associated with great earthquakes and longer-term deformation resulting from movement on upper plate faults complicates the pattern of relative sea-level change along the Chilean coast. While field evidence supports mid Holocene sea levels above present (Isla *et al*., 2012), the relative contributions of tectonic uplift and GIA are difficult to disentangle for each location.

North of 25°S, evidence for Holocene sea levels above present occurs at Caleta Michilla (22°43'S; figure 2.6), where Leonard and Wehmiller (1991) identified a terrace approximately five metres above the modern tidal platform. The elevation of the terrace implies at least some contribution from tectonic uplift to emergence, as ongoing GIA processes would be insufficient alone to account for the elevation (Leonard and Wehmiller, 1991). Tectonic uplift of the Coquimbo block

and recent movement on the Puerto Aldea Fault may explain the elevation of a series of mid Holocene palaeobeach and estuarine deposits at Los Choros (29°15'S) (Castro and Bignardello, 2005), Bahía Herradura (29°58'S) (Radtke, 1989) and Bahía Tongoy (30°15'S) (Ota and Paskoff, 1993). At Algarrobo (33°22'S), elevated sediments indicative of shallow marine conditions suggest a post highstand sea-level fall of not less than 3.8 m (Encinas *et al*., 2006). At least 21 exposed beach berms on Isla Santa Maria (37°02'S) indicate both uplift and tilting of the island over the late Holocene (Bookhagen *et al*., 2006). The uppermost berms lie approximately eight metres above present mean sea level and reflect upper plate thrust faulting in addition to GIA-induced relative sea level fall (Melnick *et al*., 2006). Thrust faulting is also the inferred cause for the 38 m relative sea-level fall on Isla Mocha (38°22'S) over the last 6000 years (Kaizuka *et al*., 1973; Nelson and Manley, 1992). At the archaeological site of Chan-Chan (39°30'S), a beach berm eight metres above present mean sea level may indicate the maximum Holocene sea level in this area (Pino and Navarro, 2005). Less than fifty kilometres to the south, at Isla Mancera (39°53'S), Villalobos Silva (2005) identified a terrace 3.9 m above modern sea level as reflecting the highstand elevation. Raised intertidal deposits around the Maullín estuary (41°35'S) suggest net emergence has prevailed over at least the last 5000 years (Atwater *et al*., 1992), however the presence of organic soils below the current elevation of organic deposition (Cisternas *et al*., 2005) suggests a period of more recent relative sea-level rise. While Hervé and Ota (1993) identify rapid uplift of sites in Fiordo Reloncavi (41°30'S), Bahía Hualaihue (42°02'S) and south of Castro on Isla de Chiloé (42°30'S), the indicative meaning of their sea level indicators in not clear, the elevation errors are large and some samples may be reworked or originate from midden deposits that are frequent in this area (Bird, 1938). At Chepu (42°03'S), northwest Isla de Chiloé, organic material within a terrace 5 m above present sea level yielded a mid Holocene radiocarbon age (Radtke, 1989). South of Isla de Chiloé on Isla Guafo (43°36'S), evidence for marine deposition on a presently forested coastal plain implies net late Holocene sea-level fall (Melnick *et al*., 2010).

Due to its high degree of inaccessibility, no Holocene relative sea level records currently exist for the section of Chilean coastline between 43°40'S and 53°35'S (figure 2.6). Around the Strait of Magellan, low terraces suggest Holocene sea levels higher than present (Porter *et al*., 1984). At Puerto del Hambre (53°35'S), a marine diatom and foraminifera-bearing clay suggests a highstand at least 3.5 m above present (Porter *et al*., 1984; McCulloch and Davies, 2001). McCulloch and Bentley (1998) and Bentley and McCulloch (2005) highlight substantial changes in the elevation of the site due to postglacial fault reactivation; however, the majority of this movement may have occurred before the deposition of the marine layer. Emergent beaches at Peninsula Gusano and Punta Piedra Buena in the Beagle Channel (54°55'S) both imply a similar elevation for the highstand (Porter *et al*., 1984). Rabassa *et al*. (1986) and Gordillo *et al*. (1992), however, report

raised beaches up to ten metres above present mean sea level within the Beagle Channel, reflecting the importance of local faulting.

In summary, field evidence from the Chilean coastline, particularly between 29°S to 42°S and from southern Patagonia supports the occurrence of Holocene sea levels above present. The extent to which the elevation of the highstand reflects processes related to GIA, rather than local or regional-scale tectonics varies from site to site and is generally unknown. Further GIA modelling approaches may assist by providing a correction tailored to the best estimates of the rheology underlying western South America.

The implications of falling late Holocene relative sea level may be considerable for the preservation of sedimentary evidence for earthquakes in coastal environments. Based on the dating of palaeoseismic evidence in Indonesia, Dura *et al*. (2011) and Grand Pre *et al*. (2012) suggest rising relative sea level provides accommodation space and promotes preservation, while stratigraphic evidence for earthquakes is unlikely to be preserved during periods of relative sea-level fall. Nelson *et al*. (2009) evoked falling relative sea level and consequent subaerial erosion for the lack of palaeoseismic evidence in the Valdivia estuary, south central Chile (39°52'S). Similarly, sea-level fall may explain the lack of late Holocene intertidal and tsunami deposition at Quintero (32°48'S) in central Chile (Dura *et al*., 2012). As mentioned above, however, the presence of buried soils at Maullín highlights the potential for preservation of recent evidence in the Valdivia seismic segment.

2.2.5 Coastal processes

The Chilean coastline subdivides into three principal zones. North of 41°30'S the central depression lies above sea level and the coastline is situated to the west of the coastal cordillera. The exposed coastline promotes the formation of actively eroding cliffs and high-energy beaches and constrains low energy sedimentary environments to estuarine settings. Along-shore sediment transport results in the formation of sand spits which deflect rivers northwards, as seen at Río Mataquito (35°S), and bars, which result in perched water surfaces, such as at Bucalemu (34°38'S). Between 41°30'S and 46°30'S the central depression lies beneath sea level and the coastal range forms a series of islands, with the largest, Isla de Chiloé, in the north separated from the numerous islands of the Chonos Archipelago by the Boca del Guafo. The islands provide shelter and low energy sedimentary environments, including tidal marshes, fringe many of the small bays and estuaries of this region. South of the Taitao Peninsula (46°30'S), the central

depression in absent and the main cordillera is fronted by a large number of islands, separated by deep fjords and fjord-like channels.

The northern, central and south central Chilean coastline is predominantly micro- to mesotidal, with tidal ranges largely in the region of 1.5 to 2.0 m (Aiken, 2008). While the outer coast of the archipelagos maintains this range, the semi-enclosed waters of the southern Chilean fjords feature tidal amplification. This is greatest at Puerto Montt, northwest of Isla de Chiloé, where the tidal range is approximately 7 m (Fierro, 2008). Less than 100 km to the west, close to the modern and fossil sites introduced in section 2.3, the tidal range is typically in the region of 2.0 m (Fierro, 2008; IOC, 2012).

2.2.6 Climate and vegetation

Contemporary climatic variations reflect Chile's elongated shape and varied topography. Following Fernandez *et al*. (2000), the coastline divides into four climatic zones:

1) An arid or hyperarid coastal zone extends from 18°S to 27°S. Certain areas have no historically documented rainfall. The Köppen climate classification system classes the area as *BWk*, indicating a desert climate with at least one month averaging below 0 °C (Peel *et al*., 2007).
2) From 27° S to 32° S, the coast is semiarid, with winter rainfall and dry summers leading to a Köppen classification of *Csb* (Peel *et al*., 2007).
3) The coastline from 32°S to 42°S is temperate and oceanic, with increasing rainfall totals and decreasing seasonality in precipitation to the south (Köppen classification of *Csb or Cfb* (Peel *et al*., 2007)).
4) The archipelagos and fjord systems from 42°S to 56°S are oceanic in climate, with high rainfall totals evenly distributed throughout the year. The Köppen classification of *Cfb* or *Cfc* reflects the prevalence of rainfall, with *ET* classifications at high altitudes and south of 54°S suggesting tundra climates (Peel *et al*., 2007).

The periodic climatic phenomenon *El Niño* brings increased rainfall and milder winters to the Chilean coast and may also increase sea levels by over 0.1 m in northern Chile and Peru (Enfield, 1989).

Linked to the latitudinal variation in climate, Chilean vegetation shows a high degree of zonation. Between 36°S and 43°S, the region of interest to this thesis, deciduous woodland and broadleaf

coniferous temperate rainforests occupy the littoral zone and the coastal cordillera (Goodspeed, 1945; Chester, 2008). Deforestation following Spanish settlement in the 16th century has converted much of lowland Chiloé into farmland. Chapter four describes the intertidal vegetation of this region.

2.3 Field sites

This section describes the location of the field sites that provide evidence to approach the hypotheses set out in chapter one. Section 2.3.1 focuses on the sites required for the characterisation of modern tidal marshes and development of transfer functions. Section 2.3.2 describes the locations of the *Sediment Signatures* project sites employed in this thesis to test the performance of the deformation reconstruction approach (see also Garrett *et al*., accepted; appendix 1.1). Section 2.3.3 describes the sites investigated for long records of earthquake occurrence and relative sea level change.

2.3.1 Contemporary tidal marshes

The modern tidal marsh sites are located on Isla de Chiloé in the centre of the 1960 rupture zone and approximately 350 km south of the southern limit of the 2010 rupture (figure 2.7a, b). Glacial deposits mantle the lower lying eastern half of the island, while Palaeozoic metamorphic rocks characterise the higher relief of the west (Watters and Flemming, 1972). In the northwest of Chiloé, numerous sheltered bays and inlets allow low energy sedimentation and tidal marsh formation. The modern tidal marshes sampled in this thesis lie within Bahía Quetalmahue (figure 2.7c), in close proximity to the long record sites (figure 2.7b, c; section 2.3.3).

Estero Guillingo

The 2011 field season provided modern samples from Estero Guillingo, a small, bifurcated estuary in the northwest of Bahía Quetalmahue (figure 2.7c). Here, two small unnamed streams drain two adjacent catchments, each approximately 7 km^2 in area. Vegetated tidal marshes in the two branches of the estuary occupy a total area of approximately 0.1 km^2. I collected samples from a single transect of approximately 100 m in length from the western bank of the western branch (figure 2.8). Chapter three discusses the sampling methods used to recover modern and fossil samples. The site lies 3.5 km northeast of the principal long record site at Chucalen (section 2.3.3).

Puente Quilo

Modern sampling in 2012 focused on a small tidal marsh (approximately 0.01 km^2 vegetated area) close to the mouth of the Río Quilo in the southwest of Bahía Quetalmahue (figure 2.7c). The name *Puente Quilo* reflects the site lying immediately adjacent to a bridge over the Río Quilo. The river drains a small tidal inlet, referred to by Bartsch-Winkler and Schmoll (1993) as Estero Quetalmahue. The inlet occupies an area of approximately 2 km^2 and drains several small streams. A 100 m long modern sampling transect from the marsh at the mouth of the inlet (figure 2.9) provided samples for further analyses (chapter 4).

2.3.2 *Sediment Signatures* project sites

Río Andalién

The site at Río Andalién lies within the sheltered, north-facing Bahía Concepción, immediately west of the town of Penco and close to the Talcahuano – Concepción conurbation (figure 2.10). Broad, low-lying floodplains and tidal marshes associated with the Andalién and San Pedro rivers lie behind a modern beach berm. The *Sediment Signatures* project investigated two transects from the eastern edge of the embayment, alongside the Río Andalién, and retrieved a monolith from a marsh front exposure (figure 2.10d).

Estimates of coseismic movement in 2010 indicate uplift exceeding 0.5 m at Talcahuano and the Tumbes Peninsula, eight kilometres to the west of the sampling site (Farías *et al.,* 2010; Fritz *et al*., 2011; Melnick *et al.,* 2012; figure 2.10) and marginal subsidence at Concepción to the south (Vigny *et al*., 2011). Watermarks in Talcahuano and Penco suggest 2010 tsunami flow depths of between 4 and 7 m (Fritz *et al*., 2011) and a maximum inundation distance across the low lying tidal marshes of 2.6 km (Morton *et al*., 2011; figure 2.10). Comparison of pre- and post-earthquake Google Earth imagery does not reveal substantial geomorphological changes (figures 2.10c, d). The erosional backwash scours found by Morton *et al.* (2011) closer to Talcahuano are notably absent from the sampling site.

Tide gauge data from Talcahuano indicate that the 1960 tsunami reached heights of 3 m within Bahía de Concepción (Sievers *et al*., 1963). Plafker and Savage (1970) suggested marginal uplift in 1960 based on tidal observations at a location to the west of Talcahuano (figure 2.10).

Tubul

The Tubul and Raqui rivers drain a substantial sheltered tidal and freshwater marsh on the northern edge of the Arauco Peninsula (figure 2.11). The *Sediment Signatures* project provided a monolith from the edge of a tidal channel of the Río Raqui adjacent to the eastern edge of the marsh complex (figure 2.11d).

Estimates of coseismic movement in 2010 indicate uplift at the site of between 1 and 2 m (Farías *et al*., 2010, Fritz *et al.,* 2011; Melnick *et al*., 2012; figure 2.11). Google Earth imagery reveals substantial geomorphological changes resulting from the rapid relative sea-level fall, including the possible change from an ebb tide delta to a flood tide delta (figure 2.11c,d). In January 2012, I observed pioneer vegetation communities colonising extensive previously unvegetated areas alongside tidal channels throughout the estuary and post-earthquake Google Earth imagery also highlights the development of vegetation behind an uplifted beach berm to the north of the river mouth (figure 2.11d).

Fritz *et al.* (2011) estimates 2010 tsunami flow depths of over 5 m at Tubul in 2010. Corresponding flow depths in 1960 are unknown. Plafker and Savage (1970) concluded that there was no vertical land-level change, based on tidal observations.

Río Tirua

The Río Tirua meanders through a low-lying coastal plain, characterised by tidal and freshwater marsh environments (figure 2.12). The *Sediment Signatures* project investigated a transect from one to two kilometres inland from the coast and recovered a core from close to the landward end of this transect (figure 2.12d).

Intertidal mussels and bleached corraline algae from the headland at the mouth of the river indicate coseismic uplift of between 0.5 and 1 m in 2010 (Farías *et al.,* 2010; Melnick *et al*., 2012; figure 2.12d). Comparison of pre- and post-earthquake Google Earth imagery does not suggest significant morphological changes resulting from uplift (figures 2.12c, d), but does highlight shaking or tsunami-induced damage to seaward end of the sea-wall on the northern bank of the river. While tsunami runup reached 20 m on the exposed rocky shoreline to the southwest, heights closer to the mouth of the Río Tirua were approximately half as large (Bahlburg and Spiske, 2012; Fritz *et al*., 2011; Vargas *et al*., 2011).

Plafker and Savage (1970) estimated slight subsidence of the rocky headland at the mouth of the river in 1960 (figure 2.12). Tsunami runup on Isla Mocha, 30 km offshore from the mouth,

exceeded 15 m in 1960 (Sievers *et al*., 1963), but the wave height as it approached the mainland in this sector is unknown. By way of comparison, runup during 2010 exceeded 20 m on Isla Mocha (Fritz *et al*., 2011); however the difference may result from the different approach directions of the two tsunamis.

2.3.3 Late Holocene sites

Like the modern tidal marsh sites, the fossil sites lie in the centre of the 1960 rupture zone (figure 2.7a, b). Evidence from the three sites described in this section is required to test the central hypothesis of this thesis; *Coastal sediments preserve evidence for late Holocene earthquakes and relative sea level change in south central Chile* and also the contributing hypotheses set out in chapter one.

Chucalen

High intertidal and freshwater marshes fringe the western margin of Bahía Quetalmahue, between the contemporary marsh sampling sites at Estero Guillingo and Puente Quilo (figure 2.13). The marsh front is actively eroding, with a metre high cliff separating the vegetated marsh from the tidal flat (figure 2.13c). The tidal marsh gives way to freshwater marsh and pasture at higher elevations. At the site of Chucalen, named for the closest small hamlet on the road between Puente Quilo and the Lacui Peninsula, a low terrace (approximately 2 m above mean sea level) separates the marsh from drier areas. A coring transect and natural exposures provided access to the stratigraphy (sampling approach described further in chapter three). To the south of the sampled area of marsh, an eroded mudstone platform outcrops (visible in figure 2.13c). Holes bored by the mollusc *Pholas chiloensis* give the platform a heavily pitted surface.

Chucalen, along with the other late Holocene sites at Maullín and Cocotue, lies to the south of the area influenced by the 2010 earthquake and tsunami. Witnesses to the 1960 tsunami suggest that a series of three waves resulted in runup exceeding 15 m on exposed headlands on the northern edge of the Lacui Peninsula, with 5 m waves striking Ancud, decreasing to 1.5 m in Bahía Quetalmahue (Sievers *et al*., 1963). Bartsh-Winkler and Schmoll (1993), however, suggested waves of several times this magnitude may have entered the Quetalmahue estuary across the isthmus that joins the Lacui Peninsula, close to my sampling area.

Based on the pre- and post-earthquake lower growth limits of terrestrial vegetation, Plafker and Savage (1970) estimated subsidence of 1.0 ± 0.2 m approximately 1 km south of Chucalen.

Vegetation limits suggested greater subsidence of 1.5 to 1.8 m to the east along the southern edge of Bahía Quetalmahue (figure 2.13b).

Maullín

Cisternas *et al*. (2005) worked extensively on the intertidal and freshwater lowlands on the southern side of the Maullín estuary, opposite the town of Maullín (figure 2.14). The location lies approximately 8 km inland from the mouth of the large estuary. The coastal lowlands feature a number of faint beach ridges and terraces, identified by Atwater *et al*. (1992) as resulting from net late Holocene emergence. An abandoned sea cliff and a Pleistocene terrace approximately 15 m above present limits the landward extent of the coastal lowlands (Cisternas *et al*., 2005; figure 2.14). The findings of Cisternas *et al*. (2005), discussed further in chapter six, suggest the sediments overlying the younger terraces record evidence for multiple late Holocene tsunamis and coincident deformation. I revisited Maullín in January 2012 with Marco Cisternas to obtain a new biostratigraphic record for the site. Our visit focussed on the area at the seaward end of Cisternas *et al*.'s (2005) main transect (figure 2.14c).

Estimates by local residents and using the lower growth limits of vegetation placed the magnitude of subsidence in 1960 close to the site at Maullín at 1.5 to 1.7 m (Plafker and Savage, 1970; figure 2.14b). Of the eight tsunami waves recorded in the estuary, the highest reached 14 m (Seivers *et al.*, 1963; Cisternas *et al.,* 2000).

Cocotue

Cisternas *et al*. (2007) suggest that the exposed site of Cocotue, on the western side of the isthmus that joins the Lacui Peninsula to the rest of Chiloé, also records evidence for past tsunamis, in addition to shaking-induced mass movements (figure 2.15). Here, a narrow terrace (10 m to 50 m in width, 3 m above mean sea level) lies behind the modern high-energy beach (figure 2.15b). A 40 m high former sea cliff, cut into Pleistocene glacial outwash (Marco Cisternas, pers. com., 2012), abruptly limits the landward extent of the terrace. A small river, Río Pudeyi, flows from northeast to southwest along the back of the beach, contributing to the erosion of the terrace in the northern part of the site. Southwest of the point where Río Pudeyi joins the sea, vegetation is actively colonizing the beach below the terrace (figure 2.15c).

Due to sparsely populated nature of the coastline at Cocotue, no data are available on the magnitude of subsidence in 1960. The site lies marginally to the west of Chucalen and

extrapolating the estimates of Plafker and Savage (1970) suggests subsidence at the site exceeding 1 m. Given the reported effects of the tsunami in other areas of northern Chiloé, including the substantially better sheltered Bahía Quetalmahue, it can be assumed that the tsunami was very large at Cocotue.

2.4 Summary

The subduction of the Nazca plate beneath South America causes several types of earthquake, of which large magnitude subduction megathrust events are the most damaging. Historical records of the shaking, deformation and coincident tsunamis associated with these events suggest along-strike segmentation of the subduction zone. This thesis primarily focuses on the sedimentary record of earthquakes in the Valdivia seismic segment, the 1000 km long section that ruptured during the 1960 Valdivia earthquake. Chile's glacial history contributes to an uncertain and possibly complex relative sea-level history. Falling mid to late Holocene relative sea levels, as predicted by modelling studies and identified from field evidence, are not conducive to the preservation of sedimentary evidence for earthquakes. Previously identified sites in the centre of the Valdivia segment, however, suggest that certain locations may record centennial to millennial length sedimentary records. I focus on three possible fossil sites, including a previously unreported site at Chucalen and additional sites at Maullín and Cocotue. The two modern marshes of Puente Quilo and Estero Guillingo lie close to the fossil sites and provide the samples required to characterise the modern intertidal marsh environment. Three further sites investigated by the *Sediment Signatures project* enable testing of the coseismic deformation reconstruction approach.

3. Approach

3.1 Introduction

This chapter details the methods used to fulfil the objectives set out in chapter one. Section 3.2 discusses field methods, including sediment sampling and the derivation of tidal levels for each of the field sites described in chapter two. Section 3.3 outlines the laboratory methods used to analyse modern and fossil marsh sediments. Section 3.4 and 3.5 detail the chronostratigraphic and statistical methods used to derive estimates of the age and elevation of past environments.

3.2 Field methods

3.2.1 Modern marsh sediments

Investigating evidence for past changes in tidal marsh systems starts with understanding the modern characteristics of those systems. Assuming uniformitarianism, the spatial variation in contemporary marsh environments serves as an analogy for temporal changes in the fossil environment.

Field seasons in April 2011 and January 2012 provided the opportunity to collect modern sediment samples from the marshes at Estero Guillingo and Puente Quilo respectively. A single transect at each site, ranging from the tidal mudflat to the limit of intertidal vegetation, provided samples at regular vertical intervals (5 cm). Transects aimed for areas incorporating all of the recognised vegetation zones and avoided features which might suggest erosion, such as cliffs at the seaward edge of the vegetated marsh. The number of samples per transect depended on the elevation of the marsh to upland transition and the accessibility of the tidal flat; Puente Quilo yielded 50 samples and Estero Guillingo 46. At each point along the transect I removed a 10 x 10 x 1 cm sample, which was then stored in cool, dark conditions and refrigerated on returning to the UK. Samples of this thickness average seasonal blooms in diatom assemblages, while minimising relative sea-level changes over the course of the accumulation of the sample. The potential for rapid postseismic deformation currently precludes the use of modern samples from transects in the rupture zone of the 2010 earthquake.

3.2.2 Fossil marsh stratigraphy

Exposures, hand-dug pits and gouge cores allowed investigation of the stratigraphy of the fossil sites at Chucalen, Maullín and Cocotue. The Troels-Smith (1955) scheme for the classification of the physical components of sediments provided a consistent framework for in-field sediment description. During the April 2011 field season, I collected representative sediment monoliths from a cleaned exposure at Chucalen. Sampling of exposures in January 2012 provided monoliths characteristic of the stratigraphy at Maullín and Cocotue. The monolith approach, unlike the majority of coring methods, ensures that sediments are not vertically compacted during sampling. Cleaning and flattening of the exposure reduced the probability of contamination from marine water infiltration and minimised errors associated with sample depth measuring resulting from an angled exposure face. Overlaps between closely spaced monoliths ensured the recovery of an uninterrupted sedimentary sequence. The nature of the sediments made monolith tins unnecessary, thus avoiding further disturbance of the sediments; instead, I cut blocks of sediment using a knife and immediately wrapped them in plastic for transport and storage. Garrett *et al*. (accepted) describes the recovery of the monolith and core samples used for investigation of the 1960 and 2010 earthquakes (appendix 1.1).

3.2.3 Surveying and tidal measurements

To establish the elevation of each surface sample and every exposure, pit or core top, I levelled the difference in elevation from a site-specific temporary benchmark using a Leica automatic level or a Leica differential GPS system with a Smart Rover. In the absence of maintained geodetic benchmarks, a variety of tidal measurements established the elevation of the temporary benchmarks with respect to local mean sea level and, subsequently, the elevation of each modern or fossil sample. Levelling transects consistently closed with errors of less than 0.05 m.

To account for the difference in tidal range at the different modern and fossil sites, I convert the elevations of all modern samples into a standardised water level index (SWLI). Quantitative diatom transfer functions (described in section 3.5.3) use SWLI as the environmental variable and yield palaeomarsh surface estimates for fossil samples in SWLI units. Following Hamilton and Shennan (2005a), I calculate the SWLI for each sample using the equation:

$$SWLI_n = \frac{100(h_n - h_{MSL})}{h_{MHHW} - h_{MSL}} + 100 \qquad \text{(Equation 3.1)}$$

Where:

$SWLI_n$ = Standardised water level index for sample n

h_n = Elevation of sample n (metres)

h_{MSL} = Mean sea level elevation (metres)

h_{MHHW} = Mean higher high water elevation (metres)

Rearranging equation 3.1, incorporating the appropriate levels for mean sea level and mean higher high water (MHHW) at the fossil site of interest, converts SWLI units into estimates of marsh surface elevation above mean sea level in metres.

Sample elevation and tide levels for the modern transects

The modern marsh transects at Puente Quilo and Estero Guillingo lie approximately 15 km to the west of the Ancud permanent tide gauge (figure 2.7). This gauge provides tidal observations, mainly at two minute intervals, between June 2008 and May 2012 (IOC, 2012). Having first screened the data to remove outlying samples, I derived figures for mean sea level and mean higher high water. The latter is the average of the highest tidal observations in each tidal cycle throughout the four year record. During sampling at Puente Quilo during the 2012 field season, Dr Rob Wesson of the United States Geological Survey deployed a temporary ultrasound tide gauge to record tidal fluctuations. This gauge provided high frequency observations (recordings every eight seconds) for 28 hours (figure 3.1). Cleaning this data removes outliers and corrects for variations in temperature. Variations in pressure and humidity make negligible differences to the observations. Comparison with observations from the Ancud permanent tide gauge for the same period highlights differences between tidal amplitudes at Ancud and Puente Quilo (figure 3.1). The close proximity of the permanent and temporary tide gauges suggests this is likely to reflect tidal amplification in the enclosed Bahía Quetalmahue, rather than resulting from variations in atmospheric pressure. I apply a scaling factor of 1.08 to fit the Ancud data to the Puente Quilo data and use this to derive mean higher high water at Puente Quilo (table 3.1).

Low tide falls below the safely accessible area of tidal flat at Estero Guillingo, limiting tidal observations to the top of the tidal cycle. I relate the elevation of the temporary benchmark at Estero Guillingo to mean sea level by comparing 36 tidal observations over two successive high tides with coincident tidal observations from Ancud, scaled for Puente Quilo. This approach relies on the assumption that the elevations of mean sea level and mean higher high water do not change between Puente Quilo and Estero Guillingo (table 3.1). Less than five kilometres separates

the sites, which also lie at similar distances from the mouth of the bay, suggesting that if any discrepancy exists, it is unlikely to be substantial.

Nelson *et al*. (2009) levelled the elevation of the Valdivia transect samples to mean sea level. The Corral tide gauge, located at the mouth of the Valdivia estuary, provides high frequency tidal observations (IOC, 2012). As tidal amplitude diminishes up-estuary, I scale the Corral tide gauge data using Admiralty (2004) data on tide levels at Corral and Valdivia to provide estimates of mean higher high water at Río Angachilla and Isla del Rey (table 3.1).

Sample elevation and tide levels for the fossil sites

Chucalen lies two kilometres northwest of Puente Quilo; accordingly, I also use the Puente Quilo estimates of mean higher high water and mean sea level for the fossil site (table 3.1). Two independent measures of the elevation of the cores and exposures – levelling observations of high tides at Chucalen and levelling from the Puente Quilo tide gauge to Chucalen – provided values that diverge by 0.05 m.

At Maullín, scaling of the Ancud tide gauge record by the difference between Admiralty (2004) tide levels at Ancud and Maullín provides estimates of mean higher high water and mean sea level (table 3.1). The marsh front is relatively uniform in elevation and, based on Cisternas *et al*. (2005), the top of the sampled exposure is at 1.0 ± 0.2 m above mean sea level.

Rob Wesson's ultrasound tide gauge provided tidal observations and estimates of mean higher high water and mean sea level for Cocotue (table 3.1). A levelling circuit related the elevation of the sampled exposure to the tide gauge.

Tide gauges, either in their original or a scaled form, provide tidal parameters for the *Sediment Signatures* sites (Garrett *et al*., accepted). Río Andalién uses the difference between mean sea level and mean higher high water from a multiannual, high frequency time series from the nearby tide gauge at Talcahuano (IOC, 2012). Tubul uses levels from the Lebu tide gauge time series (IOC, 2012), scaled to account for the increase in the difference between MSL and MHHW to the north of Lebu suggested by Admiralty (2004) tide levels at Lebu and Coronel. Río Tirua uses levels from the Lebu tide gauge time series, scaled to account for the increase in the difference between MSL and MHHW to the south of Lebu suggested by Admiralty (2004) tide levels at Lebu and Caleta La Hacienda.

For locations close to permanent tide gauges, I estimate errors associated with the difference between mean sea level and mean higher high water to be ± 0.05 m. For sites without tide gauges, I estimate this error to be ± 0.1 m.

3.3 Laboratory methods

The first purpose of laboratory methods is to characterise modern marsh environments. Particle size analysis and loss on ignition provide data on the variation in grain sizes and the proportion of organic content respectively. Diatom analysis establishes the modern distribution of diatoms across the intertidal zone. An understanding of the contemporary environment, combined with laboratory analyses of core or monolith particle size distributions, organic content and diatom assemblages then facilitates initial assessments of the changes in marsh surface elevation recorded by fossil sequences. Further statistical approaches (discussed in section 3.5) use the relationship between modern diatoms and elevation to quantify past changes.

3.3.1 Particle size analysis

Following the addition of hydrogen peroxide to remove organic matter and sodium hexametaphosphate as a dispersant, laser diffraction using a Beckman coulter LS 13 320 with aqueous liquid module provided particle size distributions. I present percentage data summarised into three categories: sand (2 mm to 62.5 μm), silt (62.5 – 3.9 μm) and clay (3.9 – 0.061 μm).

3.3.2 Organic content

Following Dean (1974), I define the organic content of a sample as the percentage weight lost on ignition (%LOI). Subsamples dried at 105°C for a minimum of 18 hours before being ashed at 550°C for 4 hours. Loss on ignition expresses the weight lost during ashing as a percentage of dry weight; I assume this to be proportional to the organic content of the sample (Dean, 1974; Hieri *et al.*, 2001).

3.3.3 Diatom analysis

Background to the use of diatoms in relative sea level studies

Diatoms, unicellular algae in the class *Bacillariophyceae*, inhabit freshwater, intertidal and marine environments. Their value as indicators of sea level stems from the great diversity of species found in restricted, elevation-controlled niches in intertidal environments (e.g. Nelson and Kashima, 1993; Sherrod, 1999; Zong and Horton, 1999; Sawai *et al*., 2004; Hamilton and Shennan, 2005b; Horton *et al*., 2006; Woodroffe and Long, 2009). Flooding duration and covariables such as salinity, particle size, pH, nutrient supply and vegetation play a central role in determining diatom distributions (Whiting and McIntire, 1985; Gehrels *et al*., 2001; Patterson *et al*., 2005; Roe *et al*., 2009). Consequently, different elevations across a modern tidal marsh support different diatom assemblages. Changes in assemblages in sequences of fossil samples can, therefore, provide indications of changing relative sea level over time (e.g. Zong, 1997; Sawai, 2001; Hamilton and Shennan, 2005a; Long *et al*., 2010). In section 3.5, I discuss how statistical approaches use diatom assemblages to provide quantitative reconstructions of past marsh surface elevations.

Diatoms, unlike foraminifera, another microfossil widely used in relative sea-level investigations (e.g. Scott and Medioli, 1978; Horton and Edwards, 2006), are not subject to problems of infaunality due to the majority of species relying on light for photosynthesis (cf. Duchemin *et al.*, 2005). Furthermore, diatoms are highly abundant and well preserved in fossil sediments due to their siliceous cell walls. I assume evolution in morphology or habitat preference is negligible over the short time interval of interest.

Methodology for preparation and counting

Processing of subsamples for diatom counting followed the standard procedures of the laboratories of the Department of Geography, Durham University. Following the addition of hydrogen peroxide to remove organic material and disaggregate diatom chains into individual frustules, I mounted slides using Naphrax and counted diatom valves using a Leica DM LB2 microscope with an oil-immersion lens at a magnification of x1000. Minimum counts of 250 valves per sample ensure confidence intervals for taxon proportions are within acceptable limits (Fatela and Taborda, 2002; Woodroffe, 2006). Identifications follow Rivera and Valdebenito (1979), Hartley *et al*. (1996), Siqueiros-Beltrones and López-Fuerte (2006), Cremer *et al*. (2007), Horton *et al*. (2011) and digital reference collections held by Durham University, The University of Colorado

(2010, 2012) and The Academy of Natural Sciences of Drexel University (2012). Use of the World Register of Marine Species (Appeltans *et al.*, 2012) ensures up-to-date nomenclature.

I use C2 version 1.7.2 (Juggins, 2011) to draw assemblage diagrams. As salinity is not the primary environmental variable of interest, assemblage diagrams presented here do not split diatoms into traditional halobian classes (Hemphill-Haley, 1993), but rather into elevation categories defined by species optima calculated during transfer function development (section 3.5.3).

3.4 Chronological methods

Radiometric dating methods contribute to achieving objectives relating to constraining the timing of palaeoearthquakes and comparing the timing of stratigraphically defined earthquakes with historical records. A well constrained chronology also assists in determining rates of relative sea-level change. I primarily apply Accelerator Mass Spectrometry (AMS) radiocarbon dating, but also discuss a relative caesium-137 (^{137}Cs) concentration approach as a method for quickly establishing whether certain deposits relate to the 1960 earthquake and tsunami.

3.4.1 Radiocarbon dating

AMS radiocarbon dating uses the radioactive decay of an isotope of carbon to provide age estimates for carbon-bearing materials (Bowman, 1990; Walker, 2005; Hua, 2009). Carbon exists primarily in two stable isotopes, ^{12}C and ^{13}C. Interaction between cosmic rays and nitrogen-14 in the lower stratosphere and upper troposphere produces a third, radioactive isotope, ^{14}C. Carbon dioxide molecules incorporating ^{14}C atoms disperse throughout the atmosphere and enter terrestrial carbon cycles through photosynthesis. ^{14}C decays, losing a beta particle and returning to stable ^{14}N. Continued atmospheric production of ^{14}C from ^{14}N counters the constant decay and terrestrial organisms remain in isotopic equilibrium with the atmosphere through photosynthesis or ingestion of plant material. The death of the organism halts this replenishment; isolation from the ^{14}C source enables decay, unsupported by photosynthesis. The relative number of ^{14}C atoms in a sample therefore reflects the time elapsed since death.

To provide a chronology for the sampled sediments at Chucalen, I use AMS radiocarbon dating to provide age estimations for a stratigraphically ordered series of samples. A Natural Environment Research Council (NERC) radiocarbon allocation (allocation number 1581.0911) provided 16 closely spaced dates. At the time of writing, December 2012, the NERC Radiocarbon Facility has

reported results for 15 of these samples. Rather than solely dating material from the uppermost parts of buried soils to limit the timing of coseismic subsidence (cf. Cisternas *et al*., 2005), I develop a full profile of dates from organic-bearing layers in a single exposure at Chucalen. This approach allows the development of age-depth models, which may better constrain the timing of subsidence and also allow age estimation for all depths within the sequence.

In an attempt to minimise the chance of selecting younger intrusive roots or more substantial reworked material I aimed to sample horizontally bedded above ground parts of herbaceous plants, including seeds (cf. Nelson, 1992; Marshall *et al*., 2007). Sample preparation followed the standard procedures of the NERC Radiocarbon Facility. Samples were digested in 1M hydrogen chloride at 80°C for 30 minutes, washed free from mineral acid with deionised water, then digested in 0.2 M potassium hydroxide at 80°C for 20 minutes. The residue was rinsed free of alkali, digested in 1 M hydrogen chloride at 80°C for one hour, then rinsed free of acid, dried and homogenised. The total carbon in a known weight of the pre-treated sample was recovered as carbon dioxide by heating with copper oxide in a sealed quartz tube. Iron/zinc reduction converted the gas to graphite. While I anticipated preparation of multiple graphite targets, the low abundance of suitable macrofossils enabled only single targets and standard rather than high analytical precision.

By convention, laboratories report radiocarbon ages in radiocarbon years before present, where present is AD 1950 (Hua, 2009). The terms percentage of modern carbon (*pMC*) or fraction (*F*) of modern carbon express the radiocarbon ages of samples postdating 1950 (Stuiver and Polach, 1977; Reimer *et al*., 2004). The variability in past atmospheric ^{14}C resulting from solar variability and anthropogenic input necessitates calibration of radiocarbon dates into calendar years. Calibration curves, predominantly based on tree ring measurements, provide a method for this conversion. For the majority a samples, I employ the southern hemisphere specific curve SHCal04 (McCormac *et al*., 2004).

The advent of sustained atmospheric nuclear weapons testing in the early 1950s dramatically increased atmospheric ^{14}C (Reimer *et al*., 2004). Year-to-year differences in the post-1955 period can be substantial, facilitating determinations with precision of a few months to a few years. For samples exceeding 100 pMC, I employ the post-bomb atmospheric southern hemisphere curve of Hua and Barbetti (2004).

P_sequence models (Bronk Ramsay, 2008, 2009a) in OxCal v.4.1 (Bronk-Ramsey, 1995) use Bayesian reasoning to develop age-depth models. The approach uses prior information on the

stratigraphic position and ordering of samples to constrain posterior age distributions. Unlike *Sequence* models (Bronk Ramsay, 1995), *P_sequence* models can provide interpolated age range estimates for any given depth within a sequence. When combined with elevation estimates from diatom data (section 3.5), this enables investigation of rates of change over time. As substantial changes in sedimentation rate may accompany the abrupt lithological changes that signify coseismic deformation, I allow the model a high degree of flexibility in this respect, assigning a *k* value of 100 (Bronk-Ramsey, 2008).

3.4.2 Caesium-137

Caesium-137 (^{137}Cs) is a short-lived radionuclide detectable in the environment since the beginning of atmospheric nuclear weapons testing (Walker, 2005). The occurrence of elevated concentrations implies deposition after the early 1950s. Predominantly northern hemisphere test sites resulted in low, but identifiable ^{137}Cs fallout in the southern hemisphere (Schuller *et al*., 1993, 2002; Arnaud *et al*., 2006). I compare concentrations in samples immediately underlying selected tsunami deposits with background concentrations to identify which relate to deposition in 1960. This approach assumes that ^{137}Cs remains immobile in the sediment column, a prerequisite that may not be met in tidal marsh settings (Morris *et al*., 2000; Harvey *et al*., 2007). Rapid changes in concentration in closely spaced samples indicate this is not an issue in the locations investigated in this thesis.

The preparation and analysis of samples for gamma spectroscopy followed the standard methods of the Department of Geography, Durham University. Freeze-drying and ball milling homogenised centimetre thick sediment samples. Material was then transferred to plastic tubes, compacted and weighed. The departments Ortec 'p' type germanium gamma ray spectrometers measured gamma ray energies, providing total ^{137}Cs activity measured in Becquerels (Bq).

3.5 Statistical analysis

3.5.1 Zonation of modern datasets

I use two complimentary methods to assess the zonation of contemporary diatom datasets: stratigraphically unconstrained CONISS (CONstrained Incremental Sum of Squares) and unconstrained ordination. CONISS, an agglomerative cluster analysis technique performed in Tilia v.1.7.16 (Grimm, 2011), provides a statistical basis for identification of groups of similar samples

in contemporary data. The resulting dendrogram links samples based on the similarity of their assemblages. Ordination methods, including Detrended Correspondence Analysis (DCA; Hill and Gauch, 1980), extract new principal axes to describe the major trends in multidimentsional data (Birks, 1995; Legendre and Legendre, 1998; Lepš and Šmilauer, 2003). In doing so, unconstrained ordination highlights groupings of samples, complementing cluster analysis (Kovach, 1995). The proximity of samples on DCA sample plots reflects the similarity between their species compositions; samples that plot close together are more similar than those that plot further apart. Investigation of the vertical distribution of clusters identified from visual assessment of CONISS dedrograms and DCA sample plots may highlight elevation-dependent zonation of the modern dataset.

3.5.2 Ordination

Ordination serves two purposes. In its unconstrained form, it may assist in the identification of clustering within a dataset (discussed above). When constrained by an environmental variable or variables, ordination quantifies the rate of species turnover along a gradient of interest and assesses the proportion of the variability in the modern diatom data that known variables explain (Birks, 1995; ter Braak, 1996). Use of the software CANOCO v.4.55 (ter Braak and Šmilauer, 2003) enabled ordination, in both unconstrained and constrained forms.

High rates of species turnover, identified when the gradient of the first Detrended Canonical Correspondence Analysis (DCCA) axis exceeds two standard deviation units, suggest species are best modelled using unimodal rather than linear response curves (Birks, 1995). This choice informs both the type of constrained ordination methods required for investigation of the dependence of diatom data on measured environmental variables and the most appropriate class of transfer function models (section 3.5.3).

Once the rate of species turnover has identified the most appropriate constrained ordination approach, the unimodal method, DCCA, or its linear equivalent, Redundancy Analysis, may provide information on the proportion of the variability in the modern dataset attributable to known environmental variables. As elevation is the variable of interest to this investigation, the proportion of the variability in modern diatom assemblages explained by SWLI is of particular relevance. If other known environmental factors, particularly those that do not covary with elevation, explain a larger proportion of the modern variability, diatoms may not provide meaningful indications of past relative sea level.

3.5.3 Transfer function development

Transfer functions use regression to express an environmental parameter as a function of a modern training set of biological data (Imbrie and Kipp, 1971; Birks, 1995, 1998). Subsequent calibration calculates quantitative estimates of the environmental parameter of interest from fossil biological data (figure 3.2). Microfossil-based transfer function – calibration approaches have provided estimates of the magnitude of coseismic deformation in the Pacific Northwest (Guilbault *et al*., 1995; Hughes *et al*., 2002; Hawkes *et al*., 2005, 2010), Alaska (Zong *et al*., 2003; Hamilton and Shennan, 2005a, b), Japan (Sawai *et al*., 2004) and New Zealand (Hayward *et al*., 2006), as well as quantifying aseismic relative sea level changes in a diverse range of locations (e.g. Horton *et al*., 2000; Edwards *et al*., 2004; Leorri *et al*., 2008; Woodroffe and Long, 2009; Kemp *et al*., 2011).

As discussed in section 3.3.3, diatoms assemblages are highly zoned with respect to the elevation gradient in intertidal environments (Nelson and Kashima., 1993; Sherrod, 1999; Zong and Horton, 1999). After applying the approaches outlined in section 3.5.2 to determine the elevational control on diatoms in south central Chilean marshes, I develop transfer functions with elevation as the environmental variable.

Transfer functions may use either linear or unimodal approaches to model species' responses to the environment. As with ordination, high rates of species turnover along the environmental gradient of interest imply unimodal models will best represent the response (figure 3.2b) (Birks, 1995). DCCA first axes lengths exceeding the cutoff of two standard deviation units are typical where samples are from a long environmental gradient and the variable influences the chosen microfossil group. Following this test, I employ the unimodal method weighted averaging partial least squares regression (WA-PLS; ter Braak and Juggins, 1993; ter Braak *et al*., 1993) in C2 version 1.7.2 (Juggins, 2011), to reconstruct marsh elevation from fossil samples.

The first component of WA-PLS uses an abundance weighted average of the SWLI values of every sample in which a particular species occurs to assign a species coefficient (ter Braak and Juggins, 1993). These species coefficients are essentially estimations of the optimum value along the elevation gradient for each species. Subsequent WA-PLS components update these species coefficients to improve the fit between the observed and predicted sample elevations using weighted averages of the residual elevation values (ter Braak and Juggins, 1993). WA-PLS offers benefits over simple Weighted Averaging regression (WA; ter Braak, 1987); it is less susceptible to edge effects, overestimation of species optima at low elevations and underestimation at high

elevations, and uses residual structure in the species data to further improve estimates of species optima (Birks, 1995, 1998). Through the inclusion of additional components, WA-PLS may better represent the true nature of the dataset, where factors other than the primary variable of interest influence the distribution of species (ter Braak and Juggins, 1993; ter Braak *et al*., 1993).

I assess the performance of transfer function models in terms of root-mean square error of prediction (RMSEP) and squared correlation (r^2) of observed versus estimated values (figure 3.2c). Bootstrapping, a method of resampling the dataset to produce pseudoreplicate training sets, is favoured over jack-knifing as the preferred method of cross-validation as it provides sample-specific errors for each fossil sample and is less prone to bias (Birks, 1995; Manly and Chotkowski, 2006). The choice of component depends upon the prediction statistics, with the lowest component that provides an acceptable model selected (Horton and Edwards, 2005). RMSEP provides a measure of the precision of the transfer function; alongside this, I also discuss predictive power, by which I mean the range of environments that the modern training set encompasses.

3.5.4 Assessing reconstruction performance

Whether statistically or ecologically sound, the calibration of biological data using a transfer function model will always produce a result (Birks, 1998). Consequently, further analysis is required to determine the reliability of the result. The primary consideration must always be whether the result makes ecological sense given the assemblage data. This may be assessed simply through visual appraisal of the diatom data alongside the transfer function reconstruction. Statistical techniques may supplement this approach, providing a more rigorous basis for assessing reconstruction performance.

The modern analogue technique in C2 v.1.7.2 (Juggins, 2011) provides minimum dissimilarity coefficients (MinDC), measures of the similarity between each fossil sample and samples in the modern training set (Birks *et al*., 1990; Simpson, 2007). Lower values indicate greater similarity with the samples in the modern training set. MinDC thresholds, based on the dissimilarity between samples in the modern training set, distinguish whether fossil samples have 'good', 'close' or 'poor' modern analogues (Birks, 1995; Horton, 1997; Hamilton and Shennan, 2005a; Woodroffe, 2009; Watcham *et al*., 2012). While other investigations have employed a wide range of threshold values, following Watcham *et al*. (2012) I use the 5th percentile of the modern dissimilarity values as the threshold between 'good' and 'close' modern analogues and the 20th percentile as the cut-off for a 'poor' modern analogue.

Other statistical approaches to comparing the similarity between modern and fossil assemblages are available. Birks (1998) proposes *analogue statistics*, based on identifying the proportions of taxa in fossil assemblages absent or poorly represented in modern samples. While this approach may supplement MinDC, the lack of accepted thresholds precludes its use as more than just a relative measure. Similarly, *constrained ordination in a mutual ordination space* (Woodroffe, 2009) lacks defined thresholds and is not applied in this thesis.

Where available, comparison of transfer function reconstructions with independent data, for example from tide gauges or GPS, provides a second measure of reconstruction performance (e.g. Gehrels *et al*., 2005; Kemp *et al*., 2009, 2011; Garrett *et al*., accepted). This approach is central to the third objective: *test the performance of the approach by reconstructing coseismic deformation associated with recent, well documented Chilean earthquakes*. Close correspondence with recent independent data is an encouraging sign of performance; however, this measure alone does not imply that the transfer function is successful throughout the sampled sequence (cf. Kemp *et al*., 2009, 2011).

3.5.5 Estimating the magnitude of coseismic deformation

The difference between their inferred elevations provides an estimate of the magnitude of elevation change between two fossil samples:

$$D_c = \mathrm{E}_{\mathrm{post}} - \mathrm{E}_{\mathrm{pre}} \qquad \text{(Equation 3.2)}$$

Where:

D_c = coseismic deformation estimate, in metres

E_{post} and E_{pre} = post-deformation and pre-deformation elevation estimates, in metres.

The resulting deformation value is negative for subsidence and positive for uplift. Following Preuss (1979), I define the error associated with this change as:

$$D_c\ error = \sqrt{(\mathrm{E}_{\mathrm{pre}}\ \mathrm{error})^2 + (\mathrm{E}_{\mathrm{post}}\ \mathrm{error})^2} \qquad \text{(Equation 3.3)}$$

Where:

$D_c\ error$ = coseismic subsidence error, in metres

$E_{pre}\ error$ and $E_{post}\ error$ = sample specific standard errors provided by the transfer function

3.5.6 Quantifying relative sea level change

The conversion of palaeomarsh surface elevation estimates into relative sea-level estimates requires the field elevation of each sample. Equation 3.4 defines relative sea level as:

$$RSL_n = FE_n - PMSE_n \quad \text{(Equation 3.4)}$$

Where:

RSL_n = Relative sea level estimate for sample n

FE_n = Field elevation of sample n (metres above mean sea level)

$PMSE_n$ = Palaeomarsh surface elevation (metres above mean sea level)

As the calculation of relative sea level incorporates the field elevation, the error associated with the estimate correspondingly increases. While I assume the transfer function sample specific error is sufficient to encompass errors relating to the estimation of PMSE and the distance between samples within a sequence, additional sources of error influence the field elevation of a sample. I define the relative sea-level error estimate as:

$$RSL\ error = \sqrt{(\text{PMSE error})^2 + (\text{FE error})^2} \quad \text{(Equation 3.5)}$$

Where:

$RSL\ error$ = error associated with a relative sea level estimate

$PMSE\ error$ = sample specific standard errors provided by the transfer function

$FE\ error$ = error in estimating the field elevation of the sample

Errors in estimating the field elevation of a sample derive from the inaccuracies of relating the core or exposure top to tidal levels and relating the sample depth to the core top. The magnitude of this error is larger at Maullín than at Chucalen due to uncertainties over the elevation of the marsh front exposure.

3.6 Summary

This chapter has described the methods used to fulfil the objectives set out in chapter one. Modern marsh sampling at Puente Quilo and Estero Guillingo enables characterisation of contemporary intertidal diatom distributions and the development of transfer functions for the purpose of reconstructing former marsh surface elevations. Visual appraisal, a statistical approach and comparison of coseismic deformation reconstructions for the 1960 and 2010 earthquakes with independent data allows assessment of transfer function reconstruction performance. Stratigraphic surveys using cores, pits and exposures allow interrogation of coastal sediments for evidence of past earthquakes. Collection of representative monoliths and cores enables further lithological, biostratigraphic and chronological analyses. Calibration of diatom assemblages provides estimates of coseismic deformation associated with palaeoearthquakes. Radiometric dating methods constrain the timing of coseismic deformation and allow comparison with historical records and other palaeoseismic investigations.

4. Results: modern Chilean intertidal marshes

4.1 Introduction

Reconstructing past changes in intertidal environments requires a comprehensive understanding of modern tidal marshes. Spatial variations in modern marshes, and the corresponding environmental controls, provide analogues for temporal changes. This chapter discusses the vertical zonation of flora, organic content and particle size in the tidal marshes of northern Isla de Chiloé. Cluster analysis and ordination relate the zonation of diatom assemblages to environmental factors including elevation, a parameter that covaries with other factors including frequency and duration of tidal inundation, salinity and pH. After establishing the link between diatoms and elevation, I develop transfer function models for the purpose of reconstructing marsh surface elevations from fossil diatom assemblage data.

4.2 Tidal marsh characteristics

4.2.1 Vegetation

Chilean intertidal marshes feature vertical zonation of vascular plants (San Martin *et al*., 1992; Jennings *et al*., 1995). I identify three intertidal floral zones at both Puente Quilo and Estero Guillingo, bounded at their lower extent by unvegetated tidal flat and by freshwater scrub at their upper limit (figure 4.1a, b, table 4.1). While vascular plants are absent, the Puente Quilo tidal flat plays host to commercial gathering of the red algae *Gracilaria chilensis*. Both sites feature eroded vegetated marsh fronts; however, where uneroded, the lower limit of vegetation occurs around 0.75 m above mean sea level at both locations. The total vertical range of low, mid and high marsh vegetation is larger at Estero Guillingo than at Puente Quilo (figure 4.2a); an unexpected result given the close proximity of the two sites and the assumed tidal range invariance. The discrepancy might reflect the influence of other factors such as variability in livestock grazing, substrate and moisture levels, or could suggest a larger tidal range and lower mean sea level at Estero Guillingo. In the absence of high frequency data for the entire tidal cycle for Estero Guillingo, I elect to assume that non-elevation related factors influence the variation in the elevation of the transition to freshwater scrub.

4.2.2 Organic content and particle size

The organic content of samples from Puente Quilo and Estero Guillingo increases with increasing elevation (figure 4.2b). Loss on ignition values vary from < 10 % on the tidal flats to over 70 % in the high marsh environments, with the transition from low to high organic content occurring in the mid marsh vegetation zone at both sites.

Sand-sized particles dominate the majority of Puente Quilo samples, with two peaks in silt-sized particles around mean sea level and above mean higher high water (figure 4.2c). The Estero Guillingo sediments are typically more silt and clay-rich, with some sandier elevations between mean sea level and mean higher high water. Inter-site variability in sedimentological parameters reflects differences in exposure to wave energy, fluvial input and sediment supply. This work does not quantify intra-site variability in particle size and organic content for a given elevation; however, this is likely in tidal marsh situations, particularly due to the presence of tidal creeks.

4.3 Modern intertidal diatoms

Ninety-six modern samples from Puente Quilo and Estero Guillingo contain 149 identified diatom species from 57 genera and seven unidentified taxa (appendix 4.1 on the attached CD). Eighty-four species are found in both transects and 25 species equal or exceed 10 % in one or more sample (figure 4.3).

The defining features of the combined Chiloé dataset are the presence of low turnover, low diversity assemblages below mean higher high water (sub-MHHW) and more variable, species-rich assemblages at higher elevations (supra-MHHW). While some living diatoms may occupy small vertical ranges due to varying tolerances to salinity, duration and frequency tidal flooding, substrate and other elevation-correlated factors (Vos and de Wolf, 1993; Zong and Horton, 1998; Sherrod, 1999), similar low elevation uniformity is also reported in other datasets, for example from northern Japan (Sawai, 2001), British Columbia (Roe *et al*., 2009) and Greenland (Woodroffe and Long, 2009). The broad elevation tolerances of certain taxa may reflect cosmopolitan distributions; however reworking and redistribution of diatom valves may also contribute to uniform low elevation assemblages (Sherrod, 1999; Sawai, 2001). While some investigations try to remove the effects of reworking by separating an assumed allochthonous component (e.g. Szkornik, 2007), no attempt is made here as this mixture of local and allochthonous valves will also occur in fossil sediments (Zong, 1997).

Figure 4.4 compares the most common diatom species at Puente Quilo and Estero Guillingo with the distribution of diatoms in samples from two transects from Río Angachilla and Isla del Rey in the Valdivia Estuary (Nelson *et al*., 2009). I have updated the species names used in the Valdivia dataset and cross-referenced each species with my identifications to ensure consistency in taxonomic subdivision and nomenclature. The 32 samples of the modified Valdivia dataset include 88 species from 54 genera (appendix 4.2 on the attached CD). Fifty species occur in both the Valdivia and Chiloé datasets. The Valdivia assemblages show less vertical zonation, however the majority of Valdivia samples are from below MHHW, with few samples from the elevations that show the clearest zonation in the Chiloé transects. There is little overlap between the dominant species in the Valdivia and Chiloé datasets, suggesting that elevation is not the sole control on diatom distributions at a regional scale.

4.4 Relating diatom distributions to elevation

Visual inspection of the species data suggests zonation along the elevation gradient. Multivariate techniques, including cluster analysis and ordination, can further detect and describe this zonation. Unconstrained cluster analysis is an agglomerative method, progressively adding the most similar samples together to form clusters on a dendrogram. The unconstrained ordination method Detrended Correspondence Analysis (DCA) represents samples in a multidimensional space, where similar samples cluster together and dissimilar apart. A constrained form of ordination, Detrended Canonical Correspondence Analysis (DCCA) assesses the independent contributions of the measured environmental variables to explaining species distributions. I present results for multivariate analyses of a *Chiloé* dataset, consisting of the samples from the two Chiloé transects and a *Regional* dataset, which also includes the Valdivia samples from Nelson *et al*. (2009).

4.4.1 Elevation-dependent zonation in the *Chiloé* dataset

Cluster analysis of the *Chiloé* dataset identifies seven clusters at a total sum of squares cutoff of two (figure 4.5a). The vertical distribution of samples within these clusters supports the identification of vertical zonation from visual assessment of the assemblage data (figure 4.5b). Four of the clusters occupy small vertical ranges above MHHW, with the remaining three clusters sharing broader ranges at lower elevations. The dendrogram and a DCA sample plot (figure 4.5c) highlight the dissimilarity between samples from the two sites. Only one cluster contains samples from both transects and the two sites occupy discrete areas of the DCA sample plot, suggesting

systematic differences between their respective assemblages. While diatoms display zonation along the elevation gradient, site-specific factors are clearly also important.

Constrained ordination methods can further investigate the relative contributions of elevation and other factors in explaining diatom distributions in the *Chiloé* dataset. When constrained by SWLI, the gradient of the first Detrended Canonical Correspondence Analysis (DCCA) axis approximates the rate of species turnover with respect to elevation. The gradient length of the first axis (3.06) exceeds 2.0 standard deviation units, again highlighting a high rate of species turnover along the elevation gradient. This supports the use of unimodal rather than linear constrained ordination methods and I use DCCA rather than linear equivalents, such as Redundancy Analysis, to assess the dependence of diatom assemblages on recorded environmental variables (ter Braak *et al*., 1993; ter Braak and Juggins, 1993; Birks, 1995, 1998).

Together, elevation, loss on ignition and particle size explain 32.5 % of the variability in the *Chiloé* dataset (figure 4.6a). Elevation (SWLI) explains 12.8 % of the total explained variation (figure 4.6b). Table 4.2 compares this result with published constrained ordination results for similar diatom-based tidal marsh studies; the proportion of the variability in the *Chiloé* dataset explained by elevation is within the expected range.

A biplot of samples and environmental variables (figure 4.7) reinforces the dependence of particle size and loss on ignition on elevation; the vectors for all of the variables align with axis 1. The covariance between the variables results in similar contributions to the explained variance (figure 4.6b). No variables strongly correlate with axis 2 of the DCCA biplot, suggesting the importance of unknown variables in controlling species distributions. The distribution of samples from the two transects, particularly those with high axis 1 scores, suggests that this factor may relate to the difference between assemblages at the two sites.

Together, the multivariate methods of cluster analysis, unconstrained and constrained ordination indicate elevation-dependent zonation of the diatom assemblages from Estero Guillingo and Chucalen. Consequently, transfer functions may provide an appropriate approach for reconstructing marsh surface elevation. Palaeoenvironmental reconstructions must assume that the covariance of other controlling environmental factors with elevation has remained constant over time (Birks, 1995).

4.4.2 Elevation-dependent zonation in the *Regional* dataset

The 128 sample *Regional* dataset divides into six clusters at a total sum of squares cut-off of four (figure 4.8a). The clusters show a degree of vertical zonation, with clusters R2, R3 and R6 occupying small vertical ranges below mean sea level, between mean sea level and MHHW and above MHHW respectively (figure 4.8b). The other three clusters, which contain the majority of the Valdivia samples and the tidal flat samples from the *Chiloé* dataset, occupy broader elevation ranges. The dendrogram and a DCA sample plot (figure 4.8c) highlight the dissimilarity between the four transects. Two of the six clusters contain samples from more than one transect and there is no mixing between the Chiloé and Valdivia samples. The four sites occupy mutually exclusive areas of the DCA sample plot, again suggesting considerable site-based differences between the diatom assemblages.

The lack of particle size and loss on ignition data for the Valdivia samples precludes the application of DCCA, constrained by multiple environmental variables, to the *Regional* dataset. DCCA, constrained by SWLI, suggests that elevation explains 7.2 % of the variation in the dataset. This percentage is in line with other investigations (table 4.2) and suggests that the vertical control on diatom assemblages at a regional scale is still strong enough for transfer function development.

4.5 Transfer function development

DCCA axis 1 gradient lengths for the *Chiloé* dataset (3.06) and *Regional* dataset (2.57) exceed 2.0 standard deviation units, indicating a high rate of species turnover along the elevation gradient. Consequently, I use a unimodal approach and develop transfer functions using Weighted Averaging Partial Least Squares regression (WA-PLS; ter Braak and Juggins, 1993; ter Braak *et al*., 1993).

4.5.1 Selecting samples and variables

Decisions relating to the samples or sites to include in a modern training set revolve around the trade-off between *precision*, the magnitude of the vertical error, and *predictive power*, the range of available modern analogues for fossil environments (Horton and Edwards, 2005; Woodroffe and Long, 2010; Wilson and Lamb, 2012). Local training sets with few samples from a single location may produce precise estimates with tightly constrained sample-specific errors, but closer modern analogues for fossil samples may be found when larger, multi-site regional training sets

are used (Watcham *et al*., 2012). By incorporating samples from multiple sites, the variation in diatom assemblages not related to elevation increases and precision correspondingly declines. Woodroffe and Long (2010) suggest that in marshes on the west coast of Greenland, the variation in non-tidal range factors (organic content, wind and wave processes) may lead to a stretching of the ecological zonation, resulting in a decrease in the precision of regional models, without necessarily providing an increase in predictive power. Such variation is likely to affect Chilean tidal marshes too; the stretching of the vegetation zonation at Estero Guillingo compared to Puente Quilo (figure 4.2) may reflect this. Diatom taxa, however, suggest more than a stretching of marsh zonation at the Chiloé sites, with different species dominant in each transect (figure 4.3). Furthermore, as I am developing transfer function models for the purpose of reconstructing changes in marsh surface elevation over periods of hundreds to thousands of years, the possibility of encountering assemblages more closely resembling spatially distant samples cannot be discounted (Watcham *et al*., 2012). I develop a *Chiloé* model, incorporating the 96 samples from the Chiloé transects and, in an attempt to characterise a greater range of environments that may be encountered in the fossil record, I also develop a *Regional* model, which includes the 32 additional samples from Valdivia.

Various authors support removing outlying samples which do not closely conform to the expected distribution (e.g. Jones and Juggins, 1995; Horton and Edwards, 2006; Woodroffe, 2009; Long *et al*., 2012). The inability of transfer function models to estimate the marsh surface elevation of these samples may result from environmental factors other than elevation driving the species compositions (Birks *et al*., 1990). Variation related to factors other than elevation will, however, also be a feature of fossil datasets and the removal of these samples during transfer function development may result in overly precise error estimates. Consequently, I choose not to develop artificially pruned models. While some authors endorse removing minor species (e.g. Sawai *et al*., 2004; Hassan *et al.*, 2009; Zong *et al*., 2010), Birks (1998) argues that they contribute coherent information to the model and, accordingly, I do not remove any species.

4.5.2 *Chiloé* transfer function model development

The *Chiloé* transfer function model struggles to predict low marsh surface elevations at the first component (figure 4.9). Samples from Puente Quilo with observed elevations below MHHW share predicted SWLI values of between 110 and 130; those from below observed values of 250 SWLI units at Estero Guillingo have predicted elevations between 135 and 165 SWLI units. The substantial structure seen in the plot of observed against residual SWLI arises from the dominance of a few key species in low intertidal assemblages at each site (figure 4.3). The first

component uses a weighted average of the abundances of each species to assign species coefficients. As the distributions of these taxa do not conform to simple unimodal distributions, their coefficients are placed in the centre of the sampled ranges and, consequently, predicted values centre on these elevations. The stratification between the two sites also reflects the difference in sampled elevations and the elevation of the transition from the homogenous low elevation assemblage to the more highly zoned high elevation assemblages at each site. Successive components update these species coefficients to provide a greater level of fit between observed and residual marsh surface elevations (table 4.3, figure 4.9). I choose the third component model as it provides a linear distribution of observed against predicted values (figure 4.9), the highest r^2 value and a RMSEP improvement of at least 5 % over the first and second component models.

The removal of all tidal flat samples could provide a vegetated marsh model with a more linear fit between observed and predicted values and a lower RMSEP. The considerable shortening of the elevation gradient would, however, result in a model incapable of reconstructing large magnitude changes in palaeomarsh surface elevation. While Hamilton and Shennan (2005b) successfully use such high precision models, their application requires independent lithological data to constrain the depositional elevation. This approach relies on minimal downward root penetration (Woodroffe and Long, 2009) and substantial interseismic sedimentation, prerequisites not met by Chilean fossil records.

4.5.3 Regional transfer function model development

The *Regional* model (figure 4.10) also struggles to predict low marsh surface elevations at the first component due to the homogeneity of low elevation assemblages (figure 4.4). The third component successfully integrates the data from the four transects and provides a model with a linear distribution of observed against predicted values. Each component provides a RMSEP improvement of at least 5 % over previous components and an increase in r^2. The ratio of the prediction error to the total sampled range suggests similar performance for the *Chiloé* and *Regional* models (table 4.3).

Sample number 46 from Puente Quilo remains a notable outlier in the third component plot (figure 4.10), with a predicted elevation more than 100 SWLI units below its observed elevation. This results from the sample containing a much higher proportion of *Navicula atomus* than other samples of similar elevation. I do not remove this or any other sample to ensure a realistic assessment of reconstruction errors.

4.5.4 Implications of model choice on estimated species optima

Figure 4.11 presents the species coefficients used in the first three components of the *Chiloé* and *Regional* transfer function models. Species coefficients used in the first component of WA-PLS lie relatively evenly throughout the elevation gradient, with few coefficients below or above the sampled range. The first component, essentially a modified form of Weighted Averaging (WA; ter Braak, 1987), is susceptible to edge effects, the overestimation of species optima at low elevations and underestimation at high elevations (Birks, 1995; Birks *et al*., 2010). With the addition of further components, species coefficients stretch over a greater range of elevation values. By using residual structure in the species data, additional WA-PLS components may better represent the true species distributions (Birks, 1995; 1998). The majority of first component coefficients that lie below MSL update to elevations below the lowest sampled elevation, with a few species lowered by over 500 SWLI units at the third component. The upper end of the elevation gradient does not see such a substantial stretching, although component 2 and 3 coefficients are generally higher than component 1 coefficients above MHHW. For the dominant modern species in both the *Chiloé* and *Regional* training sets, species coefficients generally lie within the sampled elevation range and are relatively consistent between components (figure 4.12).

Updating species coefficients during the process of improving the fit between observed and predicted marsh surface elevations inevitably leads to certain coefficients, particularly those of infrequently occurring species, being moved drastically beyond their observed modern distributions. As part of the development of their *Small Tolerances* model, Woodroffe and Long (2009) remove species with coefficients outside their sampling range. Coefficients beyond the ends of the sampled gradient are, however, to be expected; it is highly unlikely that the modern training sets incorporate the full distributions of all species.

4.6 Summary

The modern tidal marshes of northern Isla de Chiloé are characterised by vertical zonation of vascular plants, sediments and diatom assemblages (figures 4.1, 4.2, 4.3). Transects at Puente Quilo and Estero Guillingo are both characterised by low diversity assemblages below MHHW and more variable, species-rich assemblages at higher elevations. Cluster analysis and ordination support zonation along the elevation gradient for both a *Chiloé* dataset containing the Chiloé samples and a *Regional* dataset, which includes samples from the Valdivia estuary (Nelson *et al*., 2009). The proportion of explained modern diatom variability in both datasets is comparable with

other tidal marsh diatom studies (figure 4.6, table 4.2). Weighted averaging partial least squares regression provides *Chiloé* and *Regional* transfer function models for the reconstruction of marsh surface elevation (figures 4.9, 4.10, table 4.3). Three component models have the highest r^2 values, linear distributions of observed against predicted values and acceptable levels of precision.

5. Reconstructing coseismic deformation: the 1960 and 2010 earthquakes

5.1 Introduction

Substantial coseismic deformation accompanied the 1960 M_w 9.5 and the 2010 M_w 8.8 earthquakes (Plafker and Savage, 1970; Delouis *et al*., 2010; Melnick *et al*., 2012a). This chapter tests whether the diatom transfer function approach can faithfully reconstruct the magnitude and direction of coseismic land-level movements from tidal marshes sequences.

As stated in chapter one, the *Sediment Signatures of the 2010 Chile M_w 8.8 Earthquake* project (NERC Urgency Grant I00503X/I) supported a rapid assessment of sediments deposited by the 2010 tsunami and subsequent postseismic accumulations. The survey in August 2010 recovered sediment blocks from three sites around the boundary between the 2010 and 1960 earthquakes: Río Andalién, Tubul and Río Tirua. Recognition of recently deposited sand sheets and older sand layers guided subsequent diatom analyses, which Dr Emma Watcham undertook. Garrett *et al*. (accepted) describes the findings of this project, including insights into tsunami biostratigraphy and postseismic sedimentation (appendix 1.1). This chapter uses the transfer functions developed in chapter four to calibrate the *Sediment Signatures* biostratigraphic records and produce estimates of coseismic deformation.

5.2 The 2010 Maule earthquake

Due to post-2010 sedimentary hiatuses at Río Mataquito and Río Tirua, reconstructions of land-level change for the 2010 earthquake are limited to two of the *Sediment Signatures* sites, Río Andalién and Tubul (figure 5.1).

5.2.1 Río Andalién

Lithology

At Río Andalién, the 2010 tsunami deposit forms a normally graded, largely continuous sand sheet, abruptly overlying highly organic and well-vegetated tidal marsh sediments (Garrett *et al*.,

accepted). In August 2010, the sand sheet remained visible at the surface in many areas, but close to the marsh front a layer of silty clay, not exceeding 20 mm, had buried the sand. A monolith from close to the marsh front provided samples for diatom analysis.

Biostratigraphy and palaeomarsh surface elevation reconstruction

Diatom assemblages in the upper part of the Río Andalién monolith contain 93 identified and one unidentified species. Of these, 71 also occur in the modern dataset and six exceed 10 % in one or more fossil sample (figure 5.2). Assemblages suggest intertidal marsh surface elevations for both pre- and post-tsunami sediments. The preseismic assemblage consists of species found both below and above mean higher high water (sub- and supra-MHHW) in the modern marsh environment. The post-tsunami deposit displays a slight increase in sub-MHHW species at the expense of supra-MHHW species, suggesting a fall in marsh surface elevation.

Quantitative reconstructions support a fall in marsh surface elevation (figure 5.3). The *Regional* model suggests a higher pre-tsunami marsh elevation than the *Chiloé* model and, consequently a larger magnitude fall in marsh elevation. Comparison of the sample immediately preceding the tsunami with the most recently deposited sample provides estimates of elevation fall of around 0.5 m to 0.75 m (table 5.1). Section 5.4 discusses the reliability of the reconstructions and the favoured model for each site.

5.2.2 Tubul

Lithology

The *Sediment Signatures* project did not detect any sand layers at or below the marsh surface at Tubul that might relate to tsunami deposition (Garrett *et al*., accepted). Tidal marsh sediment biostratigraphy may, however, record coseismic deformation in the absence of any tsunami deposit. Accordingly, the *Sediment Signatures* project recovered a silt and clay-rich monolith from a tidal channel to provide sediments for diatom analysis.

Biostratigraphy and palaeomarsh surface elevation reconstruction

Diatom assemblages in the Tubul monolith contain 65 identified and no unidentified species. Of these, 51 also occur in the modern dataset and eight exceed 10 % in one or more fossil sample (figure 5.4). Although the monolith shows no change in sediment lithology, diatom analysis

reveals a substantial change in assemblages. In the uppermost 5 mm an assemblage dominated by *Nitzschia fonticola*, a supra-MHHW species, supplants the preceding predominantly sub-MHHW assemblage (figure 5.4). This change suggests a rapid rise in marsh surface elevation.

Quantitative reconstructions corroborate the direction of change inferred from a visual assessment of the diatom assemblages (figure 5.5). The *Chiloé* and *Regional* models both indicate an increase in marsh surface elevation exceeding 0.5 m (table 5.1).

5.3 The 1960 Valdivia earthquake

Marsh surface elevation reconstructions for the 1960 earthquake are possible at three sites: Río Andalién and Río Tirua, both sampled during the *Sediment Signatures* project, and an additional site at Chucalen, northern Isla de Chiloé. The sites of Río Andalién and Río Tirua lie in the northern half of the 1960 rupture zone, the former situated close to the northernmost limit of possible displacements (figure 5.1). The *Sediment Signatures* project did not locate pre-2010 sand layers to guide sampling at Tubul. Sediments from Chucalen, which lies in the centre of the 1960 rupture area, include several minerogenic layers which may attest to tsunami deposition. In this chapter, I discuss sediments relating to the 1960 earthquake only and detail the full site stratigraphy in chapter 6.

5.3.1 Río Andalién

Lithology and chronology

A laterally continuous sand sheet lies 20 cm below the present surface at Río Andalién (Garrett *et al*., accepted). In the recovered monolith, above background caesium-137 (^{137}Cs) concentrations in sediments immediately underlying the sand layer indicate deposition no earlier than the beginning of atmospheric nuclear testing in 1952 (table 5.2). The similarities with the 2010 deposit, particularly the lateral extent and the abrupt lower contact, suggest a tsunami rather than a fluvial flood or storm surge (Garrett *et al*., accepted). Possible candidates include tsunamis resulting from the 1960 Valdivia earthquake and the 1964 Alaskan earthquake. The Alaskan tsunami coincided with a rising tide in south central Chile, but crested less than 0.75 m above sea level at the time of arrival at Talcahuano, the closest tide gauge at less than ten kilometres to the west of Río Andalién (Wilson and Tørum, 1968). The greater magnitude of the 1960 tsunami,

which resulted in flow depths of five metres in Talcahuano (Fritz *et al*., 2011) supports the Chilean event as the source of the sand layer.

Biostratigraphy and palaeomarsh surface elevation reconstruction

Diatom assemblages in the lower part of the Río Andalién monolith contain 70 identified and one unidentified species. Of these, 55 also occur in the modern dataset and six exceed 10 % in one or more fossil sample (figure 5.6). Assemblages indicate intertidal sedimentation before and after the tsunami deposit. A decline in sub-MHHW species matches an increase in two species not characterised in the modern dataset, *Navicula hamiltonii* and *Tryblionella navicularis* (figure 5.6). Both species may indicate marsh surface elevations below MHHW, with the former an epiphyte on intertidal seaweeds (Totti *et al*., 2009) and the latter a mesohalobous tidal flat species (Metcalfe *et al*., 2000).

Reconstructed palaeomarsh surface elevations generally lie between 0.75 m and 1.0 m above mean sea level. The *Chiloé* and *Regional* models do not suggest a large change in marsh elevation, with extensively overlapping error ranges before and after the tsunami deposit (figure 5.7). When corrected for the small amount of tsunami sediment accumulation, both models suggest marginal uplift (table 5.1).

5.3.2 Río Tirua

Lithology and chronology

A second sand unit forms a widespread and largely continuous stratigraphic layer below the 2010 tsunami deposit at Río Tirua (Garrett *et al*., accepted). The contact with underlying marsh sediments is abrupt. Comparisons with Ely *et al*. (2010), the testimony of local residents and elevated ^{137}Cs concentrations in a recovered core (table 5.2) link the sand layer to the tsunami following the 1960 earthquake.

Biostratigraphy and palaeomarsh surface elevation reconstruction

Diatom assemblages from the Río Tirua core contain 72 identified and no unidentified species. Of these, 61 also occur in the modern dataset and seven exceed 10 % in one or more fossil sample (figure 5.8). Supra-MHHW species characterise the diatom assemblages from the organic sediments below and above the sand layer. The presence of *Nitzschia fonticola* and *Navicula*

phyllepta probably indicates a high intertidal setting, rather than a supratidal marsh surface elevation throughout the sampling interval.

The transfer function reconstructions suggest deposition between 2 m and 2.5 m above mean sea level (figure 5.9). While the *Regional* model provides more variable post-tsunami marsh elevation estimates than the *Chiloé* model, neither model suggests a change in elevation exceeding the error term (table 5.1).

5.3.3 Chucalen

Lithology and chronology

An extensive sand sheet outcrops in marsh front exposures along the western margin of Bahía Quetalmahue. The abrupt nature of the lower contact, the presence of flattened vegetation and the coincidence of subsidence (discussed below) suggests deposition of the sand layer during a tsunami. Comparisons with preliminary investigations by Bartsch-Winkler and Schmoll (1993), ^{137}Cs concentrations (table 5.2) and statements from local residents correlate the deposit with the 1960 tsunami.

Biostratigraphy and palaeomarsh surface elevation reconstruction

Diatom assemblages from the Chucalen monolith contain 103 identified and two unidentified species. Of these, 96 also occur in the modern dataset and 12 exceed 10 % in one or more fossil sample (figure 5.10). A major change in diatom assemblages accompanies the tsunami deposit. Supra-MHHW species characterise the soil beneath the tsunami deposit. Sediments immediately overlying the sand layer from 36 cm to 38.5 cm contain a mixed assemblage incorporating both sub- and supra-MHHW components. Sub-MHHW species abruptly supplant this assemblage and dominate above 36 cm depth (figure 5.10).

Quantitative reconstructions suggest a pre-tsunami marsh surface elevation between 1.5 m and 2.0 m above mean sea level (figure 5.11). The reconstructions, in particular those from the *Chiloé* model, display a fall in elevation of approximately 0.2 m immediately preceding the abrupt contact with the tsunami deposit. While Hawkes *et al*. (2005) and Shennan and Hamilton (2006) evoke preseismic subsidence for several identified falls in palaeomarsh surface elevation in North America, downward mixing of diatom valves from the overlying tsunami deposit could also result in a similar pattern of modelled elevation change. Table 5.1 presents estimates of the total fall in

marsh surface elevation from the highest pre-tsunami elevation to the lowest post-tsunami elevation. The samples immediately overlying the tsunami provide varying elevation estimates (figure 5.11) and diatom assemblages appear to stabilise above these samples (figure 5.10).

5.4 Assessment of reconstruction performance

Although the *Regional* training set includes samples from four transects in two locations and from modern environments ranging from unvegetated tidal flat below mean sea level to above the highest limits of tidal inundation, many of the fossil samples do not have a 'good' or 'close' modern analogue (figures 5.3, 5.5, 5.7, 5.9, 5.11). This is particularly the case with Río Andalién and Río Tirua, where all samples have 'poor' modern analogues. The lack of modern analogues is a limitation of the current study and highlights the need for larger training sets, preferably from a more spatially diverse range of sites. The modern samples are from locations several hundred kilometres to the south of the *Sediment Signatures* sites and there may be a latitudinal control on diatom assemblages that I am currently unable to assess. Ongoing postseismic deformation and the lack of substantial sedimentation preclude the collection and use of samples from sites within the 2010 rupture zone and further investigations should focus on the northern half of the 1960 rupture zone.

A map of the location of the ten closest modern analogues for each fossil sample (figure 5.12) suggests that the majority of fossil samples share the greatest similarity with the modern samples from Isla de Chiloé. None of the closest modern analogues for fossil samples from Río Andalién or Tubul come from the Valdivia transects. This suggests the *Regional* model offers little or no increase in predictive power over the *Chiloé* model. Nevertheless, as the fossil sites (excluding Chucalen) lie several hundred kilometres away from the modern transects, the *Regional* model may better represent the true distributions of diatom taxa over this spatial scale, incorporating greater variation resulting from factors not related to elevation. Consequently, estimates derived from application of the larger training set are appropriate for Río Andalién, Tubul and Río Tirua. The close proximity of Chucalen to the transects of the *Chiloé* model and the dominance of these modern transects in an analysis of the location of the closest modern analogues (figure 5.12) supports the use of the *Chiloé* model at the southernmost site.

5.5 Comparison with independent estimates of deformation

The diatom-based estimates of palaeomarsh surface elevation change compare favourably with published estimates of coseismic land-level change in 2010 and 1960 (figure 5.13, table 5.3), suggesting that tidal marshes sequences can faithfully record the magnitude and direction of coseismic land-level movements. While some authors use positive comparisons with tide gauge data as justification for accepting the robustness of transfer function reconstructions (e.g. Gehrels *et al*., 2005; Kemp *et al*., 2009, 2011), I note the lack of statistically 'good' modern analogues in this investigation. For the *Sediment Signatures* sites, the percentage of fossil species also occurring in the modern dataset is high, ranging from 75 % to 85 % and rising to 91 % for Chucalen. However, a scatter plot (figure 5.14) highlights a number of species with high fossil and low modern maximum abundances. While the modern dataset provides good coverage of the species found in the fossil environment, it is the differences in abundances that result in the lack of 'good' modern analogues. Further modern samples need to locate higher modern abundances of important fossil species to ensure reconstructions fulfil statistical criteria as well as comparisons with independent data.

The transfer function underestimates 2010 uplift at Tubul and, to a lesser degree, overestimates subsidence at Río Andalién (figure 5.13). GPS vectors and benchmark relevelling provide the published estimates of 2010 coseismic deformation at these sites (table 5.3). Ground shaking and dewatering leading to consolidation of tidal marsh sediments could, therefore, be one factor contributing to the difference. Such shaking-induced consolidation occurred during the Alaskan earthquakes of 1964 and 1899 (Plafker, 1969; Plafker and Thatcher, 2008) and could lead to a bias in deformation estimates based on tidal marsh sediments. Estimates from both the transfer function approach and from Plafker and Savage (1970) for deformation in 1960 may also incorporate some local sediment consolidation. Postseismic deformation before sediment accumulation presents an alternative hypothesis for the slight offset for the 2010 earthquake (figure 5.13). This would require rapid postseismic subsidence at both sites. Postseismic movements in the six months between the 2010 earthquake and the *Sediment Signatures* field season were small, however; estimated at < 15 mm close to Río Andalién and < 50 mm elsewhere along the rupture zone (Baez *et al.*, 2010). Nevertheless, post-2010 sedimentary hiatuses at Río Tirua and Río Mataquito (Garrett *et al*., accepted) highlight the possibility for estimates of coseismic land motions based on sediment biostratigraphy to include both coseismic and some postseismic movements. In fossil sequences it may be very difficult to identify the duration of any hiatus.

5.6 Summary

The diatom-based palaeomarsh surface elevation reconstruction method is successful in matching independent estimates of coseismic land-level change. I infer 2010 marsh elevation fall at Río Andalién and marsh elevation rise at Tubul, corresponding to subsidence and uplift respectively. The offset between these reconstructions and published estimates may relate to coseismic marsh sediment consolidation. Quantitative reconstructions suggest stability at Río Andalién and Río Tirua in 1960 and marsh elevation fall at Chucalen, reflecting coseismic subsidence. The fidelity with which these test sites record the magnitude and direction of coseismic movements supports the use of diatoms to quantify deformation during previous great earthquakes in south central Chile. The absence of post-2010 sedimentation at Río Tirua and Río Mataquito serves as a reminder of the possibility of hiatuses biasing coseismic deformation estimates. The lack of 'good' modern analogues for fossil samples also remains a limitation of this study and I advocate the need for larger modern training sets from a wider range of sites.

6. Late Holocene records of earthquake occurrence

6.1 Introduction

This chapter presents evidence to test the hypothesis that coastal marshes preserve evidence for coseismic deformation and tsunamis over the late Holocene. Section 6.2 describes the lithology, biostratigraphy and chronology of the previously unreported site at Chucalen. Section 6.3 interprets these lines of evidence, in part through the application of the transfer function developed in chapter four and tested in chapter five. Sections 6.4 and 6.5 present and then interpret new biostratigraphic data from the previously reported site at Maullín (Cisternas *et al*., 2005). Sections 6.6 and 6.7 focus on new biostratigraphic data from another documented site at Cocotue (Cisternas *et al*., 2007; in prep). I discuss the limitations of the biostratigraphic approach to estimating coseismic deformation in section 6.8.

6.2 Chucalen: results

6.2.1 Lithology

Tidal marshes fringe the western margin of Bahía Quetalmahue, northern Isla de Chiloé (figure 6.1). Actively eroding cliffs truncate the marshes, revealing 0.5 m to 1.5 m high natural exposures. These exposures display a stratigraphy characterised by four abrupt transitions from organic to minerogenic deposition (figure 6.2). Marsh front exposures reveal the lateral extent of these organic – minerogenic couplets, which are continuous and largely uninterrupted for hundreds of metres. A transect of gouge cores maps the couplets as they rise across the tidal and freshwater marsh at Chucalen (figure 6.3). I refer to the four soils buried beneath minerogenic sediments as soils A, B, C and D, with A the uppermost and D the lowermost. Chapter five correlated soil A with the pre-1960 tidal marsh and the overlying minerogenic unit with the tsunami resulting from the 1960 earthquake.

Soils A, B, C and D outcrop in an exposure at the seaward end of the Chucalen transect (figures 6.2c, 6.4). Here, the soils are mid to dark brown and display varying levels of organic content (figure 6.4). Soils A and D are highly organic in the sampled exposure (> 50 % loss on ignition), with soil B only marginally more organic than the overlying minerogenic units. This soil is darker

and more organic at higher elevations, including in core CH11/28 (figure 6.3). Soil A contains abundant recognizable herbaceous plant material, including rhizomes. The remains of woody plants and large tree stumps occur in soil A at elevations not more than 0.5 m above the elevation of the soil in the sampled exposure (figure 6.5a). Soils B, C and D contain fewer recognizable plant fragments. Inorganic components of the soils vary in particle size, with soils C and D finer grained than soils A and B (figure 6.4).

The minerogenic units overlying each buried soil are light grey-brown or, in the case of the deposit overlying soil A, mid grey in colour. They contain little identifiable organic matter, save for roots that have penetrated downwards from overlying sediments. Loss on ignition values do not exceed 10 % (figure 6.4). Sand-sized particles are dominant, with the units overlying soils C and D finer grained than those overlying soils A and B.

The boundaries between the organic soils and the overlying minerogenic units are abrupt. While herbaceous plants are flattened and encased by the minerogenic deposit at the top of soil A, the upper margins of soils B, C and D do not feature vegetation flattening and show signs of mixing in the exposure. While still displaying easily distinguished upper boundaries, these soils feature numerous small inclusions of the overlying minerogenic deposits (figure 6.5b). I encountered intact upper contacts with no evidence for mixing for soils B and D elsewhere in the Chucalen tidal marsh, however the minerogenic inclusions are a ubiquitous feature of soil C. With the exception of the distinct upper boundary of the minerogenic unit overlying soil A, the transitions from minerogenic to organic sedimentation are diffuse in all exposures and cores (figure 6.2).

The recent marsh sediments are organic, with frequent in situ roots and rhizomes of *Juncus* spp. and *Scirpus californicus*. Larger woody plants and their detrital and in-situ remains only occur above the terrace which lies at approximately 2 m above mean sea level. Here, the dominant woody species are typically shrubs, including *Berberis* spp. and *Myrtaceae* spp.. The minerogenic component of the recent marsh sediment is typically sandy, with abundant thin (a few grains to 2 mm), discontinuous sand laminae in the uppermost 20 cm (figure 6.4). The frequency of these laminae rapidly decreases within a few metres of the marsh front and deposits a few metres inland are typically silt-rich. Similar thin sand layers do not occur within any of the buried soils.

6.2.2 Biostratigraphy

Diatom assemblages in samples from the marsh front exposure and core CH11/28 contain species indicative of intertidal environments. Of the 139 identified and four unidentified taxa, 117 also

occur in the modern training set, 110 appear in more than one fossil sample and 21 exceed 10 % of the total diatom assemblage in one or more fossil sample (figures 6.6, 6.7). Appendices 6.1 and 6.2 (on the attached CD) list the percentage abundances of all species in the exposure and core CH11/28 respectively. Sub-MHHW species occur throughout the sampled exposure, with peaks in supra-MHHW species coinciding with buried soils A, C and D (figure 6.6). *Eunotia* spp. and *Pinnularia appendiculata*, the main supra-MHHW species found in soil A, occur at higher modern elevations than *Diploneis ovalis* and *Karayevia oblongella*, the supra-MHHW species in soils C and D. Sub-MHHW species dominate samples from soil B and, while similar species occur in the overlying minerogenic unit, the boundary does feature abrupt transitions in several of the less abundant supra-MHHW species.

In core CH11/28, a shift from predominantly supra-MHHW species to a more mixed assemblage accompanies the transition from organic to minerogenic sedimentation at the top of buried soil B (figure 6.7).

6.2.3 Chronology

Fifteen AMS radiocarbon samples provide a chronology for the Chucalen exposure (table 6.1). Calibrated ages indicate the sampled exposure represents approximately the last 1000 years of sediment accumulation.

Visual inspection of calibrated age ranges highlights several discrepancies, where samples have younger ages that their stratigraphic position and the age of adjacent samples would suggest (figure 6.8). Downward root penetration and misidentification of root material as above ground plant matter provides a possible explanation for the offset. Despite lying 29 cm below the present surface, comparison of sample CH11/R1 with data from Graven *et al*. (2012) suggests a calibrated age of 2004 – 2005 (Pauline Gulliver, NERC Radiocarbon Facility, pers. com., 2012). Both samples CH11/R5 and CH11/R6 have calibrated ages in the mid to late 1950s, however sample CH11/R6 is younger than the overlying sample CH11/R5. I elect to remove sample CH11/R6 and favour sample CH11/R5, which is from flattened and still rooted vegetation lying immediately beneath a minerogenic unit, as this is more likely to consist of in situ, above ground plant material. The calibrated age of sample CH11/R8 is similar to that of CH11/R6 and younger than CH11/R7 and CH11/R5. Likewise, sample CH11/R15 provides calibration solutions younger than samples CH11/R14 and CH11/R13, which lie above it (figure 6.8). I remove samples CH11/R1, CH11/R6, CH11/R8 and CH11/R15 before commencing age-depth model development.

The remaining samples above 50 cm all display percentages of modern carbon exceeding 100 % (table 6.1). Calibration of these samples using the post-bomb atmospheric southern hemisphere ^{14}C curve (Hua and Barbetti, 2004) provides multiple possible age ranges for three of the four samples. Stratigraphic ordering can resolve two of these to single solutions (figure 6.9). Samples CH11/R3 and CH11/R2 must lie on the falling limb of the curve, supporting rejection of the older age ranges in table 6.1. Sample CH11/R4 may lie on either the rising or falling limb, while CH11/R5 provides a single calibration solution (figure 6.9; table 6.1).

Bayesian age modelling in OxCal v.4.1 (Bronk Ramsey, 1995) employs the preferred calibration solutions for the four accepted post-bomb dates and the remaining seven pre-bomb dates to produce an age-depth model for the Chucalen exposure (table 6.2; figure 6.10). I set boundaries at each abrupt lithological change to provide the model with flexibility to vary the deposition rate. The model has an overall agreement index (a measure of the similarity between prior and posterior age distributions) of 54.1 (table 6.2), less than the threshold of 60 proposed by Bronk Ramsey (2009b). Agreement indices for the individual samples (table 6.2) highlight that this arises from the dissimilarity between distributions for the lowermost sample, CH11/R16. Outlier analysis in OxCal, however, does not suggest that there is a statistical basis for removing this sample (table 6.2) and, in the absence of other criteria for rejection (c.f. Bronk Ramsey, 2009b), I elect to keep sample CH11/R16 in the model.

The general form of the age-depth model (figure 6.10) indicates substantial variability in the sedimentation rate. Between the minerogenic unit overlying buried soil D (89 cm depth) and the top of soil A (44.5 cm depth), the sedimentation rate averages approximately 0.5 mm yr^{-1}. Above buried soil A, this rate increases by an order of magnitude. The bottom of the sequence may also exhibit a faster rate of sediment accumulation; however I require further radiocarbon dates from below soil D to confirm this.

The model provides two sigma age ranges for the four abrupt transitions from organic to minerogenic sedimentation (table 6.2). The inferred timing of the boundary at the top of buried soil A, 1951 to 1967, supports the ^{137}Cs data presented in chapter five. Elevated ^{137}Cs concentrations in buried soil A (table 5.2) imply deposition no earlier than the commencement of atmospheric nuclear testing in the early 1950s. The rejection of the sample from the top of buried soil B, CH11/R8, combined with multiple calibration solutions for adjacent samples resulting from plateaux in the calibration curve, produces a two sigma age range of more than 400 years for the second boundary (table 6.2; figure 6.10). This is the part of the sequence with the poorest age control and the abrupt contact could lie anywhere between the 16th and 20th centuries. The age-

depth model provides a greater level of constraint on the timing of the burial of soils C and D (table 6.2; figure 6.10). The model places each abrupt contact within age ranges of approximately 150 years, commencing in 1270 and 1050 respectively.

6.3 Chucalen: evidence for multiple great earthquakes?

Sequences of organic intertidal soils interbedded with minerogenic units may reflect successive earthquake deformation cycles (e.g. Atwater, 1987; Darienzo and Peterson, 1990; Shennan *et al*., 1996; Sawai *et al*., 2002; Hamilton and Shennan, 2005a, b), however a range of other sedimentologic, hydrographic, oceanographic and atmospheric processes can give rise to similar stratigraphies (Long and Shennan, 1994; Nelson *et al*., 1996; Witter *et al*., 2001). In this section I use criteria set out by Nelson *et al*. (1996) to identify whether the evidence from Chucalen is consistent with the repeated coseismic deformation hypothesis.

6.3.1 Suddenness of submergence

Near instantaneous decimetre to metre-scale coseismic subsidence produces abrupt changes in lithology (Atwater, 1987; Darienzo and Peterson, 1990; Long and Shennan, 1994; Nelson *et al*., 1996). Conversely, interseismic and aseismic processes generate gradual contacts, reflecting slower rates of change. While some mixing is evident at the surface of buried soils B, C and D, all of the buried soils at Chucalen display identifiably abrupt upper contacts and transitions from organic to minerogenic sedimentation (figures 6.2, 6.3, 6.4), supporting repeated sudden falls in marsh surface elevation. Abrupt changes in particle size and organic content (figure 6.4) and in diatom assemblages (figures 6.6, 6.7) further support the suddenness of these falls, including for soil A (chapter five). Intervening minerogenic to organic contacts are visibly more gradual (figure 6.2), with slower rates of change in organic matter, particle size and diatom assemblages, implying more gradual rates of marsh surface elevation change. The nature of the stratigraphic boundaries at Chucalen is consistent with repeated earthquake deformation cycles, incorporating phases of sudden coseismic subsidence and gradual interseismic uplift (c.f. Long and Shennan, 1994; Nelson *et al*., 1996; Shennan *et al*., 1999).

Coseismic subsidence can promote rapid sedimentation; Atwater *et al.* (2001) identified minerogenic units exceeding one metre in thickness and tidal rhythmites deposited after the 1964 Alaskan earthquake. Accordingly, rapid sedimentation following an abrupt organic to minerogenic contact may suggest coseismic subsidence. The minerogenic layers at Chucalen are, however,

substantially thinner than those found in Alaska, implying low sedimentation rates. Reinhardt *et al*. (2010) found that post-1960 sedimentation rates in the Río Cruces, south central Chile, were less than postseismic accumulation rates in Alaska. Low Chilean sedimentation rates, even after known coseismic subsidence, may reflect lower sediment availability and the microtidal nature of the Chilean coastline. The lack of rapid sedimentation, therefore, does not discount the possibility of coseismic subsidence.

6.3.2 Lateral extent of organic – minerogenic couplets

Regional scale coseismic subsidence forms organic – minerogenic couplets wherever the magnitude of subsidence is sufficient to cause a change in depositionary regime. Coseismic subsidence generated couplets are, therefore, laterally extensive and are not constrained to small areas of a marsh or, indeed, to single marshes within a region (Darienzo *et al*., 1994; Nelson *et al*., 1996). Tidal marshes in aseismic locations may also record transitions from organic to minerogenic sedimentation that do not relate to any local tectonic mechanism. The lateral migration of tidal channels may produce couplets; however these are typically of limited lateral extent (Allen, 1997, 2000; Shennan *et al*., 1998). Barrier breaching and short-lived inundation events such as tsunamis and storm surges may generate more extensive couplets (e.g. Long and Innes, 1993; Witter *et al*., 2001; Long *et al*., 2006; Switzer and Jones, 2008; Williams, 2009), which may be more difficult to distinguish from coseismic deformation based on lateral extent alone.

The four organic – minerogenic couplets at Chucalen are laterally extensive, outcropping for hundreds of metres in marsh front exposures on the southwestern margin of Bahía Quetalmahue (figures 6.2, 6.3). Reconnaissance surveys of the stratigraphy at the modern transect site of Estero Guillingo in the northwest of the bay suggest the couplets may be even more widely distributed. The lateral extent is consistent with the coseismic submergence hypothesis. Local processes, including tidal channel migration, cannot explain such widespread couplets. The size and morphology of the bay and the location of the site do not favour a barrier development and breaching interpretation. The lateral extent of couplets cannot rule out short duration inundation events; tsunamis from distant sources and storm surges are capable of depositing minerogenic units over the area investigated here. I discuss evidence for tsunami deposition in the following section.

6.3.3 Coincidence of tsunami deposits

Identification of tsunami deposits concurrent with subsidence strengthens the argument for an earthquake deformation cycle interpretation of interbedded tidal marsh sequences (Atwater, 1987; Nelson *et al*., 1996; Cochran *et al*., 2005; Sawai *et al*., 2009). The 1960 and 2010 tsunamis provide analogues for tsunami deposition in Chilean intertidal environments. These events left centimetre to decimetre thick, landward thinning sand sheets across coastal marshes (Cisternas *et al*., 2000; Horton *et al*., 2011; Morton *et al*., 2011; Garrett *et al*., accepted). The fragmentary nature of the deposits, however, highlights that the absence of sand sheets does not rule out coseismic subsidence or tsunami occurrence.

Chapter five correlated an extensive sand sheet outcropping in the Chucalen marsh front exposures with a tsunami. The abrupt lower and upper contacts to the deposit overlying soil A, the presence of flattened vegetation and the coincidence of rapid submergence (sections 5.3.3, 6.3.1) are consistent with this interpretation. While tsunamis are not the only possible source of sand sheets in tidal marshes, I discount other causes in this instance. Aeolian transport from nearby beaches and dunes is unlikely to have occurred at such a rate as to flatten vegetation. The lack of rivers or streams close to the site rules out a fluvial source. Furthermore, while storm surges may deposit widespread sand sheets in coastal locations (e.g. Williams, 2009), the sheltered location at Chucalen appears to limit storm deposits to < 2 mm thick sand laminae extending only a few metres onto the vegetated marsh (figure 6.4). As at the *Sediment Signatures* sites further to the north, the diatom assemblage in the proposed tsunami deposit at Chucalen is mixed rather than marine, consisting of both sub- and supra-MHHW species (Garrett *et al*., accepted).

Following Cisternas *et al*. (2005), I use evidence for bioturbation to distinguish between tsunami sediments and tidal flat deposition for the minerogenic units overlying soils B, C and D. The minerogenic inclusions in the top of these soils are similar to infilled holes created by intertidal burrowing organisms, including worms and crabs, on modern tidal flats in Bahía Quetalmahue and at Maullín (Cisternas *et al*., 2005). Tsunami deposits that blanket marsh soils reduce or prevent bioturbation. Evidence for bioturbation suggests tsunami deposits do not cover soils B, C and D in the sampled exposure. The lack of flattened vegetation at the interface further supports this hypothesis. While the minerogenic unit overlying soil A has a well-defined upper boundary, the gradual transitions from minerogenic to organic sedimentation for the lower units suggests a more prolonged perturbation of the depositionary regime. I conclude that tidal flat sediments rather than tsunami deposits overlie soils B, C and D in the exposure. The occurrence of abrupt

contacts without signs of mixing elsewhere at Chucalen suggests tsunami deposition did occur at the time of the burial of soils B and D. Coincident tsunamis are consistent with the coseismic submergence hypothesis.

As tidal flat deposits overlie buried soils B, C and D in the sampled exposure, quantitative estimates of the magnitude of submergence must compare the inferred elevations of each soil with the immediately overlying minerogenic sediments. Estimates for the magnitude of submergence associated with the burial of soil A, as presented in chapter five, must compare the elevations below and above the inferred tsunami deposit.

6.3.4 Amount of submergence

Coseismic deformation and coseismic sediment consolidation are capable of causing abrupt, lasting, metre-scale rises in relative sea level (Nelson *et al*., 1996); consequently the magnitude of submergence provides perhaps the most important discriminator between seismic and aseismic causes of couplet formation (Shennan *et al*., 1998).

Figure 6.11 presents reconstructions of palaeomarsh surface elevation resulting from calibration of the diatom assemblage data in figure 6.6 using the *Chiloé* and *Regional* transfer function models. Figure 6.12 similarly calibrates the diatom data from core CH11/28. Palaeomarsh surface elevations lie between 0.5 m and 2 m above mean sea level. There is no long-term trend to the reconstructions from the marsh front exposure, with predicted marsh surface elevations from samples 30 cm and 95 cm below the modern marsh surface sharing overlapping error ranges. With the exception of soil B, the buried soils display consistently higher predicted elevations than the intervening minerogenic deposits. The *Chiloé* and *Regional* model predictions diverge by less than 0.3 m, with the largest differences arising from the former model employing a lower species coefficient for the most abundant sub-MHHW species, in particular *Pseudostaurosira perminuta*.

Quantitative reconstructions place soil A at a palaeomarsh surface elevation almost two metres above mean sea level (figure 6.11). This is consistent with the occurrence of tree stumps in marginally higher marsh front exposures (figure 6.5a) and the modern limit of woody vegetation at approximately two metres above mean sea level. The *Chiloé* and *Regional* models assign marsh elevations between 0.5 m and 1.5 m above mean sea level to diatom assemblages following the inferred tsunami (figure 6.11). Chapter five assigned a quantitative estimate of -1.15 ± 0.43 m. The magnitude of submergence is consistent with coseismic subsidence (Nelson *et al*., 1996) and, as

noted in the preceding chapter, closely corresponds with Plafker and Savage's (1970) estimate of subsidence in 1960.

No larger-than-error change in estimated marsh elevation accompanies the abrupt contact at the top of soil B in the exposure; predicted elevations for the soil are as low as in the overlying minerogenic unit (figure 6.11). Similarly, quantitative reconstructions for core CH11/28 do not indicate substantial submergence (figure 6.12), despite the increase in sub-MHHW diatom species (figure 6.7). I provide estimates of submergence in table 6.3, but highlight that sample specific error terms encompass a large range of possible estimates and all fossil samples lack 'good' modern analogues (discussed further in section 6.8). Submergence appears to coincide with the burial of soil B, however, at present, uncertainty over the magnitude of submergence means that reconstructions cannot conclusively falsify an aseismic hypothesis for the formation of this couplet.

Quantitative reconstructions place both soils C and D at approximately 1.5 m above mean sea level (figure 6.11). Subsequent palaeomarsh surface elevations for the overlying minerogenic sediments imply submergence in the region of one metre associated with the burial of each soil (table 6.3). While the lack of 'good' modern analogues for any of the fossil soils remains problematic, the submergence estimates make ecological sense, given the distribution of the dominant species in the modern environment. The *Chiloé* and *Regional* model outputs both feature declines in elevation immediately preceding the change in lithology at the top of soils C and D. The bioturbated nature of the upper margins of these soils may result in mixed diatom assemblages and underestimates of marsh surface elevations. Submergence for each these couplets may consequently exceed one metre; a value entirely consistent with the coseismic deformation hypothesis.

6.3.5 Synchroneity of submergence at widely spaced sites

Synchronous burial of organic soils at sites spaced along a subduction zone implies a regional mechanism for submergence (Atwater *et al*., 1991; Nelson *et al*., 1995, 1996, 2006). Processes controlling the depositionary regime at a single site or estuary are less likely to have occurred at the same time in multiple, widely distributed locations. Synchroneity is, however, difficult to identify, with single earthquakes indistinguishable from closely temporally spaced smaller ruptures due to the limitations in the precision of radiometric and other dating techniques (Nelson *et al*., 1996). At present, evidence for submergence along the Chilean subduction zone is highly limited, with few sites for age comparison. Here, I compare the modelled timing of the four

abrupt contacts with limiting dates from Maullín, 45 km to the northeast (Cisternas *et al*., 2005). More detailed discussion of possible synchroneity requires additional sites, further high precision radiocarbon determinations and, where appropriate locations exist, dendrochronological approaches (cf. Atwater *et al*., 2005; Cisternas *et al*., 2005).

The testimony of local residents and elevated ^{137}Cs concentrations in buried soil A suggest submergence correlates with the 1960 earthquake. Furthermore, the radiocarbon age-depth model limits the abrupt contact to between 1951 and 1967 (table 6.2; figure 6.10). A single radiocarbon date from Cisternas *et al*. (2005) indicates submergence of the uppermost buried soil at Maullín after the mid 17th century (figure 6.13). Based on local testimony, these authors also correlate buried soil A at Maullín with the pre-1960 earthquake marsh horizon.

The Chucalen age-depth model (figure 6.10) places the timing of burial of soil B between 1520 and 1946 (table 6.2). A pooled mean of three dates at Maullín provides a calibrated range of 1450 to 1616 to limit the oldest possible timing for submergence for the second buried soil at this site (Cisternas *et al*., 2005). While establishing synchroneity in the timing of submergence at the two sites requires further analyses, the dates presented here are not inconsistent with the hypothesis of synchroneity (figure 6.13).

The age-depth model (figure 6.10) places the timing of the abrupt contact between soil C and the overlying minerogenic unit at Chucalen at 1270 to 1410 (figure 6.13). At Maullín, calibration of the pooled mean of samples underlying the third buried soil provides an age range of 1280 to 1387 (Cisternas *et al*., 2005), entirely within the modelled range at Chucalen. Dates from the two sites do not weaken the hypothesis of synchroneity (figure 6.13).

At Chucalen, minerogenic deposits buried soil D between 1050 and 1200 (table 6.2; figure 6.13). A single date from a plant rooted in the fourth buried soil and encased in sand at Maullín provides an oldest limiting date of 1021 to 1181 (Cisternas *et al*., 2005), largely overlapping with the Chucalen modelled range. While the calibrated age ranges at both sites remain sizeable, I do not find any evidence suggesting asynchronous submergence of soils A, B, C and D at Chucalen and Maullín.

6.3.6 Summary: Chucalen records evidence for multiple great earthquakes

Repeated earthquake deformation cycles, comprising phases of gradual interseismic uplift separating four rapid coseismic subsidence events, best explain the lithological and

biostratigraphic data at Chucalen. As section 6.3.5 indicates, the precision of the radiocarbon approach is insufficient to confirm synchroneity of submergence at Chucalen and Maullín. Nevertheless, the lack of evidence for asynchronous submergence, the analogue of deformation and tsunami inundation in 1960 and the close proximity of Chucalen and Maullín favour the contention that the two sites record the same megathrust earthquakes.

6.4 Maullín: results

Using lithological and biostratigraphic evidence, Cisternas *et al*. (2005) identify up to eight tsunamis accompanied by coseismic subsidence at Maullín (figure 6.1). Until now, the magnitude of submergence associated with each of these deposits has remained unknown. Here, I present new biostratigraphic evidence to test the hypothesis that the site records evidence for repeated great earthquakes characterised by submergence exceeding 0.5 m.

6.4.1 Lithology and chronology

Cisternas *et al*. (2005) report eight buried organic soils or black humic sands, interbedded with fine to medium well-sorted sand at Maullín. The authors map the youngest four of these organic deposits as they rise across tidal marsh and freshwater lowlands to a low terrace approximately 0.4 km inland (figure 6.14a). Older buried organic deposits lie above the terrace. In a new exposure at the seaward end of Cisternas *et al*.'s (2005) main transect, sampled in January 2012, four organic soils outcrop within a metre of the modern marsh surface (figure 6.14b). Following Cisternas *et al*. (2005), I refer to the buried soils, from youngest to oldest, as A, B, C and D.

Soils A to D lie interbedded with light to mid grey silty sand. The unit overlying soil A is coarser grained than those overlying soils B, C and D and exhibits normal grading. Each buried soil displays a well-defined upper contact, although soils B, C and D show signs of mixing. Soil C in particular exhibits numerous inclusions of the over or underlying minerogenic deposits throughout its profile. This mottled appearance is a ubiquitous feature of soil C in all areas below the terrace (Cisternas *et al*., 2005). With the exception of the unit overlying soil A, the boundaries between each minerogenic deposit and the overlying soils are diffuse. The contact between the uppermost minerogenic unit and the recent marsh sediment is well defined.

Cisternas *et al*. (2005) use plant macrofossils from the upper margin of each buried organic unit for radiocarbon dating. Individual or pooled samples provide oldest limiting dates for each transition to minerogenic sedimentation (figure 6.15).

6.4.2 A new biostratigraphic record

Assemblages from the new marsh front exposure contain intertidal diatom species. Of the 105 identified and two unidentified taxa, 98 also occur in the modern training set, 95 appear in more than one fossil sample and 13 exceed 10 % of the total diatom assemblage in one or more fossil sample (figure 6.16).

As at Chucalen, sub-MHHW species occur throughout the sampled exposure, with peaks in supra-MHHW species coinciding with buried soils A, C and D. Soil B does not display a higher proportion of supra-MHHW species than the overlying minerogenic unit. At approximately 10 %, soil A contains a lower proportion of sub-MHHW species than soils C and D, where sub-MHHW species contribute between 30 % and 50 %.

6.5 Maullín: corroboration of previous interpretations?

Cisternas *et al.* (2005) interpret laterally extensive buried soils with abrupt upper contacts as evidence for coseismic submergence and concurrent tsunami deposition at Maullín. Based on the testimony of eyewitnesses, the authors correlate the uppermost sand sheet with the 1960 tsunami. The possible synchroneity in the timing of the burial of the four soils at Maullín and Chucalen (discussed in section 6.3.5) does not oppose an interpretation of coseismic deformation and tsunami inundation for any of the four Maullín couplets.

6.5.1 Tsunami deposition

While Cisternas *et al*. (2005) infer tsunamis concurrent with the burial of all of the four soils investigated here; the new marsh front exposure provides evidence for a tsunami overlying soil A only. The upper margin of this soil features an abrupt contact, with no evidence for mixing (figure 6.14b). The minerogenic unit flattens and encases herbaceous plants still rooted in the underlying soil. Unlike the lower minerogenic units, the uppermost deposit also exhibits an abrupt rather than a gradual upper contact. Diatom assemblages associated from the proposed tsunami deposit

contain higher percentages of sub-MHHW species than both the underlying and overlying minerogenic units.

Using the criterion set out by Cisternas *et al*. (2005), sand inclusions within soils B, C and D suggest bioturbation and tidal flat sedimentation rather than tsunami deposition for the lower three minerogenic units in the exposure. Cisternas *et al*. (2005) identified abrupt contacts with no evidence for mixing associated with soils A, B and D in nearby marsh front location, suggesting tsunami deposition in other areas. As at Chucalen, the absence of tsunami deposits in one location is unsurprising; such deposits are typically thin and fragmentary in Chilean marshes (Ely *et al*., 2010; Morton *et al*., 2011; Garrett *et al*., accepted). The presence of abrupt contacts with no evidence for mixing in Cisternas *et al*.'s (2005) main transect supports tsunami occurrence and strengthens the case the site recording evidence for multiple episodes of coseismic deformation.

Recognition of the absence of tsunami deposits overlying soils B, C and D in the exposure sampled in 2012 guides the sampling approach for estimating the magnitude of submergence. Quantitative estimates for soils B, C and D must compare the inferred elevations of the soils with immediately overlying minerogenic sediments. Estimates for the magnitude of submergence associated with the uppermost couplet must compare the elevations below and above the inferred tsunami deposit.

6.5.2 Amount of submergence

Cisternas *et al.* (2005) analyse diatoms from the buried soils only; quantitative reconstructions based on their data will, therefore, underestimate the magnitude of coseismic subsidence. For instance, the authors did not sample minerogenic sediments immediately overlying soil C, despite suggesting that bioturbation indicated tidal flat rather than tsunami deposition in their sampled exposure. Calibration of the new biostratigraphic record provides quantitative reconstructions of palaeomarsh surface elevation for the Maullín exposure (figure 6.17). Estimated palaeomarsh surface elevations for the sediments immediately overlying the uppermost minerogenic unit are between 1.0 m and 1.5 m lower than predictions for soil A (table 6.4). These values agree well with coseismic subsidence estimates for 1960 of -1.5 ± 0.4 m and -1.7 ± 0.4 m from Plafker and Savage (1970).

The estimated elevation of soil B is closer to the elevations of the minerogenic units than the elevations of the other buried soils (figure 6.17). Despite the stratigraphy suggesting a fall in marsh surface elevation, reconstructions indicate subsidence of less than the one sigma error

term (table 6.4). While Cisternas *et al*. (2005) inferred, but did not quantify subsidence from diatom assemblages; reconstructions from the new exposure cannot falsify an aseismic hypothesis for the burial of soil B.

Quantitative reconstructions suggest soils C and D accumulated at similar elevations to soil A (figure 6.16). Both soils exhibit a fall in palaeomarsh surface elevation before the organic – minerogenic contact, perhaps related to the inclusions resulting from bioturbation. The estimated elevations of the overlying minerogenic units imply submergence of approximately 1.0 to 1.5 m for both soils (table 6.4); consistent with the coseismic subsidence hypothesis. All samples at Maullín lack 'good' modern analogues, however the direction and magnitude of the submergence associated with each soil is consistent with the stratigraphy and the modern distributions of the dominant fossil species.

6.6 Cocotue: results

Cisternas *et al*. (2007, in prep.) interpret a sequence buried organic silty sands, interbedded with sands of low organic content and isolated fans of poorly sorted gravel as evidence for tsunamis and earthquake triggered debris flows at Cocotue (figure 6.1). In this section I present a new biostratigraphic record to investigate whether the site records evidence for submergence.

6.6.1 Lithology and chronology

A narrow terrace fringes an uplifted sea cliff cut into Pleistocene glacial outwash at Cocotue (Bartsch-Winkler and Schmoll, 1993; Cisternas *et al*., 2007). The seaward edge of the terrace lies at an elevation of approximately 3 m above mean sea level. In a new exposure, five buried mid brown organic silty sands (labelled A to E from the youngest to the oldest) lie interbedded with very light grey inorganic sands (figure 6.18). The upper boundary of each buried organic deposit is abrupt, with no evidence for mixing. Radiocarbon dates suggest burial of organic deposits A, C, D and E at similar times to the burial of soils A, B, C and D at Maullín (Cisternas *et al*., 2007, in prep.). The burial of organic deposit B lies between that of deposits A and C, with further dating currently ongoing (Marco Cisternas, pers. comm., 2012).

6.6.2 A new biostratigraphic record

Of the 106 identified and one unidentified species in the Cocotue exposure, 91 also occur in the modern training set, 81 appear in more than one fossil sample and 18 exceed 10 % of the total diatom assemblage in one or more fossil sample (figure 6.19). Assemblages from the proposed tsunami deposits typically consist of species from the highest modern intertidal elevations. Supra-MHHW species dominate organic deposits C, D and E and the overlying minerogenic deposits. Organic deposits A and B exhibit greater proportions of sub-MHHW species, alongside increased abundances of species not characterised in the modern training sets (figure 6.19).

6.7 Cocotue: corroboration of previous interpretations?

6.7.1 Tsunami deposition

While the *Sediment Signatures* project highlighted recent tsunami deposits with mixed assemblages of diatoms from different elevations (Garrett *et al*., accepted), the minerogenic deposits at Cocotue show very low abundances of sub-MHHW species (figure 6.19). This could suggest a non-marine source for the sand sheets, or could reflect post-depositional alterations to originally marine-sourced diatom assemblages. If tsunamis rework and deposit materials from offshore, nearshore or beach locations that are characterised by low abundances or are devoid of any diatoms, subsequent ponding and infiltration of freshwater could result in a freshwater diatom assemblage in a tsunami deposit. Such ponding is visible in aerial photographs taken the year after the 1960 earthquake (Marco Cisternas, pers. comm., 2012). Therefore, diatom assemblages neither confirm nor refute a tsunami source for the sand layers.

6.7.2 Amount of submergence

Throughout the whole of the sampled exposure, the Cocotue diatom assemblages suggest deposition at or above the highest sampled elevations of the modern training set. Quantitative reconstructions support this assertion, with *Chiloé* model estimates of palaeomarsh surface elevation for every sample lying between 1.5 m and 2.0 m above mean sea level (figure 6.20). The occurrence of *Achnanthidium minutissimum* and *Navicula atomus* at low elevations in the Valdivia modern samples leads to a divergence between the *Chiloé* and *Regional* models towards the top of the Cocotue exposure (figure 6.20). These species are absent from or only found in samples

from above MHHW in the *Chiloé* training set. Their occurrence below MHHW in the Valdivia transects dictates their sub-MHHW categorization.

The invariance in the *Chiloé* model reconstructions is unsurprising, given the top of the exposure lies three metres above mean sea level. The reconstructions, therefore, do not equate to stability in the elevation of the site, but rather suggests that the exposure has remained above the influence of tides throughout its accumulation. While the transfer function cannot estimate the submergence associated with the proposed tsunamis, the supra-MHHW assemblages provide constraints on the longer-term relative sea-level history of the site. At no point during the deposition of the samples investigated has the marsh surface been within the tidal range.

Quantitative estimates of coseismic deformation at Cocotue require samples with lower palaeomarsh surface elevations. Exposures at elevations closer to modern mean sea level may provide such samples, however erosion of the marsh may prevent the development of a record from this site.

6.8 Limitations of the quantitative biostratigraphic approach

Qualitative interpretations of diatom assemblages and stratigraphy support quantitative estimates of submergence associated with the buried soils at Chucalen and Maullín. As highlighted in chapter five, some relative sea level studies use favourable comparisons with independent data, such as nearby tide gauges, as confirmation of reconstruction performance (e.g. Gehrels *et al*., 2005; Kemp *et al*., 2009, 2011). Where independent estimates of coseismic deformation are available, including for the 1960 earthquake at Chucalen and Maullín, transfer functions provide comparable results. Hamilton and Shennan (2005b) and Watcham *et al*. (2012) advocate additional independent statistical testing of the goodness of fit between modern and fossil samples. No fossil sample from Chucalen, Maullín, Cocotue or the *Sediment Signatures* sites (chapter five) has a 'good' modern analogue in the *Regional* training set. Consequently, while the quantitative reconstructions make ecological sense, I adopt a cautionary approach and await a more comprehensive modern dataset for reanalysis of fossil assemblages.

The *Regional* training set typically provides fewer 'poor' modern analogues than the *Chiloé* dataset; however this reflects the increase in the percentile thresholds with a more diverse modern dataset giving greater knowledge of the population diversity, rather than a greater level of similarity with the fossil assemblages. The diversity in south central Chilean diatom assemblages is clearly larger than can be characterised by the 128 available modern samples. A

map of the location of the ten closest modern analogues for each fossil sample (figure 6.21) suggests that including the Valdivia modern samples does little to increase the predictive power of the transfer function for sites in northern Chiloé and the adjacent mainland. None of the closest analogues for the Maullín samples are located in the Valdivia transects, while only 0.5 % of analogues for the Chucalen samples not from the Chiloé transects. While this favours the application of the *Chiloé* transfer function model over the *Regional* model, such a selection is, at present, unnecessary due to the dissimilarity between the modern and fossil assemblages.

6.9 Summary

At Chucalen, the lateral extent of buried soils, repeated abrupt submergence, coincident tsunami deposits and possible synchroneity with the timing of the burial of soils at Maullín leaves the coseismic deformation hypothesis intact. This chapter supports the assertion that Chilean tidal marshes preserve evidence for multiple earthquake deformation cycles. A *P_sequence* age-depth model constrains the timing of the inferred predecessors of the 1960 earthquake to 1520 to 1946, 1270 to 1410 and 1050 to 1200. While quantitative reconstructions of metre-scale land-level change make ecological sense, the requirement for 'good' modern analogues currently remains unfulfilled and I need further modern samples to capture the diversity of south central Chilean intertidal diatoms. The close correspondence between transfer function derived reconstructions and published estimates of deformation in 1960 at Chucalen and Maullín is encouraging. Due to its elevation, the Cocotue exposure cannot constrain the magnitude of coseismic deformation; however, the site may help to constrain the long-term relative sea-level history of northern Isla de Chiloé.

7. Discussion and conclusions

7.1 Introduction

The foremost aim of this thesis is to establish whether coastal sediments preserve evidence for late Holocene earthquakes and relative sea level change in south central Chile. Chapter five established that south central Chilean tidal marshes preserve evidence for the 1960 and 2010 megathrust earthquakes. Evidence presented in chapter six strongly supports the assertion that Chucalen and Maullín also preserve evidence for predecessors to the 1960 earthquake. Chapter one outlined three additional contributory hypotheses:

1. Palaeoseismic evidence records historically documented megathrust earthquakes
2. Differences between historical and palaeoseismic records reflect coseismic deformation patterns
3. Evidence for relative sea-level change reflects both the earthquake deformation cycle and non-seismic processes

This chapter considers evidence from chapters five and six in relation to these hypotheses. Section 7.2 discusses hypothesis one, relating modelled palaeoearthquake timing to historical records. Section 7.3 investigates the spatial distribution of evidence from this and other studies to examine discrepancies between sedimentary and historical records. Section 7.4 converts palaeomarsh surface elevation data into estimates of relative sea level, discussing changes over time within a framework of previous Chilean sea level investigations and possible causal mechanisms. Section 7.5 summarises the findings of the thesis and outlines future directions for development.

7.2 Hypothesis 1: Coastal palaeoseismic evidence records historically documented megathrust earthquakes

While the precision of the radiocarbon approach is insufficient to confirm synchroneity of submergence at Chucalen and Maullín, chapter six concluded that repeated megathrust earthquakes are the best explanation for the stratigraphies of both sites. *P_sequence* age-depth modelling (section 6.2.3) constrains the timing of three predecessors to the 1960 earthquake to

1520 to 1946, 1270 to 1410 and 1050 to 1200 (figure 7.1). I refer to the proposed earthquakes using the same letters as for the buried soils that they relate to, i.e. earthquake A for the abrupt submergence and burial of soil A, earthquake B for soil B and so on.

At Chucalen, radiocarbon samples with narrow calibration solutions (section 6.3.5) and ^{137}Cs concentrations (section 5.3.3) establish the correspondence between the sedimentologically defined earthquake A and the 1960 event. Diatom-derived reconstructions of coseismic deformation show good agreement with Plafker and Savage's (1970) estimates of -1.0 ± 0.2 m at Chucalen and -1.5 ± 0.4 m for Maullín (sections 6.3.4 and 6.5.2).

Modelled two sigma age ranges for earthquake B overlap with three major historical earthquakes in 1575, 1737 and 1837 (figure 7.1). The radiocarbon evidence presented in this study cannot distinguish between these possibilities. Cisternas *et al*. (2005), however, present dendrochronological and supporting documentary data suggesting that trees near Maullín killed by submergence into the intertidal zone in 1960 had survived both the 1737 and 1837 earthquakes. On this basis, the authors attribute earthquake B to 1575. While radiocarbon data cannot rule out earthquake B representing different historical earthquakes at Chucalen and Maullín, the implied absence of evidence for the 1575 earthquake at Chucalen would be difficult to explain. If interseismic sedimentation was insubstantial, the occurrence of a second earthquake (i.e. 1837) shortly after a first earthquake (i.e. 1575) could result in the overprinting of evidence for two subsidence events. The interseismic sedimentation rates inferred from the age-depth model (section 6.2.3), however, suggest subsidence events with more than a few decades between them would be separated in the sedimentary record. Furthermore, at Río Andalién and Río Tirua, the stratigraphic separation of the 2010 and 1960 earthquakes and consequent tsunamis suggests that closely temporally spaced ruptures can be discerned (chapter five; Garrett *et al*., accepted).

The absence of evidence for the 1737 and, particularly, the 1837 earthquakes in the sedimentary records from Chucalen and Maullín is notable. Historical records for 1837 imply shaking over an extensive area, from the northern limit of the 1960 rupture area to the southern limit of Spanish occupation (and therefore documentary records), 70 km south of Chucalen (Lomnitz, 1970; Cisternas *et al*., 2005). The accompanying tsunami inundated flat land in northern Chiloé to a distance of 900 m, but caused little damage (Lomnitz, 1970). The tsunami crested over 5 metres high in Hawaii, causing extensive damage to Hilo, before inundating low lying coastal areas of Japan between Ōfunato and Sendai (Lomnitz, 1970; Lander and Lockridge, 1989; Atwater *et al*., 2005). Despite these records, the lithology and biostratigraphy for the period between the 1575

and 1960 earthquakes at Chucalen and Maullín show no evidence for tsunami inundation or land level change (figures 6.2, 6.6, 6.11). Section 7.3 discusses possible causes for the lack of stratigraphic evidence for the 1737 and 1837 earthquakes.

Historical accounts of Chilean earthquakes began in the early 16th century and the 1575 earthquake is the earliest documented in the Valdivia seismic segment (Lomnitz *et al*., 1970). Earthquakes C and D predate historical records in Chile and approximately double the length of the seismic catalogue for the Valdivia segment. The *P_sequence* model for Chucalen and limiting dates from Maullín place earthquake C between 1270 and 1410 AD. Modelled and limiting dates suggest earthquake D occurred between 1050 and 1200. Further pre- and post-earthquake radiocarbon samples, dendrochronological approaches and documentary records of tsunami occurrence in Japan could further constrain the timing of these events (cf. Atwater *et al*., 2005).

7.3 Hypothesis 2: Differences between historical and palaeoseismic records reflect coseismic deformation patterns

While the four historically documented megathrust earthquakes have an average recurrence interval of 128 years, sediments from Chucalen suggest a longer interval, averaging approximately 280 years (figure 7.1). This discrepancy both highlights that coastal sediments in south central Chile underrepresent the frequency of major earthquakes and also suggests variability in the characteristics of the historical events. The cumulative fault slip from four 1960-sized earthquakes far exceeds the slip predicted by the plate convergence rate (Stein *et al*., 1986; Barrientos and Ward, 1990). Estimated average slip in 1960 was approximately 20 m, with possible maxima of 40 m (Plafker and Savage, 1970; Kanamori and Cipar, 1974; Barrientos and Ward, 1990), substantially more than the seven to ten metres that 128 years of plate convergence accounts for (DeMets *et al*., 1990; Somoza, 1998; Angermann *et al*., 1999).

Figure 7.2 summarises evidence from historical records and palaeoseismic investigations at sites within the Valdivia segment. Evidence for the 1575 earthquake is widespread, with shaking, deformation and tsunami inundation reported from the northern limit of the 1960 rupture zone to central Chiloé (Berninghausen, 1962; Lomnitz, 1970; Cisternas *et al*., 2005). The lack of Spanish colonial outposts south of 43°S accounts for the absence of evidence from the southern portion of the Valdivia segment. In addition to the stratigraphic evidence for 1575 subsidence at Maullín and Chucalen, concurrent uplift could account for soil formation on Isla Guafo (43°36'S) (Melnick, 2010). Turbiditic deposition in Reloncaví fjord (42°S) may also attest to the effects of the same earthquake (Chapron *et al*., 2006). The distribution and nature of the evidence for the 1575

earthquake suggest a similar rupture to the 1960 earthquake (Lomnitz, 1970; Cisternas *et al*., 2005).

Evidence for the 1737 earthquake is greatly restricted in comparison to the earlier event, with only isolated accounts of damage in Valdivia (39°52'S; figure 7.2) and Chiloé (Lomnitz, 1970). Growth suppression of trees in the Nahuel Huapi national park, Argentina (41°S) suggests increased substrate instability associated with intense shaking (Kitzberger *et al*., 1995). The lack of deformation along the populated northern half of the Valdivia segment and possible large aftershocks felt on Isla Wager (48°S, not shown on figure 7.2), south of the Chile triple junction (46°S) (Byron, 1768), suggest a rupture zone south of Chiloé (red dashed ellipse in figure 7.2). This interpretation is consistent with the absence of stratigraphic evidence at Chucalen and Maullín. The lack of any reports of a tsunami following the 1737 earthquake may reflect the location of the rupture with respect to populated areas or the faulting mechanism not resulting in a large tsunami.

As summarised in section 7.2, a large trans-Pacific tsunami accompanied the 1837 earthquake (Lomnitz, 1970; Lander and Lockridge, 1989; Atwater *et al*., 2005). Evidence for the tsunami along the coast of Chile is not, however, as extensive as for the 1575 and 1960 tsunamis (figure 7.2), with no reports of extensive damage (Lomnitz, 1970; Cisternas *et al*., 2005). As with the 1737 earthquake, a lack of deformation in the populated areas north of Chiloé suggests the rupture zone was not the same as in 1575 or 1960. Reed *et al*. (1988) proposes 15 m of slip on a 750 km fault from Valdivia (39°52'S) to the Chile triple junction (46°S) (blue dashed ellipse in figure 7.2). This would account for subsidence inferred from historical accounts from close to the southern terminus (Darwin, 1851; Reed *et al*., 1988) and to the east of northern Chiloé (Cisternas *et al*., 2005). The rupture would also be consistent with intense shaking inferred from tree growth suppression in Nahuel Huapi (41°S) (Kitzberger *et al*., 1995). The lack of evidence for subsidence at Chucalen and Maullín suggests little deformation occurred in region of northern Chiloé and could limit the northward extent of Reed *et al*.'s (1988) proposed rupture zone. A smaller rupture length, perhaps involving reduced slip on a 500 km fault from the northern Chiloé to the Chile triple junction (red dashed ellipse in figure 7.2), might also better match the plate convergence budget (cf. Stein *et al*., 1986; Barrientos and Ward, 1990).

Documentary and palaeoseismic data supports substantial variability between earthquakes. While the 1575 and 1960 earthquakes share similarities, several lines of evidence suggest the intervening earthquakes were located to the south of Chiloé, ruptured smaller areas of the plate interface and did not generate tsunamis as damaging as the 1575 and 1960 events. In the absence

of further documentary records or coastal sites containing evidence for the earthquakes, speculation remains over the precise rupture locations, lengths, magnitudes and effects of the 1737 and 1837 ruptures.

7.4 Hypothesis 3: Evidence for relative sea-level change reflects both the earthquake deformation cycle and non-seismic processes

7.4.1 Relative sea level at Chucalen and Maullín

The presence of buried organic marsh soils below the elevation of contemporary soil formation indicates relative sea-level rise at both Chucalen and Maullín. By taking away palaeomarsh surface elevation estimates from the field elevation of each fossil sample (equation 3.4), the Chucalen and Maullín data provide quantitative estimates of changing relative sea level over time (figure 7.3). The *P_sequence* model (section 6.2.3) provides two sigma age ranges for each sample at Chucalen. At Maullín, samples from the top of each buried soil use dates from Cisternas *et al*. (2005). Vertical errors represent the cumulative error associated with sample specific transfer function error (± 1 standard error), core top elevation and sample depth (section 3.5.6).

The two relative sea level curves suggest between 0.5 m and 1.5 m of sea level rise over the last 1000 years, superimposed with four earthquake deformation cycles (figure 7.3). If the magnitudes of deformation resulting from interseismic strain accumulation and coseismic strain release are equal, the elevation of successive buried soils provides an estimate of the rate of non-seismic relative sea level change. The rates for each site, 0.31 mm/yr at Chucalen and 0.36 mm/yr at Maullín, are indistinguishable from one another given the magnitude of the age and elevation errors.

7.4.2 Mid to Late Holocene relative sea level change in south central Chile

Figure 7.4 displays the Chucalen and Maullín reconstructions alongside former relative sea levels inferred from locations close to Maullín (Atwater *et al*., 1992). I discard a single point from Atwater *et al*. (1992) located below present sea level due to the likelihood of compaction, as noted by the original authors. I also exclude samples from the mainland adjacent to Chiloé (Herve and Ota, 1993) due to their proximity to the Liquiñe-Ofqui Fault Zone (section 2.2.1), uncertain indicative meanings or the possibility of reworking of older material.

Together, data from Chucalen and the wider Maullín area suggest that the rising relative sea level seen over the last 1000 years is not the dominant mid to late Holocene trend (figure 7.4). Tidal marsh sediments above their contemporary depositional elevations suggest net emergence over the last 2000 to 5000 years. Bartsch-Winkler and Schmoll (1993) provide evidence from Chiloé of abandoned marine terraces, sea cliffs and stacks, in addition to shell and foraminifera-bearing low intertidal or subtidal deposits above their modern depositional elevations. While their origin and age is as yet unconfirmed, coarse sands underlying the intertidal sequence at Chucalen may also indicate a low intertidal or subtidal environment, again implying net emergence over a timescale exceeding the last 1000 years. The lack of marine influence in diatom assemblages at Cocotue indicates relative sea level did not exceed 3 m above mean sea level over the past millennium and was probably less than 2 m above present at 1000 AD. While large age and altitude errors currently limit the precision of the sea level curve (figure 7.4b), some speculation is possible on the driving mechanisms for the change from to late Holocene relative sea level fall to recent relative sea-level rise.

Mid Holocene highstands above present are a common feature of southern hemisphere mid-latitude coastlines (e.g. Isla, 1989; Schellmann and Radtke, 2003; Sloss *et al*., 2005; Woodroffe and Horton, 2005; Lessa and Masselink, 2006). Raised marine deposits also imply mid-Holocene sea levels above present in central Chile (Pino and Navarro, 2005; Encinas *et al*., 2006; Isla *et al*., 2012) and southern Chile (Porter *et al*., 1984; Isla, 1989; Gordillo *et al*., 1992; McCulloch and Davies, 2001). The subsequent mid to late Holocene relative sea level fall results from ocean syphoning following collapse of northern hemisphere forebulges and continental levering through ocean loading (Clark *et al*., 1978; Mitrovica and Peltier, 1991; Mitrovica and Milne, 2002). For a location close to the sites presented in this study, Peltier's (2004) ICE5G (VM2) model predicts a highstand approximately 8 m above present at 8 ka BP (figure 7.4a). While falling sea level following a highstand fits with the emergence identified by Atwater *et al.* (1992), the modelled rate of sea level fall exceeds the rate inferred from the data (figure 7.4b). Furthermore, the model does not incorporate any period of rising relative sea level after 8 ka BP that could match the rise implied by the presence of buried soils at Chucalen and Maullín. Studies in subduction zone settings have identified very rapid post Little Ice Age rebound, which implies a low viscosity asthenosphere (James *et al*., 2000; Ivins and James, 2002; Rignot *et al*., 2003; Larsen *et al*., 2005; Dietrich *et al*., 2010; Barlow *et al*., 2012). Such a low viscosity layer is not included in ICE5G's VM2 earth model, which is tuned for continental settings. Rapid viscoelastic response associated with lower viscosity could result in an earlier diminution of the post Last Glacial Maximum isostatic signal in south central Chile and a late Holocene relative sea-level curve closer to those modelled for north central Chile (figures 2.6; 7.4). If the long wavelength isostatic contribution to relative

sea-level change concluded by the mid Holocene, other shorter-term factors could explain the late Holocene relative sea level rise.

Following the comparative warmth of the early Holocene (Heusser and Streeter, 1980; Rabassa and Clapperton, 1990), the two Patagonian icefields underwent several phases of expansion in the mid to late Holocene (Mercer, 1970; Aniya, 1996; Glasser at al., 2004; Bertrand *et al*., 2012). These Neoglacial advances (figure 7.4c), culminating in the Little Ice Age, resulted in depression of the crust matched by recent and ongoing crustal rebound following deglaciation (Dietrich *et al*., 2010). While models of deformation do not extend to the location of this study (Ivins and James, 2002; Dietrich *et al*., 2010), Chucalen and Maullín may lie within a Neoglacial forebulge. The build-up of such a forebulge would contribute to continued mid Holocene relative sea-level fall, while the subsequent collapse could contribute to the recent relative sea-level rise (figure 7.4b).

Eustatic, local and tectonic factors may have assisted the postulated forebulge collapse and increased the magnitude of relative sea-level rise. Kemp *et al*. (2011) infer a eustatic contribution of approximately 0.4 m over the last 1000 years. This is not, however, a globally applicable figure and the contribution to south central Chilean relative sea level over the last 1000 years is likely to be less, particularly if Antarctic melting resulted in a decreased gravitational anomaly and migration of the ocean geoid to lower latitudes (Lambeck, 2002; Whitehouse *et al*., 2012).

Autocompaction results in the lowering of sea level index points from their original depositional altitudes (Allen, 2000; Edwards, 2006; Long *et al*., 2006; Horton and Shennan, 2009; Brain *et al*., 2012). While the sediment sequences at Maullín and Chucalen are typically only around 1 m thick and, in certain locations, rest on uncompactable bedrock, the presence of highly organic buried soils could magnify the recent rise in relative sea level.

Finally, the assumption of no net tectonic deformation over multiple earthquake cycles may be incorrect. Towards the northern end of the Valdivia seismic segment at Isla Mocha, Nelson and Manley (1992) infer a 38 m relative sea level fall over the mid to late Holocene. The extremely rapid uplift rate may reflect interseismic uplift from aseismic slip on upper plate thrust faults in addition to coseismic uplift (Nelson and Manley, 1992). Similarly, Melnick *et al*. (2006) evoke thrust faulting to explain the rapid uplift and tilting of Isla Santa Maria at the northern limit of the 1960 rupture zone. While Chucalen and Maullín sit on the Chiloé block, a 1000 km long sliver detached from stable South America (Cembrano *et al*., 1996), uplift of the Arauco Peninsula (37°S) appears to accommodate the northward movement of this block (Wang *et al*., 2007; Moreno *et*

al., 2008) and Neogene movements on thrust faults have not influenced northern Chiloé (Muñoz *et al*., 1999).

7.5 Conclusions

This section reviews the principal findings of the thesis in relation to the objectives outlined in chapter 1 and presents recommendations for future palaeoseismic research in south central Chile. En route to testing the primary research hypothesis, *Coastal sediments preserve evidence for late Holocene earthquakes and relative sea level change in south central Chile*, this thesis aimed to fulfil a series of objectives:

- Characterise modern intertidal diatom distributions in south central Chilean tidal marshes
- Develop transfer function models for the purpose of reconstructing palaeomarsh surface elevation from fossil marsh sediments
- Test the performance of the approach by reconstructing coseismic deformation associated with recent, well documented Chilean earthquakes
- Interrogate coastal sediments in the Valdivia seismic segment for evidence of past earthquakes
- Reconstruct coseismic deformation associated with palaeoearthquakes
- Constrain the timing of palaeoearthquakes using a radiometric approach and compare inferred ages with historical records and other palaeoseismic investigations
- Investigate relative sea-level changes occurring over the course of multiple earthquake deformation cycles

7.5.1 Summary of findings

Characterise modern intertidal diatom distributions in south central Chilean tidal marshes

Chapter four presents data from two new tidal marsh sites, Puente Quilo and Estero Guillingo. Transects at both sites are characterised by low diversity assemblages below mean higher high water and more variable, species-rich assemblages at higher elevations. The substantial variation in contemporary diatoms suggests their suitability as indicators of different elevation-controlled environments. Constrained ordination of both the *Chiloé* dataset, consisting of the two new sites and a larger *Regional* dataset, also incorporating samples from the Valdivia estuary (Nelson *et al*.,

2009), suggests elevation and covarying environmental factors explain a considerable portion of the diatom variability.

Develop transfer function models for the purpose of reconstructing palaeomarsh surface elevation from fossil marsh sediments

Weighted averaging partial least squares regression provides *Chiloé* and *Regional* transfer function models for the purpose of reconstructing marsh surface elevation. Three component models have the highest r^2 values, linear distributions of observed against predicted values and acceptable levels of precision. The training set is the largest currently available for south central Chile and can provide a foundation for future palaeoseismic and relative sea-level investigations.

Test the performance of the approach by reconstructing coseismic deformation associated with recent, well documented Chilean earthquakes

Chapter five employs the transfer functions developed in chapter four to reconstruct coseismic deformation associated with the 2010 and 1960 earthquakes. The method is successful in matching independent estimates of land-level change in uplifting, stable and subsiding regions. The small offset between diatom-based reconstructions and published estimates may relate to coseismic marsh sediment consolidation. Despite the lack of 'good' modern analogues for fossil samples, the fidelity with which the test sites record the magnitude and direction of deformation supports the use of diatoms to quantify deformation during previous great earthquakes in south central Chile.

Interrogate coastal sediments in the Valdivia seismic segment for evidence of past earthquakes

Laterally extensive buried soils with abrupt upper contacts, coincident tsunami deposits and evidence for rapid and substantial marsh surface elevation change suggest sediments at Chucalen record evidence for repeated earthquake deformation cycles (chapter six). A new biostratigraphic record for Maullín provides support for submergence associated with tsunami deposits identified by Cisternas *et al*. (2005). Due to its supratidal elevation, Cocotue cannot provide evidence for coseismic deformation. While the freshwater diatom assemblages are unexpected in tsunami deposits, this finding does not precipitate the rejection of the hypothesis of tsunami occurrence.

Reconstruct coseismic deformation associated with palaeoearthquakes

Diatom assemblages suggest metre-scale changes in palaeomarsh surface elevation accompany most abrupt transitions from organic buried soils to minerogenic deposits at both Chucalen and Maullín. Submergence appears to coincide with buried soil B, however uncertainty over the magnitude of submergence means that reconstructions cannot yet conclusively falsify an aseismic hypothesis for the formation of this couplet. While the requirement for 'good' modern analogues currently remains unfulfilled, quantitative reconstructions of land-level change make ecological sense. The close correspondence between transfer function derived reconstructions and published estimates of deformation in 1960 at Chucalen and Maullín is also encouraging.

Constrain the timing of palaeoearthquakes using a radiometric approach and compare inferred ages with historical records and other palaeoseismic investigations

A *P_sequence* age model constrains the timing of the inferred predecessors of the 1960 earthquake at Chucalen to 1520 to 1946, 1270 to 1410 and 1050 to 1200. These ages closely correspond with limiting dates for tsunami deposition and subsidence at Maullín (Cisternas *et al*., 2005) suggesting a high probability of synchroneity. Radiocarbon data, combined with dendroecological approaches at Maullín (Cisternas *et al*., 2005), indicate that the four earthquakes do not correspond to the four historically documented megathrust earthquakes of the past 450 years. Instead, the 1000 year long record only incorporates the 1960 and 1575 earthquakes, with no evidence for the intervening 1737 and 1837 events. Combination of the evidence presented here with historical records implies the absent earthquakes were smaller and occupied rupture zones south of Chiloé.

Investigate relative sea-level changes occurring over the course of multiple earthquake deformation cycles

The presence of palaeoseismic records in south central Chile implies rising relative sea levels over the last 1000 years. While stacks of repeated organic – minerogenic couplets are unlikely to form during periods of relative sea-level fall, field and modelling studies suggest that emergence characterises much of the mid to late Holocene. Initial speculation links the recent relative sea-level rise to early diminution of post Last Glacial Maximum glacio-isostatic uplift and possibly the formation and collapse of a Little Ice Age forebulge. The complex interplay between eustatic, tectonic and local factors may also contribute. Net emergence over timescales exceeding the last 1000 years may prevent the formation of longer palaeoseismic records.

7.5.2 Recommended future research directions

Modern diatom distributions

While transfer reconstructions made ecological sense and match independent estimates of deformation, the lack of 'good' modern analogues for fossil assemblages suggests the modern diatom dataset does not yet adequately reflect the variability in south central Chilean assemblages. Future work should expand the database, collecting further modern samples from additional marsh sites.

Locating the 1737 and 1837 earthquakes

The 1737 and 1837 earthquakes are notable by their absence in the Chucalen and Maullín records. If 1960-style ruptures reflect the culmination of longer cycles involving smaller intervening earthquakes, future research must also place emphasis on understanding these smaller ruptures. At present, palaeoseismic records may only incorporate the largest south central Chilean earthquakes. While substantially smaller, the mid-cycle earthquakes may still exceed magnitude 7.5 to 8.5. The damaging trans-Pacific tsunami of 1837 highlights that events of this size may still be highly destructive. Future work should focus on finding the sedimentary signatures of these events in their likely source regions, namely areas south of Chiloé.

Modelling earthquake magnitude

Studies by Leonard *et al.* (2004, 2010) and Hawkes *et al*. (2011) demonstrate the potential for comparison of microfossil-derived estimates of coseismic subsidence with predictions from elastic dislocation models. Further refinement of the coseismic deformation reconstruction approach may enable dislocation modelling for Chilean megathrust earthquakes, constrained by diatom-based estimates of deformation.

Modelling relative sea level change along tectonically active margins

The Holocene relative sea-level history of the Chilean coastline remains poorly understood. Data presented in this thesis highlight discrepancies between glacio-isostatic adjustment models and field evidence. Future research should focus on obtaining high quality relative sea-level datasets to constrain new earth models. Such an approach would further assist in disentangling the multifarious contributions to relative sea-level change.

Cited literature

THE ACADEMY OF NATURAL SCIENCES OF DREXELL UNIVERSITY. 2012. ANSP Algae Image Database from the Phycology Section, Patrick Center for Environmental Research, The Academy of Natural Sciences. Accessed at: http://diatom.acnatsci.org/AlgaeImage/

ADMIRALTY TIDE TABLES. 2004. Volume 1, 2004, United Kingdom and Ireland. Hydrographer of the Navy.

AIKEN, C.M. 2008. Barotropic tides of the Chilean Inland Sea and their sensitivity to basin geometry. *Journal of Geophysical Research*, 113, C08024

ALLEN, J. R. L. 1997. Simulation models of salt-marsh morphodynamics: some implications for high-intertidal sediment couplets related to sea-level change. *Sedimentary Geology,* 113, 211-223.

ALLEN, J. R. L. 2000. Morphodynamics of Holocene salt marshes: a review sketch from the Atlantic and Southern North Sea coasts of Europe, *Quaternary Science Reviews,* 19*,* 1155 -1231

ANDERSON, M., ALVARADO, P., ZANDT, G., BECK, S. 2007. Geometry and brittle deformation of the subducting Nazca Plate, Central Chile and Argentina. *Geophysical Journal International,* 171, 419-434.

ANGERMANN, D., KLOTZ, J., REIGBER, C. 1999. Space-geodetic estimation of the Nazca-South America Euler vector. *Earth and Planetary Science Letters,* 171, 329-334.

ANIYA, M. 1995. Holocene glacial chronology in Patagonia: Tyndall and Upsala glaciers. *Arctic Alpine Res*earch, 27, 311–322

ANIYA, M. 1996. Holocene variations of Ameghino Glacier, southern Patagonia. *Holocene*, 6, 247–252

APPELTANS W., BOUCHET P., BOXSHALL G.A., DE BROYER C., DE VOOGD N.J., GORDON D.P., HOEKSEMA B.W., HORTON T., KENNEDY M., MEES J., POORE G.C.B., READ G., STÖHR S., WALTER T.C., COSTELLO M.J. (eds). 2012. *World Register of Marine Species*. Accessed at: http://www.marinespecies.org

ARNAUD, F., MAGAND, O., CHAPRON, E., BERTRAND, S., BOE, X., CHARLET, F. MELIERES, M.-A. 2006. Radionuclide dating (210Pb, 137Cs, 241Am) of recent lake sediments in a highly active geodynamic setting (Lakes Puyehue and Icalma—Chilean Lake District). *Science of the Total Environment,* 366, 837 – 850.

ATWATER, B. F. 1987. Evidence for Great Holocene earthquakes along the outer coast of Washington State. *Science,* 236, 942-944.

ATWATER, B. F., YAMAGUCHI, D. K. 1991. Sudden, probably coseismic submergence of Holocene trees and grass in coastal Washington-State. *Geology,* 19, 706-709.

ATWATER, B.F., STUIVER, M., YAMAGUCHI, D.K., 1991. A radiocarbon test of earthquake magnitude at the Cascadia subduction zone. *Nature,* 353, 156-158.

ATWATER, B., JIMÉNEZ, H., VITA-FINZI, C. 1992. Net late Holocene emergence despite earthquake-induced submergence, South Central Chile. *Quaternary International*, 15/16, 77-85.

ATWATER, B. F., YAMAGUCHI, D. K., BONDEVIK, S., BARNHARDT, W. A., AMIDON, L. J., BENSON, B. E., SKJERDAL, G., SHULENE, J. A., NANAYAMA, F. 2001. Rapid resetting of an estuarine recorder of the 1964 Alaska earthquake. *Geological Society of America Bulletin,* 113, 1193-

1204.

ATWATER, B.F., MUSUMI-ROKKAKU, S., SATAKE, K., TSUJI, Y., UEDA, K., YAMAGUCHI, D. 2005. *The Orphan Tsunami of 1700*. Virginia, United States Geological Survey.

BARAZANGI, M., ISACKS, B. L. 1976. Spatial distributions of earthquakes and subduction of Nazca Plate beneath South-America. *Geology,* 4, 686-692.

BARLOW, N.L.M., SHENNAN, I., LONG, A.J. 2012. Relative sea-level response to Little Ice Age ice mass change in south central Alaska: Reconciling model predictions and geological evidence. *Earth and Planetary Science Letters,* 315-316, 62-75

BARRIENTOS, S. E. 1996. On predicting coastal uplift and subsidence due to large earthquakes in Chile. Third ISAG Meeting, September 17-19, 1996 St Malo, France. 145-148.

BARRIENTOS, S. E. 2007. Earthquakes in Chile. *In:* MORENO, T., GIBBONS, W. (eds.) *The Geology of Chile.* London: The Geological Society. pp. 263-287.

BARRIENTOS, S. E., WARD, S. N. 1990. The 1960 Chile Earthquake – inversion for slip distribution from surface. *Geophysical Journal International,* 103, 589-598.

BARRIENTOS, S. E., PLAFKER, G., LORCA, E. 1992. Postseismic coastal uplift in southern Chile. *Geophysical Research Letters,* 19, 701-704.

BARTSCH-WINKLER, S., SCHMOLL, H. 1993. Evidence for late Holocene relative sea-level fall from reconnaissance stratigraphical studies in an area of earthquake-subsided intertidal deposits, Isla Chiloe, southern Chile. *In:* FROSTWICK, L. E., STEEL, R. J. (eds.) *Tectonic controls and signatures in sedimentary successions.* International Association of Seismologists. pp. 91-108.

BECK, M. E., ROJAS, C., CEMBRANO, J. 1993. On the nature of buttressing in margin-parallel strike-slip fault systems. *Geology,* 21, 755-758.

BENSON, B.E., ATWATER, B.F., YAMAGUCHI, D.K., AMIDON, L.J., BROWN, S.L., LEWIS, R.C., 2001. Renewal of tidal forests in Washington state after a subduction earthquake in A.D. 1700. *Quaternary Research,* 56, 139–147.

BENTLEY, M.J., MCCULLOCH, R.D. 2005. Impact of Neotectonics on the Record of Glacier and Sea Level Fluctuations, Strait of Magellan, Southern Chile. *Geografiska Annaler*, 87A: 393-402

BERNARD, E. N., MOFJELD, H. O., TITOV, V., SYNOLAKIS, C. E., GONZALEZ, F. I. 2006. Tsunami: scientific frontiers, mitigation, forecasting and policy implications, *Phil. T. R. Soc. A.*, 364, 1989–2007.

BERNINGHAUSEN, W. H. 1962. Tsunamis reported from the west coast of South America, 1562-1960, *Bulletin of the Seismological Society of America*, 52, 915-921.

BERTRAND S., CHARLET F., CHAPRON E. 2008. Reconstruction of the Holocene seismotectonic activity of the Southern Andes from seismites recorded in Lago Icalma, Chile, 39°S. *Palaeogeography Palaeoclimatology Palaeoecology,* 259, 301–322.

BERTRAND, S., HUGHEN, K. A., LAMY F., STUUT, J.-B. W., TORREJON, F., LANGE, C. B. 2012. Precipitation as the main driver of Neoglacial fluctuations of Gualas glacier, Northern Patagonian Icefield. Climate of the Past, 8, 1–16.

BILEK, S. L. 2010. Seismicity along the South American subduction zone: Review of large earthquakes, tsunamis, and subduction zone complexity *Tectonophysics, 495, 2-14.*

BIRD, J., 1938. Antiquity and Migrations of the Early Inhabitants of Patagonia. *Geographical Reviews* 28, 250-275.

BIRKS, H. J. B. 1995. Quantitative palaeoenvironmental reconstructions. *In:* MADDY, D. A. B., J.S. (ed.) *Statistical modelling of Quaternary science data.* Cambridge: Quaternary Research Association. pp. 161-254.

BIRKS, H. J. B. 1998. D.G. Frey, E.S. Deevey review #1 - Numerical tools in palaeolimnology -

Progress, potentialities, and problems. *Journal of Paleolimnology,* 20, 307-332.

BIRKS, H.J.B., LINE, J.M., JUGGINS, S., STEVENSON, A.C., TER BRAAK, C.J.F. 1990. Diatoms and pH reconstruction. *Philosophical Transactions of the Royal Society of London B,* 327, 263-278.

BOOKHAGEN, B., ECHTLER, H. P., MELNICK, D., STRECKER, M. R., SPENCER, J. Q. G. 2006. Using uplifted Holocene beach berms for paleoseismic analysis on the Santa Maria Island, south-central Chile. *Geophysical Research Letters,* 33, L15302.

BOURGEOIS, J. 2006. Earthquakes - A movement in four parts? *Nature,* 440, 430-431.

BOWMAN, S. 1990. Radiocarbon dating. London, British Museum Publications for the Trustees of the British Museum.

BRAIN, M.J., LONG, A.J., WOODROFFE, S.A., PETLEY, D.N., MILLEDGE, D.G., PARNELL, A.C. 2012. Modelling the effects of sediment compaction on salt marsh reconstructions of recent sea-level rise. *Earth and Planetary Science Letters*, 345-348, 180-193.

BRIGGS, R. W., SIEH, K., MELTZNER, A. J., NATAWIDJAJA, D., GALETZKA, J., SUWARGADI, B., HSU, Y. J., SIMONS, M., HANANTO, N., SUPRIHANTO, I., PRAYUDI, D., AVOUAC, J. P., PRAWIRODIRDJO, L., BOCK, Y. 2006. Deformation and slip along the Sunda Megathrust in the great 2005 Nias-Simeulue earthquake. *Science,* 311, 1897-1901.

BRONK RAMSEY, C., 1995. Radiocarbon calibration and analysis of stratigraphy: The OxCal program. *Radiocarbon,* 37, 425-430.

BRONK RAMSEY, C., 2008. Deposition models for chronological records. *Quaternary Science Reviews*, 27, 42-60.

BRONK RAMSEY, C., 2009a. Bayesian Analysis of Radiocarbon Dates. *Radiocarbon,* 51, 337-360.

BRONK RAMSEY, C. 2009b. Dealing with outliers and offsets in radiocarbon dating. *Radiocarbon,* 51, 1023-1045.

BRYANT, S. 2008. *Tsunami: the underrated hazard*. Springer Praxis

CAHILL, T., ISACKS, B. L. 1992. Seismicity and shape of the subducted Nazca plate. *Journal of Geophysical Research-Solid Earth,* 97, 17503-17529.

CALDENIUS, C. 1932. Las glaciaciones cuaternarias en la Patagonia y Tierra del Fuego. *Geografiska Annaler*, 14,1-164.

CAMPOS, J., HATZFELD, D., MADARIAGA, R., LOPEZ, G., KAUSEL, E., ZOLLO, A., IANNACONE, G., FROMM, R., BARRIENTOS, S., LYON-CAEN, H. 2002. A seismological study of the 1835 seismic gap in south-central Chile. *Physics of the Earth and Planetary Interiors,* 132, 177-195.

CASTRO, C., BIGNARDELLO. L. 2005. Geomorfología aplicada a la ordenación territorial de litorales arenosos. Orientaciones para la protección, usos y apovechamiento sustentables del sector de Los Choros, comuna de La Higuera, IV Región. *Revista Geográfica Norte Grande,* 33, 33–57.

CEMBRANO, J., HERVE, F., LAVENU, A. 1996. The Liquine Ofqui fault zone: A long-lived intra-arc fault system in southern Chile. *Tectonophysics,* 259, 55-66.

CEMBRANO, J., LAVENU, A., YANEZ, G., RIQUELME, R., GARCIA, M., GONZALEZ, G., HERAIL, G. 2007. Neotectonics. *In:* MORENO, T., GIBBONS, W. (eds.) *The Geology of Chile.* London: The Geological Society. pp. 231-262.

CHAPPELL, J., POLACH, H., 1991. Post-glacial sea-level rise from a coral record at Huon Peninsula, Papua New Guinea. *Nature* 349, 147–149.

CHAPRON, E., ARIZTEGUI, D., MULSOW, S., VILLAROSA, G., PINO, M., OUTES, V., JUVIGNIÉ, E., CRIVELLI, E., 2006. Impact of the 1960 major subduction earthquake in Northern Patagonia (Chile, Argentina). *Quaternary International,* 158, 58–71.

CHESTER, S. 2008. *A wildlife guide to Chile*. London, A&C Black.

CIFUENTES, I. L. 1989. The 1960 Chilean earthquake. *Journal of Geophysical Research,* 94, 665-680.

CISTERNAS, M., CONTRERAS, I., ARANEDA, A. 2000. Recognition and characterisation of the sedimentary facies deposited by the 1960 tsunami in the Maullín estuary, Chile. *Revista Geologica De Chile,* 27, 3-11.

CISTERNAS, M., ATWATER, B. F., TORREJON, F., SAWAI, Y., MACHUCA, G., LAGOS, M., EIPERT, A., YOULTON, C., SALGADO, I., KAMATAKI, T., SHISHIKURA, M., RAJENDRAN, C. P., MALIK, J. K., RIZAL, Y., HUSNI, M. 2005. Predecessors of the giant 1960 Chile earthquake. *Nature,* 437, 404-407.

CISTERNAS, M., LAGOS, M., SRINIVASALU, S. 2007. A Millennium of Great, and Perhaps Lesser, Earthquakes Recorded by Unusual Landslide and Tsunami Deposits in Chiloe, South-Central Chile. AGU Joint Assembly 2007, Acapulco, Mexico. T43B-08

CISTERNAS, M., TORREJÓN, F., GORIGOITIA, N. Amending and complicating Chile's seismic catalog with the Santiago earthquake of 7 August 1580. *Journal of South American Earth Sciences,* 33, 102-109

CLAGUE, J. J. 1997. Evidence for large earthquakes at the Cascadia subduction zone. *Reviews of Geophysics,* 35, 439-460.

CLARK, J.A., FARRELL, W.E., PELTIER, W.R., 1978. Global changes in postglacial sea level: a numerical calculation. *Quaternary Research,* 9, 265–287.

CLARKE, S. H., CARVER, G. A. 1992. Late Holocene tectonics and paleoseismicity, southern Cascadia subduction zone. *Science,* 255, 188-192.

COBBOLD, P. R., ROSSELLO, E. A., ROPERCH, P., ARRIAGADA, C., GOMEZ, L. A., LIMA, C. 2007. Distribution, timing, and causes of Andean deformation across South America. *Geological Society, London, Special Publications,* 272, 321-343.

COCHRAN, U., BERRYMAN, K.R., MILDENHALL, D.C., HAYWARD, B.W., SOUTHALL, K., HOLLIS, C.J., 2005. Towards a record of Holocene tsunami and storms for Northern Hawke's Bay, New Zealand. *New Zealand Journal of Geology and Geophysics,* 48, 507–515.

COHEN, S. C., FREYMUELLER, J. T. 2004. Crustal deformation in the southcentral Alaska subduction zone. *Advances in Geophysics,* 47, 1-63.

COMBELLICK, R. A. 1991. Paleoseismicity of the Cook Inlet Region, Alaska: Evidence from peat stratigraphy in Turnagain and Knik Arms. *State of Alaska, Department of Natural Resources, Division of Geological and Geophysical Surveys.*

COX, D. Mink, J. F. 1963. The Tsunami of 23 May 1960 in the Hawaiian Islands, *Bulletin of the Seismological Society of America*, 53, 1191-1209

CREMER, H., SANGIORGI, F., WAGNER-CREMER, F., MCGEE, V., LOTTER, A.F., VISSCHER, H. 2007. Diatoms (Bacillariophyceae) and Dinoflagellate Cysts (Dinophyceae) from Rookery Bay, Florida, USA. *Caribbean Journal of Science*, 43, 23–58.

DARIENZO, M.E., PETERSON, C.D., 1990. Episodic tectonic subsidence of late Holocene salt marshes, Northern Oregon coast, central Cascadia margin, U.S.A. *Tectonics*, 9, 1-22.

DARIENZO, M.E., PETERSON, C.D., CLOUGH, C., 1994. Stratigraphic evidence for great subduction zone earthquakes at four estuaries in Northern Oregon, USA. *Journal of Coastal Research* 10, 850-876.

DARWIN, C. 1839. *Journal of Researches into the Geology and Natural History of the countries visited during the Voyage of H.M.S. "Beagle" round the world.,* London, Colburn.

DEAN, W.E. 1974. Determination of carbonate and organic matter in calcareous sediments and sedimentary rocks by loss on ignition: comparison with other methods. *Journal of Sedimentary Petrology,* 44, 242-248.

DELOUIS, B., NOCQUET, J.-M., VALLÉE, M. 2010. Slip distribution of the February 27, 2010 Mw = 8.8 Maule Earthquake, central Chile, from static and high-rate GPS, InSAR, and broadband teleseismic data, *Geophysical Research Letters*, 37, L17305.

DENTON, G.H., HEUSSER, C.J., LOWELL, T.V., MORENO, P.I., ANDERSEN, B.G., HEUSSER, L.E., SCHLUCHTER, C., MARCHANT, D.R. 1999. Interhemispheric linkage of paleoclimate during the last glaciation. *Geografiska Annaler* 81A, 107–153.

DEMETS, C., GORDON, R. G., ARGUS, D. F., STEIN, S. 1990. Current plate motions. *Geophysical Journal International,* 101, 425-478.

DIETRICH, R., IVINS, E.R., CASASSA, G., LANGE, H., WENDT, J., FRITSCHE, M., 2010. Rapid crustal uplift in Patagonia due to enhanced ice loss. *Earth and Planetary Science Letters,* 289, 22-29.

DRAGERT, H., WANG, K. L., JAMES, T. S. 2001. A silent slip event on the deeper Cascadia subduction interface. *Science,* 292, 1525-1528.

DUCHEMIN, G., JORISSEN, F.J., REDOIS, F., DEBENAY, J.-P., 2005. Foraminiferal microhabitats in a high marsh: consequences for reconstructing past sea levels. *Palaeogeography, Palaeoclimatology, Palaeoecology,* 226, 167–185.

DURA, T., RUBIN, C. M., KELSEY, H. M., HORTON, B. P., HAWKES, A., VANE, C. H., DARYONO, M., PRE, C. G., LADINSKY, T., BRADLEY, S. 2011. Stratigraphic record of Holocene coseismic subsidence, Padang, West Sumatra, *Journal of Geophysical Research,* 116, B11306

DURA, T., CISTERNAS, M., HORTON, B.P., ELY, L.L., WESSON, R.L., REBOLLEDO, L. 2012. The application of micropaleontology to recognize coseismic uplift and characterize tsunami deposits on the central Chilean coast. Geological Society of America *Abstracts with Programs*, Vol. 44, No. 7, p. 300

EDWARDS, R.J., 2006. Mid- to late-Holocene relative sea-level change in southwest Britain and the influence of sediment compaction. *Holocene,* 16, 575-587.

EDWARDS, R.J., WRIGHT, A.J., VAN DE PLASSCHE, O., 2004. Surface distributions of salt-marsh foraminifera from Connecticut, USA: modern analogues for high-resolution sea level studies. *Marine Micropaleontology,* 51, 1-21.

ELY, L.L., CISTERNAS, M., WESSON, R.L., LAGOS, M. 2010. Geological Evidence of Predecessors to the 2010 Earthquake and Tsunami in South-Central Chile. American Geophysical Union Fall Meeting, G32A-05.

ENFIELD, D.B., 1989. El Niño, past and present. *Reviews of Geophysics*, 27, 159-187.

ENCINAS, A., HERVE, F., VILLA-MARTINEZ, R., NIELSEN, S. N., FINGER, K. L., PETERSON, D. E. 2006. Finding of a Holocene marine layer in Algarrobo (33 degrees 22 ' S), central Chile. Implications for coastal uplift. *Revista Geologica De Chile,* 33, 339-345.

FAIRBANKS, R.G., 1989. A 17,000 year glacio-eustatic sea level record: influence of glacial melting rates on the Younger Dryas event and deep ocean circulation. *Nature*, 342, 637-642.

FARIAS, M., VARGAS, G., TASSARA, A., CARRETIER, S., BAIZE, S., MELNICK, D., BATAILLE, K. 2010. Land-Level Changes Produced by the M-w 8.8 2010 Chilean Earthquake. *Science,* 329, 916-916.

FATELA, F., TABORDA, R., 2002. Confidence limits of species proportions in microfossil assemblages. *Marine Micropaleontology*, 45, 169-174.

FERNANDEZ, M., JARAMILLO, E., MARQUET, P.A., MORENO, C.A., NAVARETE, S.A., OJEDA, F.P., VALDOVINOS, C.R., VASQUEZ, J.A. 2000. Diversity, dynamics and biogeography of Chilean benthic nearshore ecosystems: an overview and guidelines for conservation. *Revista Chilena de Historia Natural*, 73, 797-830.

FIERRO, J.J.2008. Tides in the austral Chilean channels and fjords. In: SILVA, N., PALMA, S. *Avances en el conocimiento oceanográfico de las aguas interiores chilenas, Puerto Montt a cabo de Hornos*. Comité Oceanográfico Nacional - Pontificia Universidad Católica de Valparaíso, Valparaíso, pp. 63-66.

FITZROY, R. N. 1839. Narrative of the surveying voyages of His Majesty's Ships Adventure and Beagle between the years 1826 and 1836, describing their examination of the southern shores of South America, and the Beagle's circumnavigation of the globe. Proceedings of the second expedition, 1831-36, under the command of Captain Robert Fitz-Roy. London: Colburn.

FLEMING, K., JOHNSTON, P., ZWARTZ, D., YOKOYAMA, Y., LAMBECK, K. CHAPPELL, J. 1998. Refining the eustatic sea-level curve since the Last Glacial Maximum using far- and intermediate-field sites. *Earth and Planetary Science Letters,* 163, 1-4, 327-342.

FLETCHER, C. H., VANPELT, J. E., BRUSH, G. S., SHERMAN, J. 1993. Tidal wetland record of Holocene sea-level movements and climate. *Palaeogeography Palaeoclimatology Palaeoecology,* 102, 177-213.

FRITZ, H.M., PETROFF, C.M., CATALÁN, P., CIENFUEGOS, R., WINCKLER, P., KALLIGERIS, N., WEISS, R., BARRIENTOS, S.E., MENESES, G., VALDERAS-BERMEJO, C., EBELING, C., PAPADOPOULOS, A., CONTRERAS, M., ALMAR, R., DOMINGUEZ, J.C., SYNOLAKIS, C.E. 2011. Field Survey of the 27 February 2010 Chile Tsunami. Pure and Applied Geophysics, 168, 1989-2010.

GARCÍA, J. L. 2012. Late Pleistocene ice fluctuations and glacial geomorphology of the Archipiélago de Chiloé, southern Chile. Geografiska Annaler, 94A: 459–479.

GARRETT, E., SHENNAN, I., WATCHAM, E.P., WOODROFFE, S.A. Reconstructing paleoseismic deformation, 1: modern analogues from the 1960 and 2010 Chilean great earthquakes. Submitted to *Quaternary Science Reviews* October 2012; accepted March 2013.

GEHRELS, W. R., ROE, H. M., CHARMAN, D. J. 2001. Foraminifera, testate amoebae and diatoms as sea-level indicators in UK saltmarshes: a quantitative multiproxy approach. *Journal of Quaternary Science,* 16, 201-220.

GEHRELS, W.R., KIRBY, J.R., PROKOPH, A., NEWNHAM, R.M., ACHTERBERG, E.P., EVANS, H., BLACK, S., SCOTT, D.B., 2005. Onset of recent rapid sea-level rise in the western Atlantic Ocean. *Quaternary Science Reviews,* 24, 2083.

GLASSER, N.F., HARRISON, S., WINCHESTER, V., ANIYA, M., 2004. Late Pleistocene and Holocene palaeoclimate and glacier fluctuations in Patagonia. *Global and Planetary Change,* 43, 79-101.

GLASSER, N., JANNSON, K., HARRISON, S., KLEMANN, J., 2008. The glacial geomorphology and Pleistocene history of South America between 38 and 56°S. *Quaternary Science Reviews*, 27, 356–390.

GLASSER, N. F., HARRISON, S., JANSSON, K. N., ANDERSON, K., COWLEY,A. 2011. Global sea-level contribution from the Patagonian Icefields since the Little Ice Age maximum, *Nature Geoscience*, 4, 303–307.

GOFF, J., NICHOL, S., CHAGUE-GOFF, C., HORROCKS, M., MCFADGEN, B., CISTERNAS, M. 2010. Predecessor to New Zealand's largest historic trans-South Pacific tsunami of 1868 AD. *Marine Geology,* 275, 155-165.

GOODSPEED, TH. 1945. Notes on the vegetation and plant resources of *Chile*. In: VERDOORN, F. (ed). *Plants and Plant Science in Latin America*, Waltham, MA, pp.145-149.

GORDILLO, S., BUJALESKY, G. G., PIRAZZOLI, P. A., RABASSA, J. O., SALIEGE, J. F. 1992. Holocene raised beaches along northern coast of the Beagle Channel, Tierra del Fuego, Argentina. *Palaeogeography, Palaeoclimatology Palaeoecology,* 99, 41–54.

GRAND PRE, C., HORTON, B.P., KELSEY, H.M., RUBIN, C.M., HAWKES, A.D., DARYONO, M., ROSENBERG, G., CULVER, S.J. 2012. Stratigraphic evidence for an early Holocene earthquake in Aceh, Indonesia. Quaternary Science Reviews, 54, 142-151

GRAVEN, H. D., GUILDERSON, T. P., KEELING, R. F. 2012. Observations of radiocarbon in CO_2 at seven global sampling sites in the Scripps flask network: Analysis of spatial gradients and seasonal cycles. *Journal of Geophysical Research,* 117, D02303.

GRIMM, E.C. 2011. *Tilia software package v.1.7.16*. Illinois State Museum. Research and Collection Center.

GUILBAULT, J. P., CLAGUE, J. J., LAPOINTE, M. 1995. Amount of subsidence during a late Holocene earthquake – evidence from fossil tidal marsh foraminifer at Vancouver Island, west coast of. *Palaeogeography Palaeoclimatology Palaeoecology,* 118, 49-71.

GUTSCHER, M. A., SPAKMAN, W., BIJWAARD, H., ENGDAHL, E. R. 2000. Geodynamics of flat subduction: Seismicity and tomographic constraints from the Andean margin. *Tectonics,* 19, 814-833.

HAMILTON, S., SHENNAN, I. 2005a. Late Holocene great earthquakes and relative sea-level change at Kenai, southern Alaska. *Journal of Quaternary Science,* 20, 95-111.

HAMILTON, S., SHENNAN, I. 2005b. Late Holocene relative sea-level changes and the earthquake deformation cycle around upper Cook Inlet, Alaska. *Quaternary Science Reviews,* 24, 1479-1498.

HANEBUTH, T., STATTEGGER, K., GROOTES, P.M. 2000. Rapid Flooding of the Sunda Shelf: A Late-Glacial Sea-Level Record. Science, 288, 1033-1035.

HARTLEY, B., BARBER, H.G., CARTER, J.R., 1996. *An Atlas of British Diatoms*. Biopress, Bristol.

HARVEY, M.M., HANSOM, J.D., MACKENZIE, A.B., 2007. Constraints on the use of anthropogenic radionuclide-derived chronologies for saltmarsh sediments. *Journal of Environmental Radioactivity,* 95, 126-148.

HASSAN, G.S., ESPINOSA, M.A., ISLA, F.I., 2006. Modern diatom assemblages in surface sediments from estuarine systems in the southeastern Buenos Aires province, Argentina. *Journal of Paleolimnology,* 35, 39-53.

HAWKES, A. D., SCOTT, D. B., LIPPS, J. H., COMBELLICK, R. 2005. Evidence for possible precursor events of megathrust earthquakes on the west coast of North America. *Geological Society of America Bulletin,* 117, 996-1008.

HAWKES, A.D., HORTON, B.P., NELSON, A.R., HILL, D.F., 2010. The application of intertidal foraminifera to reconstruct coastal subsidence during the giant Cascadia earthquake of AD 1700 in Oregon, USA. *Quaternary International* 221, 116-140.

HAWKES, A., HORTON, B.P. NELSON, A., VANE, C., SAWAI, Y. 2011. Coastal subsidence in Oregon, USA, during the giant Cascadia earthquake of AD 1700. *Quaternary Science Reviews*, 30, 364–376.

HAYWARD, B. W., GRENFELL, H. R., SABAA, A. T., CARTER, R., COCHRAN, U., LIPPS, J. H., SHANE, P. R., MORLEY, M. S. 2006. Micropaleontological evidence of large earthquakes in the past 7200 years in southern Hawke's Bay, New Zealand. *Quaternary Science Reviews,* 25, 1186-1207.

HECK, N.H., 1934. List of seismic waves. *Annales de la Commission pour l'Etude des Raz de Maree,* 4, 20-41

HEMPHILL-HALEY, E., 1993. Taxonomy of recent and fossil (Holocene) diatoms (Bacilloriophyta) from northern Willapa Bay, Washington. *US Geological Survey Open File Report* 93-289, 1-151.

HERVE, F., OTA, Y. 1993. Fast Holocene uplift rates at the Andes of Chiloé, southern. *Revista Geologica De Chile,* 20, 15-23.

HEUSSER, C. J. 1990. Ice age vegetation and climate of subtropical Chile. *Palaeogeography, Palaeoclimatology, Palaeoecology*, 80, 107–127.

HEUSSER, C.J., FLINT, R.F. 1977. Quaternary glaciations and environments 01 northern Isla Chiloé, Chile. *Geology,* 5, 305-308.

HEUSSER, C.J., STREETER, S.S., 1980. A temperature and precipitation record of the past 16,000 years in southern Chile. *Science* 210, 1345–1347.

HEIRI, O., LOTTER, A.F., LEMCKE, G. 2001. Loss on ignition as a method for estimating organic and carbonate content in sediments: reproducibility and comparability of results. *Journal of Paleolimnology,* 25, 101-110.

HILL, M. O., GAUCH, H. G. 1980. Detrended correspondence-analysis - an improved ordination technique. *Vegetatio,* 42, 47-58.

HORTON, B. P. 1997. *Quantification of the indicatie meaning of a range of Holocene sea-level index points from the Western North Sea.* Unpublished PhD thesis, University of Durham.

HORTON, B.P., EDWARDS, R.J., 2005. The application of local and regional transfer functions to the reconstruction of Holocene sea levels, north Norfolk, England. *Holocene,* 15, 216-228.

HORTON, B.P., EDWARDS, B.P., 2006. Quantifying Holocene Sea-Level Change using Intertidal Foraminifera: Lessons from the British Isles. Cushman Foundation for Foraminiferal Research, Special Publication, vol. 40, 97 pp.

HORTON, B., SHENNAN, I., 2009. Compaction of Holocene strata and the implications for relative sea level change on the east coast of England. *Geology,* 37, 1083-1086.

HORTON, B.P., CORBETT, R., CULVER, S.J., EDWARDS, R.J., HILLIER, C., 2006. Modern saltmarsh diatom distributions of the Outer Banks, North Carolina, and the development of a transfer function for high resolution reconstructions of sea level. *Estuarine, Coastal and Shelf Science*, 69, 381-394.

HORTON BP, EDWARDS RJ, LLOYD JM. 2000. Implications of a microfossil transfer function in Holocene sea-level studies. In: SHENNAN I, ANDREWS JE (eds). *Holocene Land–Ocean Interaction and Environmental Change around the North Sea*, Geological Society Special Publication 166: Geological Society Publishing House: Bath, pp. 41–54.

HORTON, B.P., SAWAI, Y., HAWKES, A.D., WITTER, R.C. 2011. Sedimentology and paleontology of a tsunami deposit accompanying the great Chilean earthquake of February 2010. *Marine Micropaleontology*, 79, 132–138.

HUA, Q., 2009. Radiocarbon: A chronological tool for the recent past. *Quaternary Geochronology*, 4, 378-390.

HUA, Q., BARBETTI, M., 2004. Review of tropospheric bomb C-14 data for carbon cycle modelling and age calibration purposes. *Radiocarbon*, 46, 1273-1298.

HUGHES, J.F., MATHEWES, R.W., CLAGUE, J.J., 2002. Use of pollen and vascular plants to estimate coseismic subsidence at a tidal marsh near Tofino, British Columbia. Palaeogeography, Palaeoclimatology, Palaeoecology 185, 145–161.

HULTON, N.R.J., PURVES, R.S., MCCULLOCH, R.D., SUGDEN, D.E., BENTLEY, M.J., 2002. The last glacial maximum and deglaciation in southern South America. *Quaternary Science Reviews,* 21, 233–241.

HUPPERT, H.E., SPARKS, R.S.J. 2006. Extreme Natural Hazards: population growth, globalization and environmental change. *Philosophical Transactions of the Royal Society,* 364A, 1875-1888.

HYNDMAN, R.D., WANG, K., 1993. Thermal constraints on the zone of major thrust earthquake failure: the Cascadia subduction zone. *Journal of Geophysical Research*, 98, 2039-2060.

HYNDMAN, R. D., WANG, K. 1995. Current deformation and thermal constraints on the zone of potential great earthquakes on the Cascadia subduction thrust. *Journal of Geophysical Research*, 100, 22133-22154.

IMBRIE, J., KIPP, N.G., 1971. A new micropaleontological method for quantitative paleoclimatology: application to a Late Pleistocene Caribbean core, In: TUREKIAN, K.K. (Ed.), *The Late Cenozoic Glacial Ages*. Yale University Press, New Haven, pp. 71-181.

INTERGOVERNMENTAL OCEANOGRAPHIC COMMISSION (IOC). 2012. Sea Level Station Monitoring Facility. Accessed at: http://www.ioc-sealevelmonitoring.org/

ISLA, F. I. 1989. The Southern Hemisphere sea level fluctuation. *Quaternary Science Reviews*, 8, 359–368.

ISLA, F.I., QUEZADA FLORY, J., MARTÍNEZ, C., FERNÁNDEZ, A., JAQUE, E. 2012. The Evolution of the Bío Bío Delta and the Coastal Plains of the Arauco Gulf, Bío Bío Region: the Holocene Sea-Level Curve of Chile. *Journal of Coastal Research,* 28, 102-111.

IVINS, E.R., JAMES, T.S., 1999. Simple models for late Holocene and present-day Patagonian glacier fluctuations and predictions of a geodetically detectable isostatic response. *Geophysical Journal International* 138, 601-624.

JAMES, T.S., CLAGUE, J.J., WANG, K., HUTCHINSON, I., 2000. Postglacial rebound at the northern Cascadia subduction zone. *Quaternary Science Reviews*, 19, 1527-1541.

JANKAEW, K., ATWATER, B. F., SAWAI, Y., CHOOWONG, M., CHAROENTITIRAT, T., MARTIN, M. E., PRENDERGAST, A. 2008. Medieval forewarning of the 2004 Indian Ocean tsunami in Thailand. *Nature,* 455, 1228–1231.

JENNINGS, A.E., NELSON, A.R., SCOTT, D.B., ARAVENA, J.C., 1995. Marsh foraminiferal assemblages in the Valdivia Estuary, south-central Chile, relative to vascular plants and sea level. *Journal of Coastal Research*, 11, 107–123.

JONES, V. J., JUGGINS, S. 1995. The construction of a diatom-based chlorophyll a transfer function and its application at three lakes on Signy Island (maritime Antarctic) subject to differing degrees of nutrient enrichment. *Freshwater Biology,* 34, 433-445.

JUGGINS, S. 2011. *C2 software package*. Newcastle University

KAIZUKA, S., MATSUDA, T., NOGAMI, M., YONEKURA, N. 1973. Quaternary tectonic and seismic crustal movements in the Arauco Peninsula and its environs, central Chile. *Geographical Reports Tokyo Metropolitan University*, 8, 1–49.

KANAMORI, H., CIPAR, J. J., 1974, Focal process of the great Chilean earthquake May 22, 1960. *Physics of the Earth and Planetary Interiors*, 9, 128-136.

KELLEHER, J. A. 1972. Rupture zones of large South-American earthquakes and some predictions. *Journal of Geophysical Research,* 77, 2087.

KELLEHER, J., MCCANN, W. 1976. Buoyant zones, great earthquakes and unstable boundaries of. *Journal of Geophysical Research,* 81, 4885-4896.

KEMP, A.C., HORTON, B.P., CULVER, S.J., CORBETT, D.R., VAN DE PLASSCHE, O., GEHRELS, W.R., DOUGLAS, B.C., 2009. The timing and magnitude of recent accelerated sea-level rise (North Carolina, USA). *Geology*, 37, 1035-1038.

KEMP, A.C., HORTON, B.P., DONNELLY, J.P., MANN, M.E., VERMEER, M., RAHMSTORF, S., 2011. Climate related sea-level variations over the past two millennia. *Proceedings of the National Academy of Sciences* doi:10.1073/pnas.1015619108.

KEYS, J.G. 1963. The tsunami of 22 May 1960, in the Samoa and Cook Islands, *Bulletin of the Seismological Society of America*, 53, 1211-1227.

KITZBERGER T., VEBLEN, T.T, VILLALBA, R. 1995. Tectonic influences on tree growth in northern Patagonia, Argentina: the roles of substrate stability and climatic variation. *Canadian Journal of Forest Research,* 25, 1684-1696.

KOVACH, W. L. 1995. Multivariate data analysis. In: MADDY, D. A. B., J.S. (ed.) *Statistical modelling of Quaternary science data.* Cambridge, Cambridge University Press.

LAMBECK, K. 2002. Sea level change from mid Holocene to Recent time: An Australian example with global implications. In: MITROVICA, J.X., VERMEERSEN, B.L.A. (eds) *Ice Sheets, Sea Level and the Dynamic Earth*. Washington, D. C., American Geophysical Union. pp. 33–50

LANDER, J. F., LOCKRIDGE, P. A., 1989, *United States tsunamis 1690-1988*. National Geophysical Data Center publication, v. 41-42.

LARSEN, C.F., MOTYKA, R.J., FREYMUELLER, J.T., ECHELMEYER, K.A., IVINS, E.R., 2005. Rapid viscoelastic uplift in southeast Alaska caused by post-Little Ice Age glacial retreat. *Earth and Planetary Science Letters,* 237, 548-560.

LAY, T., AMMON, C. J., KANAMORI, H., KOPER, K. D., SUFRI, O., HUTKO, A. R., 2010. Teleseismic inversion for rupture process of the 27 February 2010 Chile (Mw 8.8) earthquake. *Geophysical Research Letters*, 37, L13301.

LEGENDRE, P., LEGENDRE, L. 1998. *Numerical ecology,* Amsterdam, Elsevier.

LEONARD, E. M. WEHMILLER, J. F. 1990. Geochronology of marine terraces at Caleta Michilla, Northern Chile. Implications for Late Pleistocene and Holocene uplift. *Revista Geológica de Chile,* 18, 81–86.

LEONARD, L.J., HYNDMAN, R.D., MAZZOTTI, S., 2004. Coseismic subsidence in the 1700 great Cascadia earthquake: coastal estimates versus elastic dislocation models. *Geological Society of America Bulletin,* 116, 655-670.

LEONARD, L.J., CURRIE, C.A., MAZZOTTI, S., HYNDMAN, R.D., 2010. Rupture area and displacement of past Cascadia great earthquakes from coastal coseismic subsidence. *Geological Society of America Bulletin*. doi:10.1130/B30108.1.

LEORRI, E., HORTON, B.P., CEARRETA, A., 2008. Development of a foraminifera-based transfer function in the Basque marshes, N. Spain: implications for sea-level studies in the Bay of Biscay. *Marine Geology,* 251, 60-74.

LEPŠ, J., ŠMILAUER, P. 2003. *Multivariate analysis of ecological data using CANOCO,* Cambridge, Cambridge University Press.

LESSA, G., MASSELINK, G. 2006. Evidence of a Mid-Holocene sea level highstand from the sedimentary record of a macrotidal barrier and paleoestuary system in Northwestern Australia. *Journal of Coastal Research*. 22, 100– 112.

LOMNITZ, C. L. 1970. Major earthquakes and tsunamis in Chile during the period 1535 to 1955. *Geologische Rundshau,* 59, 938-960.

LONG, A. J., INNES, J. B. 1993. Holocene sea-level changes in Romney Marsh and Southeast England, U.K. *Proceedings of the Geologists' Association*. 104,223-237.

LONG, A.J., SHENNAN, I., 1994. Sea level changes in Washington and Oregon and the "Earthquake deformation cycle". *Journal of Coastal Research*, 10, 825-838.

LONG, A.J., WALLER, M.P., STUPPLES, P., 2006. Driving mechanisms of coastal change: Peat compaction and the destruction of late Holocene coastal wetlands. *Marine Geology,* 225, 63-84.

LONG, A.J., WOODROFFE, S.A., MILNE, G.A., BRYANT, C.L., WAKE, L.M., 2010. Relative sea level change in west Greenland during the last millennium. *Quaternary Science Reviews,* 29, 367-383.

LONG, A.J., WOODROFFE, S.A., MILNE, G.A., BRYANT, C.L., SIMPSON, M.J.R., WAKE, L.M. 2012. Relative sea-level change in Greenland during the last 700 yrs and ice sheet response to the Little Ice Age. *Earth and Planetary Science Letters*. 315-316, 76-85.

MANLY, B. F. J., CHOTKOWSKI, M. 2006. Two new methods for regime change analyses. *Archiv Fur Hydrobiologie,* 167, 593-607.

MARSHALL, W.A., GEHRELS, W.R., GARNETT, M.H., FREEMAN, S., MADEN, C., XU, S., 2007. The use of 'bomb spike' calibration and high-precision AMS C-14 analyses to date salt-marsh sediments deposited during the past three centuries. *Quaternary Research,* 68, 325-337.

MCCALPIN, J., CARVER, G. 2009. Paleoseismology of compressional tectonic environments. In: MCCALPIN, J. (ed.) *Paleoseismology.* Amsterdam: Elsevier.

MCCORMAC, F. G., HOGG, A. G., BLACKWELL, P. G., BUCK, C. E., HIGHAM, T. F. G., REIMER, P. J. 2004. SHCal04 Southern Hemisphere Calibration 0–11.0 cal kyr BP. *Radiocarbon,* 46, 1087–1092.

MCCULLOCH, R.D., BENTLEY, M.J. 1998. Late glacial ice advance in the Strait of Magellan, southern Chile. *Quaternary Science Reviews*, 17, 775-787.

MCCULLOCH, R.D., DAVIES, S.J., 2001. Late-glacial and Holocene palaeoenvironmental change in the central Strait of Magellan, southern Patagonia. *Palaeogeography Palaeoclimatology Palaeoecology*. 173, 143– 162.

MCCULLOCH, R.D., BENTLEY, M.J., PURVES, R.S., SUGDEN, D.E., CLAPPERTON, C.M. 2000. Climatic interferences form glacial and palaeocological evidence at the last glacial termination, Southern South America. *Journal of Quaternary Science*, 15, 409-417.

MCGRANAHAN, G., BALK, D., ANDERSON, B. 2007 The rising tide: assessing the risks of climate change and human settlements in low elevation coastal zones. *Environ Urban* 19, 17–37.

MELNICK, D. 2010. Megathrust earthquakes over the past 1.7 ka at Guafo island, south Chile. Chapman Conference: Great earthquakes and their tsunamis. Valparaiso, May 2010. 16P-9

MELNICK, D., BOOKHAGEN, B., ECHTLER, H. P., STRECKER, M. R. 2006. Coastal deformation and great subduction earthquakes, Isla Santa Maria, Chile (37 degrees S). *Geological Society of America Bulletin,* 118, 1463-1480.

MELNICK, D., BOOKHAGEN, B., STRECKER, M. R., ECHTLER, H. P. 2009. Segmentation of megathrust rupture zones from fore-arc deformation patterns over hundreds to millions of years, Arauco peninsula, Chile. *Journal of Geophysical Research-Solid Earth,* 114, B01407

MELNICK, D., CISTERNAS, M., MORENO, M., NORAMBUENA, R., 2012a, Estimating coseismic coastal uplift with an intertidal mussel: calibration for the 2010 Maule Chile earthquake (Mw=8.8): *Quaternary Science Reviews*. 42, 29-42.

MELNICK, D., MORENO, M., MOTAGH, M., CISTERNAS, M., WESSON, R., 2012b, Splay fault slip during the Mw 8.8 2010 Maule Chile earthquake. *Geology*, 40, 251-254.

MELTZNER, A. J., SIEH, K., ABRAMS, M., AGNEW, D. C., HUDNUT, K. W., AVOUAC, J. P., NATAWIDJAJA, D. H. 2006. Uplift and subsidence associated with the great Aceh-Andaman earthquake of 2004. *Journal of Geophysical Research-Solid Earth.* 111, B02407.

MERCER, J.H., 1968. Variations of some Patagonian glaciers since the Late-Glacial. *American Journal of Science.* 266, 91–109.

MERCER, J.H., 1970. Variations of some Patagonian glaciers since the Late-Glacial: II. *American Journal of Science,* 269, 1 –25.

METCALFE, S.E., ELLIS, S., HORTON, B.P., INNES, J.B., MCARTHUR, J.J., MITLEHNER, A., PARKES, A., PETHICK, J.S., REES, J.G., RIDGWAY, J., RUTHERFORD, M.M., SHENNAN, I., TOOLEY, M. 2000. The Holocene Evolution of the Humber Estuary: reconstructing change in a dynamic environment. In: SHENNAN, I., ANDREWS, J.E. *Holocene Land-Ocean Interaction and Environmental Change around the North Sea*. Geological Society special publication. 166

MILNE, G. A., LONG, A. J., BASSETT, S. E. 2005. Modeling Holocene relative sea-level observations from the Caribbean and South America, *Quaternary Science Reviews*. 24, 1183–1202.

MITROVICA, J.X., MILNE, G.A., 2002. On the origin of late Holocene sea-level highstands within equatorial ocean basins. *Quaternary Science Reviews,* 21, 2179-2190.

MITROVICA, J.X., PELTIER, W.R. 1991. On postglacial geoid subsidence over the equatorial oceans. *Journal of Geophysical Research,* 96, 20,053

MOERNAUT, J., DE BATIST, M., CHARLET, F., HEIRMAN, K., CHAPRON, E., PINO, M., BRÜMMER, R., URRUTIA, R., 2007. Giant earthquakes in south-central Chile revealed by Holocene mass-wasting events in Lake Puyehue. *Sedimentary Geology,* 195, 239–256.

MORENO, M. S., KLOTZ, J., MELNICK, D., ECHTLER, H., BATAILLE, K. 2008. Active faulting and heterogeneous deformation across a megathrust segment boundary from GPS data, south central Chile (36-39 degrees S). *Geochemistry Geophysics Geosystems*, 9, Q12024.

MORENO, M., MELNICK, D., ROSENAU, M., BAEZ, J. C., KLOTZ, J., ONCKEN, O., TASSARA, A., BATAILLE, K., CHEN, J., SOCQUET, A., BEVIS, M., BOLTE, J., VIGNY, C., BROOKS, B., SIMONS, M., GRUND, V., SMALLEY, R., CARRIZO, D., BARTSCH, M., HASE, H., 2012, Toward understanding tectonic control on the Mw 8.8 2010 Maule Chile earthquake. *Earth and Planetary Science Letters*, 321, 152-165.

MORRIS, K., BUTTERWORTH, J.C., LIVENS, F.R., 2000. Evidence for the remobilization of Sellafield Waste Radionuclides in an Intertidal Salt Marsh, West Cumbria, U.K. Estuarine. *Coastal and Shelf Science,* 51, 613–625.

MORTON, R.A., GELFENBAUM, G., JAFFE, B.E., 2007. Physical criteria for distinguishing sandy tsunami and storm deposits using modern examples. *Sedimentary Geology,* 200, 184–207.

MUÑOZ, J., DUHART, P., HUFMANN, L., MASSONE, H., STERN, C. 1999. Geologic and structural setting of Chiloé Island, Chile. In: Congreso Geológico Argentino, No. 14, Actas 1: 182-184. Salta.

NELSON, A.R., 1992. Holocene Tidal-Marsh Stratigraphy in South-Central Oregon-Evidence for Localized Sudden Submergence in the Cascadia Subduction Zone. *SEPM,* 48, 287-301.

NELSON, A. R. 2007. Tectonic locations. In: ELIAS, S. (ed.) *The Encyclopedia of Quaternary Science.* Elsevier.

NELSON, A.R., KASHIMA, K., 1993. Diatom zonation in southern Oregon tidal marshes relative to vascular plants, foraminifera, and sea level. *Journal of Coastal Research*, 9, 673–697.

NELSON, A. R., MANLEY, W. F. 1992. Holocene coseismic and aseismic uplift of Isla Mocha, south-central Chile. *Quaternary International,* 15/16, 61-76.

NELSON, A.R., ATWATER, B.F., BOBROWSKY, T., BRADLEY, L.-A., CLAGUE, J.J., CARVER, G.A., DARIENZO, M.E., GRANT, W.C., KRUEGER, H.W., SPARKS, R., STAFFORD JR., T.W., STUIVER, M., 1995. Radiocarbon evidence for extensive plate boundary rupture about 300 years ago at the Cascadia subduction zone. *Nature*, 378, 371–374.

NELSON, A. R., SHENNAN, I., LONG, A. J. 1996. Identifying coseismic subsidence in tidal-wetland

stratigraphic sequences at the Cascadia subduction zone of western North America. *Journal of Geophysical Research-Solid Earth,* 101, 6115-6135.

NELSON, A. R., KASHIMA, K., BRADLEY, L. A. 2009. Fragmentary Evidence of Great-Earthquake Subsidence during Holocene Emergence, Valdivia Estuary, South Central Chile. *Bulletin of the Seismological Society of America,* 99, 71-86.

NELSON, A. R., KELSEY, H. M., WITTER, R. C. 2006. Great earthquakes of variable magnitude at the Cascadia subduction zone. *Quaternary Research,* 65, 354-365.

OTA, Y., PASKOFF, R. 1993. Holocene deposits on the coast of north central Chile – Radiocarbon ages and implications for coastal changes. *Revista Geologica De Chile,* 20, 25-32.

OZAWA, S., NISHIMURA, T., SUITO, H., KOBAYASHI, T., TOBITA, M., IMAKIIRE, T. 2011. Coseismic and postseismic slip of the 2011 magnitude-9 Tohoku-Oki earthquake, *Nature*, 475, 373–376.

PATTERSON, R. T., DALBY, A. P., ROE, H. M., GUILBAULT, J. P., HUTCHINSON, I., CLAGUE, J. J. 2005. Relative utility of foraminifera, diatoms and macrophytes as high resolution indicators of paleo-sea level in coastal British Columbia, Canada. *Quaternary Science Reviews,* 24, 2002-2014.

PEEL, M. C., FINLAYSON, B. L., MCMAHON, T. A. 2007. *Updated world map of the Köppen-Geiger climate classification*. University of Melbourne.

PELTIER, W.R., 2004. Global glacial isostasy and the surface of the ice-age earth: The ICE-5G (VM2) model and GRACE. *Annual Review of Earth and Planetary Sciences*, 32, 111-149.

PIERSANTI, A. 1999. Postseismic deformation in Chile: Constraints on the asthenospheric viscosity. *Geophysical Research Letters,* 26, 3157-3160.

PINO, M., NAVARRO, R. X. 2005. Geoarchaeology of the archaic site Chan-Chan 18, coast of Valdivia: environmental discrimination of human occupation and its relation with the middle Holocene marine transgression. *Revista Geologica De Chile,* 32, 59-75.

PIRAZZOLI, P. A. 1991. *World Atlas of Holocene sea-level changes,* Amsterdam, Elsevier

PLAFKER, G. 1969. The Alaska Earthquake, Regional Effects, Tectonics. *U.S. Geological Survey Professional Paper 543-I.*

PLAFKER, G., SAVAGE, J. C. 1970. Mechanisms of Chilean earthquakes of May 21 and May 22, 1960. *Geological Society of America Bulletin,* 81, 1001-1030.

PLAFKER, G., THATCHER, W., 2008. Geological and geophysical evaluation of the mechanisms of the great 1899 Yakutat Bay earthquakes, In: FREYMUELLER, J.T., HAEUSSLER, P., WESSON, R.L., EKSTROM, G. (Eds.), *Active Tectonics and Seismic Potential of Alaska*. AGU Geophysical Monograph Series, 179, Washington, DC, pp. 215-236.

PORTER, S. C., STUIVER, M., HEUSSER, C. J. 1984. Holocene sea-level changes along the Strait of Magellan and Beagle Channel, southernmost South America. *Quaternary Research,* 22, 59–67.

PREUSS, H., 1979. Progress in computer evaluation of sea level data within the IGCP Project No. 61. In: *Proceedings of the 1978 International Symposium of Coastal Evolution in the Quaternary*, Sao Paulo, Brazil, 104-134.

RABASSA, J., CLAPPERTON, C.M., 1990. Quaternary glaciations of the southern Andes. *Quaternary Science Reviews*, 9, 153–174.

RABASSA, J., HEUSSER, C. J., STUCKENRATH, R. 1986. New data on Holocene sea transgression in the Beagle Channel: Tierra del Fuego, Argentina. *Quaternary of South America and Antarctic Peninsula,* 4, 291–309.

RADTKE, U. 1989. Marine terrassen und korallenriffe. Das problem der Quartären Meeresspiegelschwanckungen erläutert an fallstudien aus Chile, Argentinien und

Barbados. Universität Dusseldorf: Düsseldorfer Geographisches Schriften. 27, 246 pp.

REED D.J., MUIR-WOOD, R., BEST, J. 1988. Earthquakes, rivers and ice: Scientific research at Laguna San Rafael, southern Chile, 1986. *The Geographical Journal,* 154, 392-405.

REHAK, K., STRECKER, M. R., ECHTLER, H. P. 2008. Morphotectonic segmentation of an active forearc, 37 degrees-41 degrees S, Chile. *Geomorphology,* 94, 98-116.

REIMER, P.J., BAILLIE, M.G.L., BARD, E., BAYLISS, A., BECK, J.W., BERTRAND, C.J.H., BLACKWELL, P.G., BUCK, C.E., BURR, G.S., CUTLER, K.B., DAMON, P.E., EDWARDS, R.L., FAIRBANKS, R.G., FRIEDRICH, M., GUILDERSON, T.P., HOGG, A.G., HUGHEN, K.A., KROMER, B., MCCORMAC, G., MANNING, S., RAMSEY, C.B., REIMER, R.W., REMMELE, S., SOUTHON, J.R., STUIVER, M., TALAMO, S., TAYLOR, F.W., VAN DER PLICHT, J., WEYHENMEYER, C.E., 2004. IntCal04 terrestrial radiocarbon age calibration, 0-26 cal kyr BP. *Radiocarbon* 46, 1029-1058.

REINHARDT, E. G., NAIRN, R. B., LOPEZ, G. 2010. Recovery estimates for the Rio Cruces after the May 1960 Chilean earthquake. *Marine Geology,* 269, 18-33.

RIGNOT, E., RIVERA, A., CASASSA, G., 2003. Contribution of the Patagonia Icefields of South America to sea level rise. *Science,* 302, 434-437.

RIVERA, P., VALDEBENITO, H. 1979. Diatomeas recolectadas en las desembocaduras de los rios Chivilingo, Laraquete y Carampangue, Chile. *Gayana Botanica*, 35, 1-97.

ROE, H.M., DOHERTY, C.T., PATTERSON, R.T., SWINDLES, G.T., 2009. Contemporary distributions of saltmarsh diatoms in the Seymour-Belize Inlet Complex, British Columbia, Canada: Implications for studies of sea-level change. *Marine Micropaleontology,* 70, 134-150.

ROELOFFS, E. A. 2006. Evidence for aseismic deformation rate changes prior to earthquakes. *Annual Review of Earth and Planetary Sciences,* 34, 591-627.

RUFF, L. J. 1989. Do trench sediments affect great earthquake occurrence in subduction zones. *Pure and Applied Geophysics,* 129, 263-282.

RYAN, W.B.F., CARBOTTE, S.M., COPLAN, J.O., O'HARA, S., MELKONIAN, A., ARKO, R., WEISSEL, R.A., FERRINI, V., GOODWILLIE, A., NITSCHE, F., BONCZKOWSKI, J., ZEMSKY, R. 2009. Global Multi-Resolution Topography synthesis, Geochemistry Geophysics Geosystems, 10, Q03014

SAN MARTÍN, C., CONTRERAS, D., SAN MARTÍN, J., RAMÍREZ, Y.C. 1992. Vegetación de las marismas del centro-sur de Chile. *Revista Chilena de Historia Natural,* 65, 327-342.

SAVAGE, J.C. 1983. A dislocation model of strain accumulation and release at a subduction zone. *Journal of Geophysical Research,* 88, 4984-4996.

SAVAGE, J. C., PLAFKER, G. 1991. Tide-gauge measurements of uplift along the south coastal of Alaska. *Journal of Geophysical Research-Solid Earth and Planets,* 96, 4325-4335.

SAVAGE, J. C., PRESCOTT, W. H. 1978. Asthenosphere readjustment and the earthquake cycle, Journal of Geophysical Research, 83, 3369– 3376.

SAWAI, Y. 2001. Episodic emergence in the past 3000 years at the Akkeshi Estuary, Hokkaido, Northern Japan. *Quaternary Research,* 56, 231-241.

SAWAI, Y., NASU, H., YASUDA, Y. 2002. Fluctuations in relative sea-level during the past 3000 yr in the Onnetoh estuary, Hokkaido, northern Japan. *Journal of Quaternary Science,* 17, 607-622.

SAWAI, Y., HORTON, B.P., NAGUMO, T., 2004. The development of a diatom-based transfer function along the Pacific coast of eastern Hokkaido, northern Japan - An aid in palaeoseismic studies of the Kuril subduction zone. *Quaternary Science Reviews,* 23, 2467-2483.

SAWAI, Y., JANKAEW, K., MARTIN, M.E., PRENDERGAST, A., CHOOWONG, M., CHAROENTITIRAT, T. 2009. Diatom assemblages in tsunami deposits associated with the 2004 Indian Ocean tsunami at Phra Thong Island, Thailand. *Marine Micropaleontology,* 73, 70-79.

SAWAI, Y., NAMEGAYA, Y., OKAMURA, Y., SATAKE, K., SHISHIKURA, M. 2012. Challenges of anticipating the 2011 Tohoku earthquake and tsunami using coastal geology. *Geophysical Research Letters* 39, L21309

SCHELLMANN, G. RADTKE, U. 2003. Coastal terraces and Holocene sea-level changes along the Patagonian Atlantic coast. *Journal of Coastal Research,* 19, 983–996.

SCHULLER, P., LOVENGREEN, C., HANDL, J. 1993. 137Cs concentration in soil, prairie plants, and milk from sites in southern Chile. *Health Physics* 64, 157– 61.

SCHULLER, P., VOIGT, G., HANDL, J., ELLIES, A., OLIVA, L. 2002. Global weapons' fallout 137Cs, in soils and transfer to vegetation in South-Central Chile. *Journal of Environmental Radioactivity*, 62, 181– 93.

SCOTT, D.B*.,* MEDIOLI, F.S. 1978. Vertical zonations of marsh foraminifera as accurate inidicators of former sea-levels. *Nature,* 272, 528-531.

SIEVERS, H.A., VILLEGAS, G., BARROS, G., 1963. The seismic sea wave of 22 May 1960 along the Chilean Coast. *Bulletin of the Seismological Society of America,* 53, 1125–1190.

SIQUEIROS-BELTRONES, D. A., LÓPEZ-FUERTE, F. O. 2006. Epiphytic diatoms associated with red mangrove (Rhizophora mangle L.) prop roots in Bahía Magdalena, B. C. S., México. *Revista Biología Tropical*, 54, 287-297.

SHENNAN, I., HAMILTON, S. 2006. Coseismic and pre-seismic subsidence associated with great earthquakes in Alaska. *Quaternary Science Reviews,* 25, 1-8.

SHENNAN, I., HORTON, B.P., 2002. Holocene land- and sea-level changes in Great Britain. *Journal of Quaternary Science* 17, 511-526.

SHENNAN, I., LONG, A.J., RUTHERFORD, M.M., GREEN, F.M., INNES, J.B., LLOYD, J.M., ZONG, Y., WALKER, K.J., 1996. Tidal marsh stratigraphy, sea-level change and large earthquakes, I: A 5000 year record in Washington, USA. *Quaternary Science Reviews,* 15, 1023-1059.

SHENNAN, I., LONG, A.J., RUTHERFORD, M.M., KIRKBY, J., GREEN, F.M., INNES, J.B., WALKER, K., 1998. Tidal marsh stratigraphy, sea level change and large earthquakes, II: Events during the last 3500 years at Netarts Bay, Oregon, USA. *Quaternary Science Reviews,* 17, 365-393.

SHENNAN, I., SCOTT, D. B., RUTHERFORD, M., ZONG, Y. Q. 1999. Microfossil analysis of sediments representing the 1964 earthquake, exposed at Girdwood Flats, Alaska, USA. *Quaternary International,* 60, 55-73.

SHENNAN, I., BRUHN, R., PLAFKER, G. 2009. Multi-segment earthquakes and tsunami potential of the Aleutian megathrust. *Quaternary Science Reviews,* 28, 7-13.

SHENNAN, I., MILNE, G., BRADLEY, S. 2012. Late Holocene vertical land motion and relative sea-level changes: lessons from the British Isles. *Journal of Quaternary Science*. 27, 64-70.

SHERROD, B.L., 1999. Gradient analysis of diatom assemblages in a Puget Sound salt marsh: can such assemblages be used for quantitative paleoecological reconstructions? *Paleogeography Paleoclimatology Paleoecology,* 149, 213-226.

SIEH, K. 2006. Sumatran Megathrust Earthquakes - From Science to Saving Lives. *Philosophical Transactions of the Royal Society,* 364, 1947 – 1963.

SIMONS, M., MINSON, S. E., SLADEN, A., ORTEGA, F., JIANG, J., OWEN, S. E., MENG, L., AMPUERO, J-P., WEI, S., CHU, R., HELMBERGER, D. V., KANAMORI, H., HETLAND, E., MOORE, A. W., WEBB, F.H. 2011. The 2011 Magnitude 9.0 Tohoku-Oki Earthquake: Mosaicking The Megathrust From Seconds To Centuries, *Science,* 322, 1421,

SIMPSON, G.L. 2007. Analogue methods in palaeoecology: Using the analogue package. *Journal of Statistical Software* 22, 1–29.

SLOSS, C. R., JONES, B. G., MURRAY-WALLACE, C. V., MCCLENNEN, C. E. 2005. Holocene sea level fluctuations and the sedimentary evolution of a barrier estuary: Lake Illawarra, New South Wales, Australia. *Journal Of Coastal Research,* 21, 943–959.

SOMOZA, R. 1998. Updated Nazca (Farallon) - South America relative motions during the last 40 My: implications for mountain building in the central Andean region. *Journal of South American Earth Sciences,* 11, 211-215.

SPARKES, R., TILMAN, F., HOVIUS, N., HILLIER, J. 2010. Subducted seafloor relief stops rupture in South American great earthquakes: Implications for rupture behaviour in the 2010 Maule, Chile earthquake. *Earth and Planetary Science Letters*, 298, 89-94.

STEIN, S., OKAL, E. A. 2011. The size of the 2011 Tohoku earthquake need not have been a surprise. *Eos Transactions of the American Geophysical Union*, 92, 227.

STEIN, S., ENGELN, J. F., DEMETS, C., GORDON, R. G., WOODS, D., LUNDGREN, P., ARGUS, D., STEIN, C., WIENS, D. A. 1986. The Nazca-South America convergence rate and the recurrence of the great 1960 Chilean earthquake. *Geophysical Research Letters,* 13, 713-716.

STERN, C.R., MORENO, H., LÓPEZ-ESCOBAR, L., CLAVERO, J.E., LARA, L.E., NARANJO, J.A., PARADA, M.A., SKEWES, M.A. 2007. Chilean Volcanoes. In: MORENO, T., GIBBONS, W. (eds). *The Geology of Chile*. Geological Society of London, pp.149-180.

STUIVER, M., POLACH, H., 1977. Reporting of 14C data. *Radiocarbon,* 19, 355–363.

SUBARYA, C., CHLIEH, M., PRAWIRODIRDJO, L., AVOUAC, J. P., BOCK, Y., SIEH, K., MELTZNER, A. J., NATAWIDJAJA, D. H., MCCAFFREY, R. 2006. Plate-boundary deformation associated with the great Sumatra-Andaman earthquake. *Nature,* 440, 46-51.

SWITZER, A.D., JONES, B.G. 2008. Large-scale washover sedimentation in a freshwater lagoon from the southeast Australian coast: sea-level change, tsunami or exceptionally large storm? *The Holocene,* 18, 787–803.

SZKORNIK, K. 2007. *Middle to late Holocene sea-level change in western Denmark: A diatom based study*. Unpublished PhD thesis, University of Plymouth.

TASSARA, A., GOTZE, H. J., SCHMIDT, S., HACKNEY, R. 2006. Three-dimensional density model of the Nazca plate and the Andean continental margin. *Journal of Geophysical Research-Solid Earth,* 111, B09404.

TER BRAAK, C. J. F. 1987. *Unimodal models to relate species to environment.* Doctorate thesis, University of Wageningen.

TER BRAAK, C. J. F. 1996. *Unimodal models to relate species to environment,* Wageningen, DLOAgricultural Mathematics Group.

TER BRAAK, C.J.F., JUGGINS, S., 1993. Weighted averaging partial least squared regression (WAPLS): an improved method for reconstructing environmental variables from species assemblages. *Hydrobiologia,* 269/270, 485-502.

TER BRAAK, C.J.F., JUGGINS, S., BIRKS, H.J.B., VAN DE VOET, H., 1993. Weighted averaging partial least squared regression (WA-PLS): definition and comparison with other methods for species environmental calibration, In: PATIL, G.P., RAC, C.R. (eds.), *Multivariate Environmental Statistics*. Elsevier Science Publishers, Amsterdam, pp. 525-560.

THATCHER, W. 1984. The Earthquake Deformation Cycle At The Nankai Trough, Southwest Japan. *Journal of Geophysical Research,* 89, 3087-3101.

TOTTI, C., POULIN, M., ROMAGNOLI, T., PERRONE, C., PENNESI, C., DE STEFANO, M. 2009. Epiphytic diatom communities on intertidal seaweeds from Iceland. *Polar Biology*, 32, 1681-1691.

TROELS-SMITH, J. 1955. Characterization of unconsolidated sediments. *Danmarks Geologiske Undersogelse,* 4, 1-73.

THE UNIVERSITY OF COLORADO. 2010. *Diatoms of the Unites States.* Accessed at: http://westerndiatoms.colorado.edu/

THE UNIVERSITY OF COLORADO. 2012. Antarctic Freshwater diatoms. Accessed at: http://huey.colorado.edu/diatoms/about/database.php

VIGNY, C., SOCQUET, A., PEYRAT, S., RUEGG, J. C., MÉTOIS, M., MADARIAGA, R., MORVAN, S., LANCIERI, M., LACASSIN, R., CAMPOS, J., CARRIZO, D., BEJAR-PIZARRO, M., BARRIENTOS, S., ARMIJO, R., SSN TEAM, LIA-MDB TEAM, AND CAP TEAM, 2011. The 2010 (Mw 8.8) Maule megathrust earthquake of central Chile, monitored by GPS, *Science,* 332, 1417–1421.

VILLALOBOS, F. 2011. Crustal deformation associated with the 1960 Earthquake events in the south of Chile. *5th International Conference on Earthquake Geotechnical Engineering*. Santiago, Chile. CDDFV

VILLALOBOS SILVA, M. P. 2005. *Evidencias de la fluctuación del nivel del mar y alzamientos tectónicos desde el Pleistoceno tardío en isla Mancera X Región de Los Lagos - Chile: registro estratigráfico y sedimentológico.* Unpublished thesis, Universidad Austral de Chile.

VOS, P.C., DE WOLF, H., 1988. Methodological aspects of palaeo-ecological diatom research in coastal areas of the Netherlands. *Geologie en Mijnbouw,* 67, 31-40.

WALKER, M.J.C. 2005. *Quaternary Dating Methods*. John Wiley and Sons

WALKER, M.J.C., BERKELHAMMER, M., BJORCK, S., CWYNAR, L.C., FISHER, D.A., LONG, A.J., LOWE, J.J., NEWNHAM, R.M., RASMUSSEN, S.O., WEISS, H. 2012. Formal subdivision of the Holocene Series/Epoch: a Discussion Paper by a Working Group of INTIMATE (Integration of ice-core, marine and terrestrial records) and the Subcommission on Quaternary Stratigraphy (International Commission on Stratigraphy). *Journal of Quaternary Science,* 27, 649–659.

WANG, K., HU, Y., BEVIS, M., KENDRICK, E., SMALLEY JR., R., BARRIGA-VARGAS, R., LAURÍA, E. 2007. Crustal motion in the zone of the 1960 Chile earthquake: Detangling earthquake-cycle deformation and forearc-sliver translation. *Geochemistry, Geophysics, Geosystems* 8, Q10010.

WATCHAM, E.P., SHENNAN, I., BARLOW, N.L.M. 2012. Scale considerations in using diatoms as indicators of sea-level change: lessons from Alaska. *Journal of Quaternary Sci*ence, In press, doi: 10.1002/jqs.2592

WATTERS, W.A., FLEMING, C.A. 1972. Contributions to the geology and paleontology of Chiloe Island, southern Chile. Philosophical Transactions of the Royal Society of London, 263B, 369-408.

WHITEHOUSE, P., BENTLEY, M.J., LE BROCQ, A.M. 2012. A deglacial model for Antarctica: geological constraints and glaciological modelling as a basis for a new model of Antarctic glacial isostatic adjustment. *Quaternary Science Reviews*, 32, 1-24.

WHITING, M.C., MCINTIRE, C.D. 1985. An investigation of distributional patterns in the diatom flora of Netarts Bay, Oregon, by correspondence analysis. *Journal of Phycology,* 21, 655-66.

WILLIAMS, H.F.L. 2009. Stratigraphy, sedimentology, and microfossil content of Hurricane Rita storm surge deposits on southwest Louisiana. *Journal of Coastal Research,* 25, 1041–1051.

WILSON, G.P., LAMB, A.L. 2012. An assessment of the utility of regional diatom-based tidal-level transfer functions. *Journal of Quaternary Science*, 27, 360-370.

WILSON, B.W., TØRUM, A. 1968. *The tsunami of the Alaskan Earthquake, 1964—Engineering evaluation*. U.S. Army Corps of Engineers, Technical memorandum no. 25, 401 pp.

WILSON, P., ORFORD, J. D., KNIGHT, J., BRALEY, S. M., WINTLE, A. G. 2001. Late-Holocene (post-4000 years BP) coastal dune development in Northumberland, northeast England. *Holocene,* 11, 215-229.

WITTER, R. C., KELSEY, H. M., HEMPHILL-HALEY, E. 2001, Pacific storms, El Nino and Tsunamis, Competing mechanisms for sand deposition in a coastal marsh, Euchre Creek, Oregon, *Journal of Coastal Research*, 17, 563-583.

WITTER, R.C., KELSEY, H.M., HEMPHILL-HALEY, E., 2003. Great Cascadia earthquakes and tsunamis of the past 6700 years, Coquille River estuary, southern coastal Oregon. *Geological Society of America Bulletin,* 115, 289-1306.

WRIGHT, C., MELLA, A. 1963. Modifications to the soil pattern of south-central Chile resulting from seismic and associated phenomena during the period May to August 1960. *Seismological Society of America Bulletin,* 53, 1367-1402.

WOODROFFE, S.A., 2006. *Holocene relative sea-level changes in Cleveland Bay, North Queensland, Australia.* Unpublished PhD Thesis, Durham University.

WOODROFFE, S.A., 2009. Recognising subtidal foraminiferal assemblages: implications for quantitative sea-level reconstructions using a foraminifera-based transfer function. *Journal of Quaternary Science,* 24, 215-223.

WOODROFFE*,* S.A*.,* HORTON*,* B.P. 2005. Holocene sea-level changes in the Indo-Pacific. *Journal of Asian Earth Sciences*, 25, 29-43.

WOODROFFE, S.A., LONG, A.J., 2009. Salt marshes as archives of recent relative sea level change in West Greenland. *Quaternary Science Reviews,* 28, 1750-1761.

ZONG, Y. 1997. Mid- and Late-Holocene sea-level changes in Roudsea Marsh, northwest England: A diatom biostratigraphical investigation. *The Holocene,* 7, 309-321.

ZONG, Y., HORTON, B. P., 1999. Diatom-based tidal-level transfer functions as an aid in reconstructing Quaternary history of sea-level movements in Britain. *Journal of Quaternary Science*, 14, 153-167.

ZONG, Y.Q., HORTON, B.P., 1999. Diatom-based tidal-level transfer functions as an aid in reconstructing Quaternary history of sea-level movements in the UK. *Journal of Quaternary Science,* 14, 153-167.

ZONG, Y., SHENNAN, I., COMBELLICK, R. A., HAMILTON, S. L., RUTHERFORD, M. M. 2003. Microfossil evidence for land movements associated with the AD 1964 Alaska earthquake. *Holocene,* 13, 7-20.

ZONG, Y., KEMP, A.C., YU, F., LLOYD, J.M., HUANG, G., YIM, W.W.-S. 2010. Diatoms from the Pearl River estuary, China and their suitability as a water salinity indicator for coastal environments. *Marine Micropaleontology*, 75, 38-49.

Biostratigraphic constraints on megathrust earthquake deformation history in south central Chile

Two volumes

Volume 2: figures, tables and appendices

Ed Garrett

Thesis submitted for the degree of Doctor of Philosophy

Department of Geography

Durham University

April 2013

Contents

Volume 2

List of figures and tables

1. Framework: figures and tables

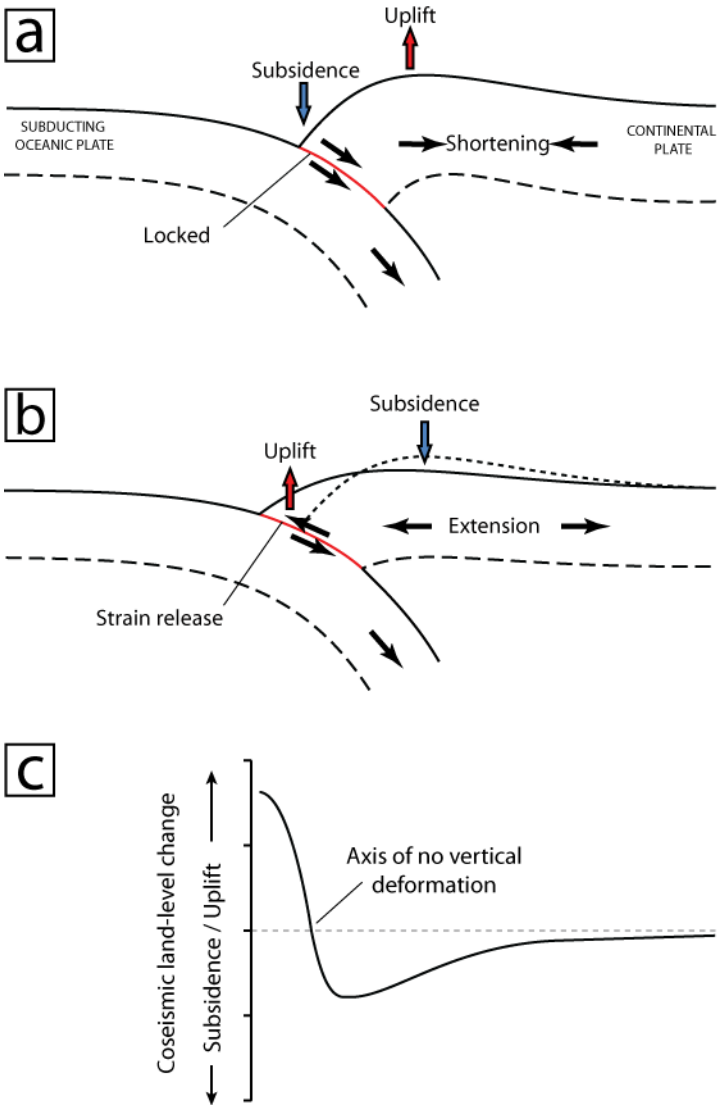

Figure 1.1: A simple graphical model of a subduction megathrust during a. interseismic strain accumulation and b. coseismic strain release, with c. the hypothetical cross-section of coseismic displacement of the continental plate (after Nelson et al., 1996). The vertical scales are highly exaggerated, with vertical movements in the order of ± 5 m over horizontal distances of 100 to 400 km.

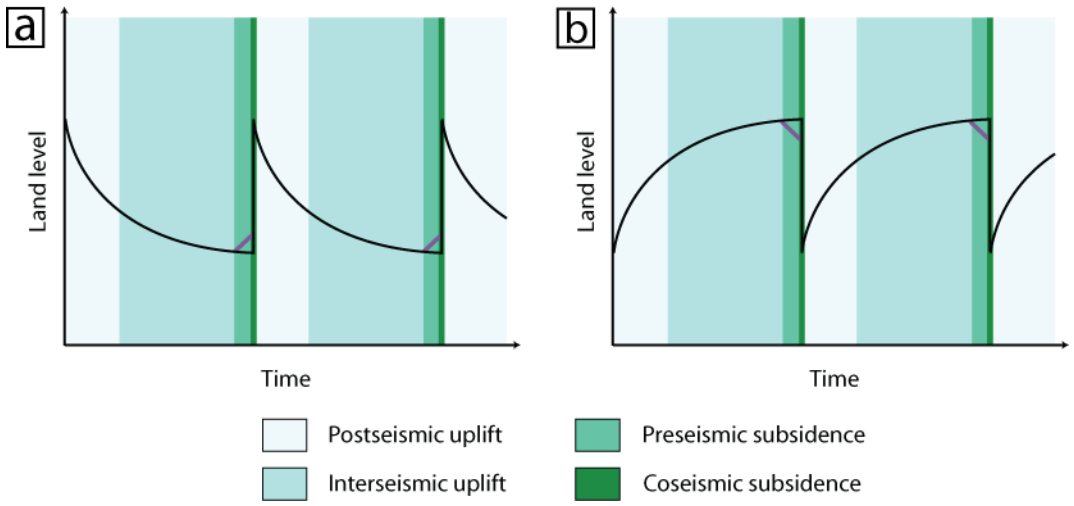

Figure 1.2: Graphical representation of land-level change over the course of two earthquake deformation cycles of consistent return period and deformation magnitude. a. location seaward of the axis of null coseismic displacement; b. location landward of the axis of null coseismic displacement (after Bourgeois, 2006). Black lines indicate accepted tripartite sequence; additional purple lines show hypothesised preseismic deformation (after Shennan and Hamilton, 2006).

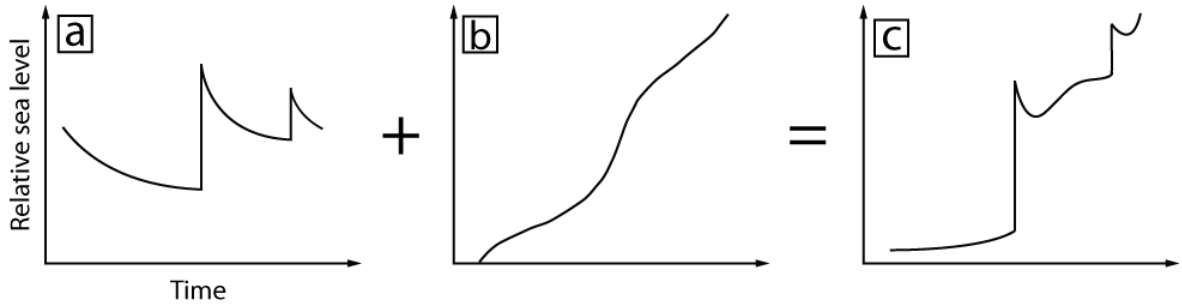

Figure 1.3: The components of relative sea-level change over the course of two successive earthquake cycles of different return period and deformation magnitude for a hypothetical location in the region of interseismic uplift, coseismic subsidence and aseismic sea-level rise (modified from Nelson, 2007). a. tectonic component; b. the sum of all aseismic processes, including isostatic, eustatic and local changes; c. the resulting relative sea-level record over time.

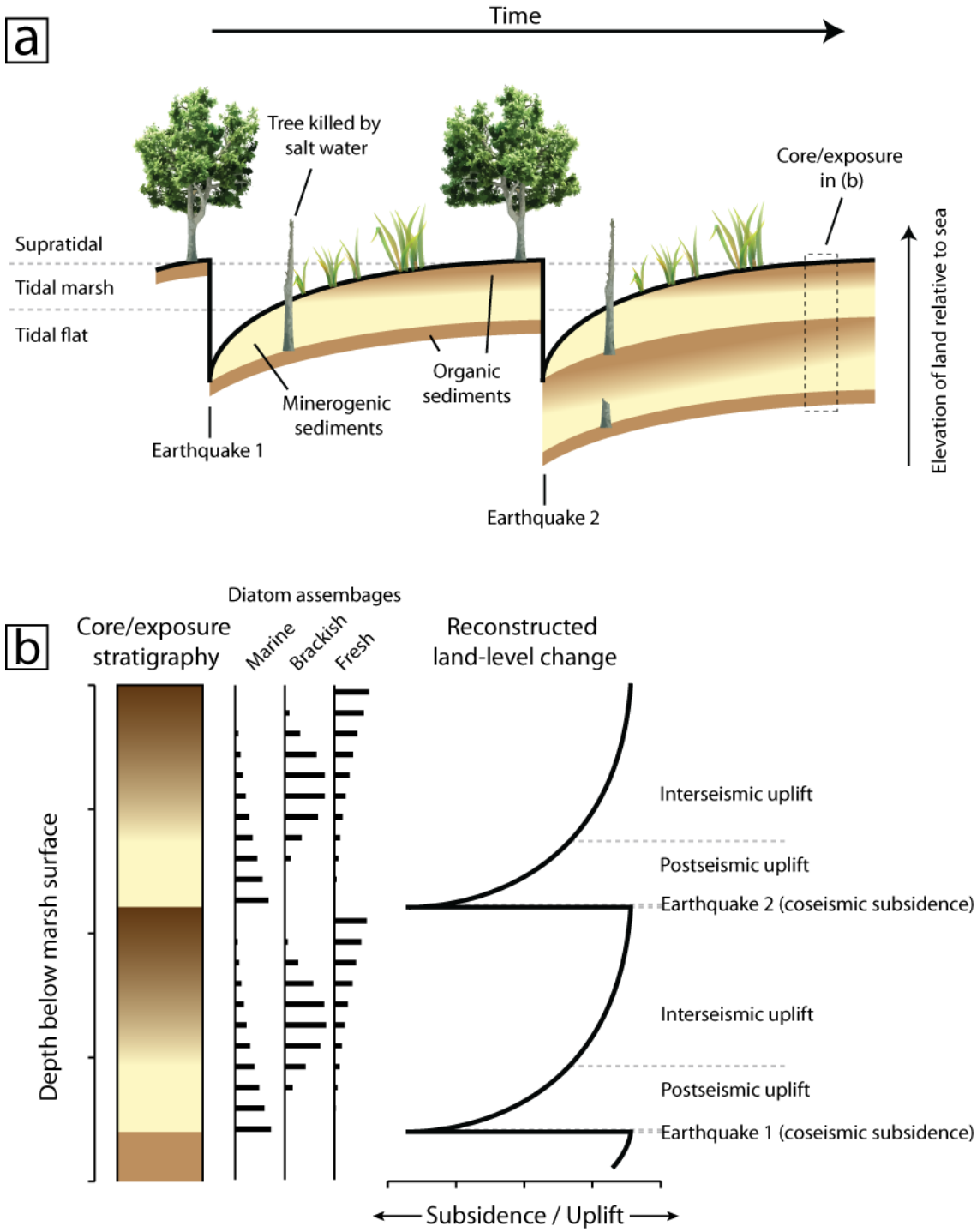

Figure 1.4: Coastal sedimentation in response to tectonic deformation. a. Schematic model of sedimentation over the course of two earthquake cycles (following Benson *et al.*, 2001). The thick black line shows the land level-change over time. Subsidence during earthquakes 1 and 2 lower organic soils to the elevation of tidal flat sedimentation, forming an organic – minerogenic couplet. b. a core or exposure (marked at the right hand side of (a)) provides sediments and diatom assemblages which record the occurrence of earthquakes 1 and 2. The use of transfer functions to calibrate diatom assemblages can provide reconstructions of land level change over time.

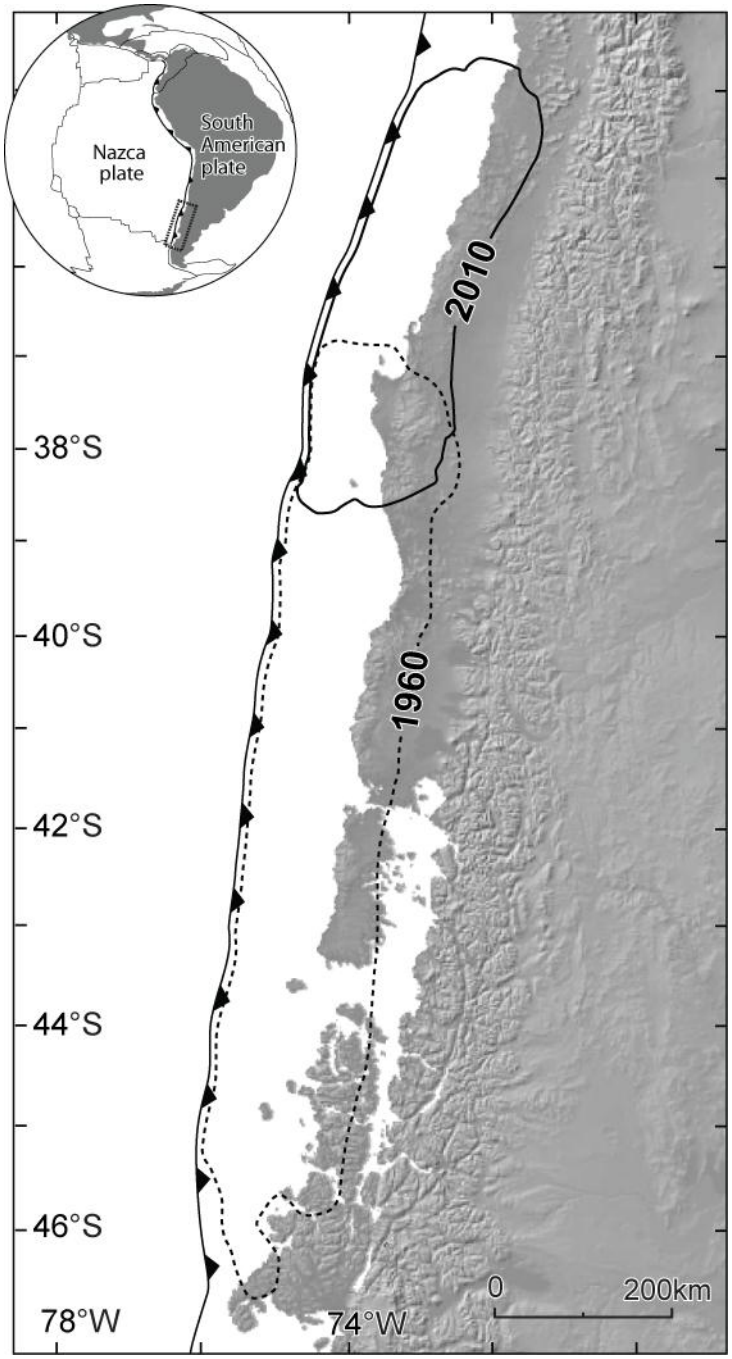

Figure 1.5: Location of the rupture zones of the 1960 Valdivia and the 2010 Maule earthquakes (after Plafker and Savage, 1970; Moreno *et al*., 2012). The Valdivia seismic segment is defined by the extent of the 1960 earthquake.

2. Study area: figures and tables

Figure 2.1: South America, including locations mentioned in the text. Dashed line indicates the Chilean border. Basemap from GeoMapApp (Ryan *et al*., 2009).

Figure 2.2: Tectonic setting of the Chilean subduction zone. Pa: Panamanian plate, NA: North Andes plate. Plate motions following DeMets *et al*. (1990); Somoza (1998) and Angermann *et al*. (1999).

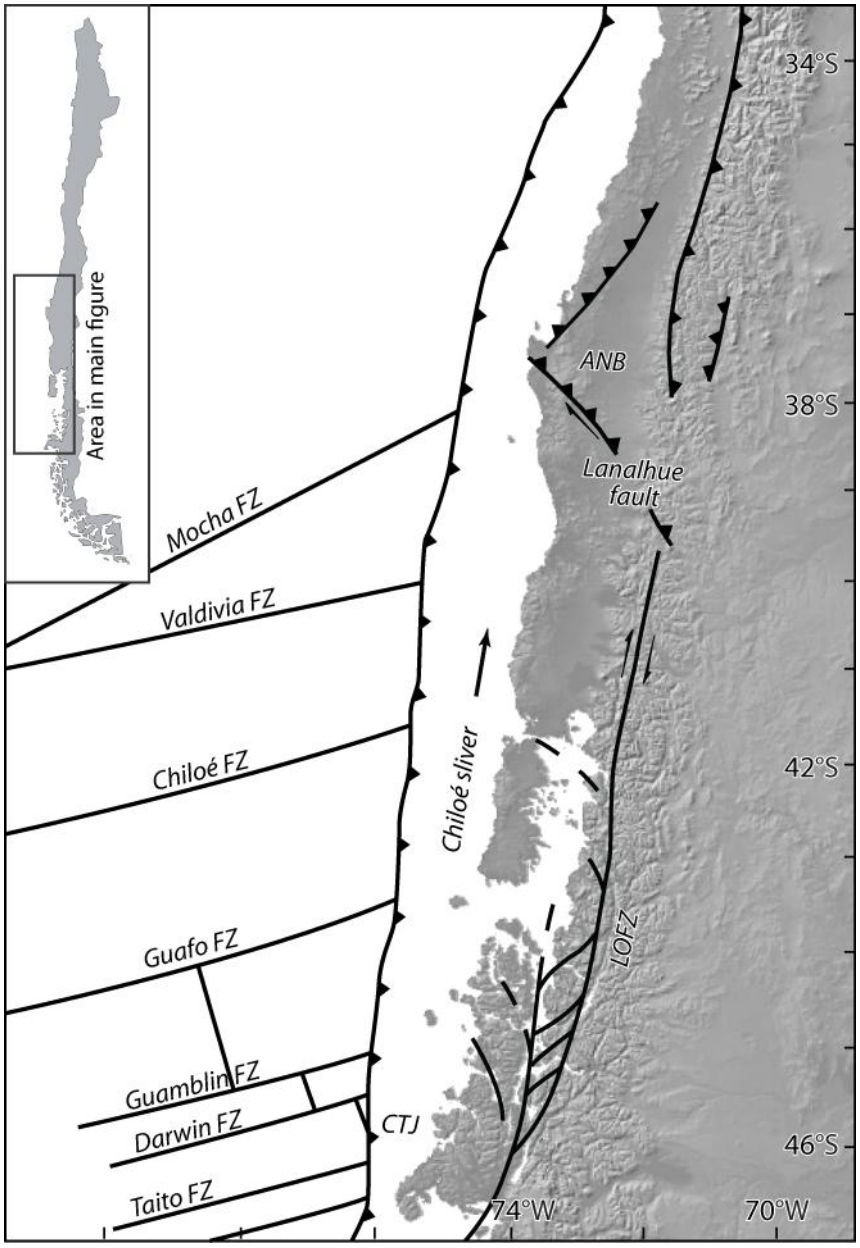

Figure 2.3: Fracture zones and upper plate fault systems within the area of interest to this thesis (following Cembrano *et al*., 1996; 2007; Melnick *et al*., 2006). The inset map highlights the area of Chile mapped in the main figure. ANB: Arauco-Nahuelbuta block, LOFZ: Liquiñe-Ofqui Fault Zone to LOFZ, FZ: fracture zone, CTJ: Chile Triple Junction.

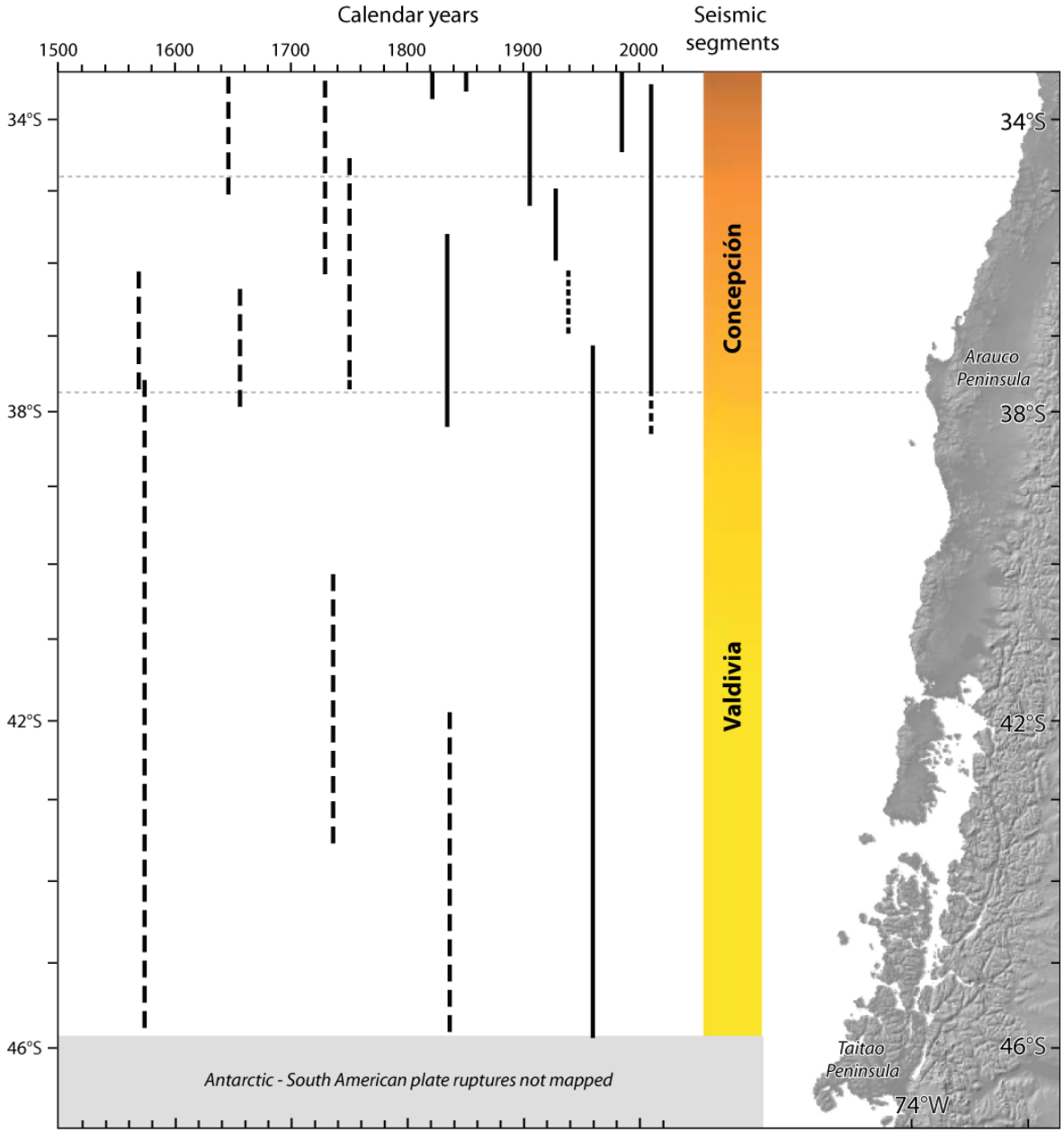

Figure 2.4: Historical subduction megathrust earthquakes along the Chilean subduction zone (compiled from Lomnitz, 1970; Kelleher, 1972; Beck et al., 1998; Campos et al., 2002; Cisternas et al., 2005). Less well constrained rupture zones indicated by dashed lines; the dotted line marks the location of 1939 intraplate event. The mechanism responsible for 1647 rupture is debated and, while mapped here as an interplate event, it may have been an Andean intraplate event (Lomnitz, 1970).

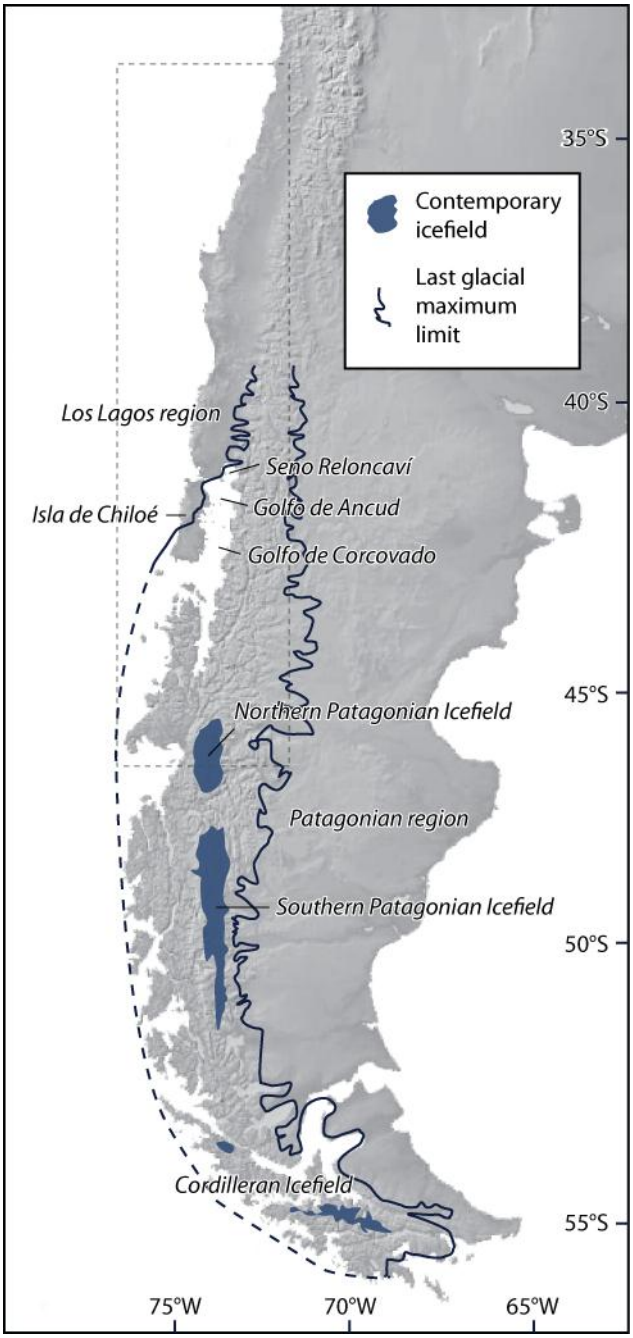

Figure 2.5: The limits of the Patagonian Icesheet at the last glacial maximum and the distribution of existing icefields (Hulton *et al*., 2002). The dashed box shows the area mapped in figures 2.3, 2.4, 2.7 etc.

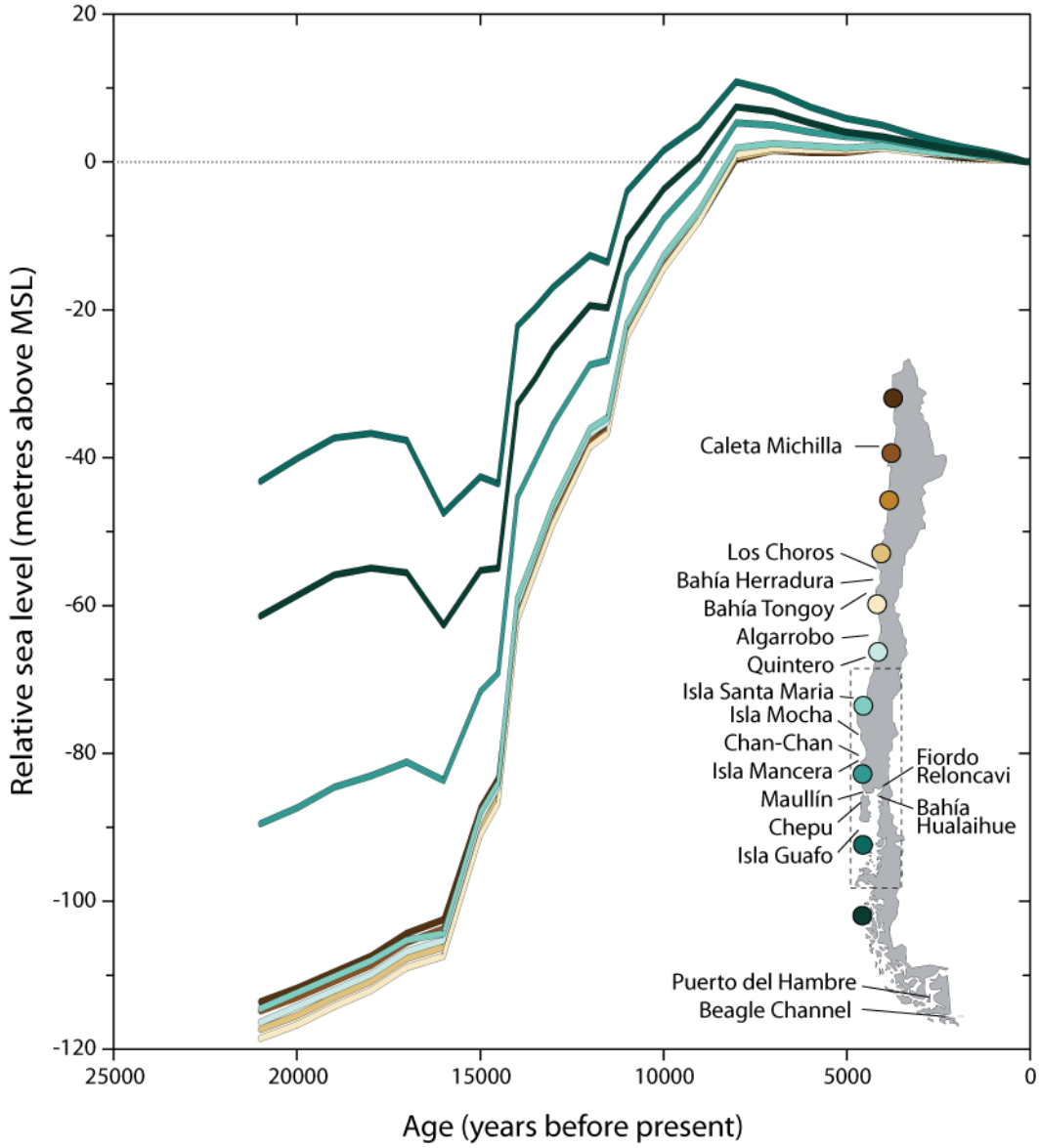

Figure 2.6: ICE5G (Peltier, 2004) simulation of relative sea-level change over the last 21 ka at 10 sites along the Chilean coastline (coloured circles in inset map). Data provided by Pippa Whitehouse (pers. com., 2012). The inset map also includes the locations of the previously documented field sites mentioned in the text, with the dashed box highlighting the area mapped in figures 2.3, 2.4, 2.7 etc.

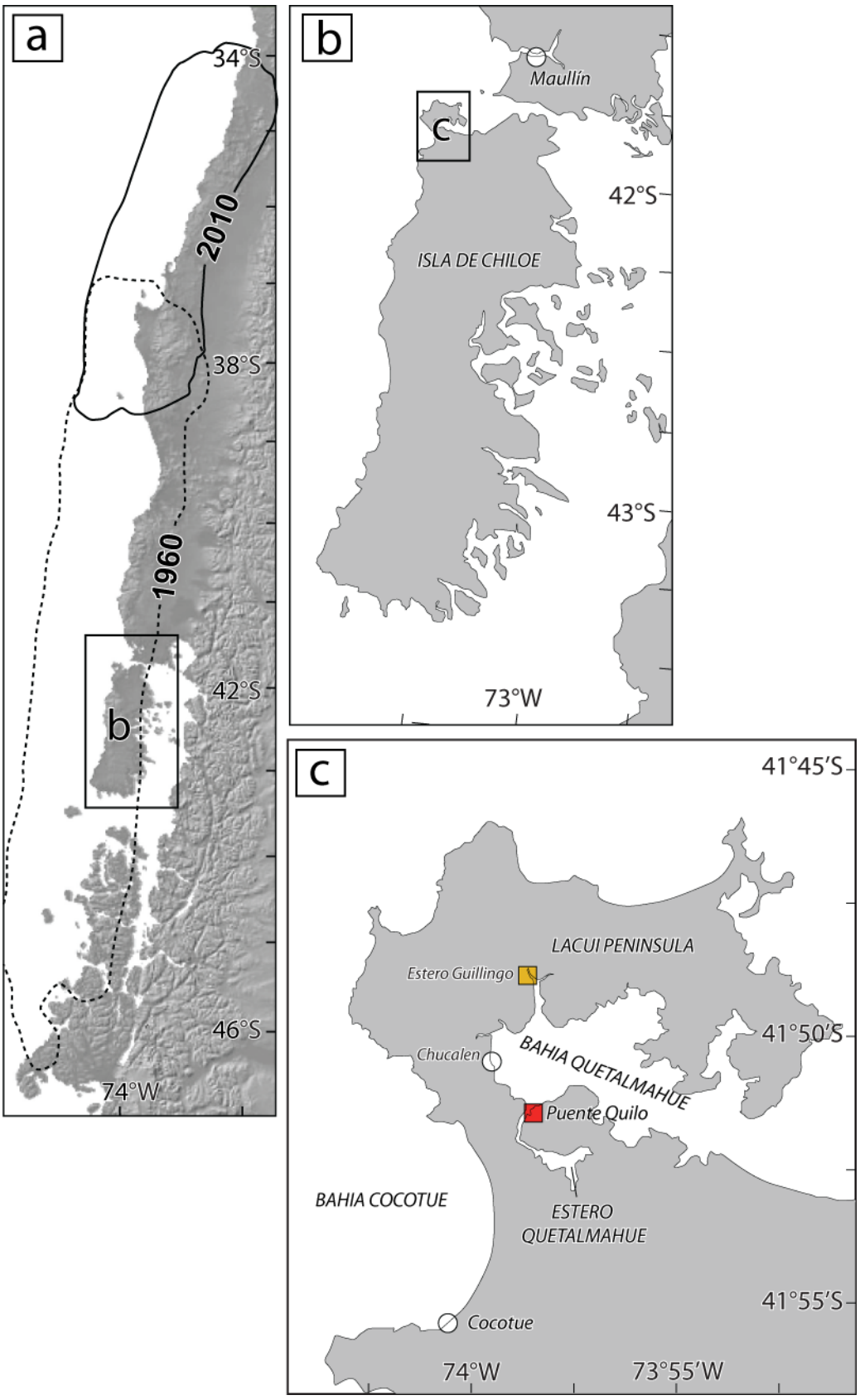

Figure 2.7: The location of the modern marsh transects at Puente Quilo and Estero Guillingo and the long record sites at Maullín, Chucalen and Cocotue. a. South central Chile including the location of the 1960 and 2010 ruptures (following Plafker and Savage, 1970; Moreno *et al*., 2012); b. Isla de Chiloé and the adjacent mainland, including the site identified by Cisternas *et al*. (2005) at Maullín; c. the modern marsh sites (coloured squares) and fossil sites (white circles) surrounding Bahía Quetalmahue, northwest Isla de Chiloé.

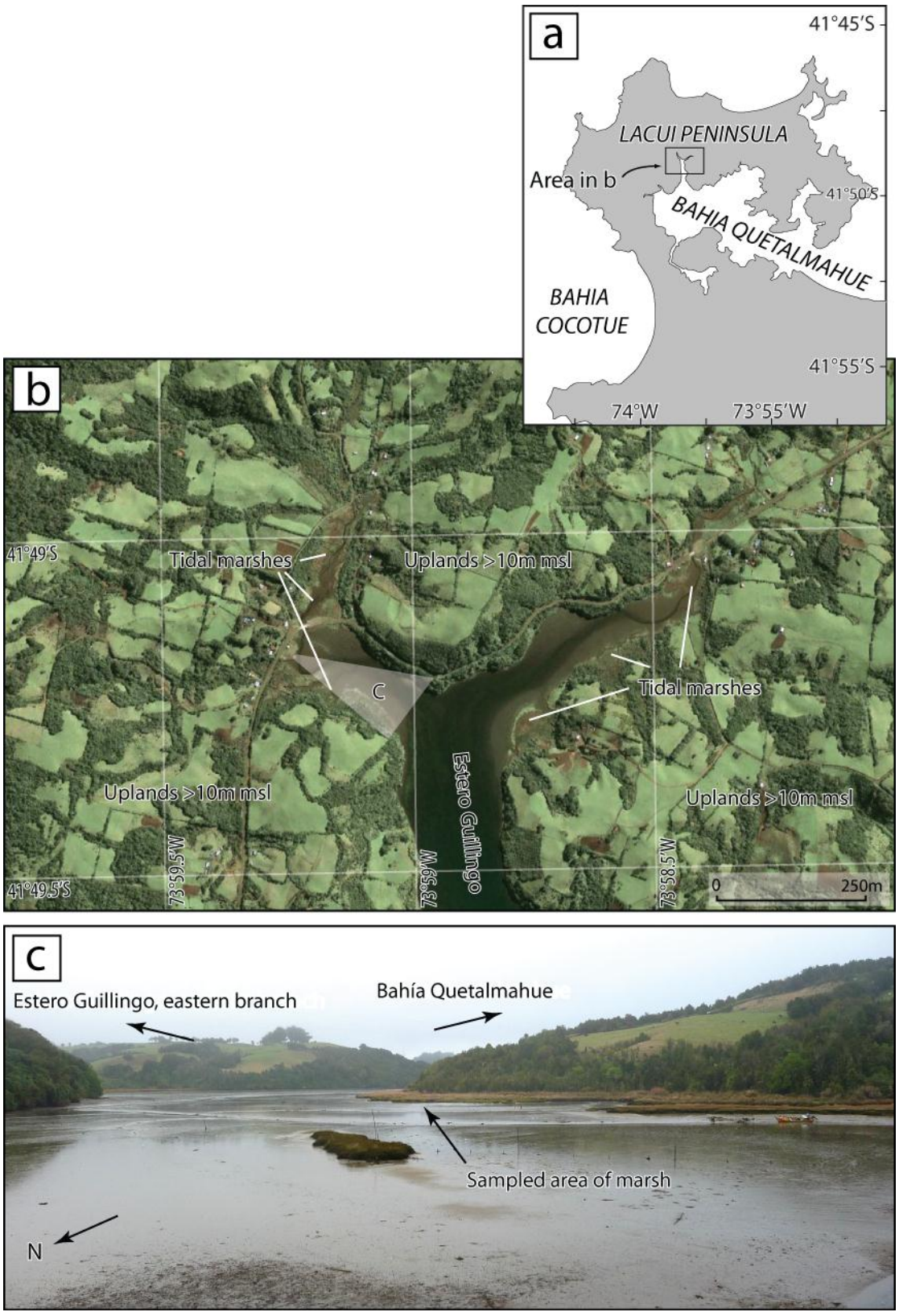

Figure 2.8: The setting of the modern marsh site at Estero Guillingo. a. Northwestern Isla de Chiloé, including the location of b. the site at Estero Guillingo (Google Earth image from September 2009). c. Photograph of the western branch of Estero Guillingo, looking southeast towards the confluence with the eastern branch of the estuary and the entrance to Bahía Quetalmahue. For scale, the sampled area of marsh is approximately 200 m from the photographer and the boat on the right is approximately 3 m in length.

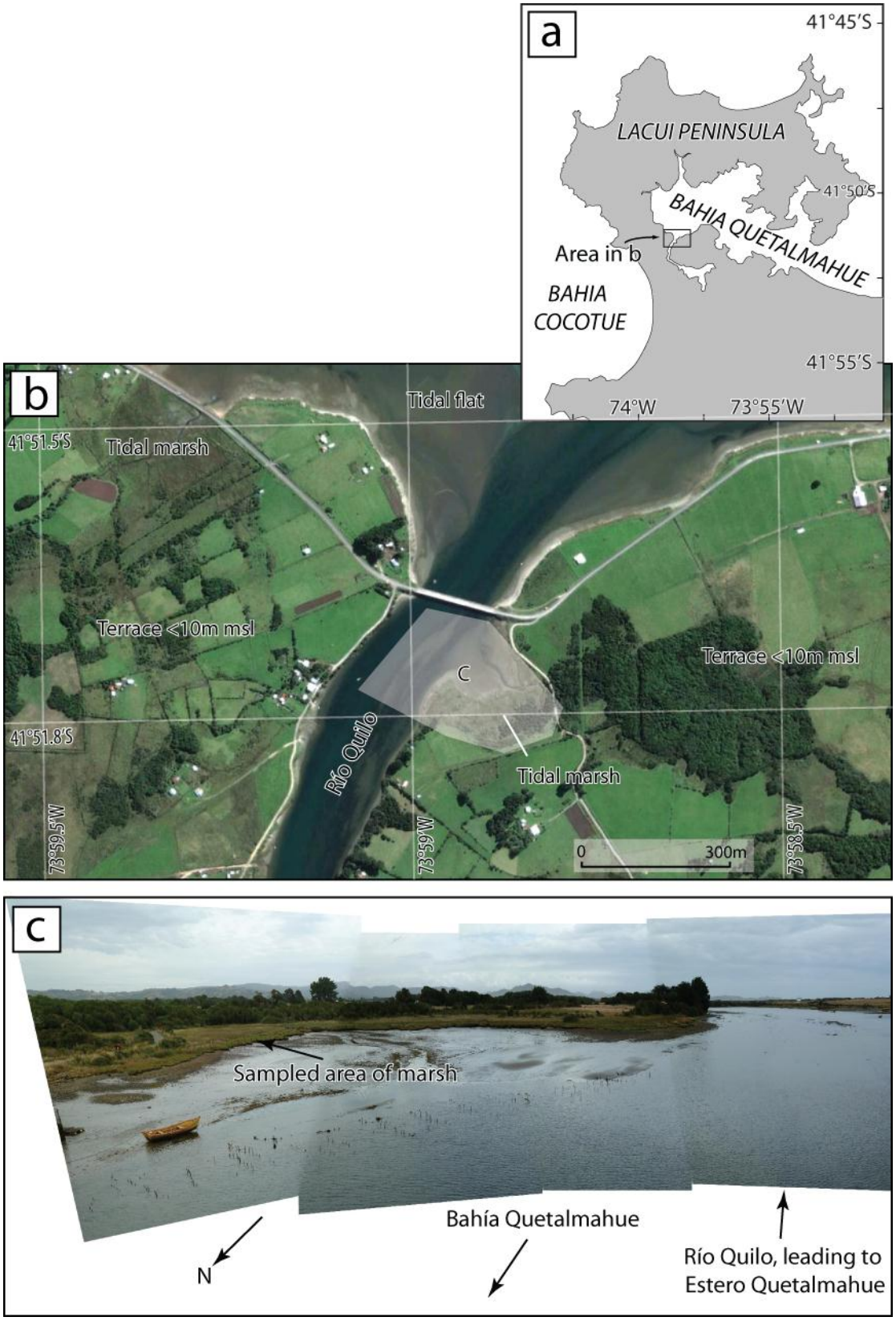

Figure 2.9: The setting of the modern marsh site at Puente Quilo. a. Northwestern Isla de Chiloé, including the location of b. the site at Puente Quilo (Google Earth image from March 2012). c. Panorama of Puente Quilo, looking south from the bridge over the Río Quilo. The tidal marsh lies on the east bank of the river, in the centre and left of the photo. For scale, the sampled area of marsh is approximately 200 m from the photographer and the boat in the lower left is approximately 4 m in length.

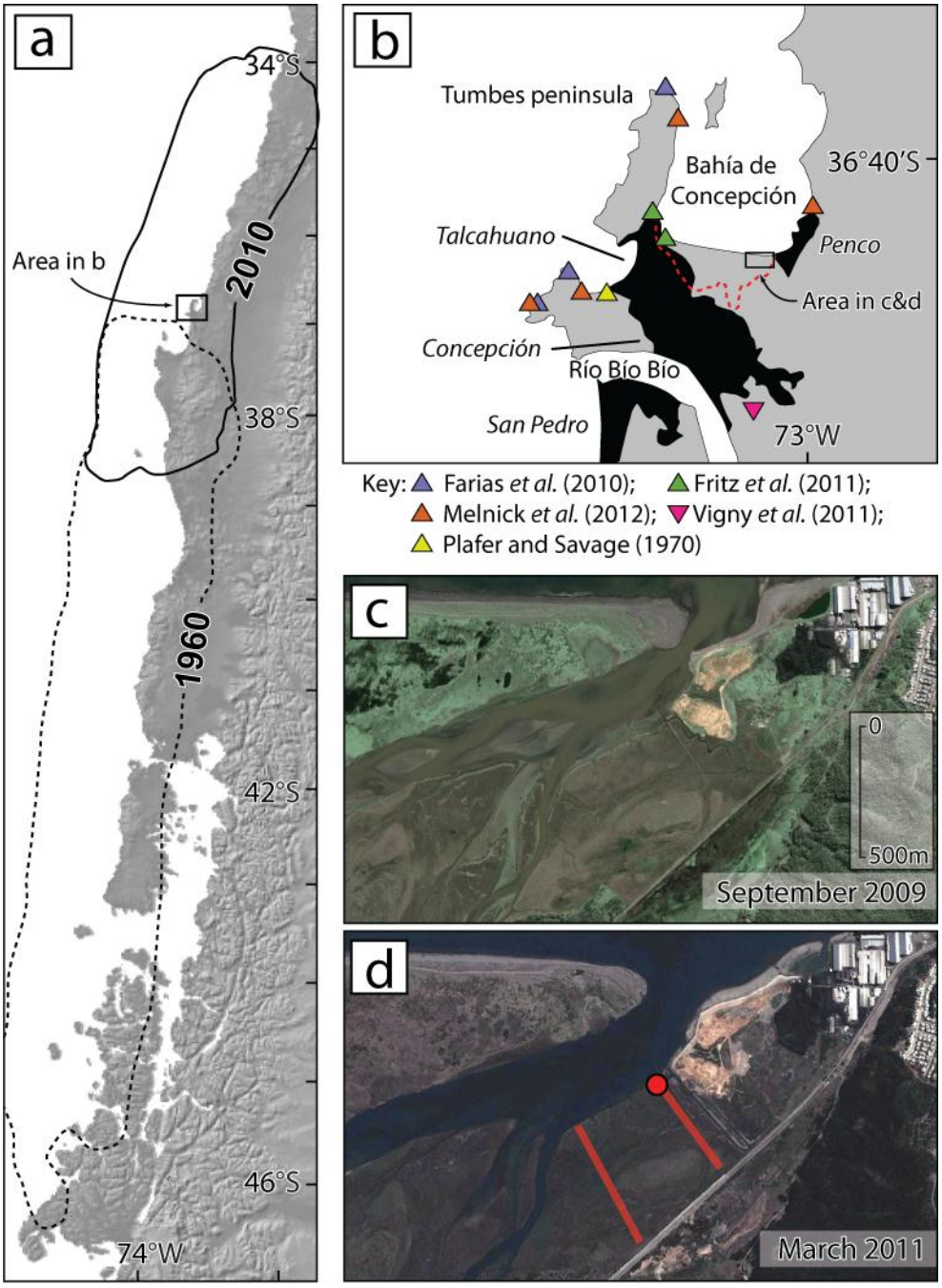

Figure 2.10: The location of the *Sediment Signatures* project site at Río Andalién, a. with respect to the 2010 and 1960 rupture zones; b. Bahía Concepción and the Tumbes Peninsula, including the 2010 tsunami inundation limit (red dashed line) and locations of published deformation estimates for 2010 and 1960 (coloured triangles; Δ indicates uplift, ∇ indicates subsidence); c., d. Google Earth images of the mouth of Río Andalién from before and after the February 2010 Maule earthquake, including the location of the *Sediment Signatures* project coring transect (red lines) and the sampled monolith (red circle). The state of the tide in each image is unknown.

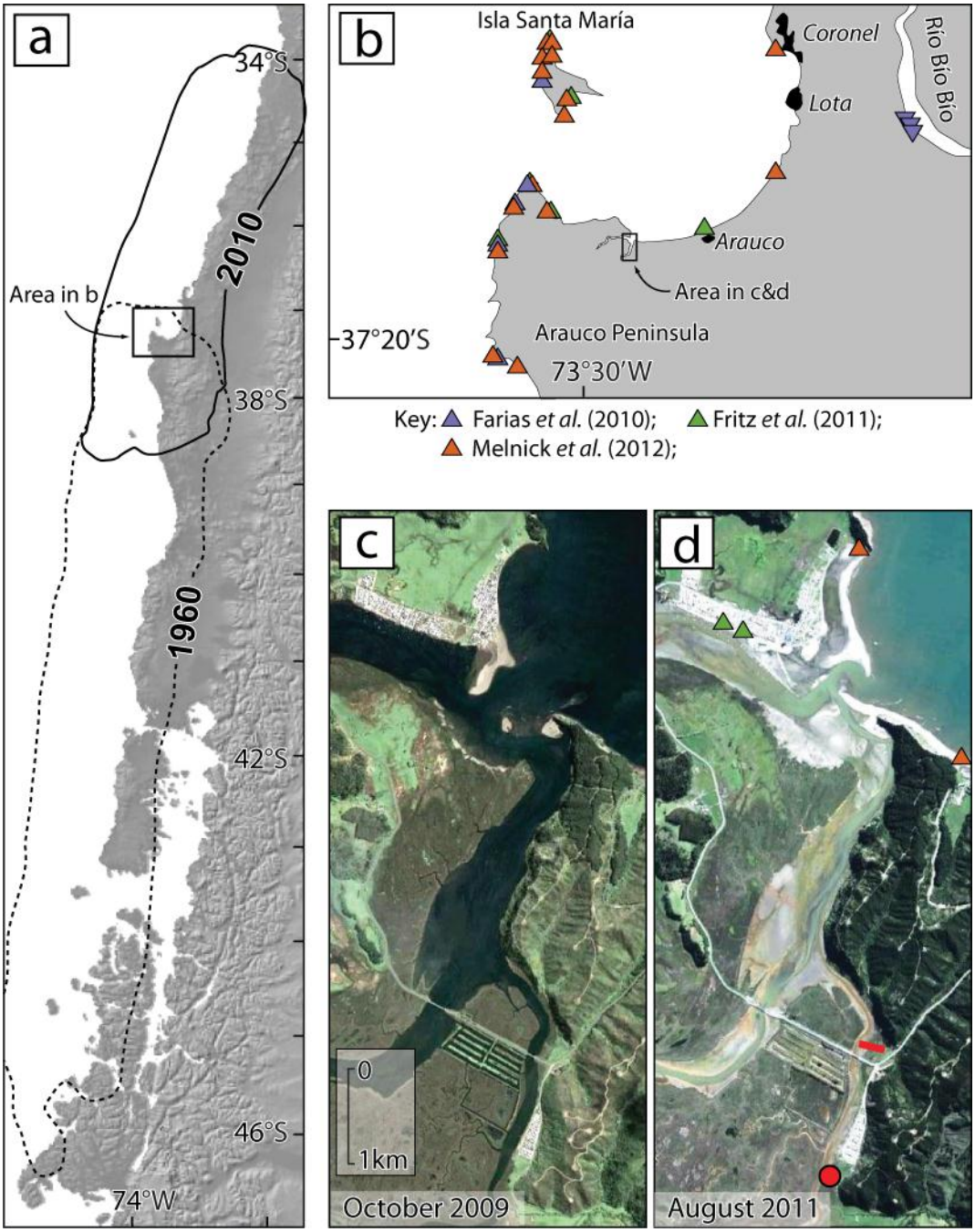

Figure 2.11: The location of the *Sediment Signatures* project site at Tubul, a. with respect to the 2010 and 1960 rupture zones; b. the Arauco Peninsula, including the locations of published deformation estimates for 2010 (coloured triangles; Δ indicates uplift, ∇ indicates subsidence); c., d. Google Earth images of Tubul from before and after the February 2010 Maule earthquake, including the location of the *Sediment Signatures* project coring transect (red line) and the sampled monolith (red circle). The state of the tide in each image is unknown.

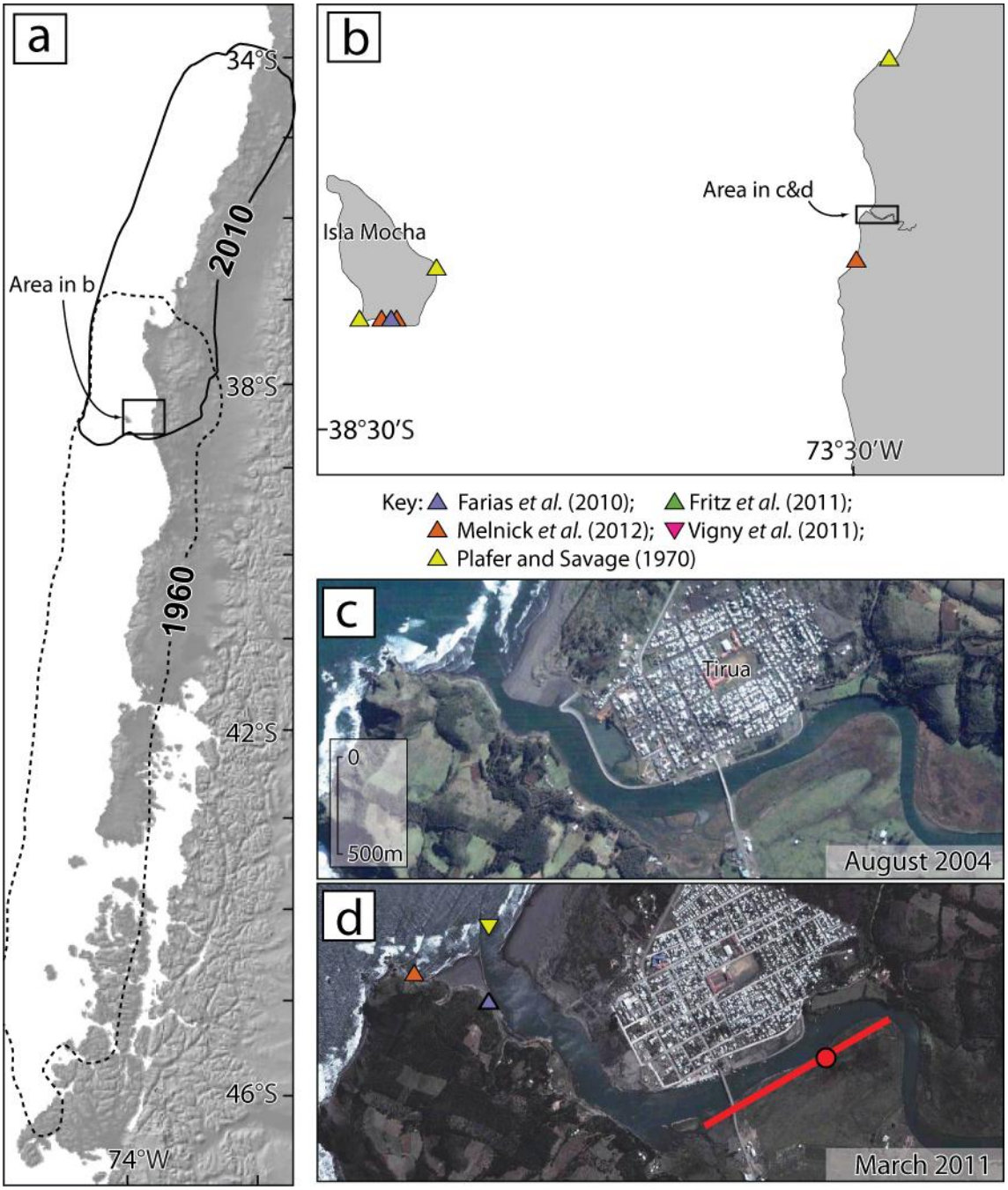

Figure 2.12: The location of the *Sediment Signatures* project site at Río Tirua, a. with respect to the 2010 and 1960 rupture zones; b. the coastline adjacent to Río Tirua, including the locations of published deformation estimates for 2010 and 1960 (coloured triangles; Δ indicates uplift, ∇ indicates subsidence); c., d. Google Earth images of Río Tirua from before and after the February 2010 Maule earthquake, including the location of the *Sediment Signatures* project coring transect (red line) and the sampled core (red circle). The state of the tide in each image is unknown.

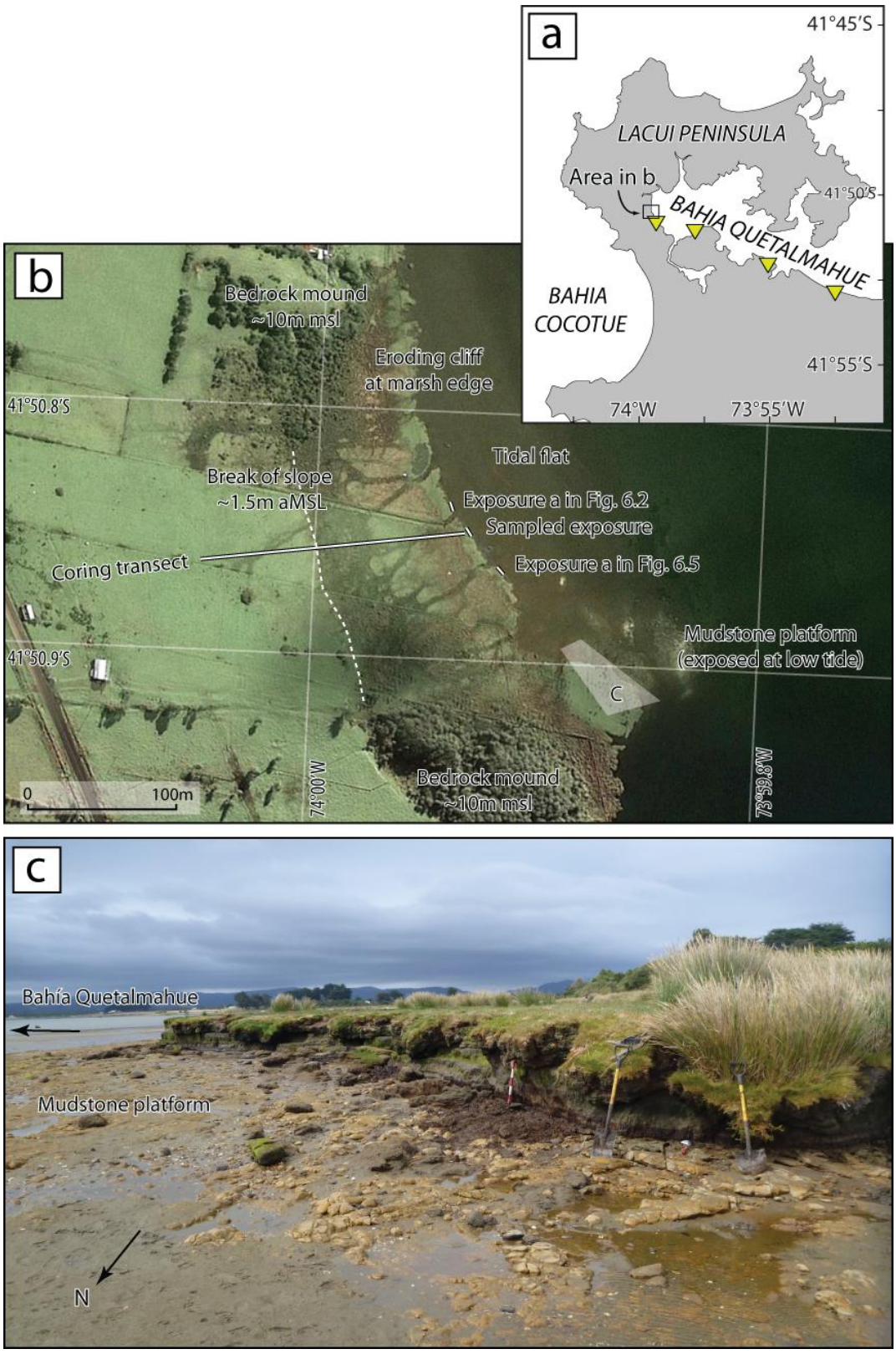

Figure 2.13: The setting of the site at Chucalen. a. Northwestern Isla de Chiloé, including the location of 1960 deformation estimates (yellow triangles; Plafker and Savage, 1970) and b. the site at Chucalen (Google Earth image from September 2009). c. Photograph of the ~1 m high cliff separating the vegetated marsh from the tidal flat (or in this instance, a mudstone platform) on the western margin of Bahía Quetalmahue. The sampled marsh at Chucalen lies approximately 150 m to the northeast of the area in this photo. The red and white shovel handle is 50 cm in length. Photograph courtesy of Rob Wesson.

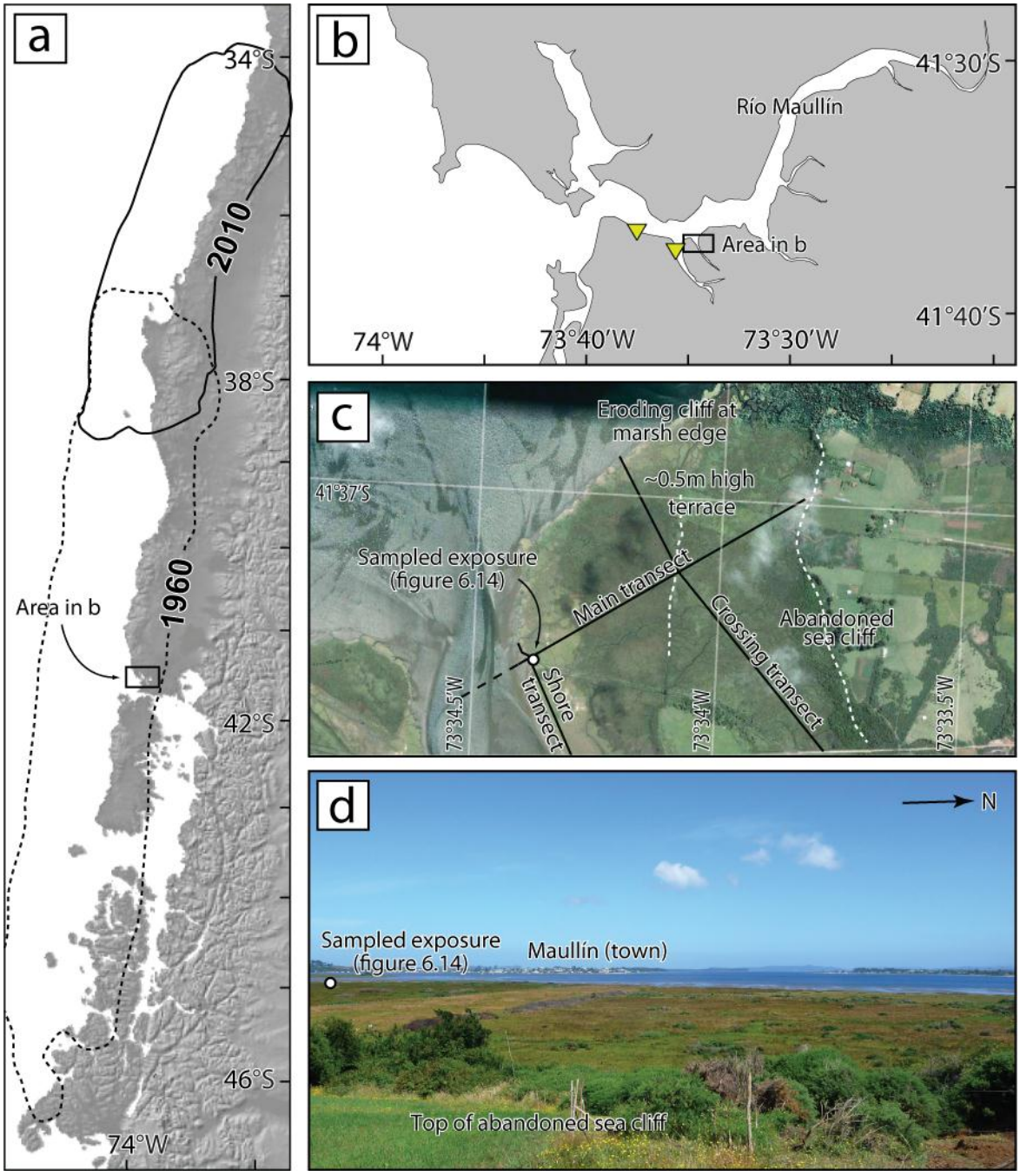

Figure 2.14: The setting of the site at Maullín, a. with respect to the 1960 and 2010 rupture zones. b. The Maullín estuary, including the location of 1960 deformation estimates (yellow triangles; Plafker and Savage, 1970); c. the site (Google Earth image from December 2005) including the location of Cisternas *et al.*'s (2005) sampling transects and the exposure discussed in this thesis; d. photograph of the site looking west from the abandoned sea cliff.

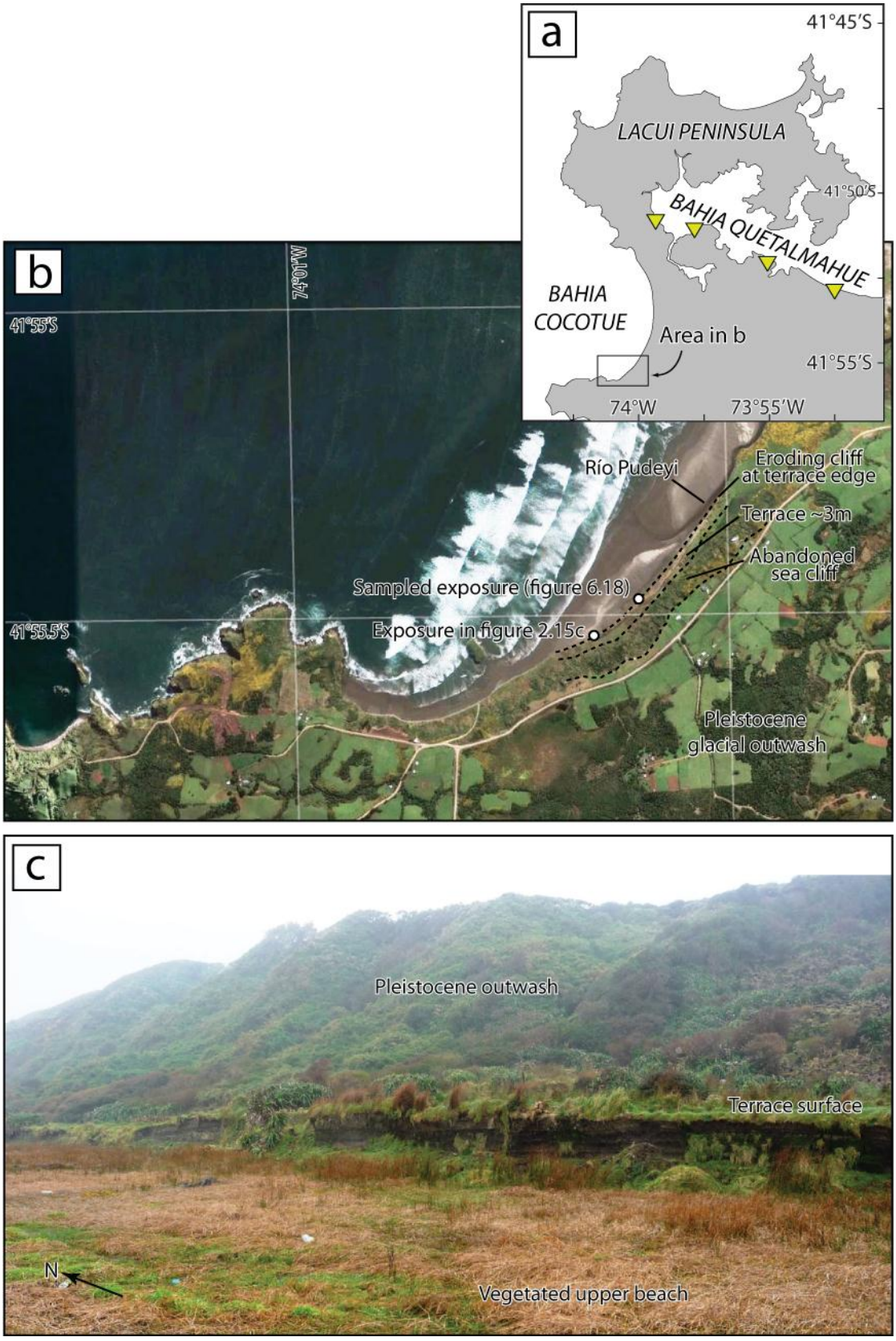

Figure 2.15: The setting of the site at Cocotue. a. Northwestern Isla de Chiloé, including the location of 1960 deformation estimates (yellow triangles; Plafker and Savage, 1970) and b. the site at Cocotue (Google Earth image from October 2010). c. Photograph of the narrow terrace situated between a highly eroded former sea cliff cut into Pleistocene glacial outwash and the beach at Cocotue. The exposed face of the terrace is approximately 1.5 m in height.

3. Approach: figures and tables

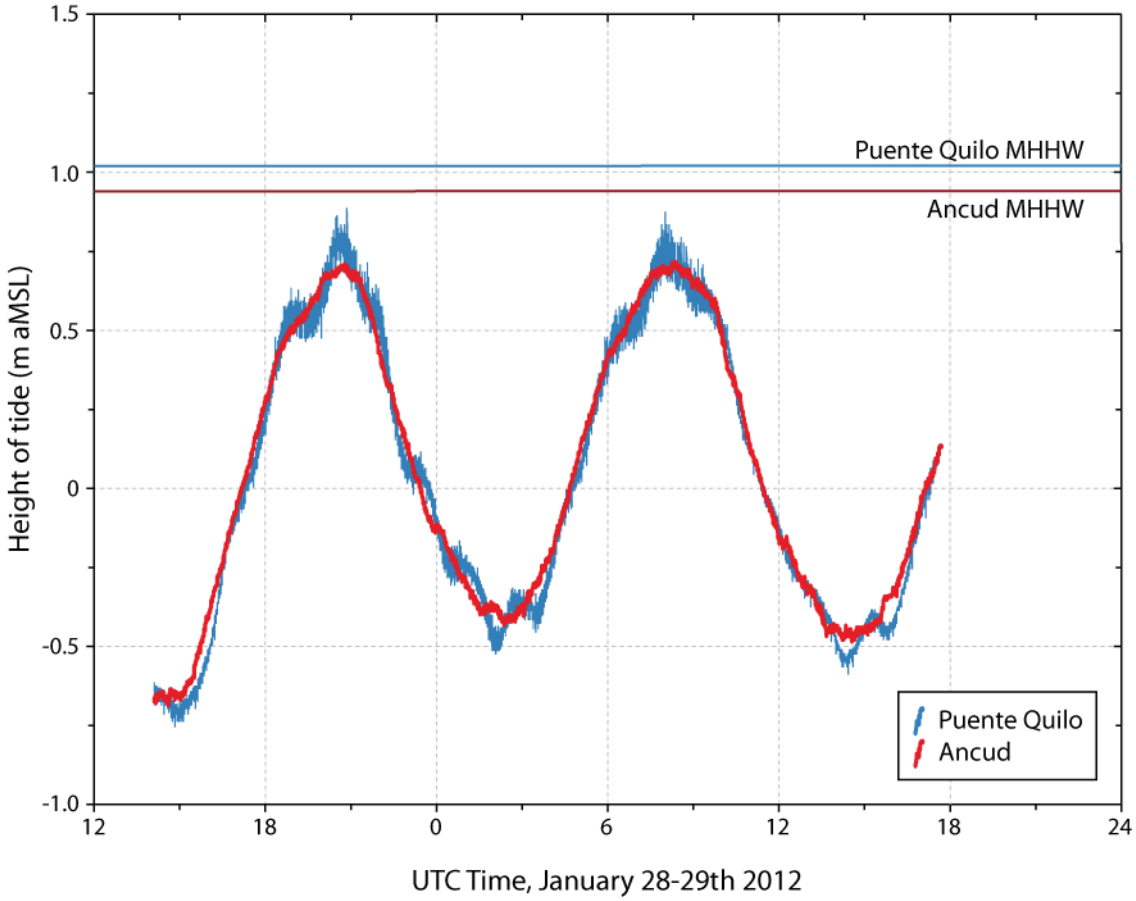

Figure 3.1: Comparison of tides surveyed at Puente Quilo using a portable ultrasound tide gauge (data supplied by Rob Wesson, 2012) and tidal observations from the gauge at Ancud (IOC, 2012). Mean higher high water elevations derived for Ancud from a four year time series and for Puente Quilo by scaling the Ancud data.

Site	Difference between MSL and MHHW (m)
Modern transects	
Puente Quilo	1.02
Estero Guillingo	1.02
Río Angachilla	0.80
Isla del Rey	0.73
Fossil sites	
Chucalen	1.02
Maullín	1.05
Cocotue	1.00
Río Andalién*	0.72
Tubul*	1.16
Río Tirua*	1.24

Table 3.1: Tidal inputs for derivation of standardised water level index values for the modern transects and the back-calculation of standardised water level index values into metres above mean sea level for the fossil sites and the *Sediment Signatures* project sites (*).

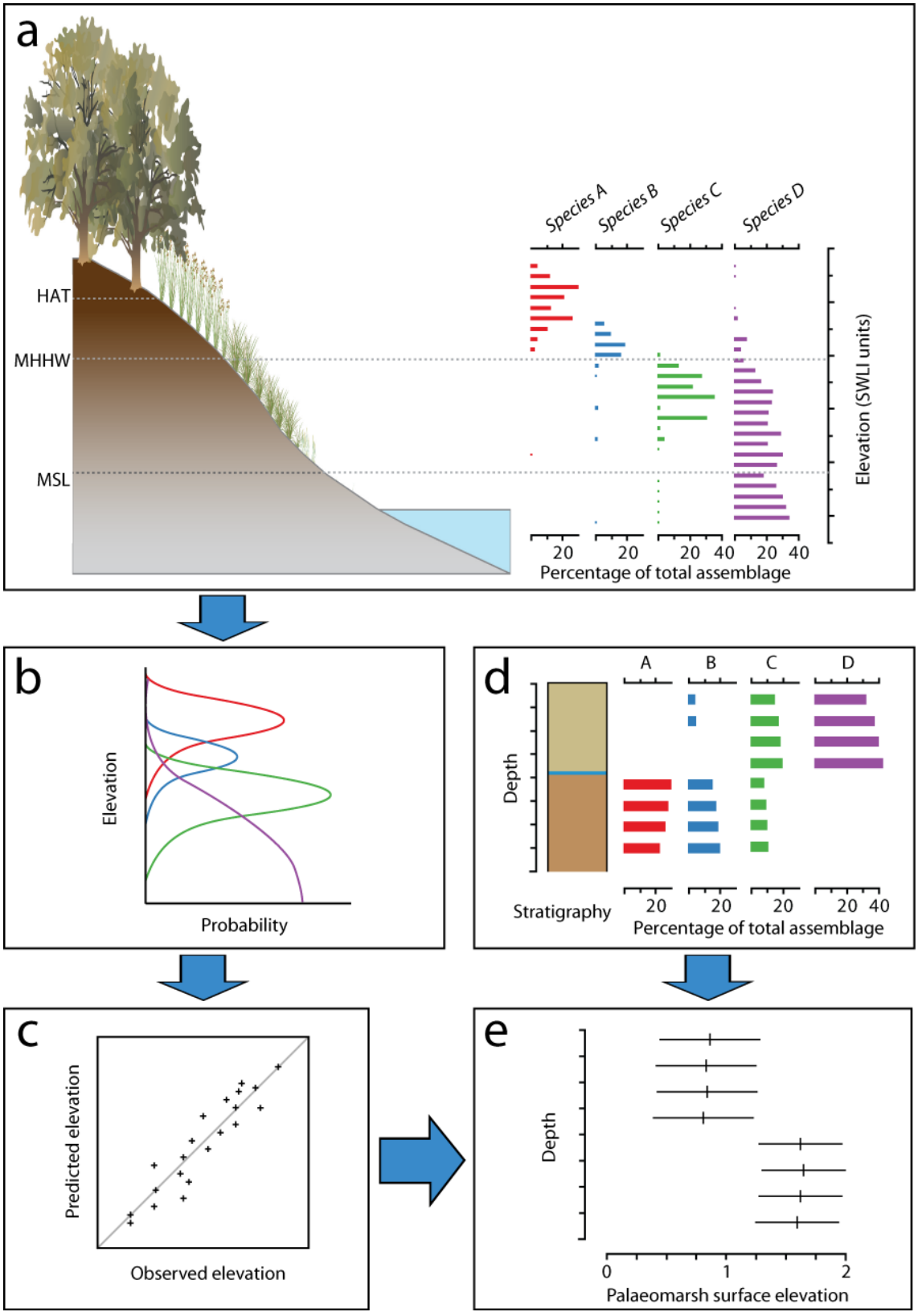

Figure 3.2: A graphical representation of the transfer function process. a. I characterise the distribution of modern diatoms in a transect across a contemporary tidal marsh; b. the transfer function assigns a unimodal curve to model the distribution of each species along the elevation gradient; c. a scatter plot of observed and estimated marsh surface elevations displays the performance of the model; d. a core or exposure provides fossil diatom assemblages; e. fossil assemblages are calibrated using the transfer function to produce estimates of marsh surface elevation, including a sample specific error.

4. Results: modern Chilean intertidal marshes: figures and tables

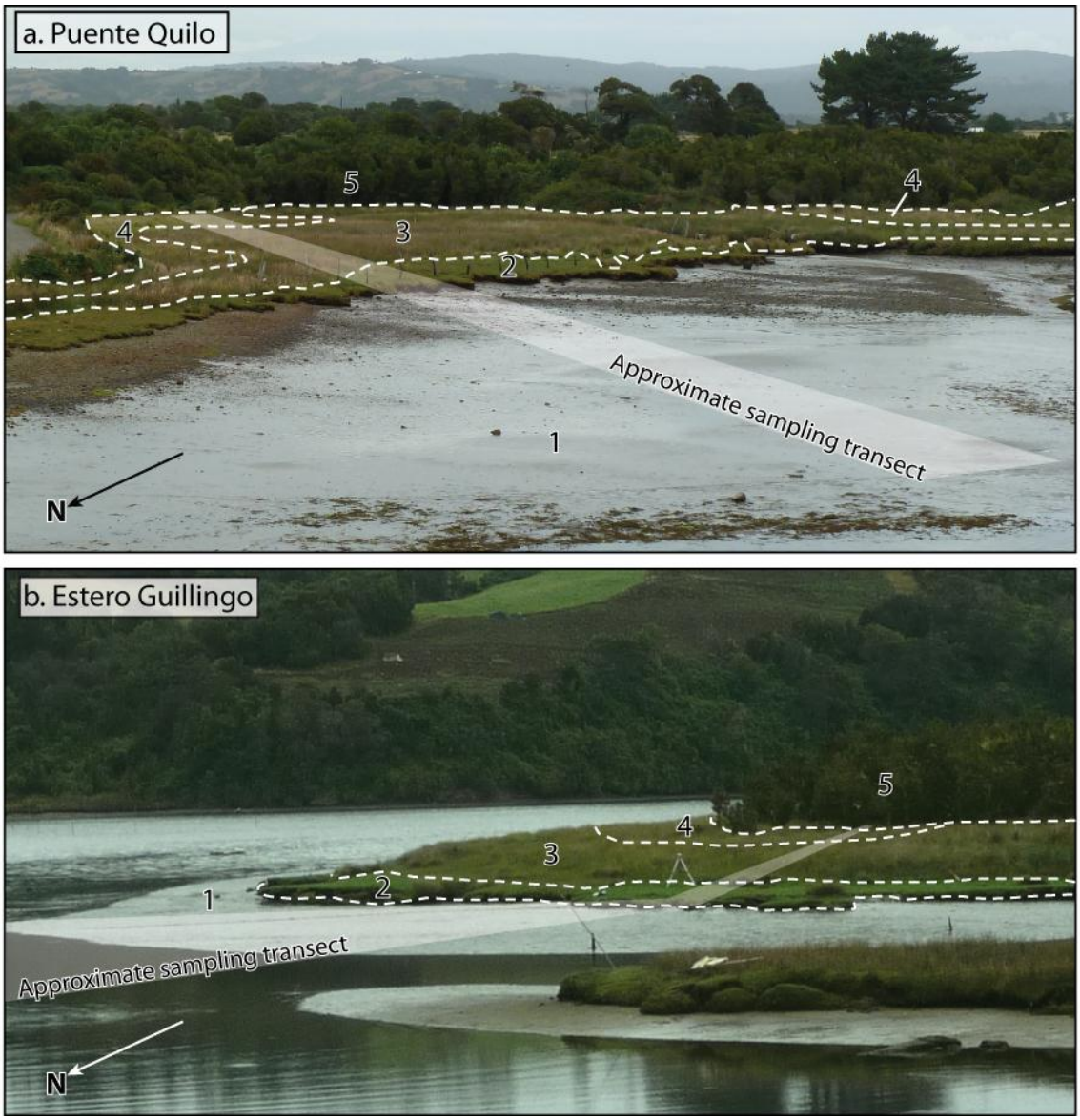

Figure 4.1: Modern intertidal marsh zonation at a. Puente Quilo and b. Estero Guillingo. Numbers refer to vegetation zones listed in table 4.1.

Vegetation zone	Dominant plant species
5 (freshwater scrub)	*Drimys winteri*
	Myrtaceae sp.
	Ulex europaeus
	Berberis darwinii
	Berberis microphylla
	Luma apiculata
	Gunnera tinctoria
	Blechnum chilense
4 (high marsh)	*Bromus* sp.
	Lotus uliginosus
	Rumex cuneifolius
3 (mid marsh)	*Spartina densiflora*
	Juncus balticus
	Scirpus californicus
	Carex sp.
	Holcus lanatus
2 (low marsh)	*Triglochin* sp.
	Selliera radicans
	Sarcocornia fruticosa
	Eleocharis macrostachya
	Carex sp.
	Holcus lanatus
	Cotula coronopifolia
1 (tidal flat)	*Gracilaria chilensis*

Table 4.1: Summary of the dominant plants in the Isla de Chiloé tidal marsh vegetation zones.

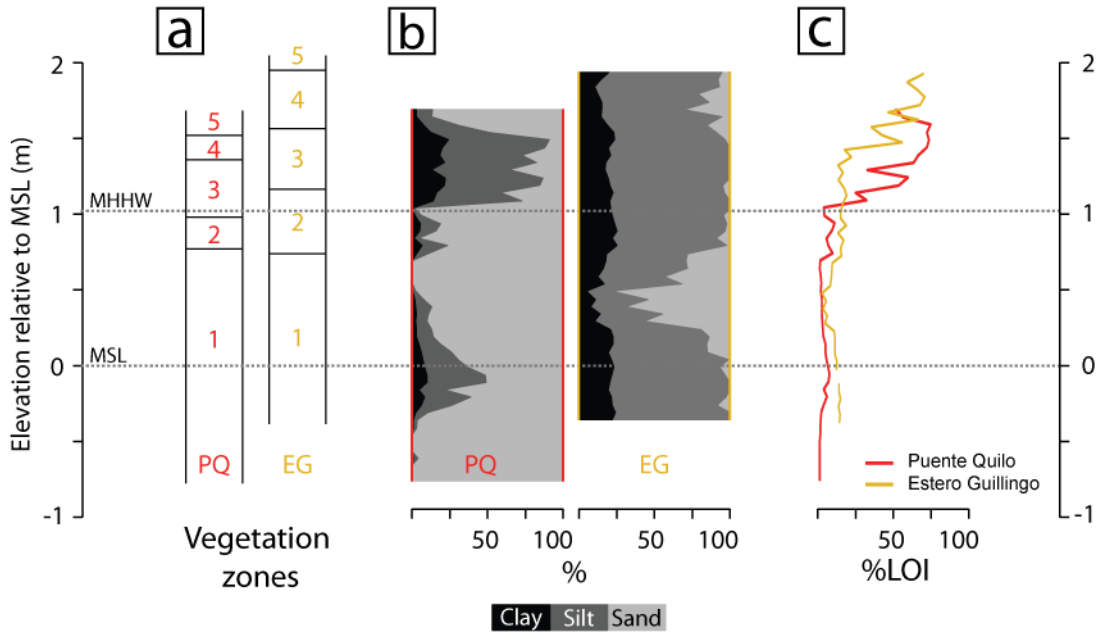

Figure 4.2: Puente Quilo (PQ) and Estero Guillingo (EG) intertidal zonation in a. vegetation zones (numbers refer to zones listed in table 4.1); b. particle size; c. organic content, as estimated by percentage loss on ignition (%LOI).

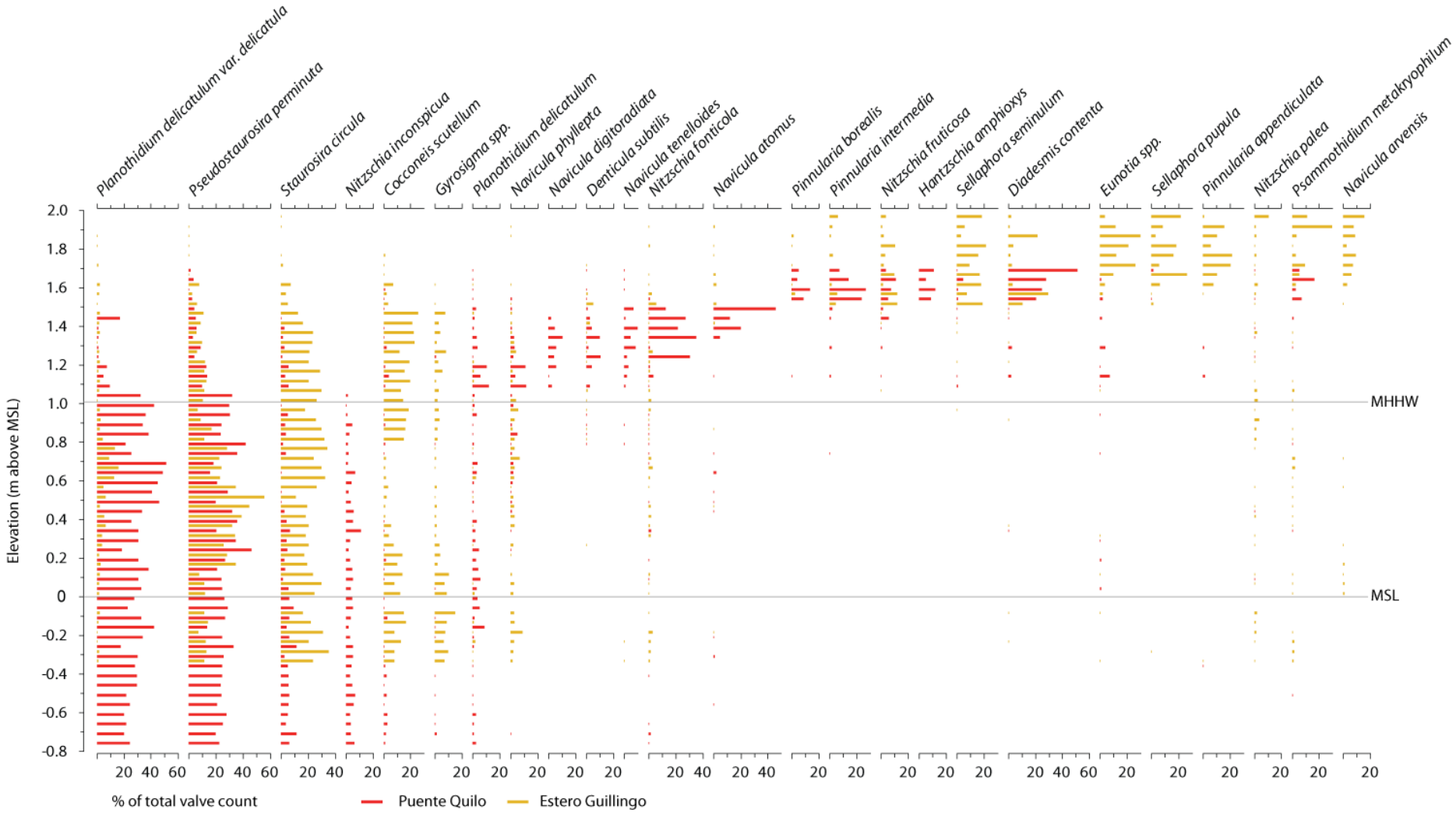

Figure 4.3: Modern diatom distributions (species exceeding 10 %) against elevation (m above MSL) at Puente Quilo and Estero Guillingo. Estero Guillingo sample elevations offset by +0.025 m to avoid overlaying Puente Quilo samples.

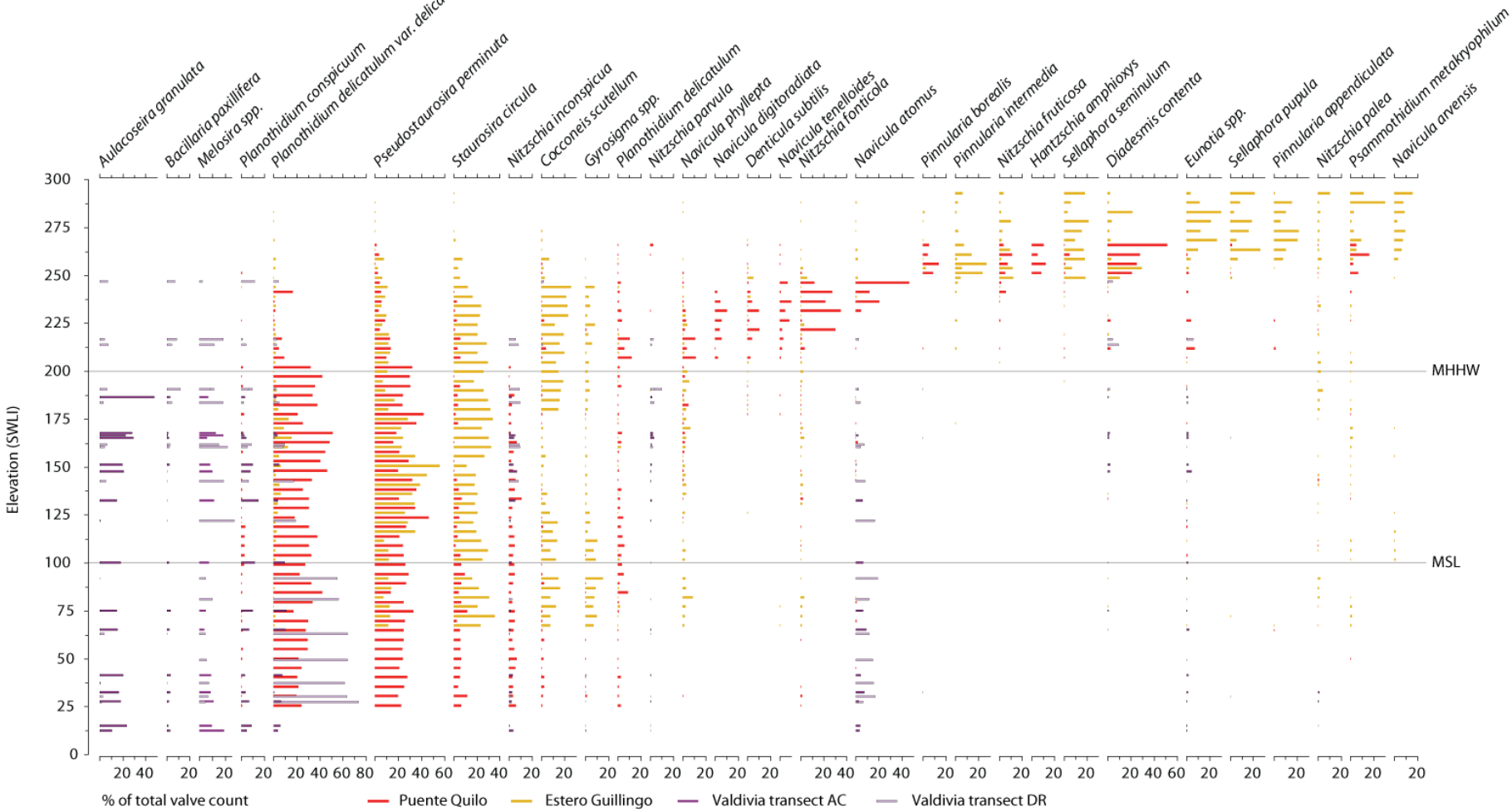

Figure 4.4: Modern diatom distributions (species exceeding 10 %) against elevation (Standardised Water Level Index) in the Chiloé transects (Puente Quilo and Estero Guillingo transects) and the Valdivia transects (Río Angachilla and Isla del Rey transects, Nelson *et al*., 2009). Estero Guillingo sample elevations offset by +2.5 SWLI units to avoid overlaying Puente Quilo samples.

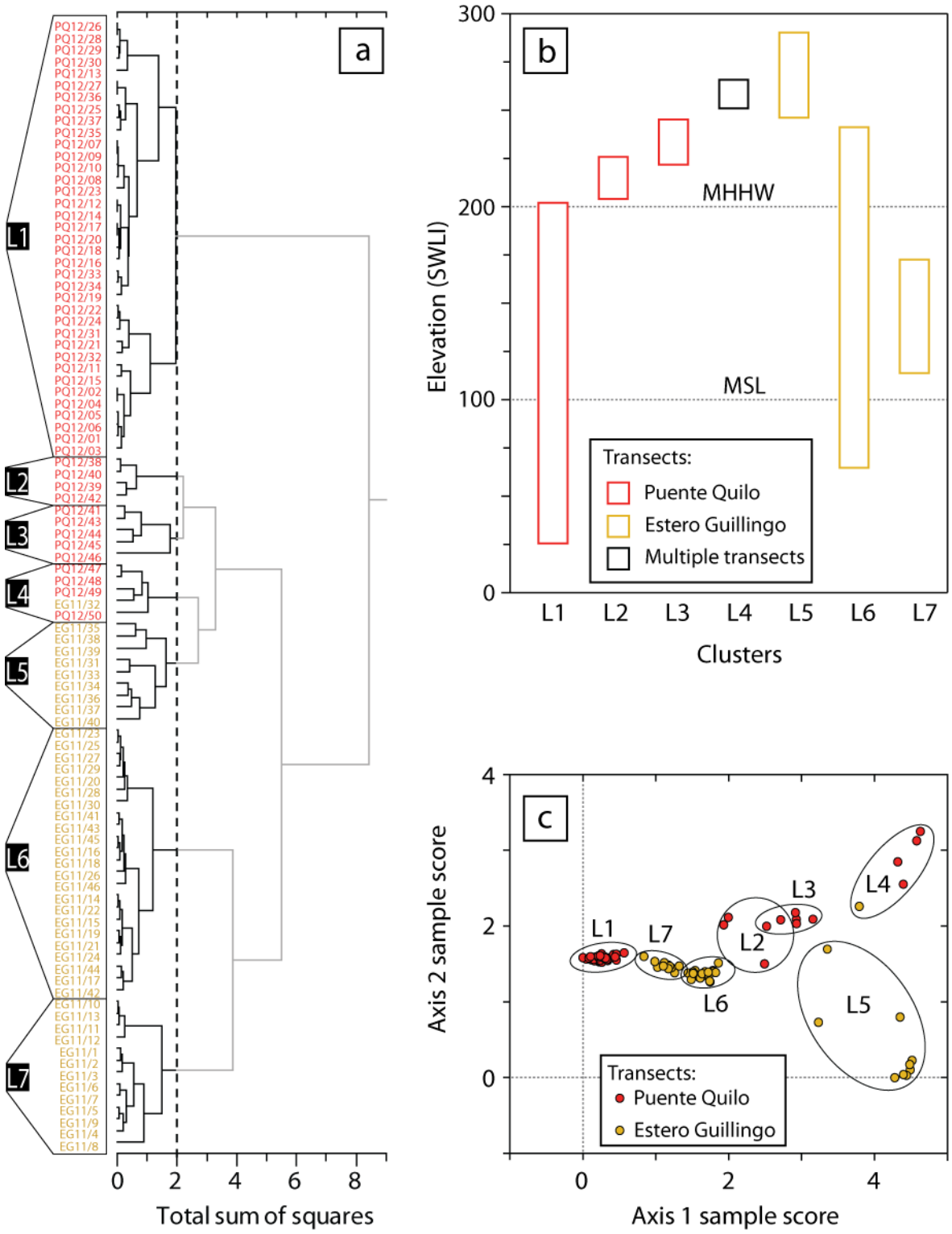

Figure 4.5: Multivariate analysis of the *Chiloé* modern diatom dataset. a. Unconstrained cluster analysis dendrogram (incremental sum of squares, Euclidean distance, un-weighted, no data transformation or standardisation). b. Elevation (SWLI) ranges of the clusters defined by cluster analysis. Coloured outlines indicate clusters that consist entirely of samples from a single site, black outlines indicate clusters incorporating samples from more than one transect. c. Detrended Correspondence Analysis sample plot. Ovals surround clusters defined by cluster analysis.

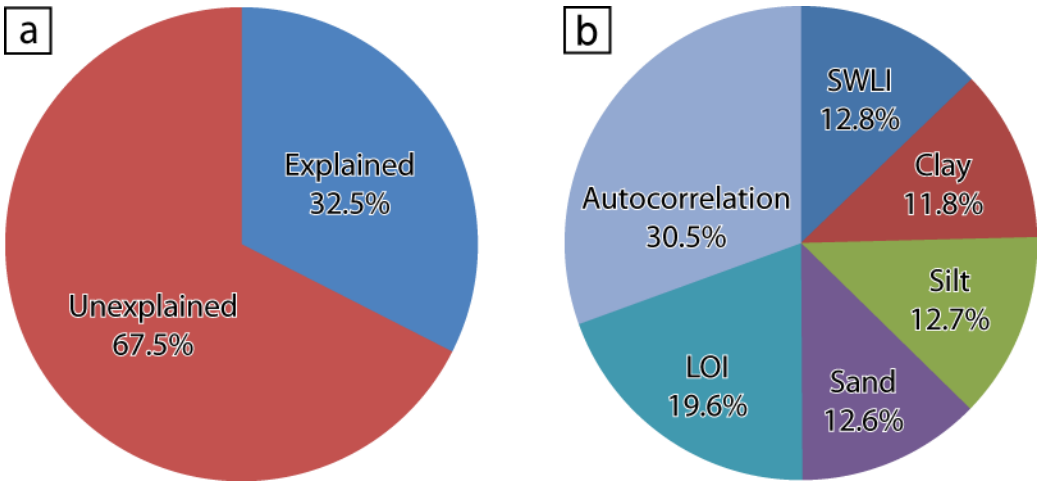

Figure 4.6: Pie charts showing the variation in the *Chiloé* dataset divided into a. explained and unexplained sectors derived from DCCA and b. the individual contributions of the environmental variables as percentages of the total explained variation.

Dataset	**Number of samples**	**Variance explained by all known variables (%)**	**Variance explained by elevation (%)**	**Elevation as percentage of total explained variance (%)***	**Reference**
Chiloé	96	32.5	10.7	12.8	This study
Regional, south central Chile	128	-	7.2	100†	This study
British Isles	88	21.6	8.6	23.3	Zong and Horton (1999)
Hokkaido, Japan	78	20.2	4.5	15.1	Sawai *et al*. (2004)
Ho Bugt, western Denmark	40	37.9	27.9	24	Szkornik *et al*. (2006)
British Columbia, Canada	48	39.1	6.7	7.98	Roe *et al*. (2009)
Alaska	272	-	2.7	100†	Watcham *et al*. (2012)
Scotland	215	-	3.6	100†	Barlow *et al*. (submitted)

Table 4.2: Comparison of ordination results from the *Chiloé* and *Regional* datasets with published results from diatom-based tidal marsh studies in selected locations worldwide.
* Includes autocorrelation between variables.
† Elevation is the only known environmental variable.

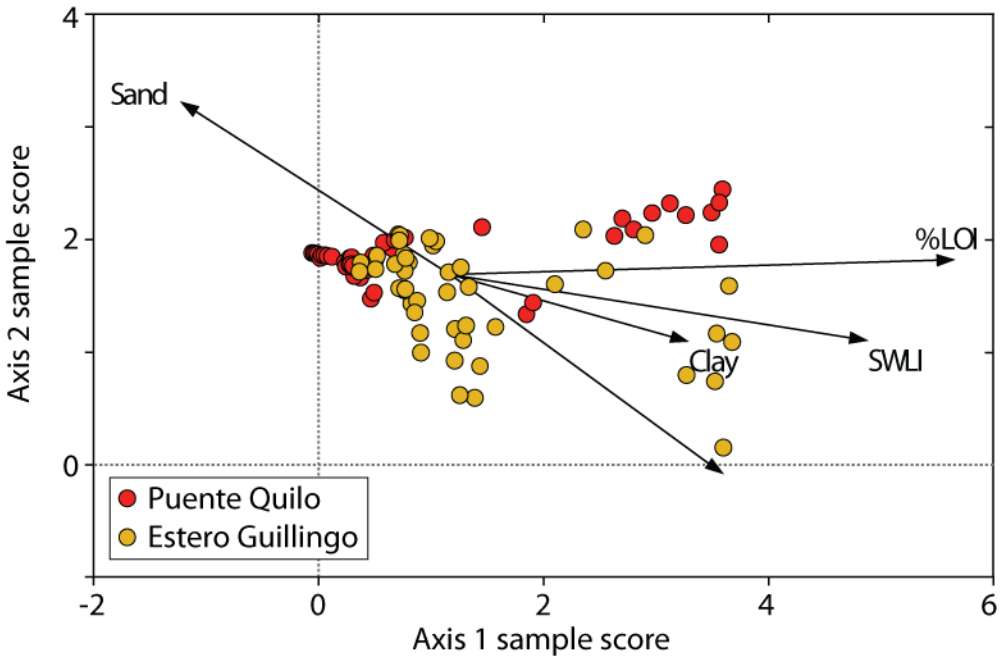

Figure 4.7: Detrended Canonical Correspondence Analysis biplot of samples and environmental variables from the *Chiloé* dataset. Each arrow points in the direction of the steepest increase in an environmental variable; samples can be perpendicularly projected onto each arrow to approximate their environmental variable value.

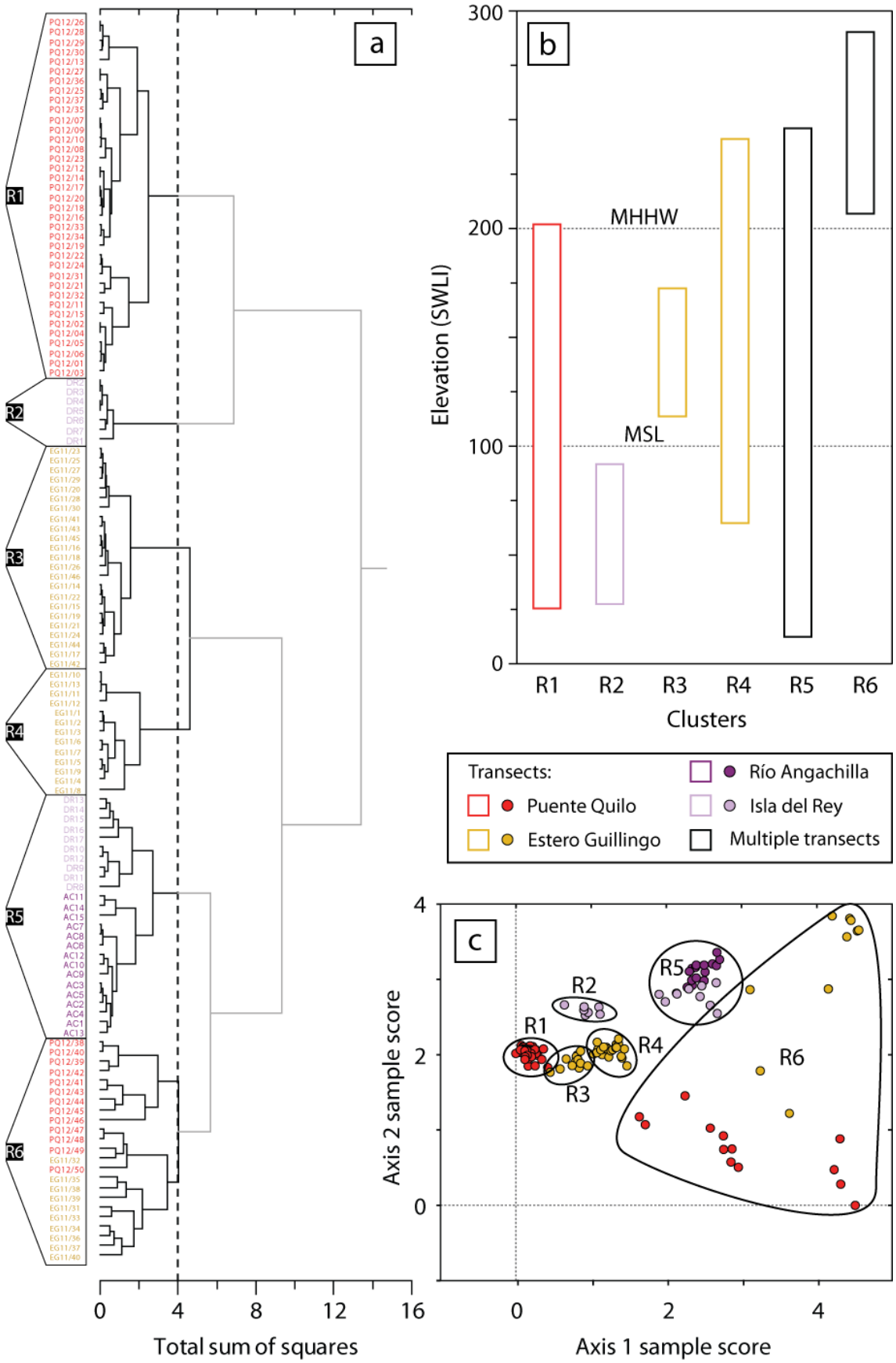

Figure 4.8: Multivariate analysis of the *Regional* modern diatom dataset. a. Unconstrained cluster analysis dendrogram (incremental sum of squares, Euclidean distance, un-weighted, no data transformation or standardisation). b. Elevation (SWLI) ranges of the clusters defined by cluster analysis. Coloured outlines indicate clusters that consist entirely of samples from a single site, black outlines indicate clusters incorporating samples from more than one transect. c. Detrended Correspondence Analysis sample plot. Ellipses surround clusters defined by cluster analysis.

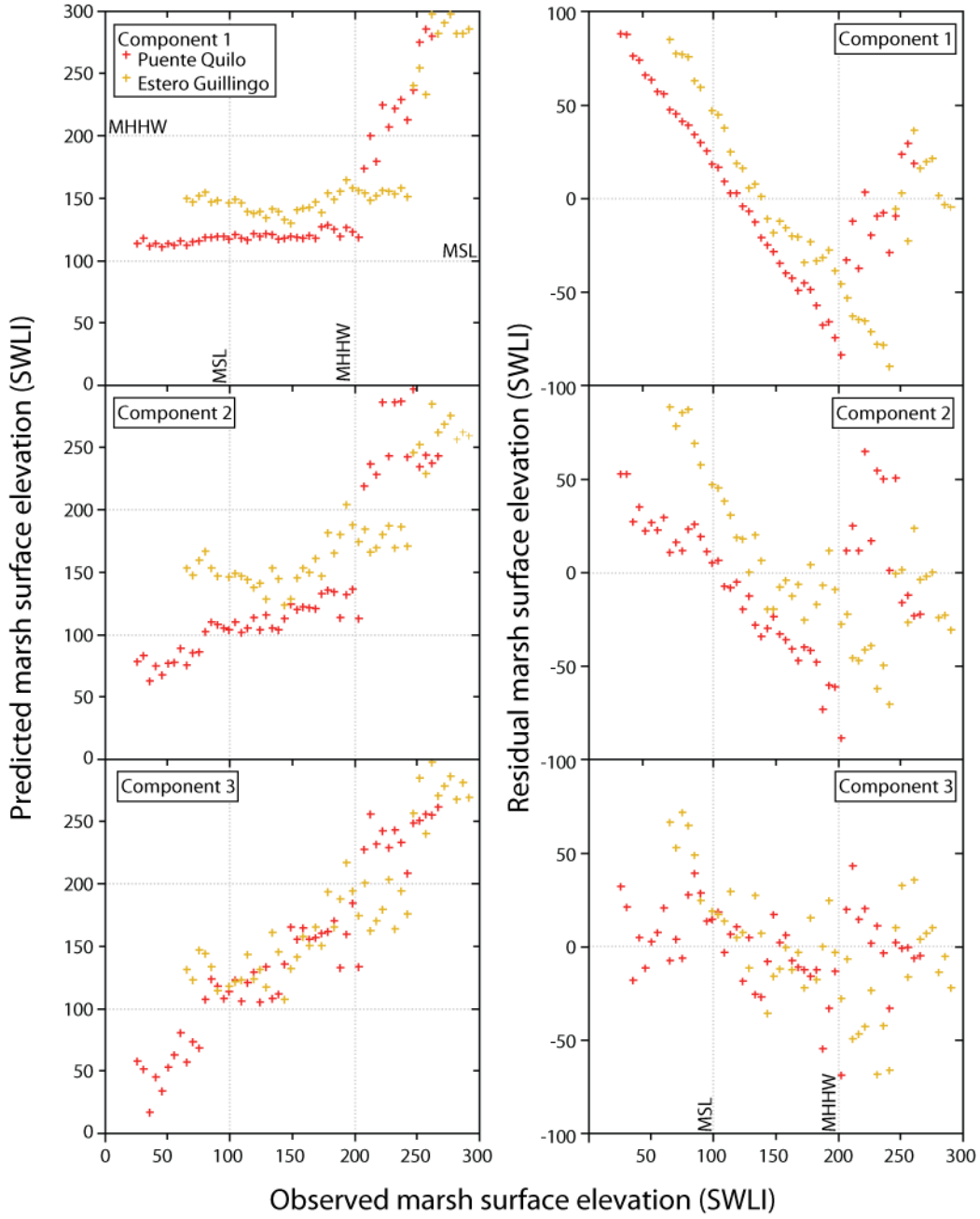

Figure 4.9: Observed vs. predicted (left hand side) and observed vs. residual (right hand side) plots for the first three components of the *Chiloé* transfer function model (96 samples from Puente Quilo and Estero Guillingo). Transfer function models are developed in C2 (Juggins, 2011) using WA-PLS regression (ter Braak and Juggins, 1993; ter Braak *et al*., 1993).

Transfer function model	Number of samples	WA-PLS component	R^2_{boot}	RMSEP (SWLI)	RSMEP as percentage of sampled range (%)
Chiloé	96	1	0.60	44.96	17.0
		2	0.72	39.05	14.8
		3	0.85	29.46	11.1
Regional	128	1	0.53	50.45	18.2
		2	0.67	44.18	15.9
		3	0.77	37.56	13.5

Table 4.3: Summary of WA-PLS transfer function model performance. RMSEP: Root Mean Square Error of Prediction. No species or environmental variable transformation is applied and bootstrapping (1000 permutations) is used for cross validation. I chose to employ the third component of the Regional model, incorporating all of the available samples from the four transects at Chiloé (Puente Quilo and Estero Guillingo) and Valdivia (Río Angachilla and Isla del Rey), as it provides a significant increase in performance over the first and second components. The Regional model allows a more appropriate assessment of reconstruction precision and a larger range of potential modern analogues than the local model.

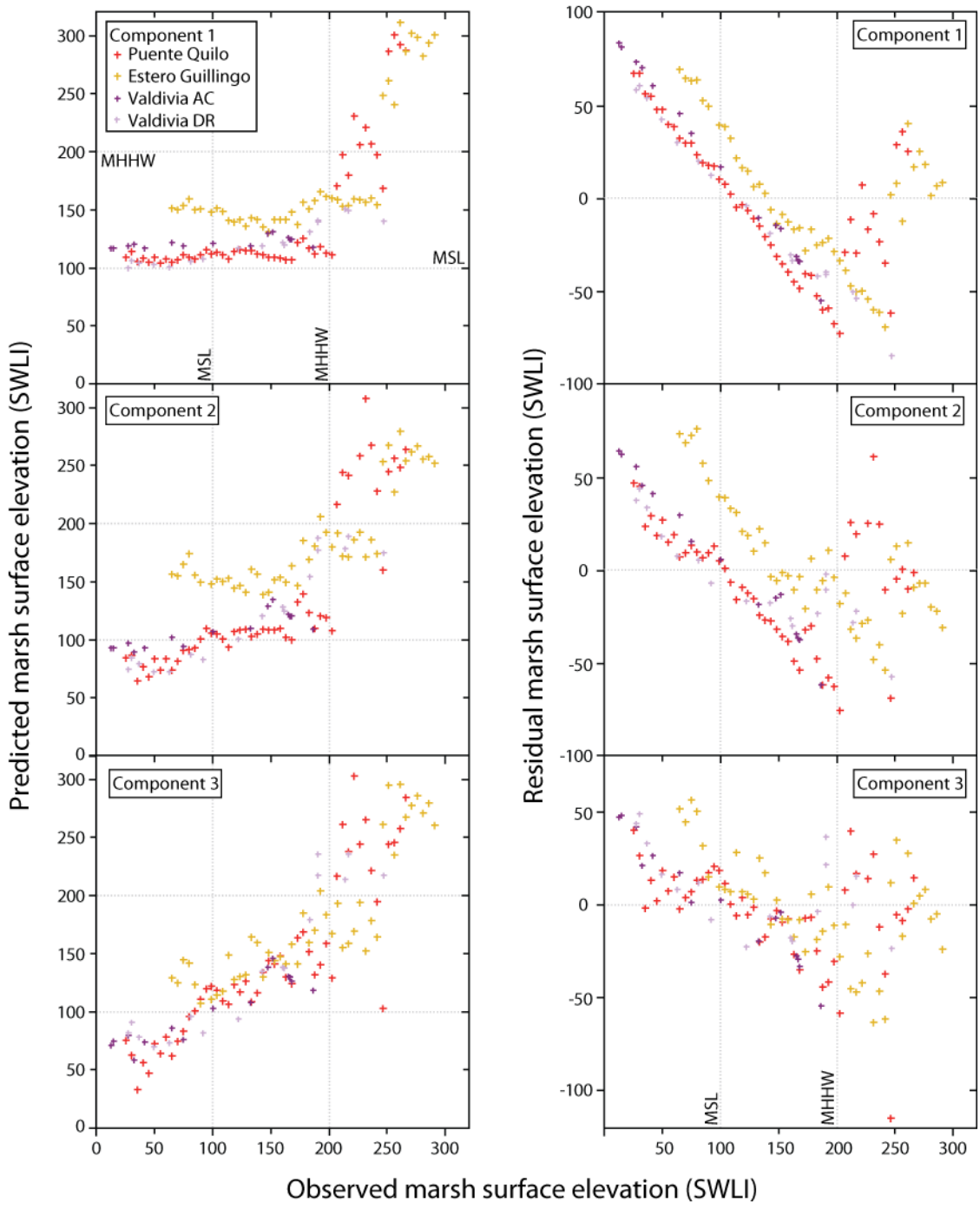

Figure 4.10: Observed vs. predicted (left hand side) and observed vs. residual (right hand side) plots for the first three components of the *Regional* transfer function model (128 samples from Puente Quilo, Estero Guillingo, Río Angachilla and Isla del Rey). Transfer function models are developed in C2 (Juggins, 2011) using WA-PLS regression (ter Braak and Juggins, 1993; ter Braak *et al.*, 1993).

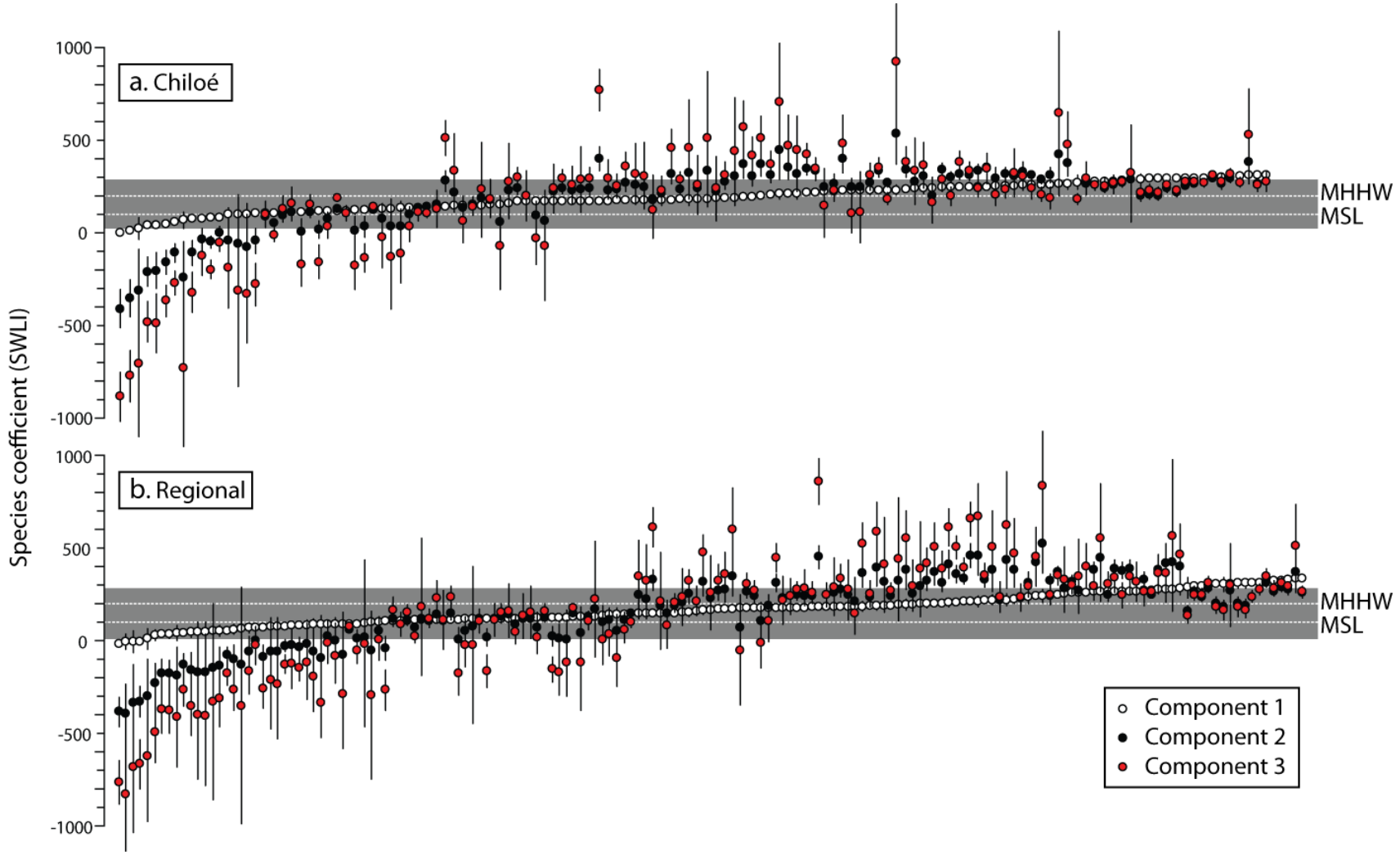

Figure 4.11: Comparison of first, second and third component species coefficients and bootstrapped errors (vertical bars) for all species included in a. the *Chiloé* model and b. the *Regional* model. Species coefficients are plotted relative to tidal levels, with the grey box indicating the sampled elevation range.

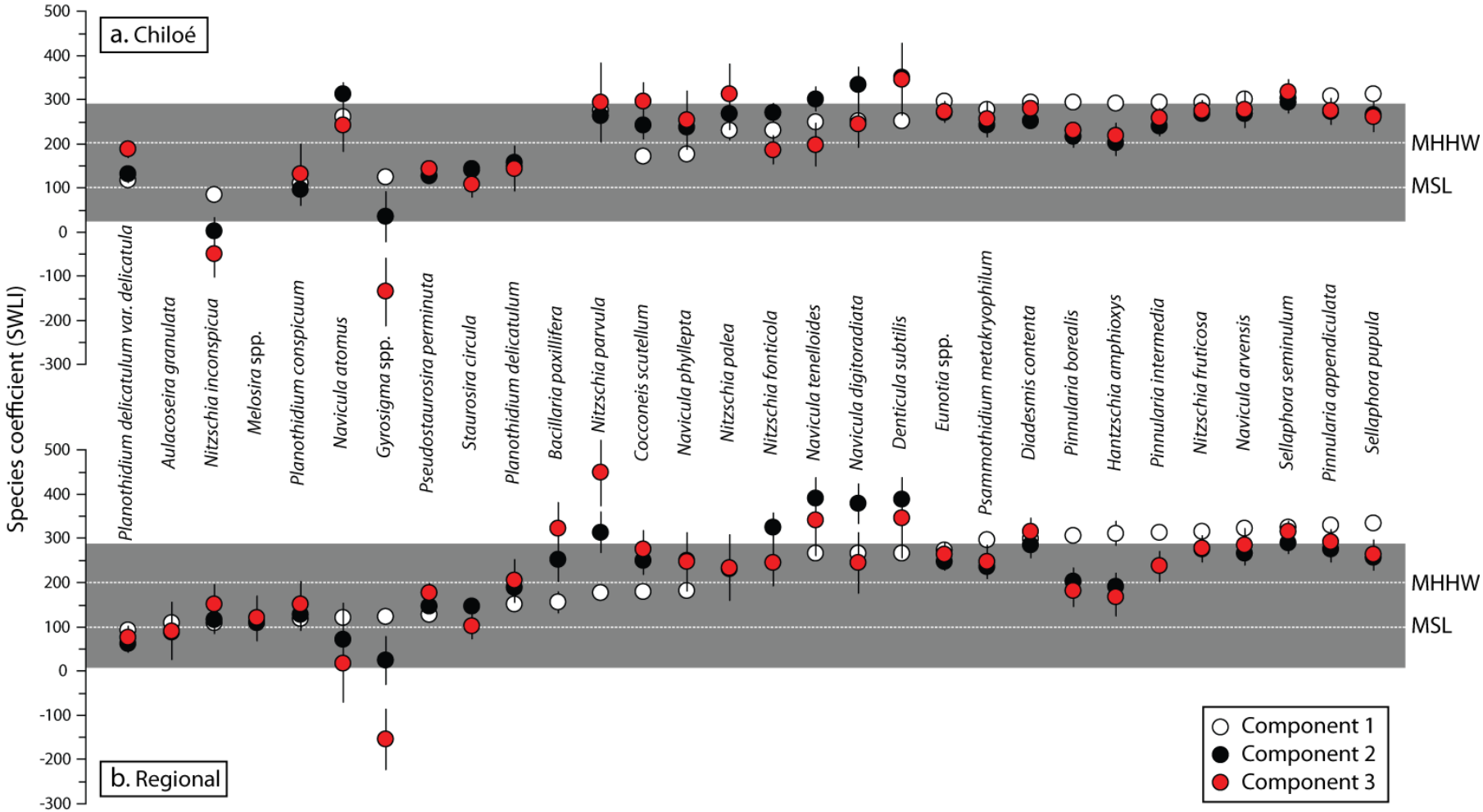

Figure 4.12: Comparison of first, second and third component species coefficients and bootstrapped errors (vertical bars) for species exceeding 10 % in a. the *Chiloé* model and b. the *Regional* model. Missing coefficients for the Chiloé plot indicate species not encountered in this training set. Species are ordered by the Regional model component 1 species coefficients. Species coefficients are plotted relative to tidal levels, the grey box indicates the sampled elevation range.

5. Reconstructing coseismic deformation: the 1960 and 2010 earthquakes: figures and tables

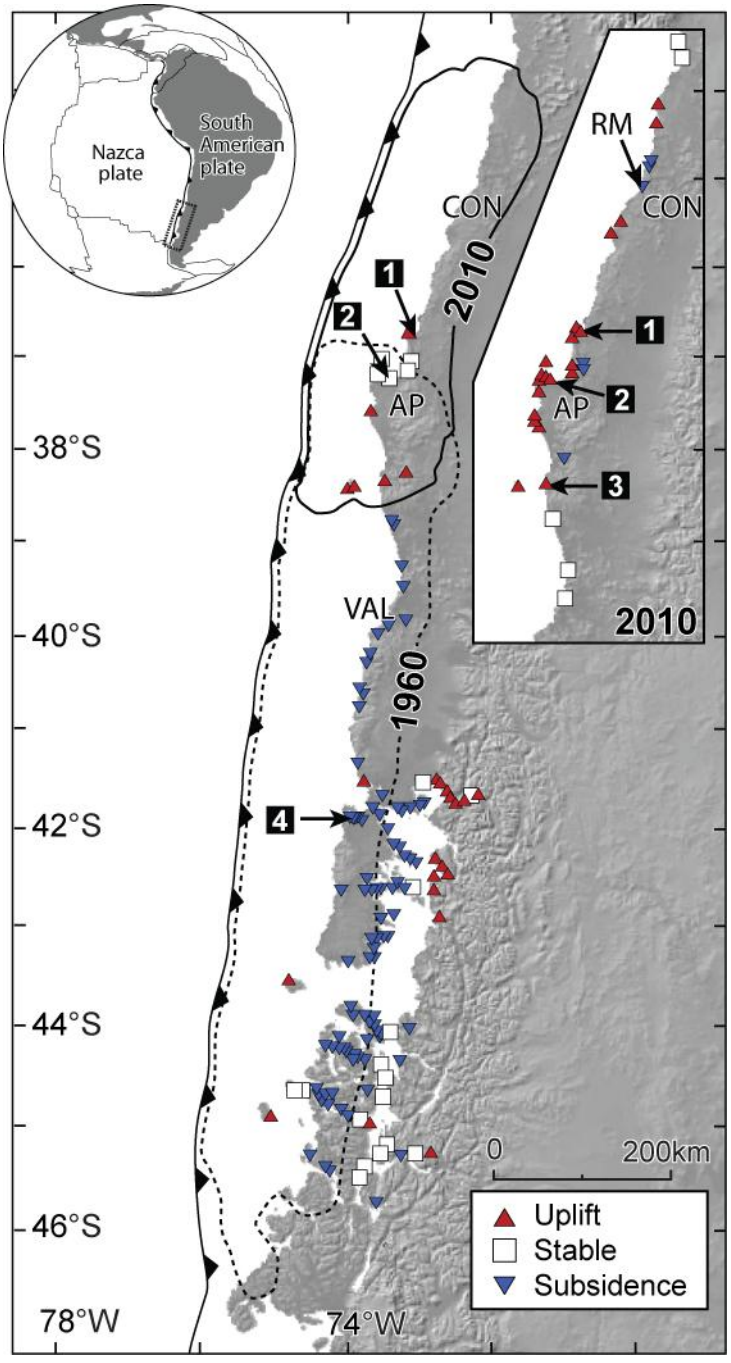

Figure 5.1: Earthquake rupture zones and vertical land level changes in 1960 (main figure, after Plafker and Savage, 1970) and 2010 (inset, after Moreno et *al*., 2012) and the location of the sites and places mentioned in the text. 1: Río Andalién, 2: Tubul, 3: Río Tirua, 4: Chucalen, RM: Río Mataquito, CON: Constitution, AP: Arauco Peninsula, VAL: Valdivia.

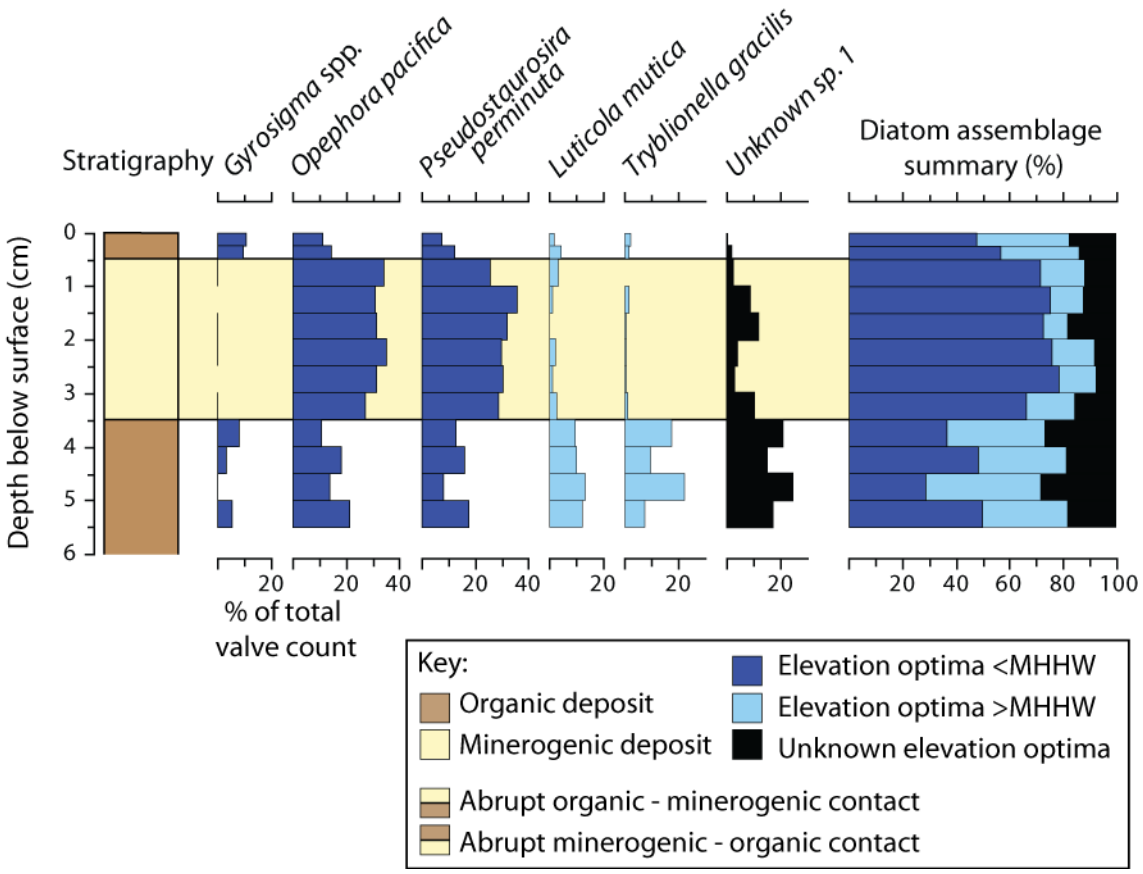

Figure 5.2: Río Andalién 2010. Fossil diatom assemblages (species exceeding 10% only) from the uppermost 6 cm of the sediment monolith. Assemblage summary based on modern species coefficients derived from the *Regional* WA-PLS transfer function model. Dr Emma Watcham counted all diatoms from Río Andalién as part of the *Sediment Signatures* project.

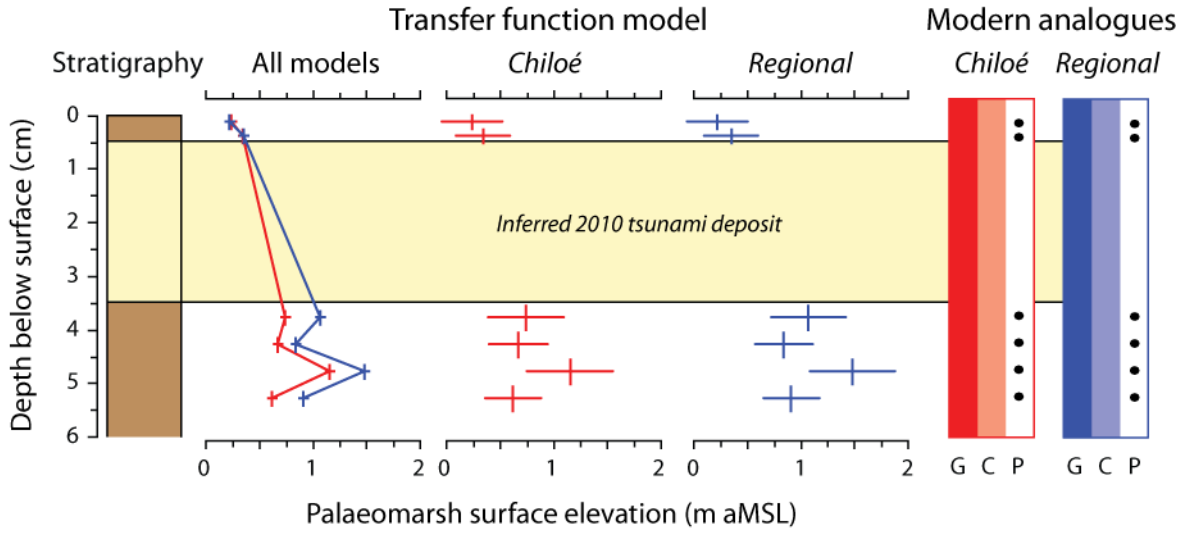

Figure 5.3: Río Andalién 2010. Palaeomarsh surface elevation reconstructions for the uppermost 6 cm of the sediment monolith using the *Chiloé* and *Regional* transfer function models. The graphs for the individual models show the sample specific standard errors. The modern analogue graphs on the right hand side summarise whether fossil samples have good (G), close (C) or poor (P) modern analogues in each model. I use the 5th percentile of the modern dissimilarity values as the threshold for a good modern analogue and the 20th percentile as the division between close and poor modern analogues.

Site	**Earthquake**	**Palaeomarsh surface elevation change (m ± 1σ)**	
		Chiloé	***Regional***
Río Andalién	2010	-0.43 ± 0.43	-0.75 ± 0.43
	1960	0.10 ± 0.40	0.11 ± 0.45
Tubul	2010	0.60 ± 0.53	0.64 ± 0.67
Río Tirua	1960	0.08 ± 0.60	-0.14 ± 0.72
Chucalen	1960	-1.15 ± 0.43	-1.09 ± 0.53

Table 5.1: Comparison of palaeomarsh surface elevation change estimates using the *Chiloé* and *Regional* transfer function models (elevation rise is positive, elevation fall is negative). All estimates are corrected for sedimentation. The lack of post-tsunami sedimentation prevents a 2010 estimate for Río Tirua; Chucalen lies over 300 km to the south of displacements in 2010.

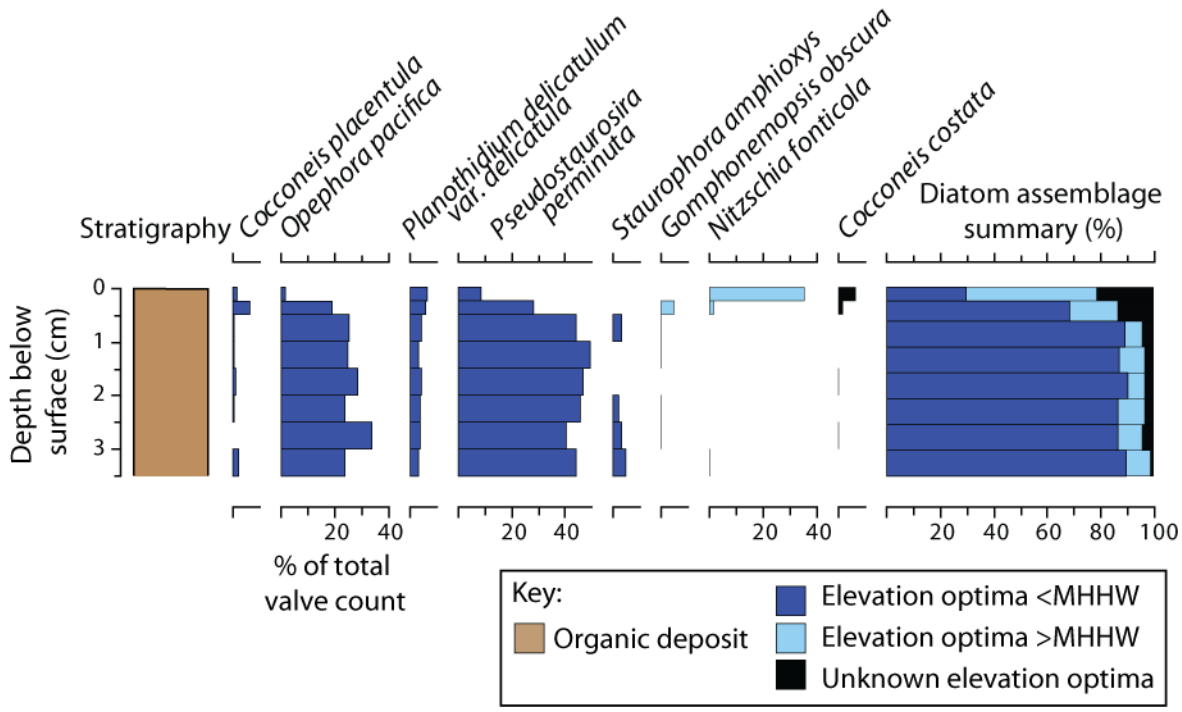

Figure 5.4: Tubul 2010. Fossil diatom assemblages (species exceeding 10% only) from the sediment monolith. Assemblage summary based on modern species coefficients derived from the *Regional* WA-PLS transfer function model. Dr Emma Watcham counted all diatoms from Tubul as part of the *Sediment Signatures* project.

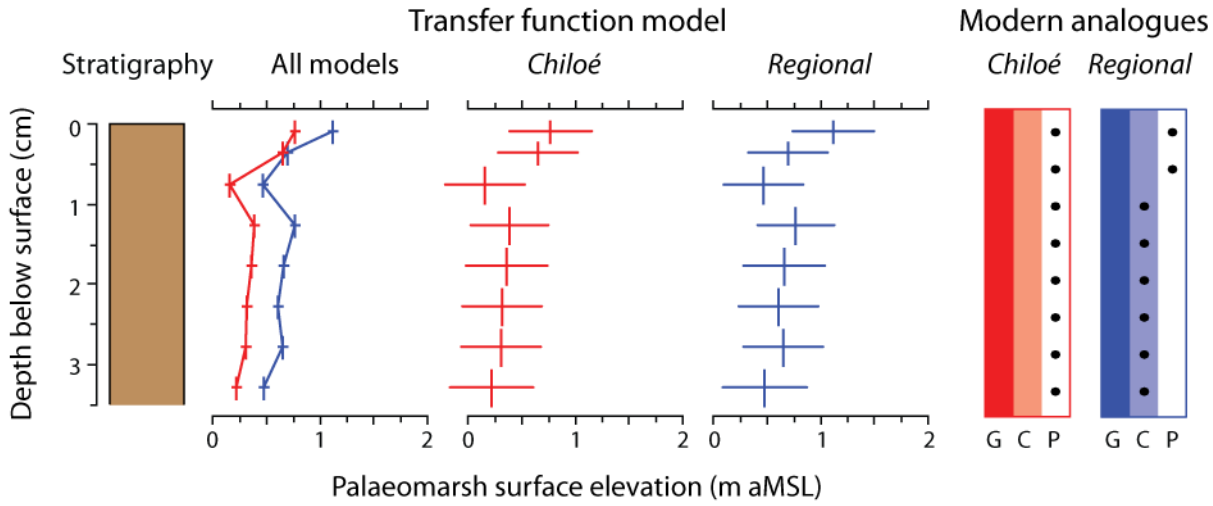

Figure 5.5: Tubul 2010. Palaeomarsh surface elevation reconstructions for the sediment monolith using the *Chiloé* and *Regional* transfer function models. The graphs for the individual models show the sample specific standard errors. The modern analogue graphs on the right hand side summarise whether fossil samples have good (G), close (C) or poor (P) modern analogues in each model. I use the 5th percentile of the modern dissimilarity values as the threshold for a good modern analogue and the 20th percentile as the division between close and poor modern analogues.

Site	Core ID	Sample depth (cm)	Cs-137 (mBq g^{-1})	Error (1σ) (mBq g^{-1})	Notes
Río Andalién	RA10/M1/2	20 – 21	4.50	1.88	Immediately beneath minerogenic layer
		26 – 27	0.87	0.73	Background level
Río Tirua	TR10/M1/1	38 – 39	8.13	1.24	Immediately beneath minerogenic layer
		44 – 45	0.87	0.73	Background level
Chucalen	CH11/M1/1	45 – 45.5	9.74	1.87	Immediately beneath minerogenic layer
		52 – 53	0.81	0.91	Background level

Table 5.2: Summary of caesium-137 concentrations in samples from the three sites with possible evidence for the 1960 earthquake and tsunami.

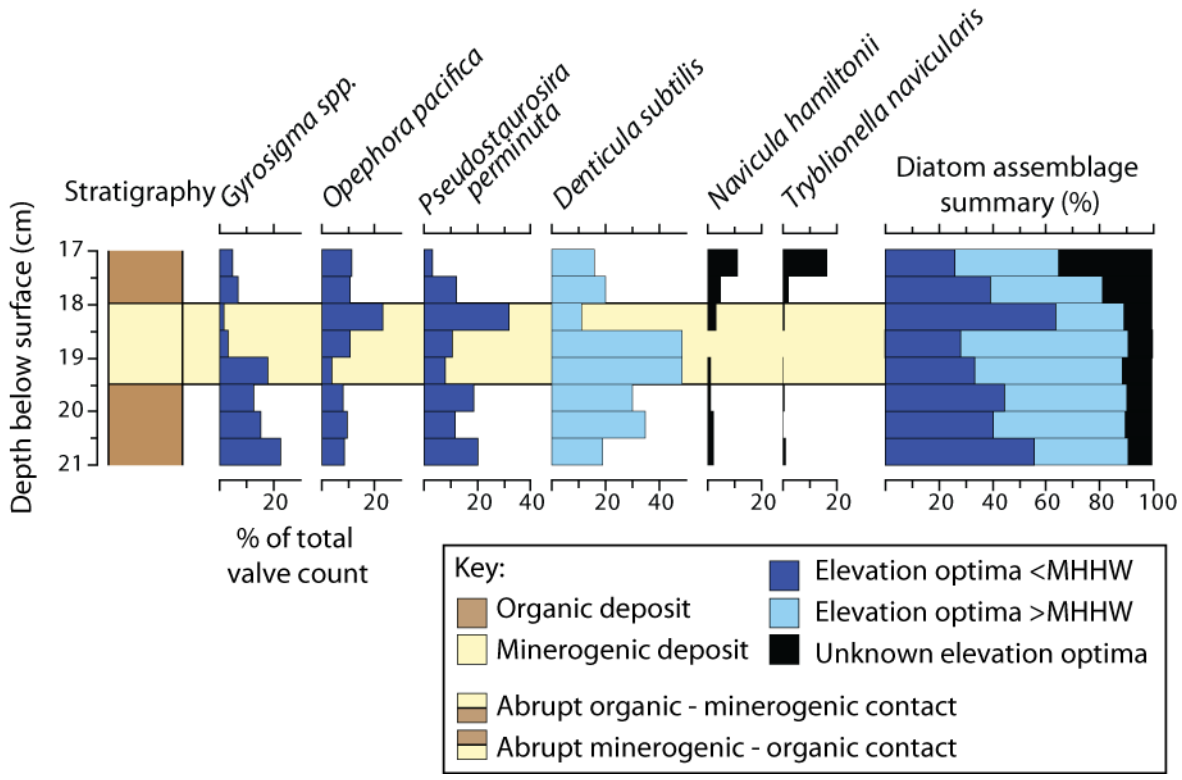

Figure 5.6: Río Andalién 1960. Fossil diatom assemblages (species exceeding 10% only) from the sediment monolith. Assemblage summary based on modern species coefficients derived from the *Regional* WA-PLS transfer function model. Dr Emma Watcham counted all diatoms from Río Andalién as part of the *Sediment Signatures* project.

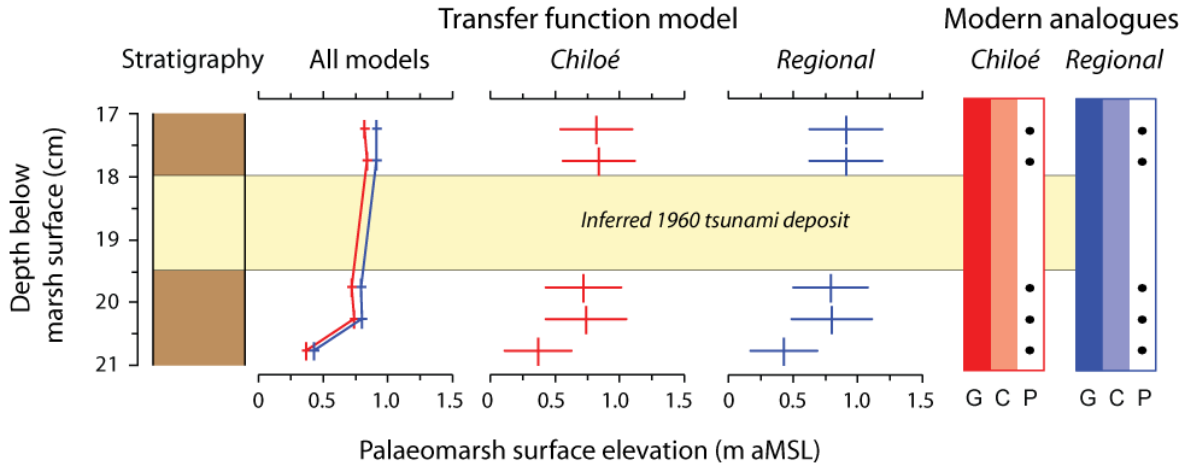

Figure 5.7: Río Andalién 1960. Palaeomarsh surface elevation reconstructions for the sediment monolith using the *Chiloé* and *Regional* transfer function models. The graphs for the individual models show the sample specific standard errors. The modern analogue graphs on the right hand side summarise whether fossil samples have good (G), close (C) or poor (P) modern analogues in each model. I use the 5th percentile of the modern dissimilarity values as the threshold for a good modern analogue and the 20th percentile as the division between close and poor modern analogues.

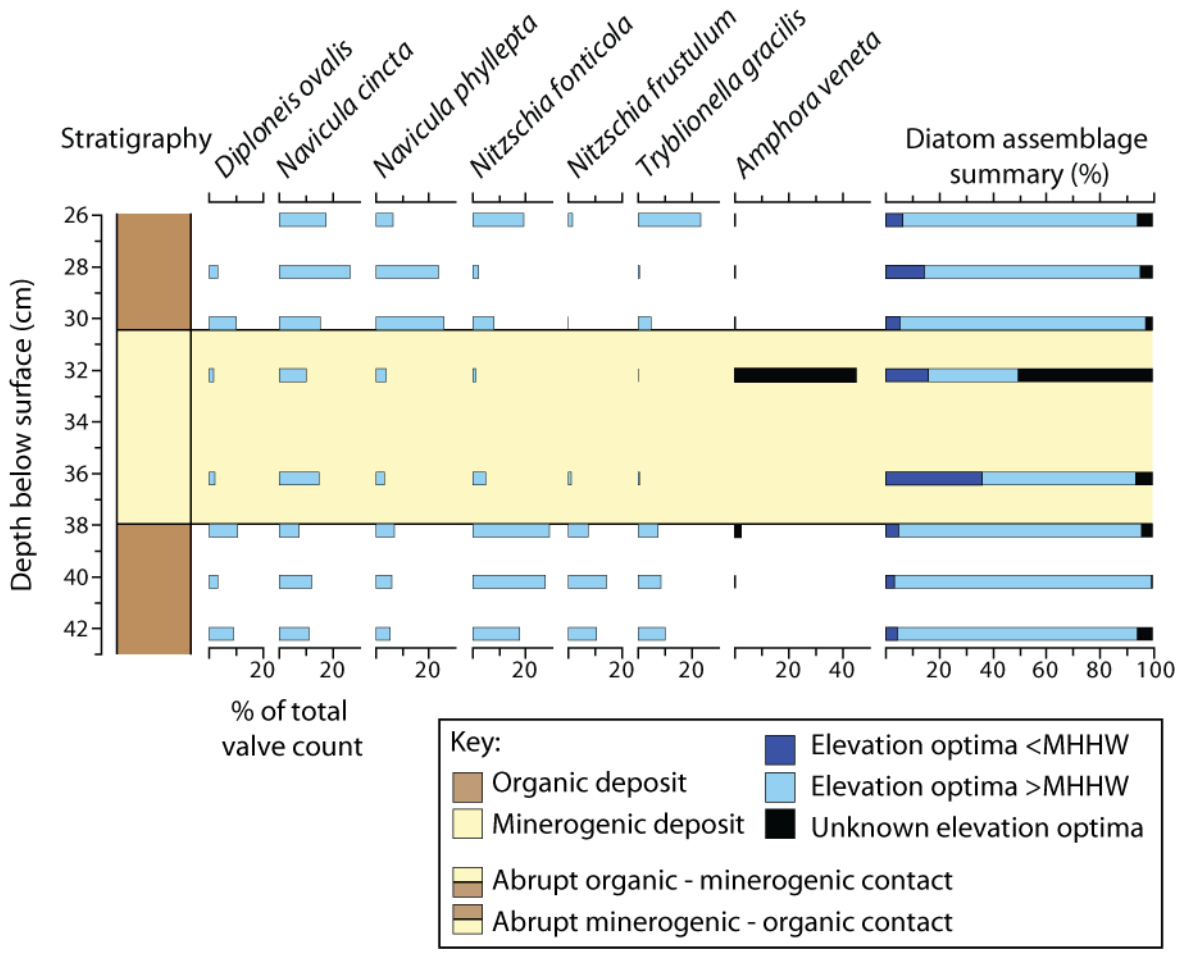

Figure 5.8: Tirua 1960. Fossil diatom assemblages (species exceeding 10% only) from the core. Assemblage summary based on modern species coefficients derived from the *Regional* WA-PLS transfer function model.

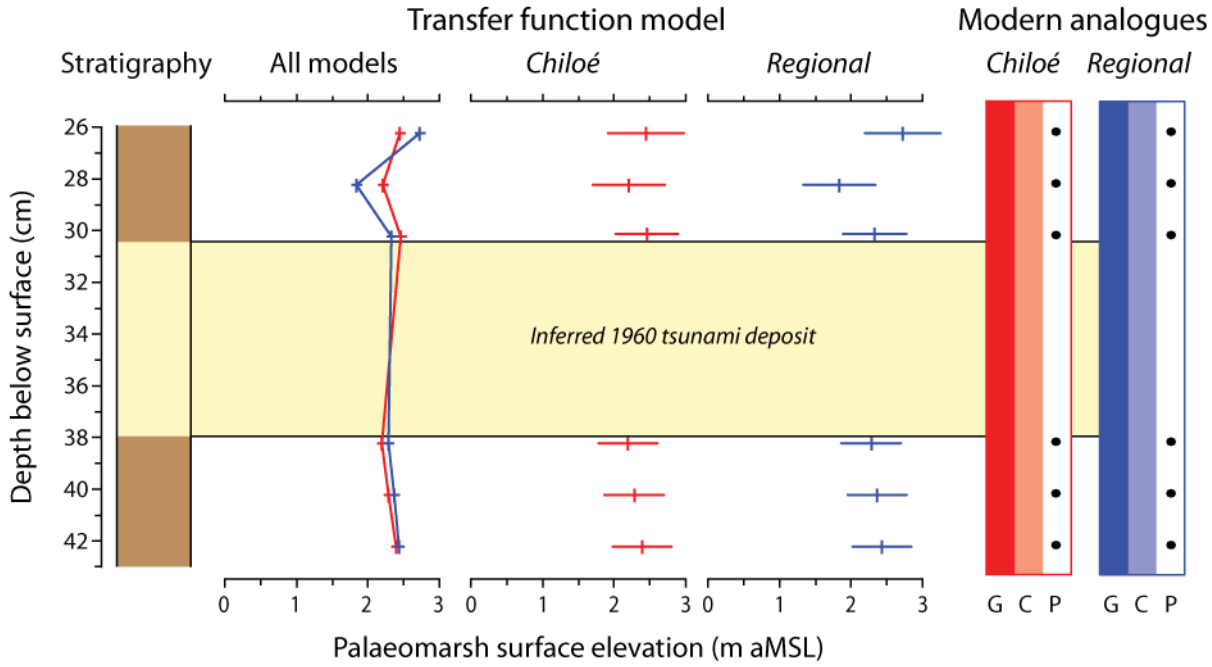

Figure 5.9: Tirua 1960. Palaeomarsh surface elevation reconstructions for the core using the *Chiloé* and *Regional* transfer function models. The graphs for the individual models show the sample specific standard errors. The modern analogue graphs on the right hand side summarise whether fossil samples have good (G), close (C) or poor (P) modern analogues in each model. I use the 5th percentile of the modern dissimilarity values as the threshold for a good modern analogue and the 20th percentile as the division between close and poor modern analogues.

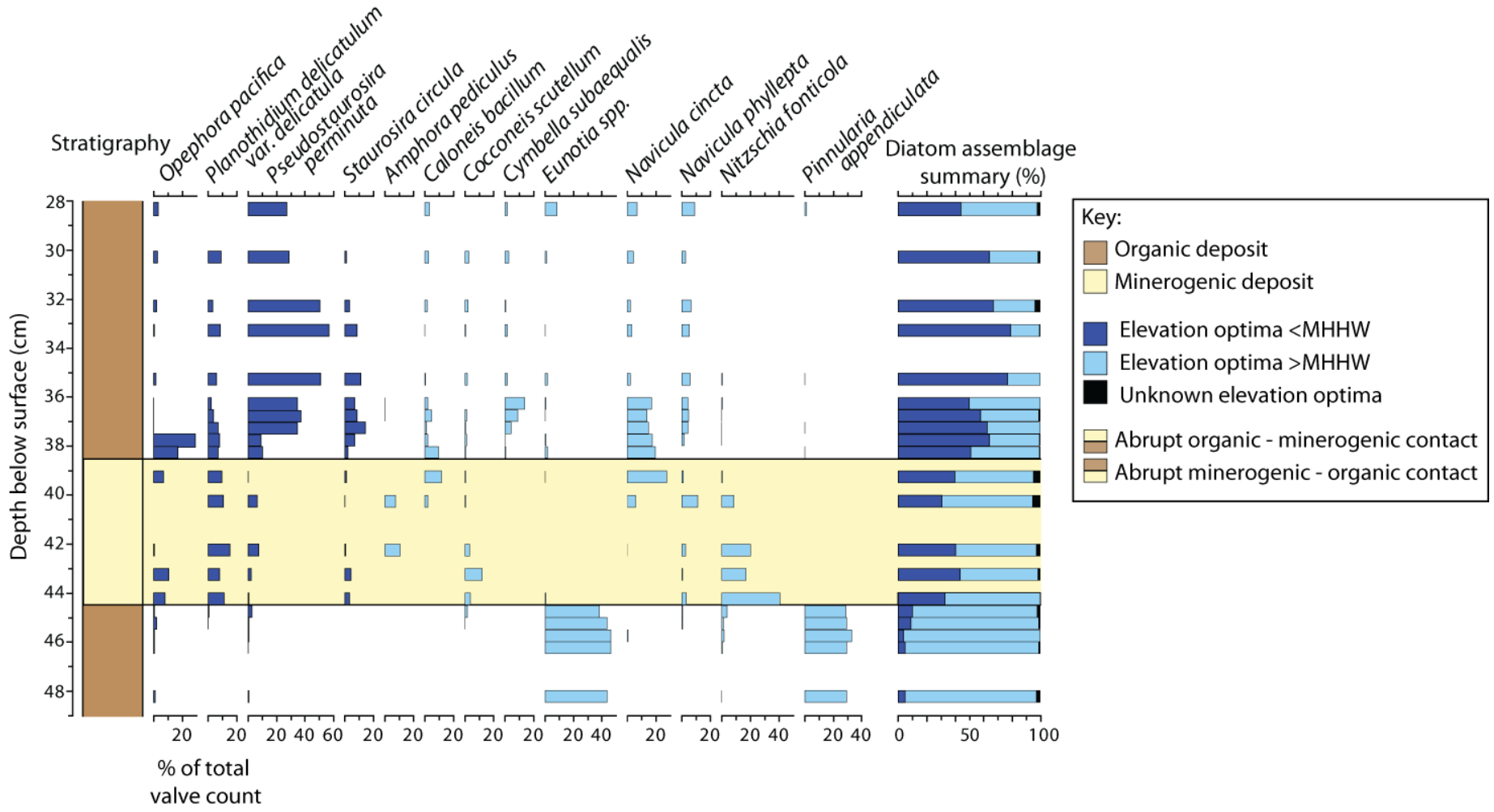

Figure 5.10: Chucalen 1960. Fossil diatom assemblages (species exceeding 10% only) from the sediment monolith. Assemblage summary based on modern species coefficients derived from the *Regional* WA-PLS transfer function model.

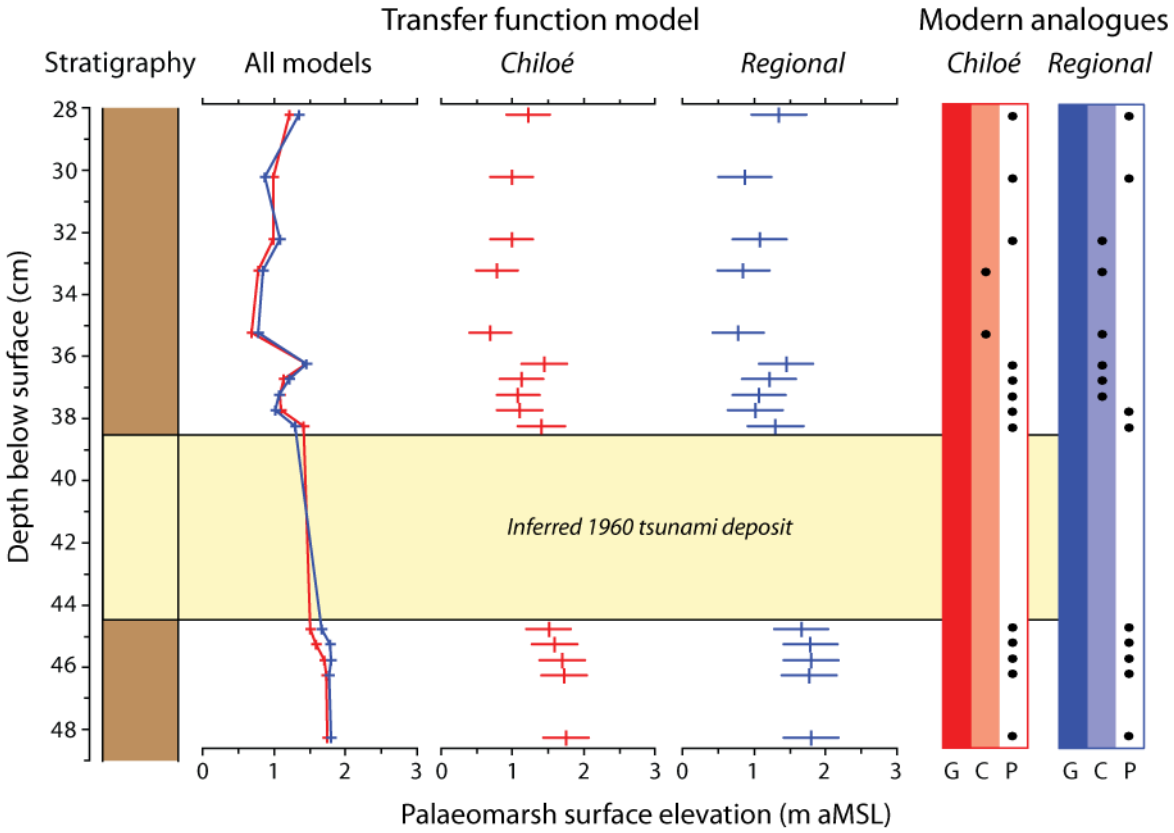

Figure 5.11: Chucalen 1960. Palaeomarsh surface elevation reconstructions for the sediment monolith using the *Chiloé* and *Regional* transfer function models. The graphs for the individual models show the sample specific standard errors. The modern analogue graphs on the right hand side summarise whether fossil samples have good (G), close (C) or poor (P) modern analogues in each model. I use the 5th percentile of the modern dissimilarity values as the threshold for a good modern analogue and the 20th percentile as the division between close and poor modern analogues.

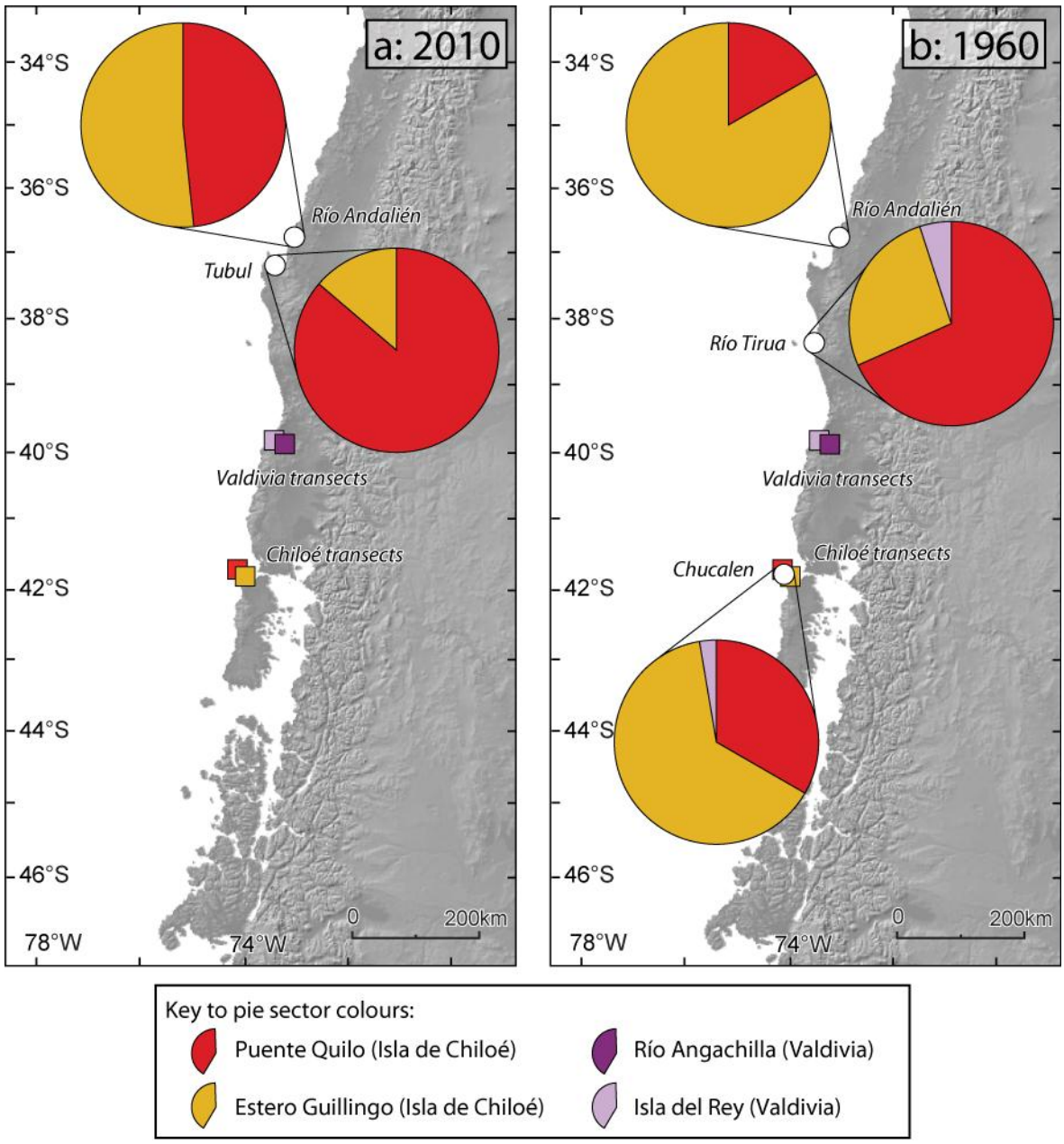

Figure 5.12: Map of south central Chile with pie charts representing the location of the 10 closest modern analogues for pre- and post-tsunami samples, a. relating to the 2010 earthquake at Río Andalién (6 samples) and Tubul (8 samples) and b. relating to the 1960 earthquake at Río Andalién (6 samples), Río Tirua (6 samples) and Chucalen (16 samples).

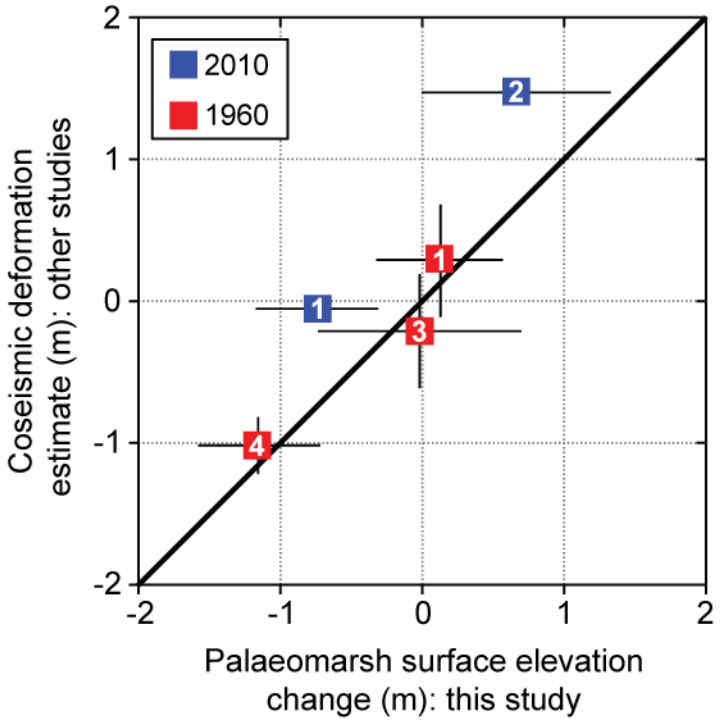

Figure 5.13: Comparison of transfer function derived estimates of palaeomarsh surface elevation change with independent estimates of coseismic deformation for 1960 and 2010 at Río Mataquito (1), Tubul (2), Río Tirua (3) and Chucalen (4). Diagonal line is the 1:1 line, not a best-fit regression line. For 1960 I compare my estimates with Plafker and Savage's (1970) sampling locations 1, 9 and 45 and for 2010 I compare with the continuous GPS station at Concepción (Vigny *et al*., 2011) and benchmark relevelling at Tubul (Melnick *et al*., 2012a).

Site	Earthquake	Palaeomarsh surface elevation rise (m ± 1σ)	Published coseismic uplift (m ± 1σ)	Reference
Río Andalién	2010	-0.75 ± 0.43	-0.035 ± 0.009	Vigny *et al*. (2011)
	1960	0.11 ± 0.45	0.30 ± 0.40	Plafker and Savage (1970)
Tubul	2010	0.64 ± 0.67	1.49 ± 0.07	Melnick *et al*. (2012)
Río Tirua	1960	-0.14 ± 0.72	-0.20 ± 0.40	Plafker and Savage (1970)
Chucalen	1960	-1.15 ± 0.43	-1.00 ± 0.20	Plafker and Savage (1970)

Table 5.3: Comparison of transfer function palaeomarsh surface elevation change reconstructions with published estimates of coseismic deformation during the 1960 and 2010 earthquakes. See table 5.1 for comparison of all transfer function model reconstructions. At Tubul, the absence of sand layers to guide sampling prevents a reconstruction for 1960. The lack of post-tsunami sedimentation prevents an estimate of 2010 deformation at Río Tirua. Chucalen lies over 300 km to the south of the displacements in 2010.

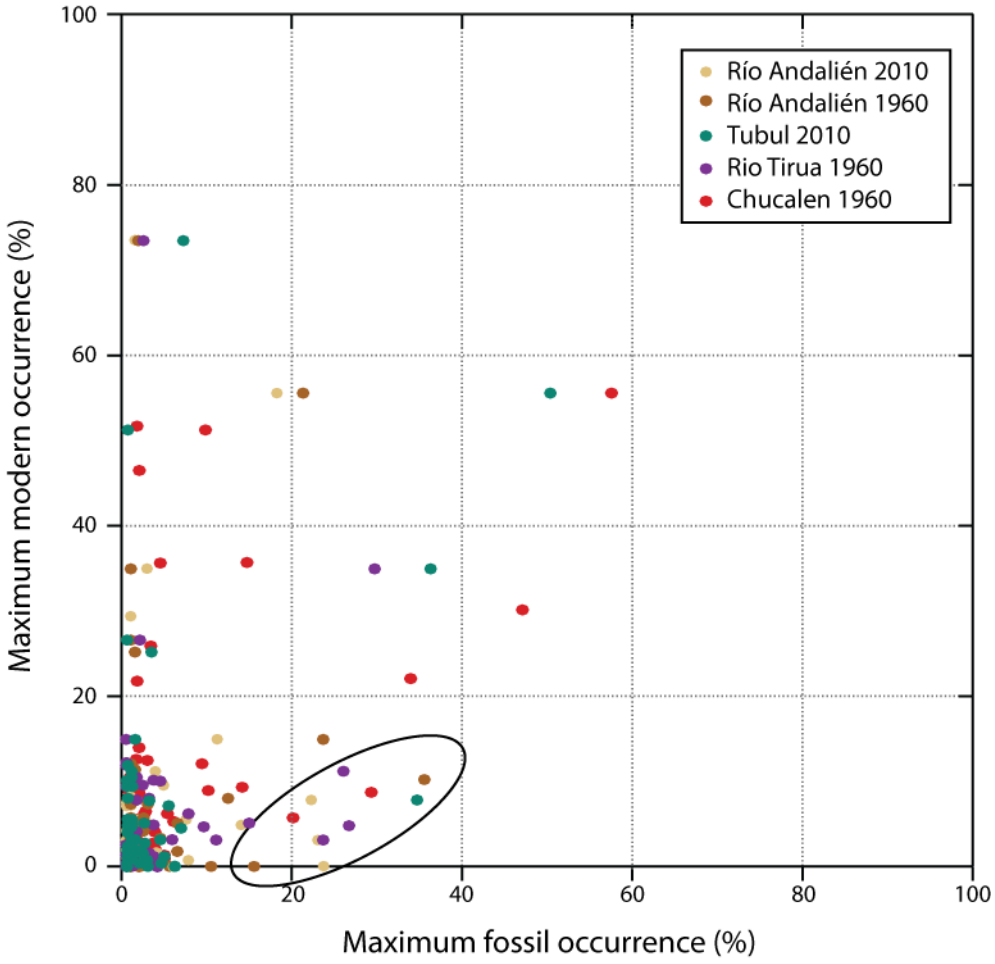

Figure 5.14: Scatter plot of maximum modern against maximum fossil abundances of all species occurring at the 2010 and 1960 sites. The black ellipse highlights species that further modern samples need to locate to ensure reconstructions fulfil statistical criteria.

6. Late Holocene records of earthquake occurrence: figures and tables

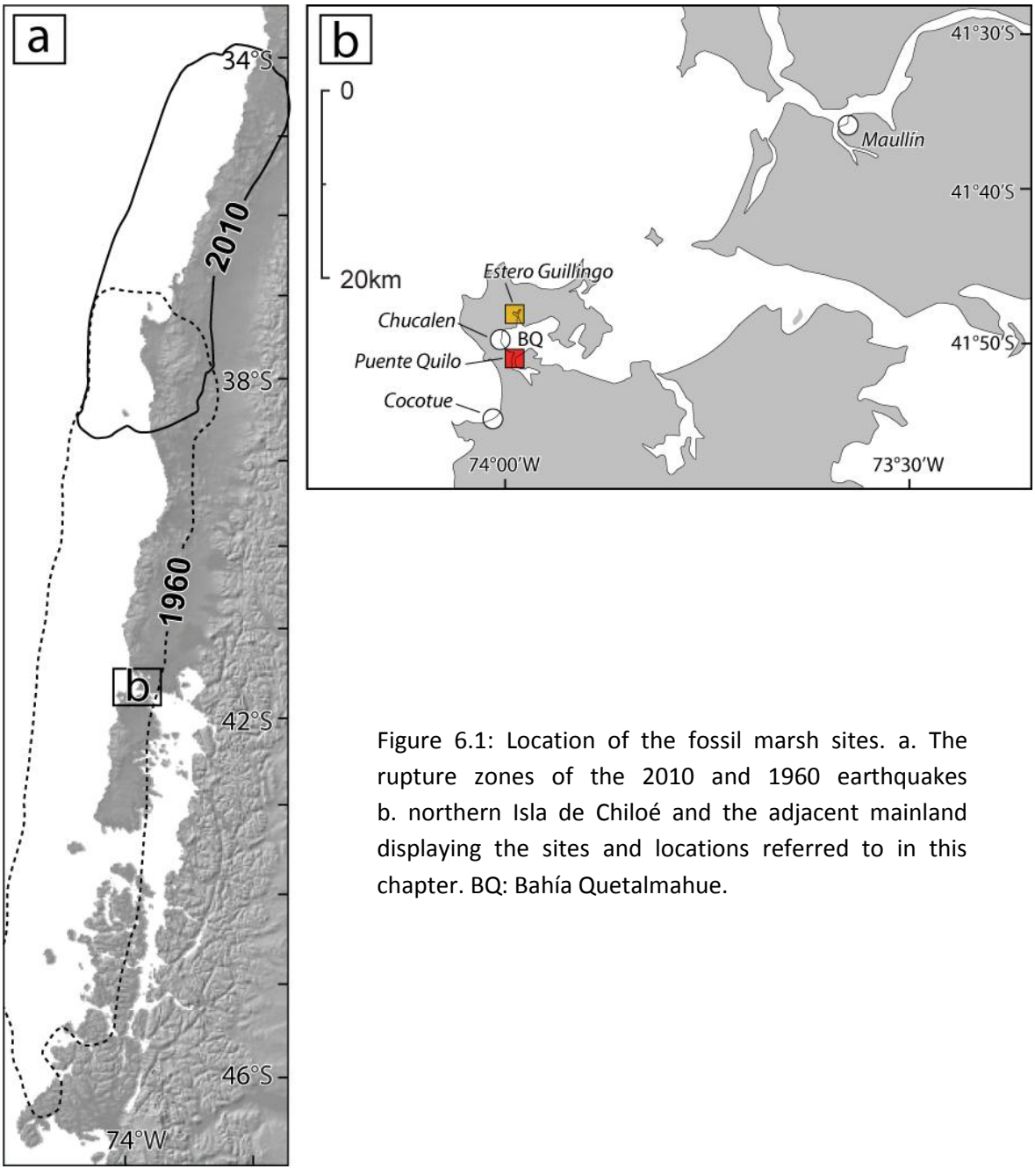

Figure 6.1: Location of the fossil marsh sites. a. The rupture zones of the 2010 and 1960 earthquakes b. northern Isla de Chiloé and the adjacent mainland displaying the sites and locations referred to in this chapter. BQ: Bahía Quetalmahue.

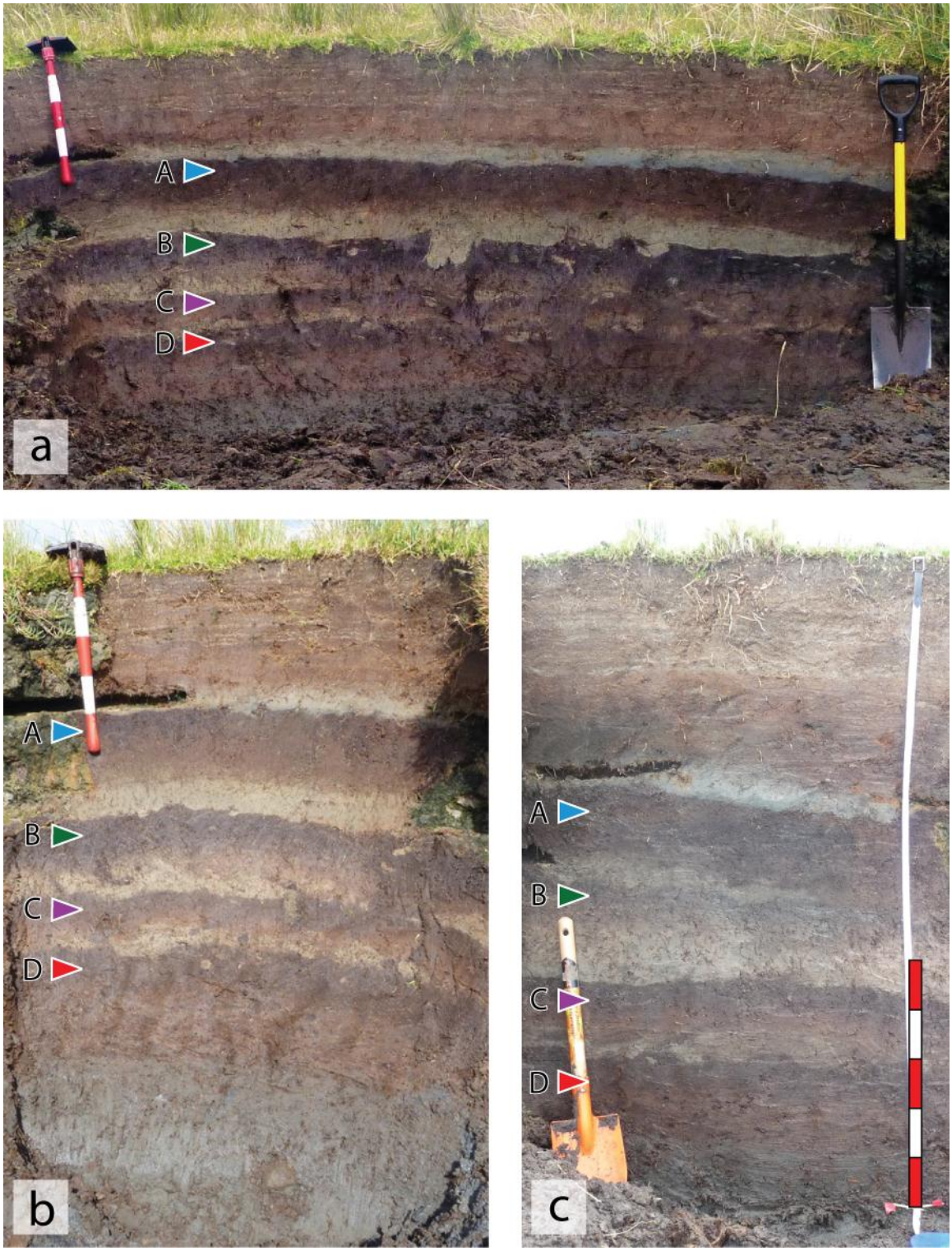

Figure 6.2: Photographs of selected cleaned marsh front exposures at Chucalen. Labels A to D denote the buried soils. Scale bar divisions are 10cm in length. Photograph (a) courtesy of Rob Wesson.

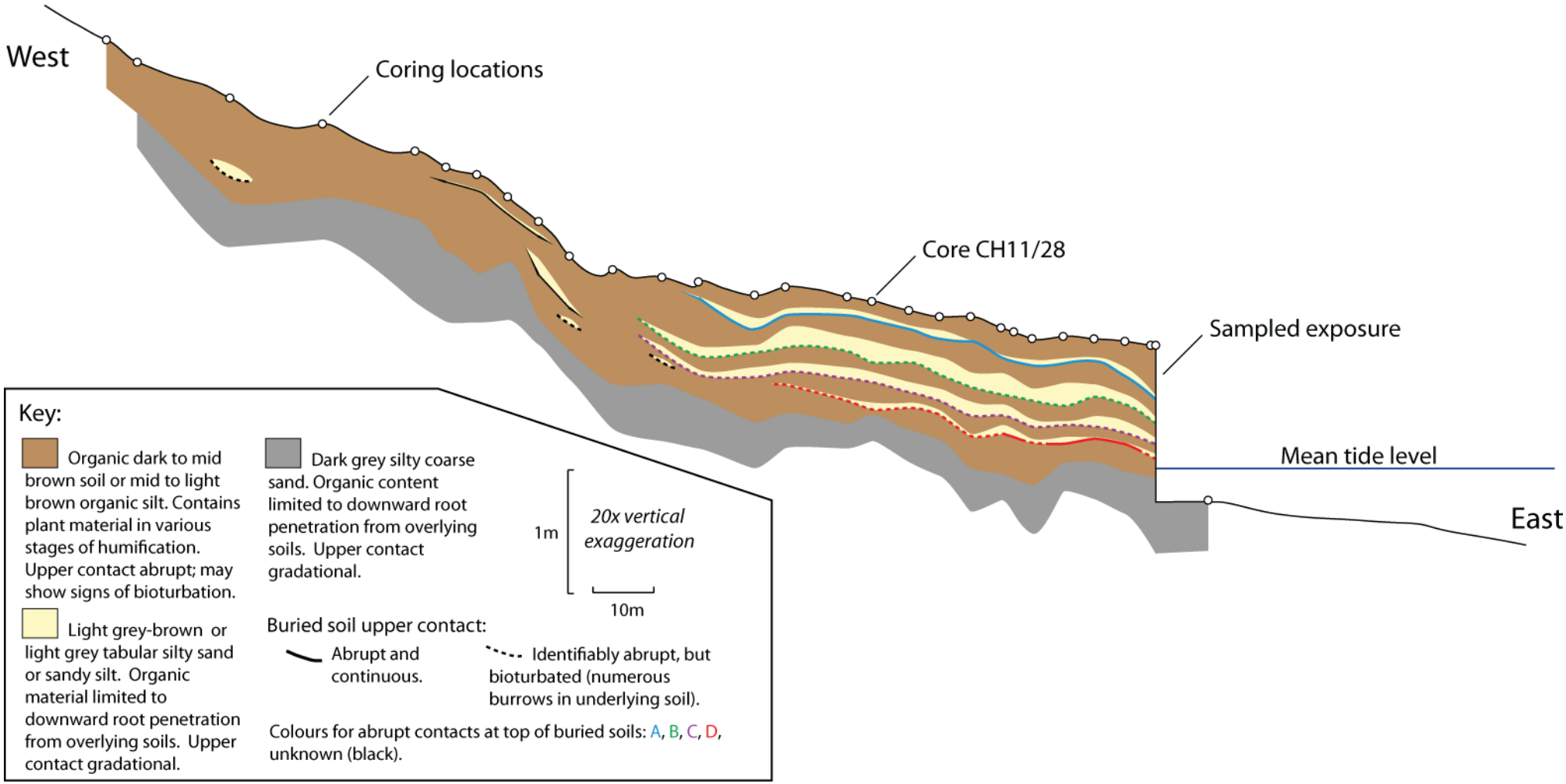

Figure 6.3: Stratigraphy of the coring transect at Chucalen.

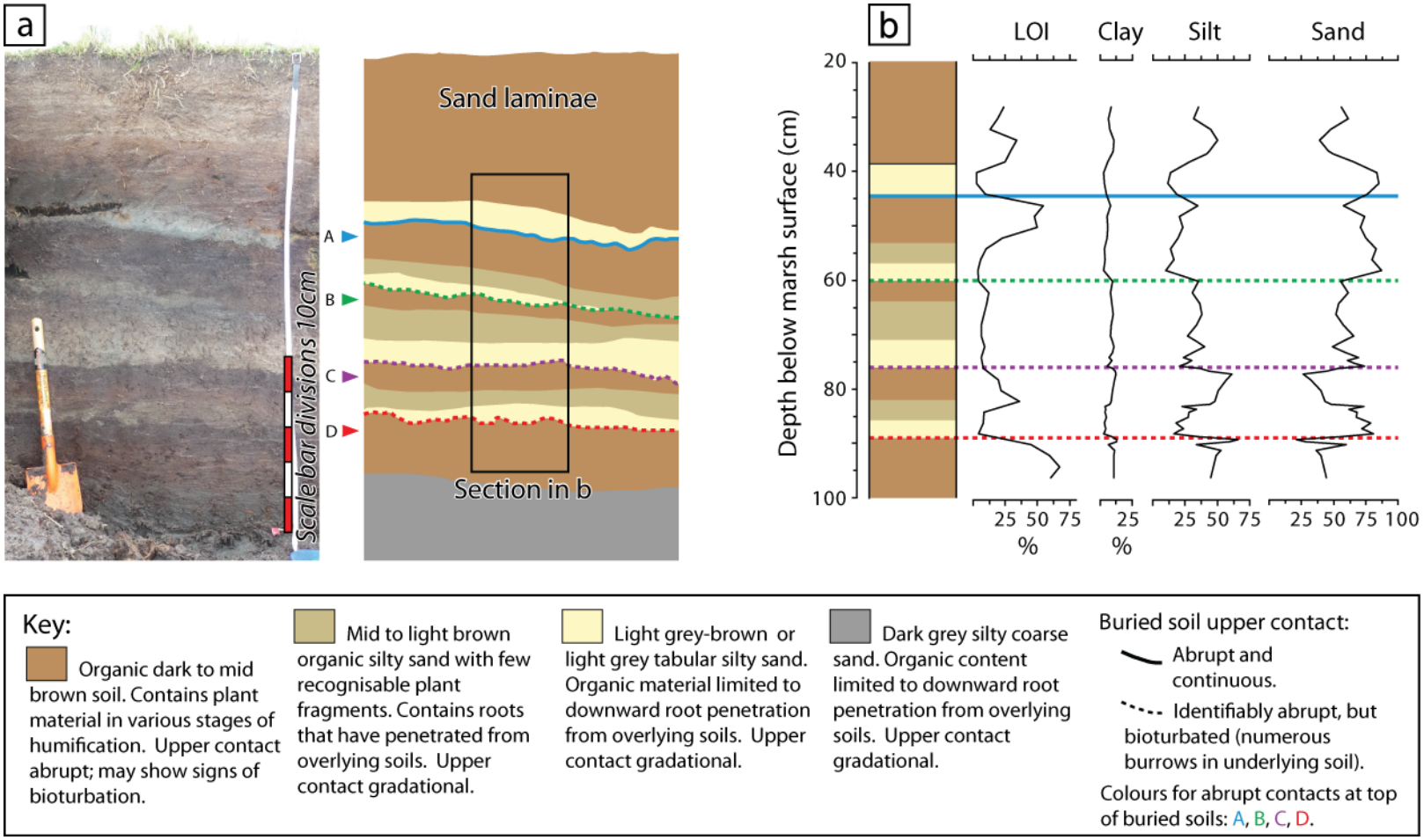

Figure 6.4: Stratigraphy of the sampled marsh front exposure at Chucalen. a. photograph and sketch of the sampled exposure, b. loss on ignition (LOI) and particle size distributions.

Figure 6.5: Photographs displaying the variability in the form of the upper boundary of the buried soils. a. tree stump rooted in buried soil A (photograph courtesy of Rob Wesson, scale bar divisions 10cm), b. minerogenic inclusions in the upper margin of soil C in a recovered monolith (ruler divisions in centimetres).

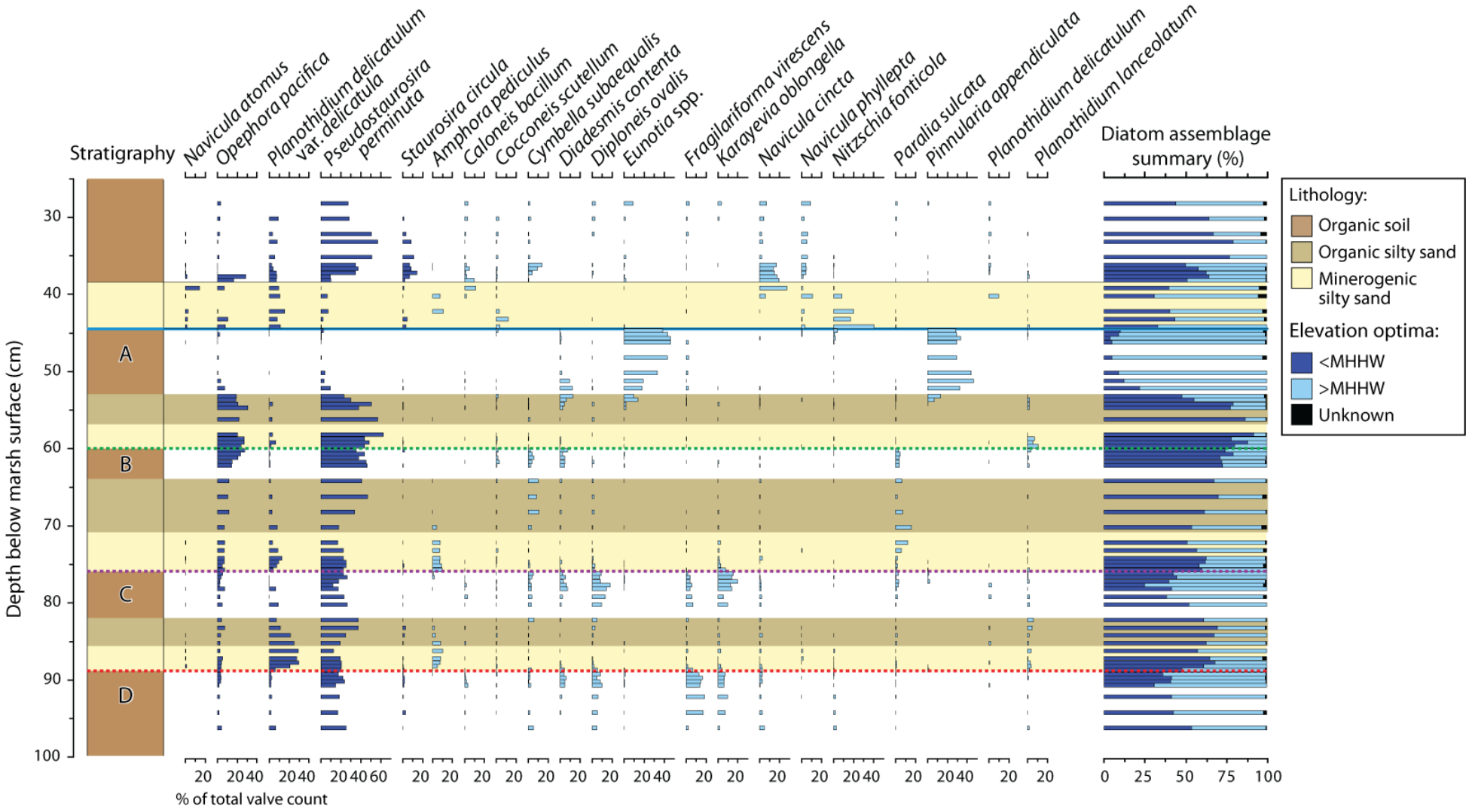

Figure 6.6: Caption on following page

Figure 6.6 (previous page): Summary of diatom assemblages from the Chucalen marsh front exposure (species exceeding 10 %). Labels A to D denote the buried soils. Species classified as sub- or supra-MHHW based on modern species coefficients derived from the *Regional* WA-PLS transfer function model. Figure 5.10 also shows levels above 48.5 cm.

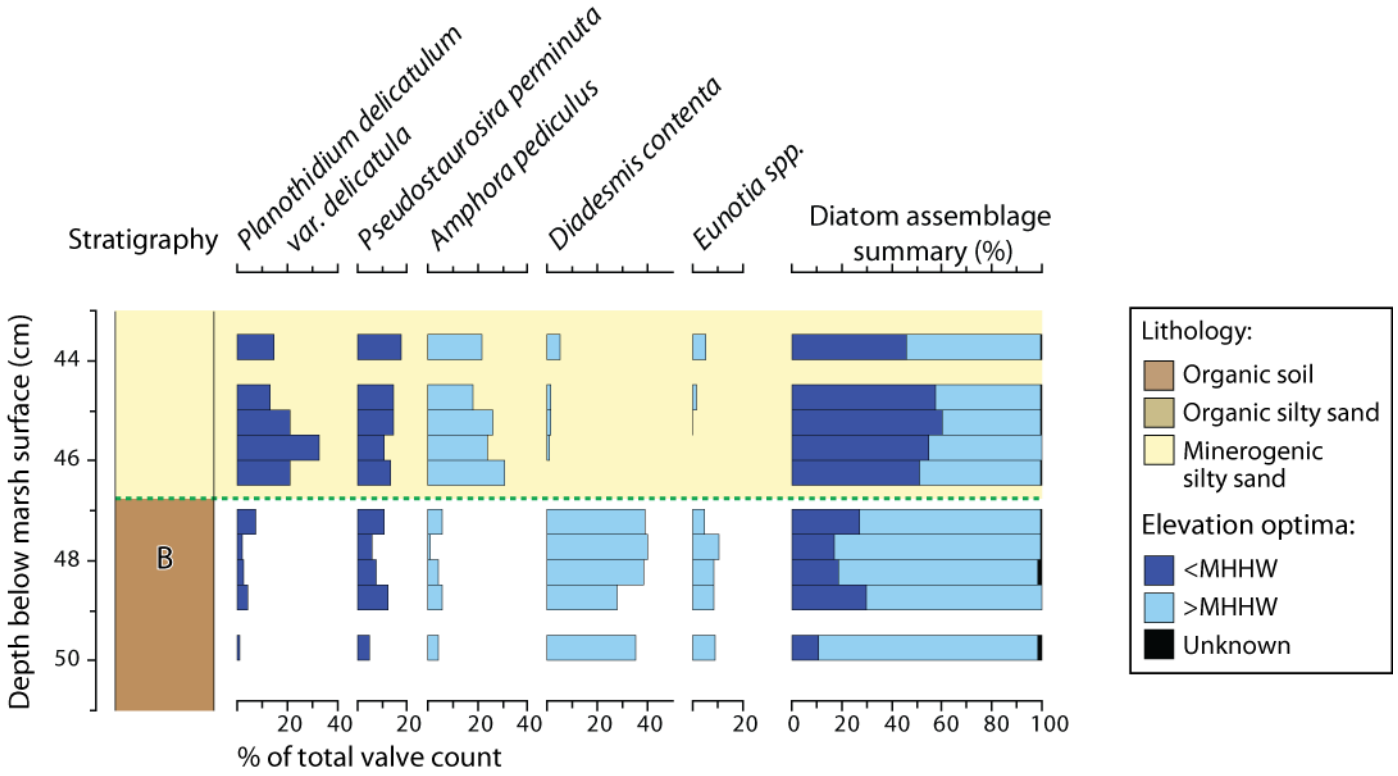

Figure 6.7: Summary of diatom assemblages from the upper contact of buried soil B in core CH11/28 at Chucalen (species exceeding 10 %). Species classified as sub- or supra-MHHW based on modern species coefficients derived from the *Regional* WA-PLS transfer function model.

Lab code	Sample code	Depth (cm)	Radiocarbon age (years BP ± 1σ)	$F^{14}C \pm 1\sigma$	Calibrated age ranges (2σ years AD)		
					Minimum	Maximum	Probability (%)
SUERC-39263	CH11/R1	29 - 29.5	modern [1]	1.0646 ± 0.0065	2004	2006	
SUERC-39264	CH11/R2	32 - 32.5	modern [2]	1.2056 ± 0.0076	1960*	1960*	31.7
					1963*	1963*	1.2
					1984	1988	62.5
SUERC-39265	CH11/R3	35 - 35.5	modern [2]	1.4537 ± 0.0092	1963*	1964*	6.5
					1972	1973	88.9
SUERC-39266	CH11/R4	38 - 38.5	modern [2]	1.5337 ± 0.0097	1964	1964	4.1
					1968	1970	91.3
SUERC-39269	CH11/R5	45 - 45.5	modern [2]	1.0159 ± 0.0064	1954	1958	95.4
SUERC-41189	CH11/R6	49 - 49.5	modern [2]	1.0964 ± 0.0048	1958	1958	2.0
					1997	>2001	93.4
SUERC-41190	CH11/R7	52 - 53	234 ± 35 [3]		1636	1705	30.4
					1721	1810	60.3
					1837	1856	0.9
					1867	1879	1.3
					1926	1953	2.5
SUERC-43050	CH11/R8	60 - 61	modern [3]	1.1042 ± 0.0052	1958	1959	2.6
					1996	2000	92.8
SUERC-43051	CH11/R9	63 - 64	285 ± 38 [3]		1505	1589	25.5
					1616	1678	45.5
					1734	1800	24.4
SUERC-43052	CH11/R10	66 - 67	427 ± 38 [3]		1441	1519	59.3
					1537	1626	36.1
SUERC-41191	CH11/R11	76 - 77	713 ± 35 [3]		1278	1328	47.5
					1338	1391	47.9
SUERC-41187	CH11/R13	82 - 82.5	950 ± 35 [3]		1041	1210	95.4
SUERC-39270	CH11/R14	89 - 89.5	979 ± 51 [3]		1020	1210	95.4
SUERC-40031	CH11/R15	92 - 92.5	680 ± 37 [3]		1290	1396	95.4
SUERC-40032	CH11/R16	95 - 95.5	881 ± 37 [3]		1053	1063	1.6
					1150	1274	93.8

Table 6.1: Radiocarbon dates from Chucalen. Dates are reported as ^{14}C years BP and calibrated to 2σ age ranges in years AD using [1] comparison with data from Graven *et al*. (2012), [2] the post-bomb atmospheric southern hemisphere curve (Hua and Barbetti, 2004) and [3] SHCal04 (McCormac *et al*., 2004) in a *P_sequence* deposition model (Bronk Ramsey, 2009a) developed in OxCal 4.1 (Bronk Ramsey, 1995), with a k value of 100 and depths in metres. At the time of writing (Dec. 2012), results for a sample at 79-80cm are not available. * Ranges rejected as $F^{14}C$ values and stratigraphic order indicate they must lie on the falling limb of the bomb spike (figure 6.9).

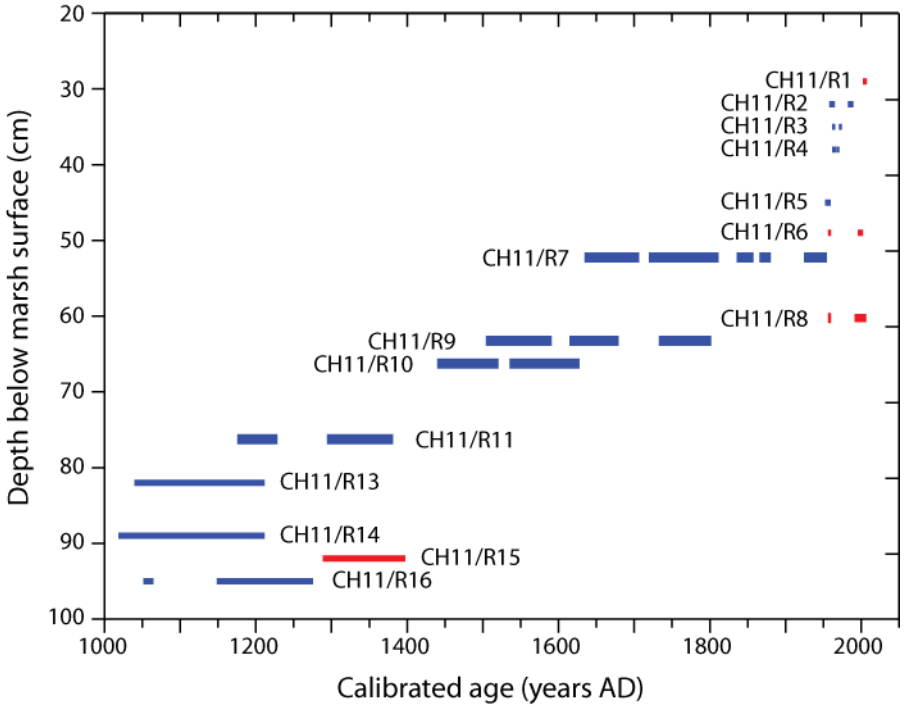

Figure 6.8: Calibrated age ranges for the Chucalen exposure radiocarbon samples. The red bars indicate the dates with calibration solutions younger than their stratigraphic position and the age of adjacent samples would suggest. Blue bars indicate the 11 samples used in the development of the age-depth model.

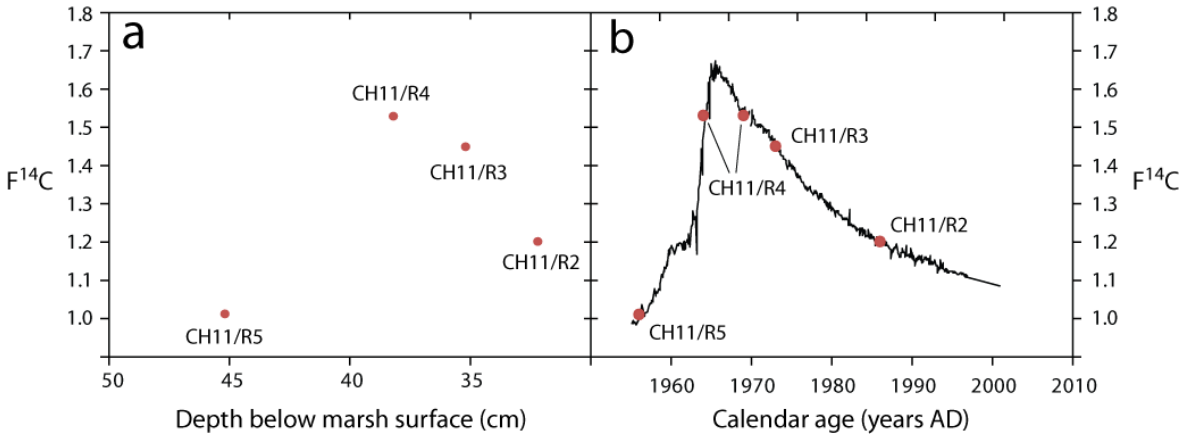

Figure 6.9: Chucalen bomb spike samples, a. plotted as $F^{14}C$ against depth below the marsh surface and b. fitted to the post-bomb atmospheric southern hemisphere ^{14}C curve (black line) of Hua and Barbetti (2004). Sample CH11/R5 must lie on the rising limb, sample CH11/R4 may lie on either the rising or the falling limb and samples CH11/R3 and CH11/R2 must lie on the falling limb.

Laboratory code	Sample code	Central depth (cm)	Radiocarbon age (years BP ± 1σ)	$F^{14}C \pm 1\sigma$	Calibrated age ranges (2σ years AD)		*P_sequence* modelled calibrated age (2σ years AD)		Posterior probability of being an outlier	Agreement index
					Minimum	Maximum	Minimum	Maximum		
Chucalen radiocarbon samples									$A_{overall}$ = 54.1	
SUERC-39264	CH11/R2	32.25	modern [1]	1.2056 ± 0.0076	1982	1990	1974	1989	0.07	80.8
SUERC-39265	CH11/R3	35.25	modern [1]	1.4537 ± 0.0092	1971	1973	1970	1974	0.02	77.2
SUERC-39266	CH11/R4	38.25	modern [1]	1.5337 ± 0.0097	1961	1973	1964	1971	0.01	116.6
SUERC-39269	CH11/R5	45.25	modern [1]	1.0159 ± 0.0064	1952	1960	1951	1959	0.02	102.3
SUERC-41190	CH11/R7	52.5	234 ± 35 [2]		1636	1953	1664	1952	0.04	100.3
SUERC-43051	CH11/R9	63.5	285 ± 38 [2]		1505	1800	1495	1676	0.03	83.8
SUERC-43052	CH11/R10	66.5	427 ± 38 [2]		1441	1626	1446	1621	0.03	107.7
SUERC-41191	CH11/R11	76.5	713 ± 35 [2]		1278	1391	1271	1389	0.04	98.2
SUERC-41187	CH11/R13	82.5	950 ± 35 [2]		1041	1210	1135	1264	0.07	76.4
SUERC-39270	CH11/R14	89.25	979 ± 51 [2]		1020	1210	1049	1200	0.03	109
SUERC-40032	CH11/R16	95.25	881 ± 37 [2]		1053	1274	1014	1207	0.10	21.6
Interpolated ages for abrupt contacts										
	A	44.5					1951	1967		
	B	60					1520	1946		
	C	76					1270	1410		
	D	89					1050	1200		

Table 6.2: Radiocarbon dates used in the development of age-depth models for the Chucalen exposure and posterior age ranges for the four abrupt contacts. Dates are reported as ^{14}C years BP and calibrated to 2σ age ranges in years AD using [1] the post-bomb atmospheric southern hemisphere ^{14}C curve (Hua and Barbetti, 2004) and [2] SHCal04 (McCormac *et al*., 2004) in a *P_sequence* deposition model (Bronk Ramsey, 2009a) in OxCal 4.1 (Bronk Ramsey, 1995), with a k value of 100 and depths in metres. Outlier analysis provides the posterior probability of each sample being an outlier; prior probabilities set to 0.05; posterior probabilities exceeding 0.4 considered to be significant outliers. The agreement index indicates samples with dissimilar prior and posterior distributions; indices below 60 suggest a poor level of fit. Two sigma posterior age ranges for the four abrupt contacts are rounded to the nearest 10 years for all pre-1900 ages.

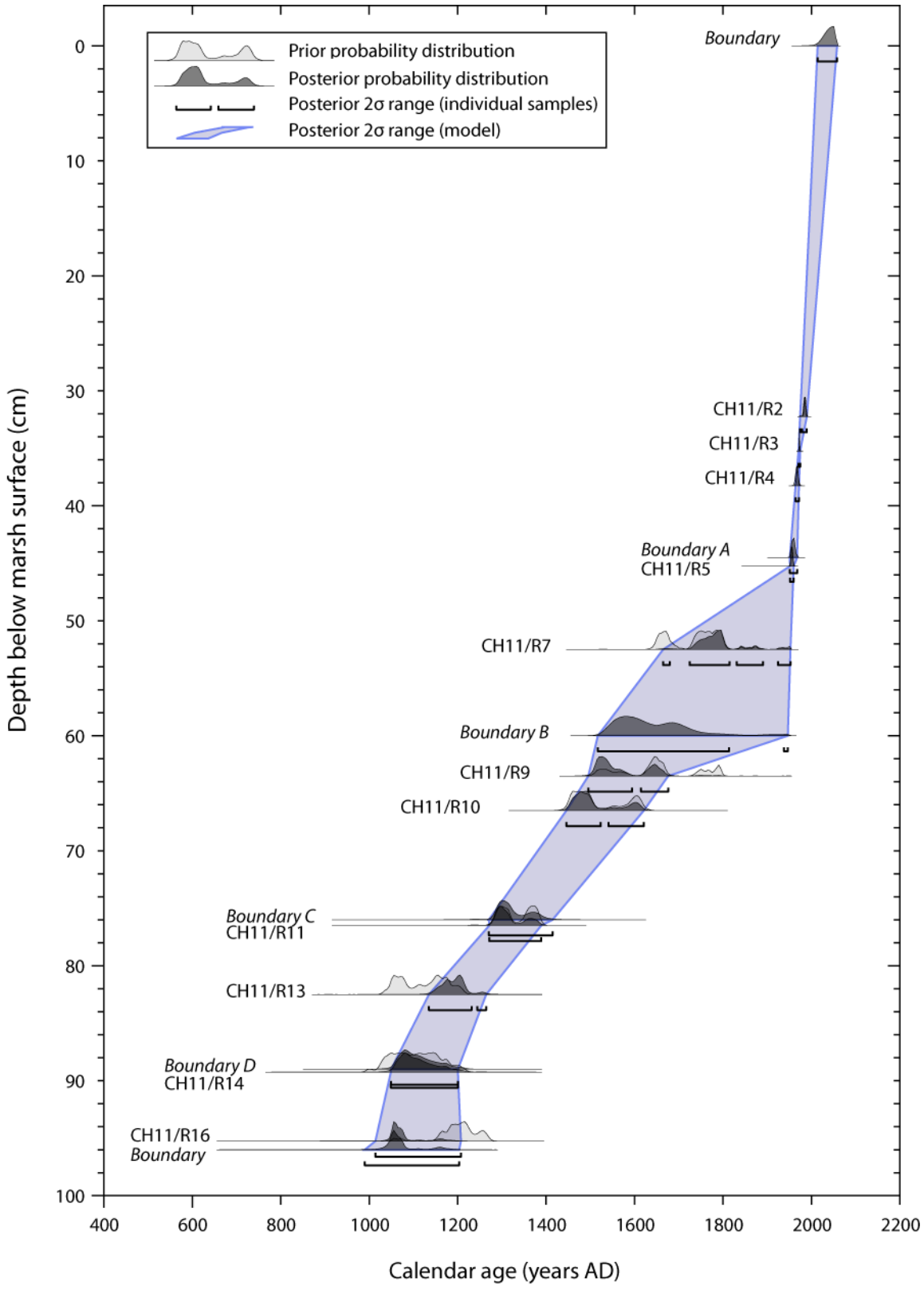

Figure 6.10: *P_sequence* age-depth model for the Chucalen exposure based on radiocarbon dates in table 6.2. Post-bomb samples are calibrated using the post-bomb atmospheric southern hemisphere ^{14}C curve (Hua and Barbetti, 2004) and entered into OxCal v.4.1 (Bronk Ramsey, 1995) as *C_Dates* to make use of the unique solutions inferred from matching samples to the rising and falling limbs of the calibration curve (figure 6.9). Pre-bomb samples are calibrated using SHCal04 (McCormac *et al*., 2004).

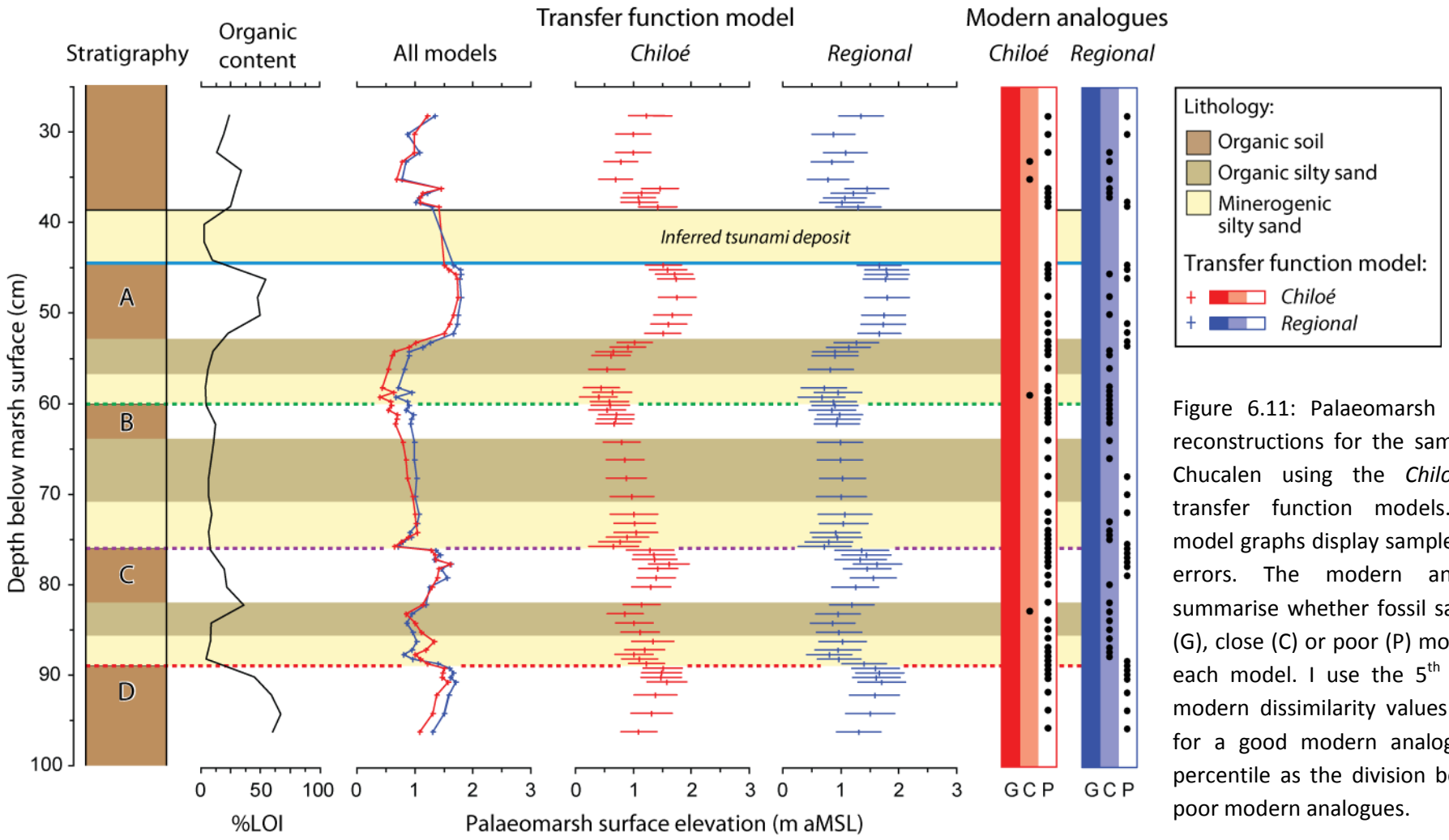

Figure 6.11: Palaeomarsh surface elevation reconstructions for the sampled exposure at Chucalen using the *Chiloé* and *Regional* transfer function models. The individual model graphs display sample specific standard errors. The modern analogue columns summarise whether fossil samples have good (G), close (C) or poor (P) modern analogues in each model. I use the 5th percentile of the modern dissimilarity values as the threshold for a good modern analogue and the 20th percentile as the division between close and poor modern analogues.

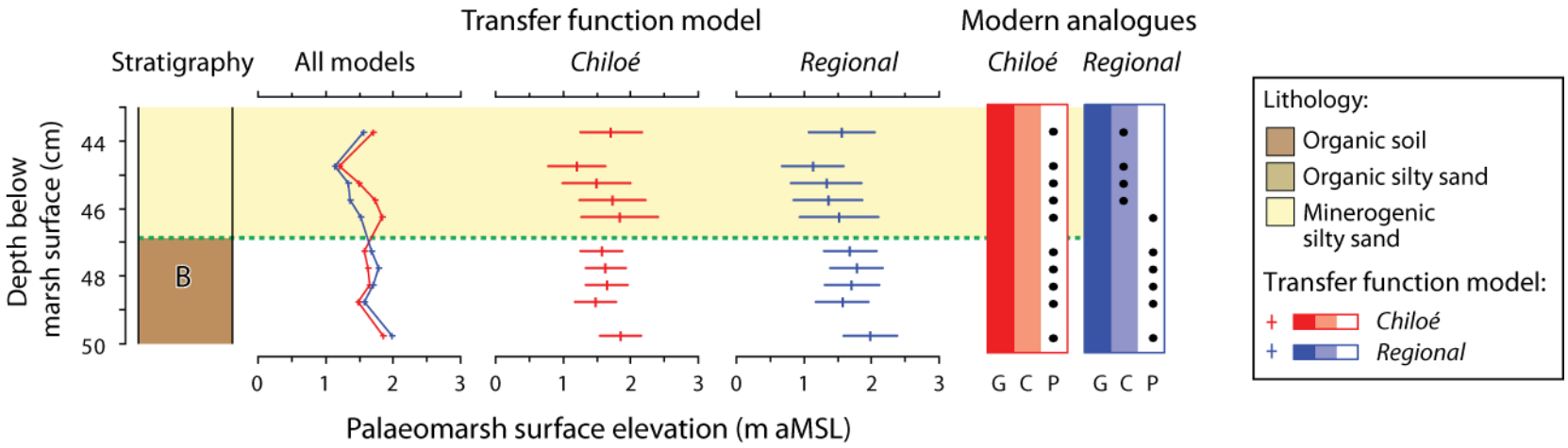

Figure 6.12: Palaeomarsh surface elevation reconstructions for the transition from organic to minerogenic sedimentation at the top of soil B in core CH11/28 at Chucalen. Reconstructions use the *Chiloé* and *Regional* transfer function models. The individual model graphs display sample specific standard errors. The modern analogue columns summarise whether fossil samples have good (G), close (C) or poor (P) modern analogues in each model. I use the 5th percentile of the modern dissimilarity values as the threshold for a good modern analogue and the 20th percentile as the division between close and poor modern analogues.

Submergence burying soil	Magnitude of change (m ± 1σ)	
	***Chiloé* model**	***Regional* model**
A	-1.15 ± 0.43	-1.09 ± 0.53
B (exposure)	-0.34 ± 0.44	-0.32 ± 0.54
B (core CH11/28)	-0.16 ± 0.58	-0.48 ± 0.65
C	-0.97 ± 0.57	-0.92 ± 0.63
D	-0.59 ± 0.47	-0.94 ± 0.57

Table 6.3: Submergence estimates for the four buried soils at Chucalen, based on the *Chiloé* and *Regional* transfer function models. All estimates are corrected for sedimentation.

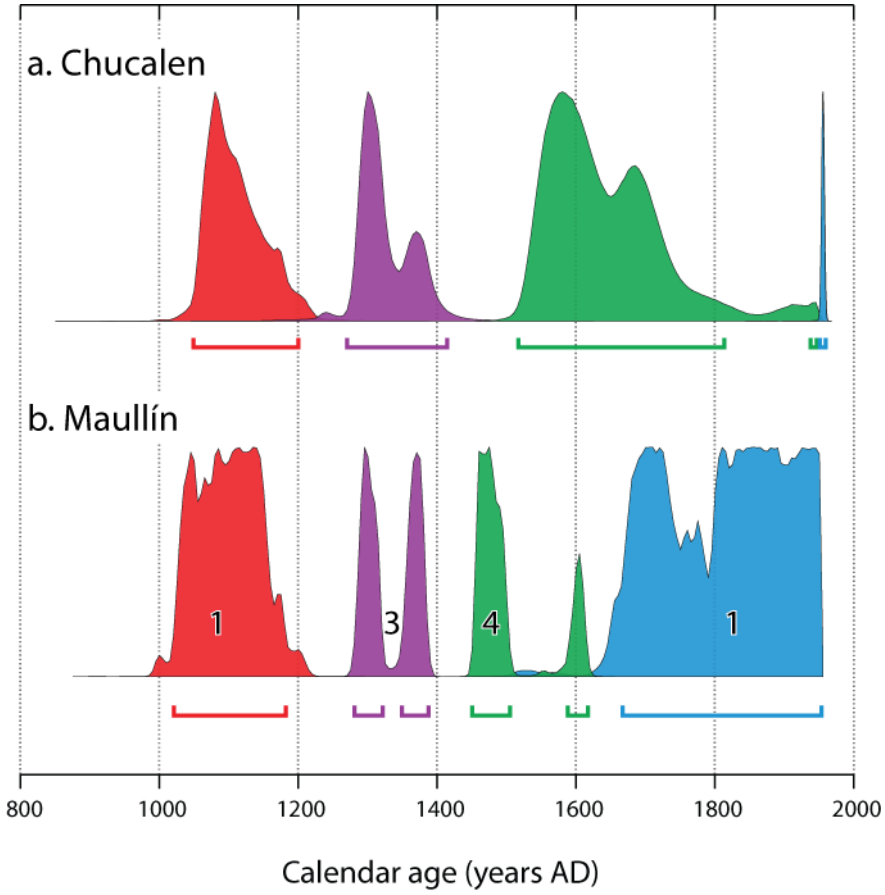

Figure 6.13: Comparison of posterior probability density functions and two sigma age ranges (coloured bars) constraining the timing of submergence events at Chucalen (derived from the age model in figure 6.10) with pooled age ranges constraining the oldest possible timing for tsunami occurrence at Maullín (Cisternas *et al.*, 2005). Numbers on Maullín curves indicate the number of dates pooled to provide the calibration solution.

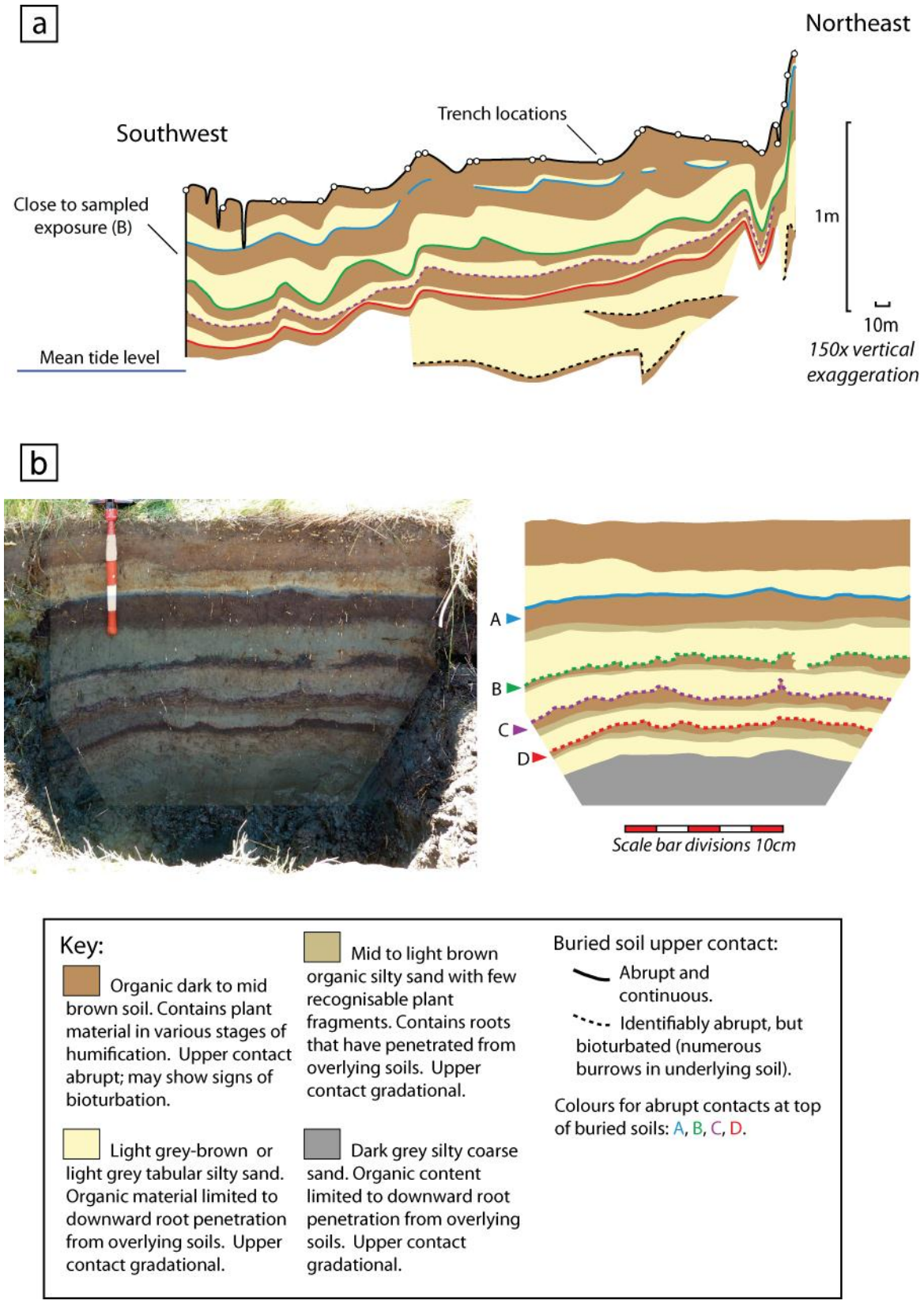

Figure 6.14: Lithology at Maullín. a. cross section of Cisternas *et al.'s* (2005) main trench transect below a low terrace approximately 0.4 km inland from the marsh front; b. photograph and sketch of the marsh front exposure sampled in 2012.

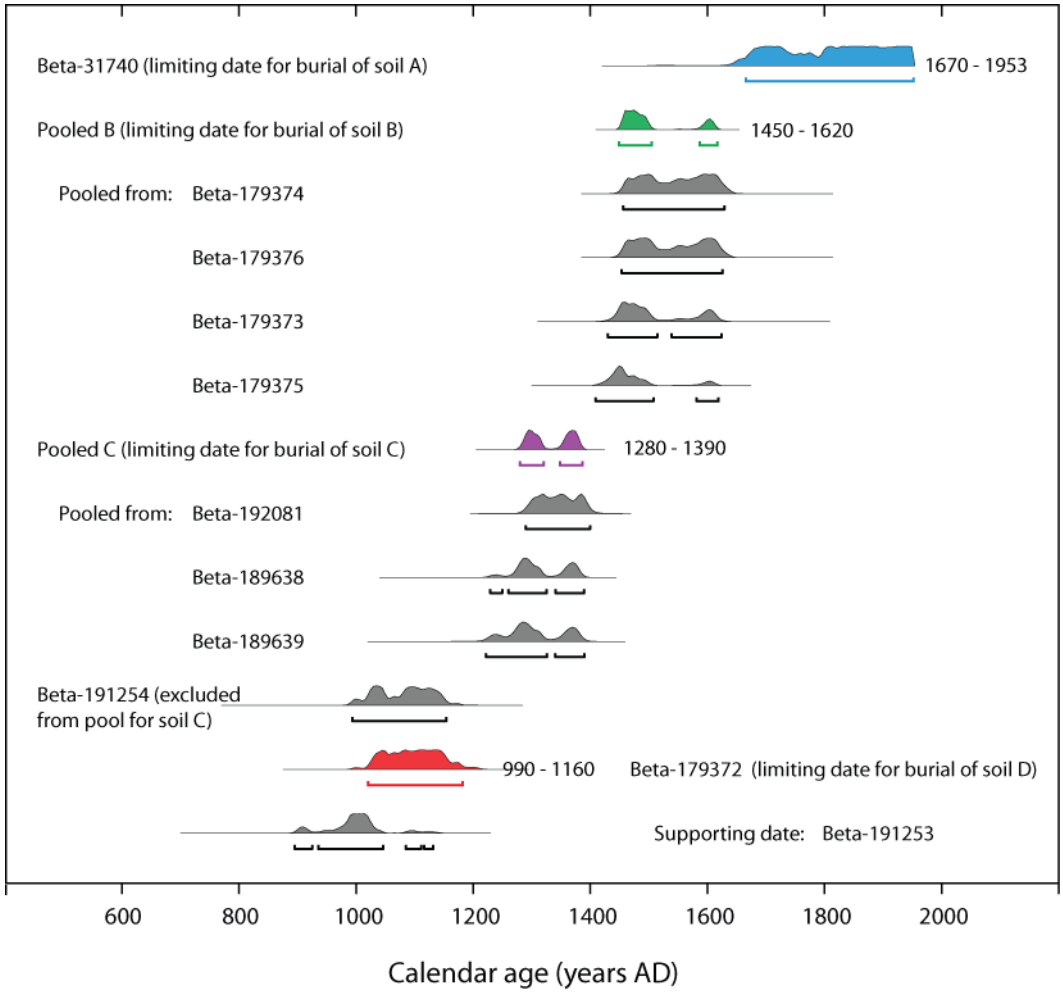

Figure 6.15: Summary of Cisternas *et al.*'s (2005) radiocarbon determinations from Maullín. Coloured probability distributions signify the samples or pooled samples that provide limiting dates for the burial of each soil. Samples combined before calibration using the *R_Combine* function in OxCal v.4.1 (Bronk Ramsay, 1995). All samples calibrated using SHCal04 (McCormac *et al.*, 2004). Horizontal lines indicate two sigma age ranges, which are given in numbers next to each limiting date. Cisternas *et al.* (2005) exclude sample Beta-191254 as it lies seven standard deviations from the pooled mean for soil C.

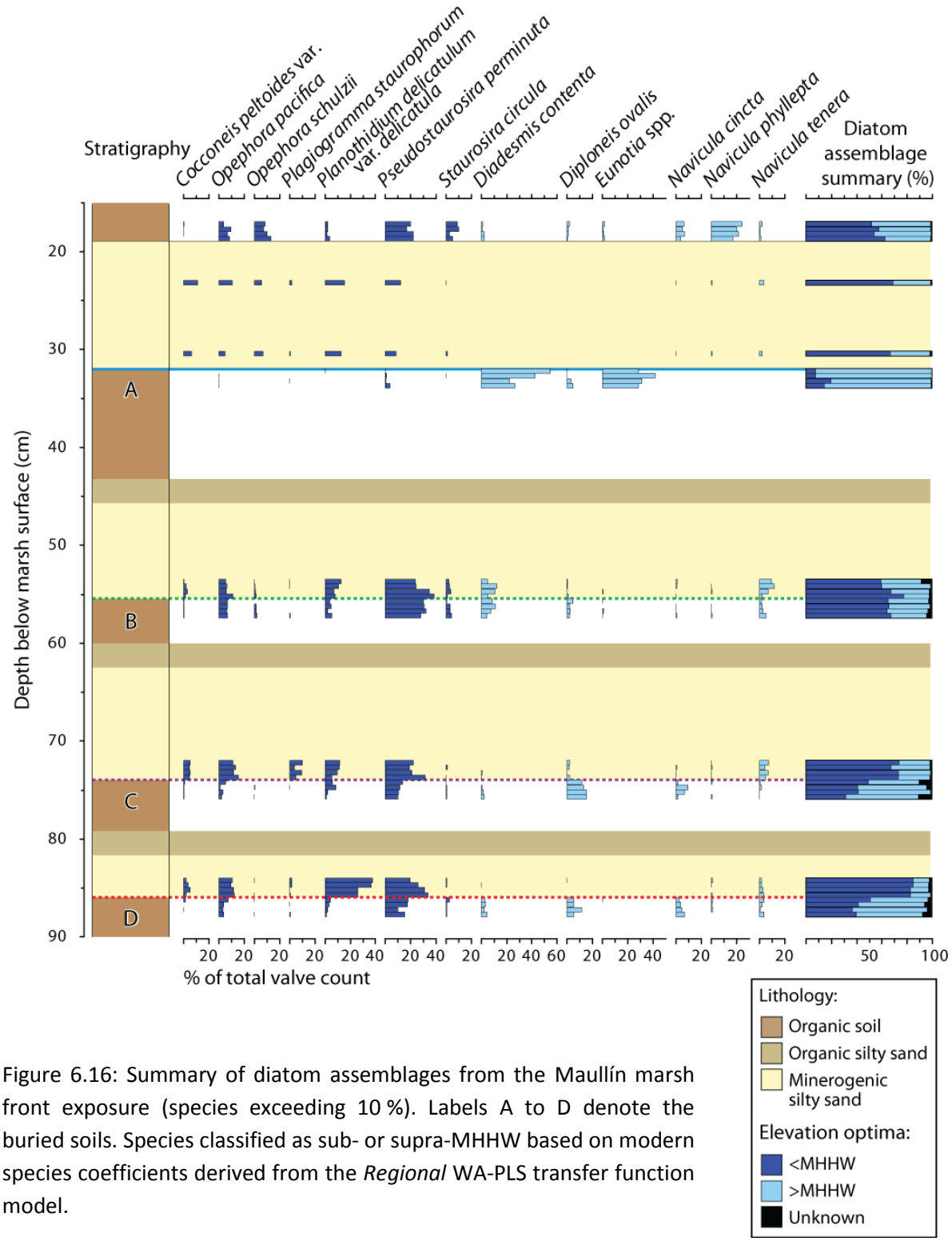

Figure 6.16: Summary of diatom assemblages from the Maullín marsh front exposure (species exceeding 10 %). Labels A to D denote the buried soils. Species classified as sub- or supra-MHHW based on modern species coefficients derived from the *Regional* WA-PLS transfer function model.

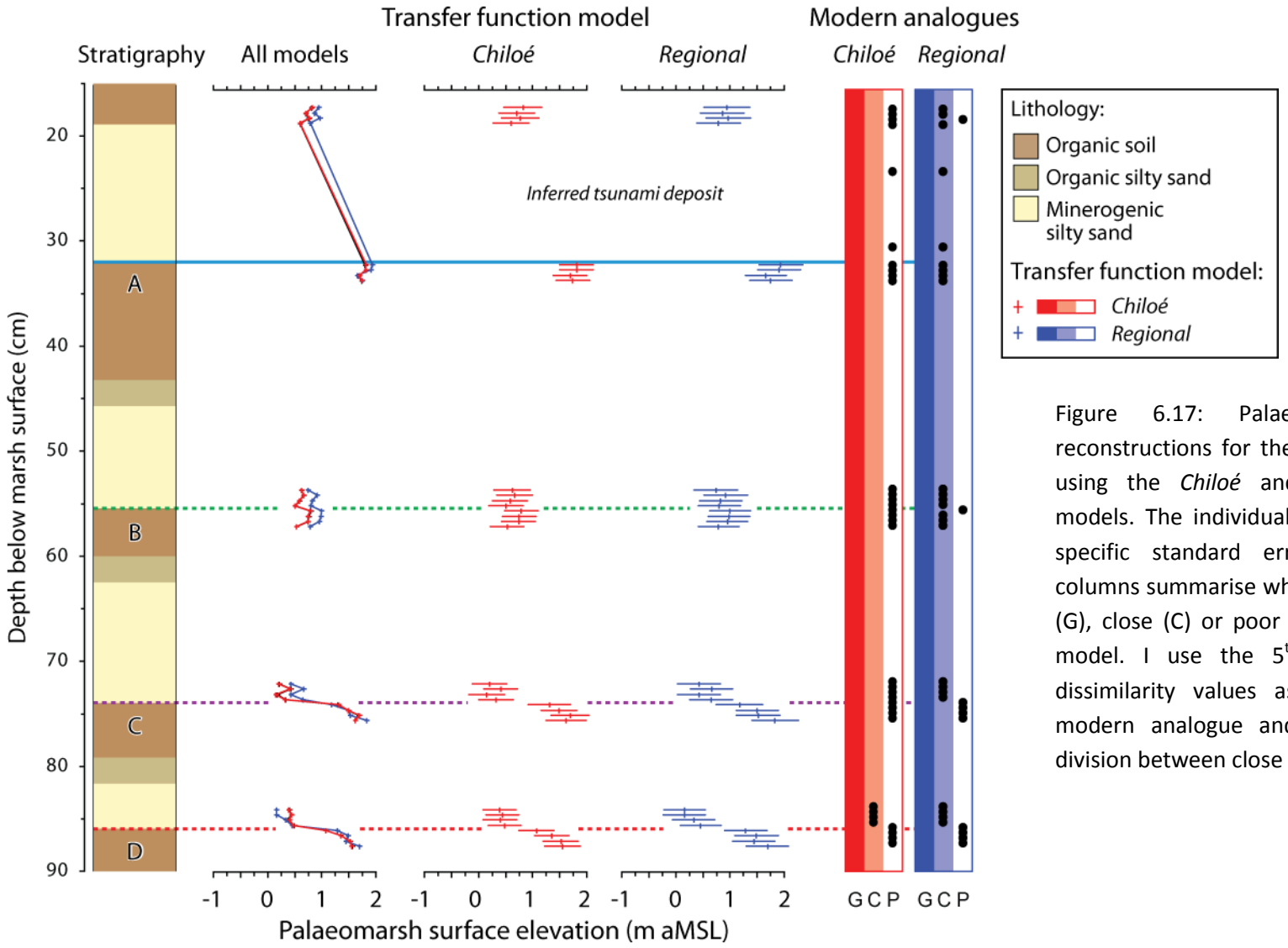

Figure 6.17: Palaeomarsh surface elevation reconstructions for the sampled exposure at Maullín using the *Chiloé* and *Regional* transfer function models. The individual model graphs display sample specific standard errors. The modern analogue columns summarise whether fossil samples have good (G), close (C) or poor (P) modern analogues in each model. I use the 5th percentile of the modern dissimilarity values as the threshold for a good modern analogue and the 20th percentile as the division between close and poor modern analogues.

Submergence burying soil	Magnitude of change (m ± 1σ)	
	***Chiloé* model**	***Regional* model**
A	-1.35 ± 0.45	-1.29 ± 0.57
B	-0.29 ± 0.44	-0.19 ± 0.54
C	-1.35 ± 0.46	-1.09 ± 0.56
D	-1.18 ± 0.45	-1.39 ± 0.55

Table 6.4: Submergence estimates for the four buried soils at Maullín, based on the *Chiloé* and *Regional* transfer function models. All estimates are corrected for sedimentation.

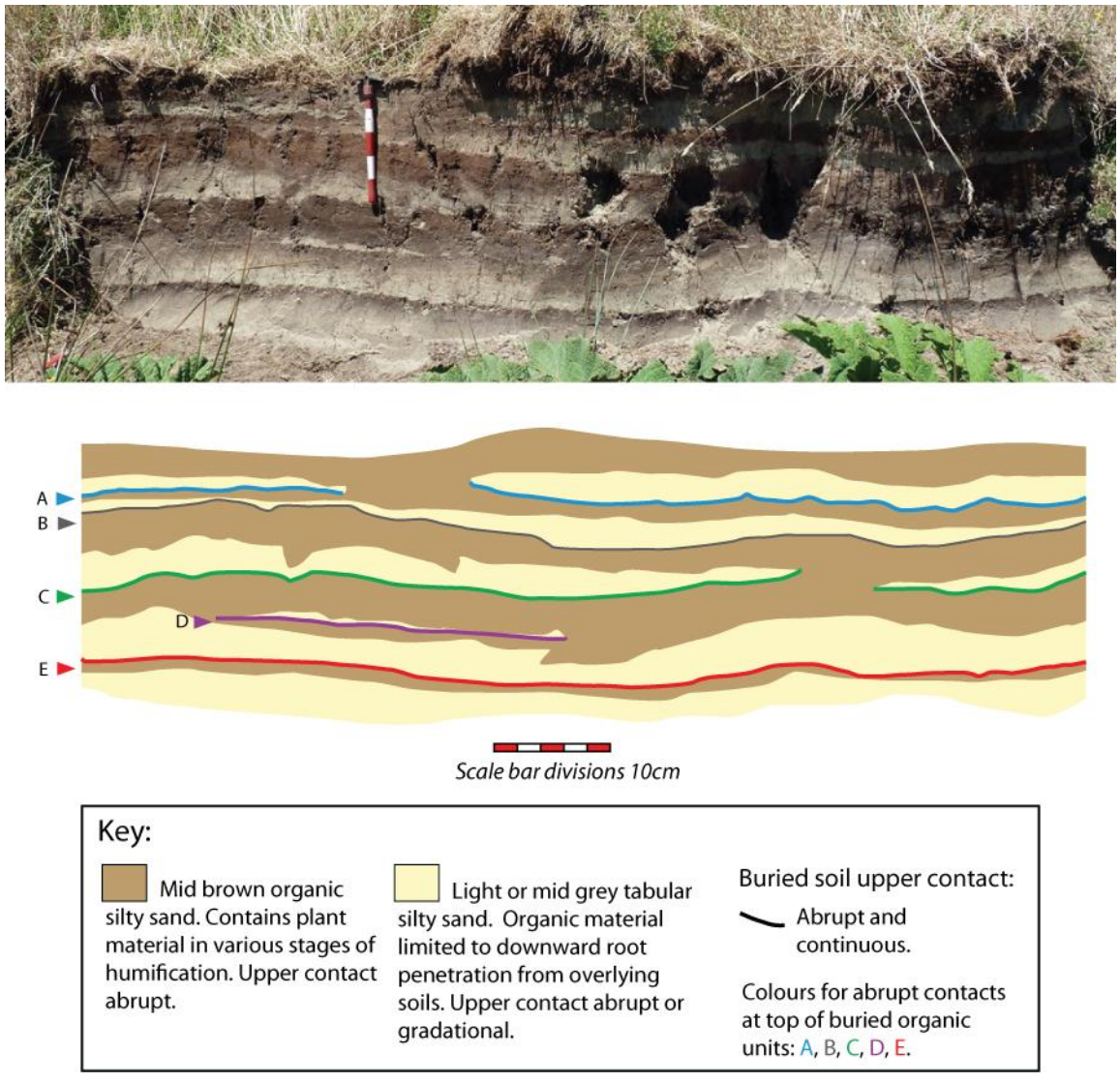

Figure 6.18: Lithostratigraphy of the sampled exposure at Cocotue. Mean sea level lies approximately two metres below the base of the exposed section.

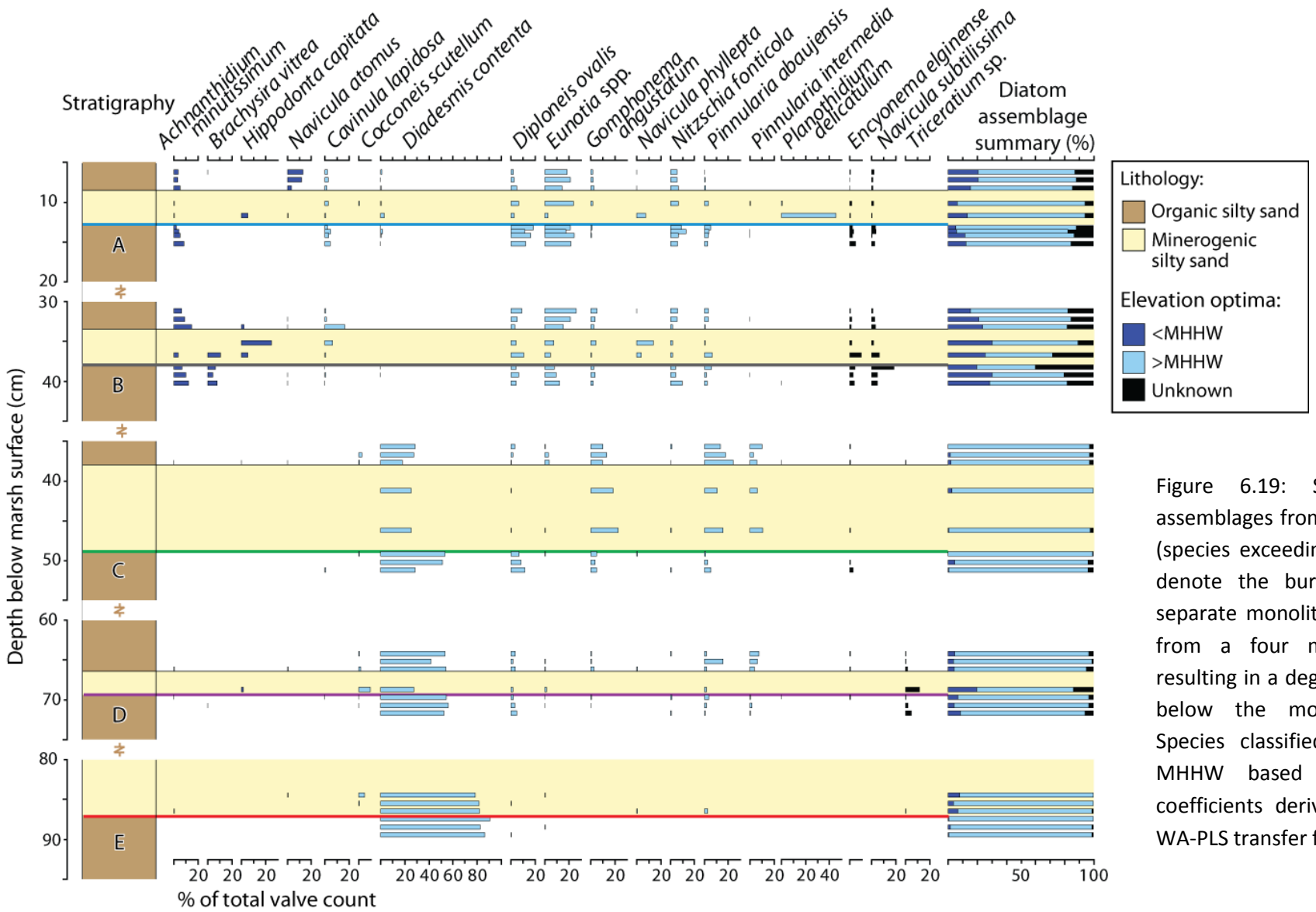

Figure 6.19: Summary of diatom assemblages from the Cocotue exposure (species exceeding 10 %). Labels A to E denote the buried soils. I recovered separate monoliths for each buried soil from a four metre wide exposure, resulting in a degree of overlap in depth below the modern marsh surface. Species classified as below or above MHHW based on modern species coefficients derived from the *Regional* WA-PLS transfer function model.

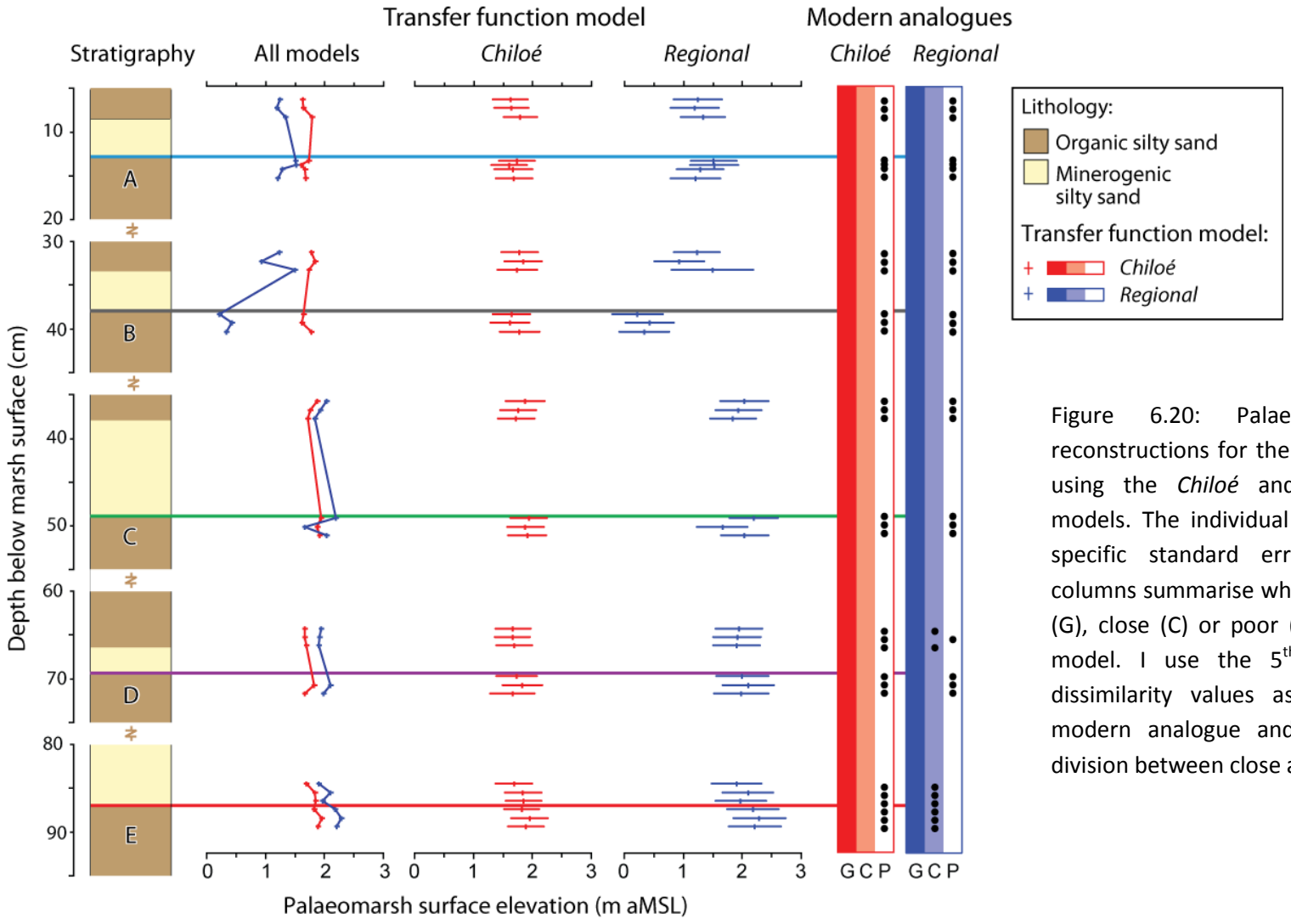

Figure 6.20: Palaeomarsh surface elevation reconstructions for the sampled exposure at Cocotue using the *Chiloé* and *Regional* transfer function models. The individual model graphs display sample specific standard errors. The modern analogue columns summarise whether fossil samples have good (G), close (C) or poor (P) modern analogues in each model. I use the 5th percentile of the modern dissimilarity values as the threshold for a good modern analogue and the 20th percentile as the division between close and poor modern analogues.

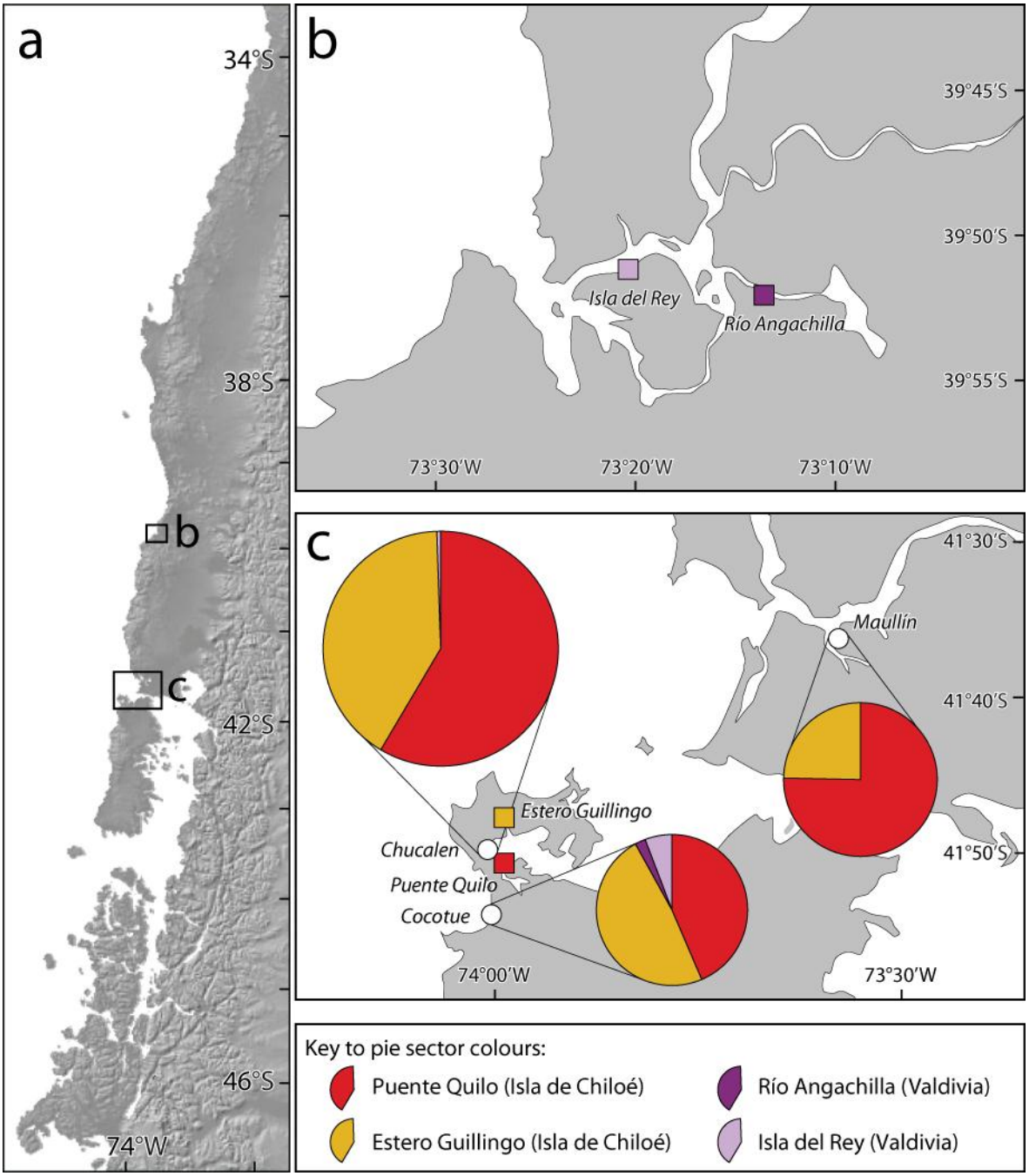

Figure 6.21: Map showing the location of the 10 closest modern analogues for fossil samples from Chucalen (75 samples), Maullín (32 samples) and Cocotue (31 samples). Map B shows the Valdivia estuary, including the location of the Isla del Rey and Río Angachilla transects (Nelson *et al*., 2009) and map C shows northern Isla de Chiloé and the adjacent mainland, including the location of the modern transects at Puente Quilo and Estero Guillingo and the fossil sites at Chucalen, Maullín and Cocotue. The data are expressed as percentages, with the pie diameter proportional to the number of samples at each site.

7. Discussion and conclusions: figures and tables

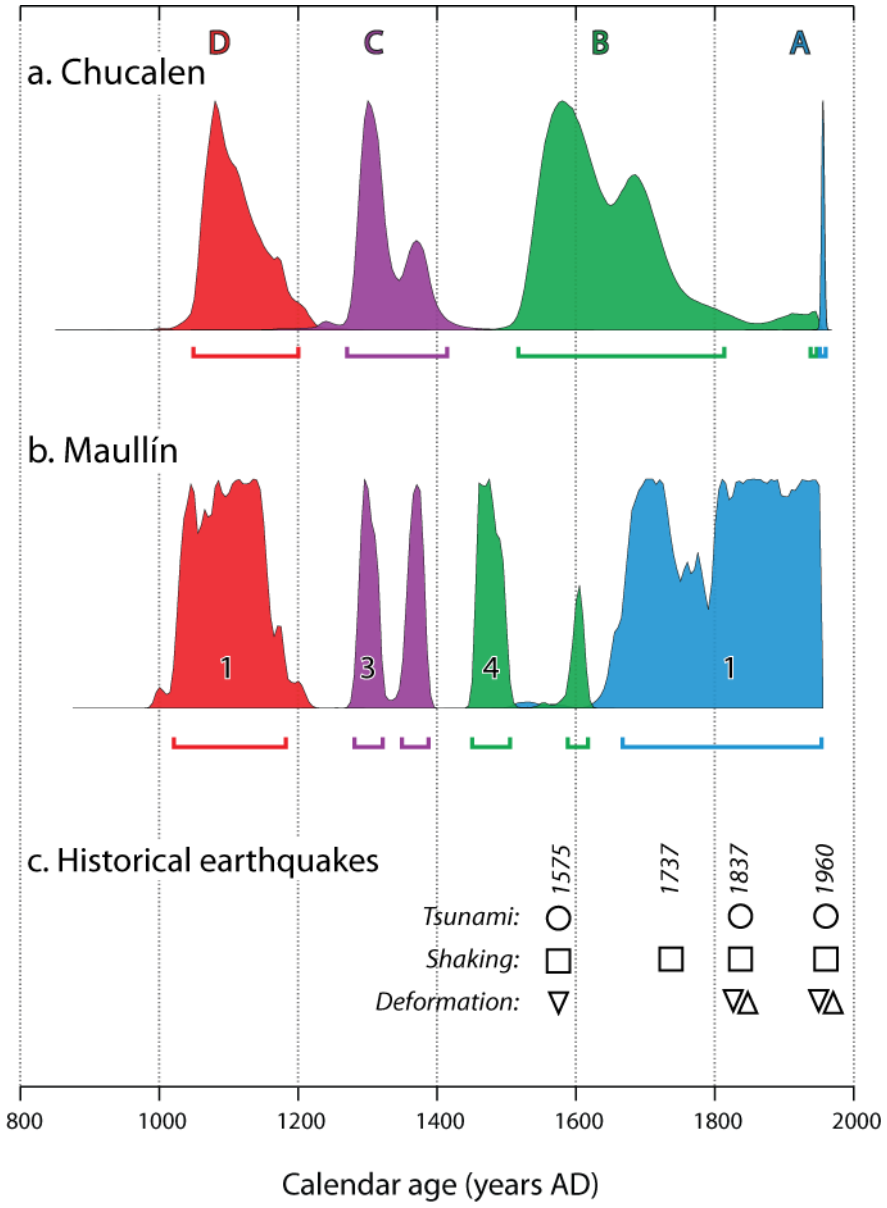

Figure 7.1: Comparison of the timing of earthquakes inferred from coastal stratigraphic records with the four historically documented south central Chilean megathrust earthquakes. a: Posterior probability distributions for the four submergence events at Chucalen derived from the age-depth model in figure 6.10, b: limiting oldest probability distributions for the four most recent submergence events at Maullín, based on individual or pooled dates from figure 6.15 (Cisternas *et al.*, 2005), c. summary of historical evidence (after Berninghausen, 1962; Lomnitz, 1970, 2004; Reed *et al.*, 1988; Cisternas *et al.*, 2005). Numbers on Maullín probability distributions refer to the number of radiocarbon dates pooled.

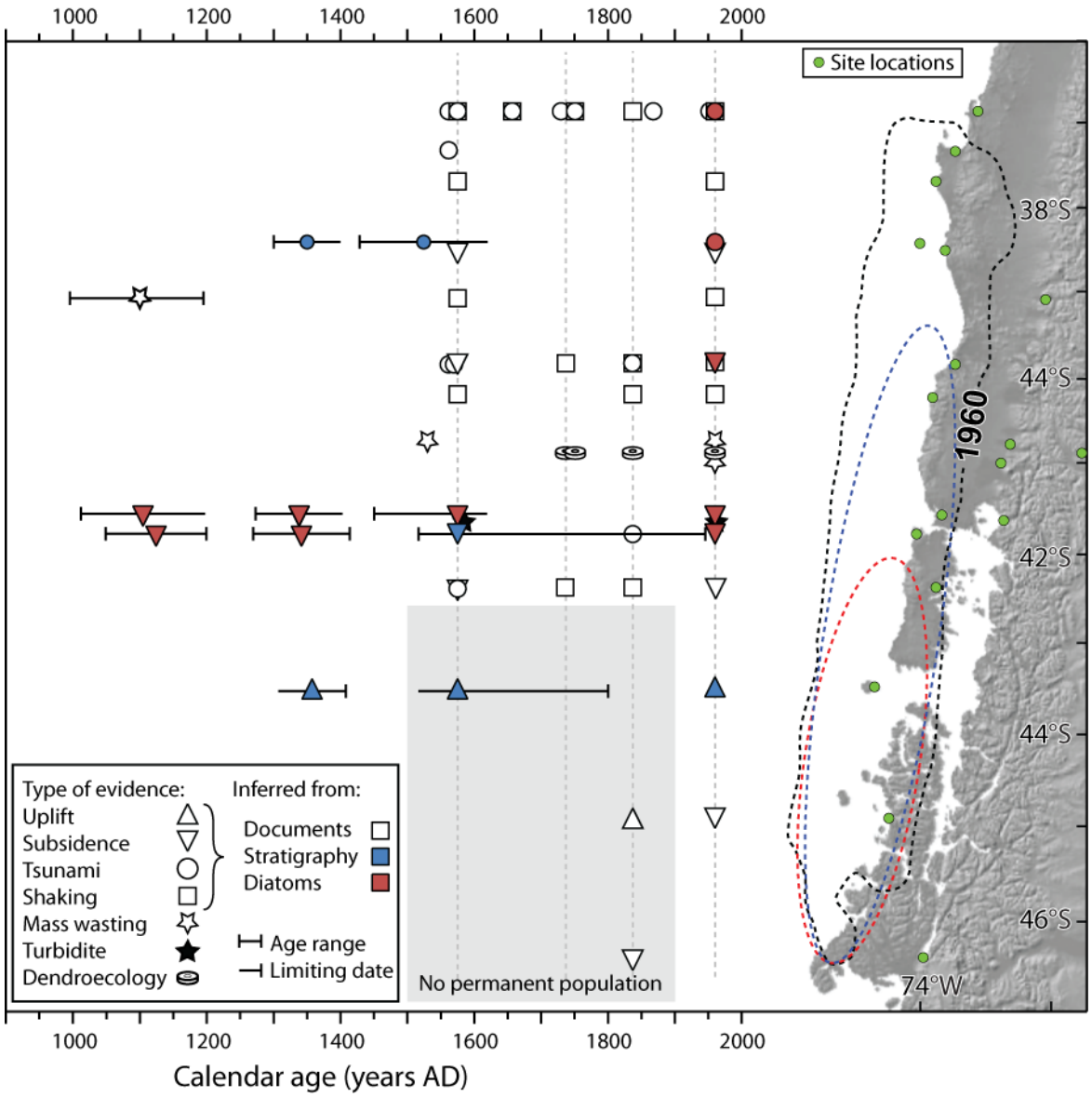

Figure 7.2: Summary of historical and palaeoseismic evidence for Valdivia segment earthquakes over the last 1000 years. Historical records summarised by Heck (1947), Berninghausen (1962); Lomnitz (1970), Reed *et al*. (1988) and Cisternas *et al*. (2005); stratigraphic and biostratigraphic evidence from Cisternas *et al*. (2005, 2007), Nelson *et al*. (2009) Ely *et al*. (2010), Melnick (2010), Garrett *et al*. (accepted) and this study; lake records from Bertrand *et al*. (2008), Moernaut *et al*. (2007), Chapron *et al*. (2006); dendroecological change from Kitzberger *et al*. (2005); marine turbidites from Chapron *et al*. (2006). The black dashed line highlights 1960 rupture zone (after Plafker and Savage, 1970); the blue dashed ellipse encompasses a 750 km hypothesised rupture zone (following Reed *et al*., 1988); the red ellipse illustrates a 500 km rupture hypothesised by this thesis. The grey shaded box indicates the area south of central Chiloé with no permanent historical population and consequently few documentary records.

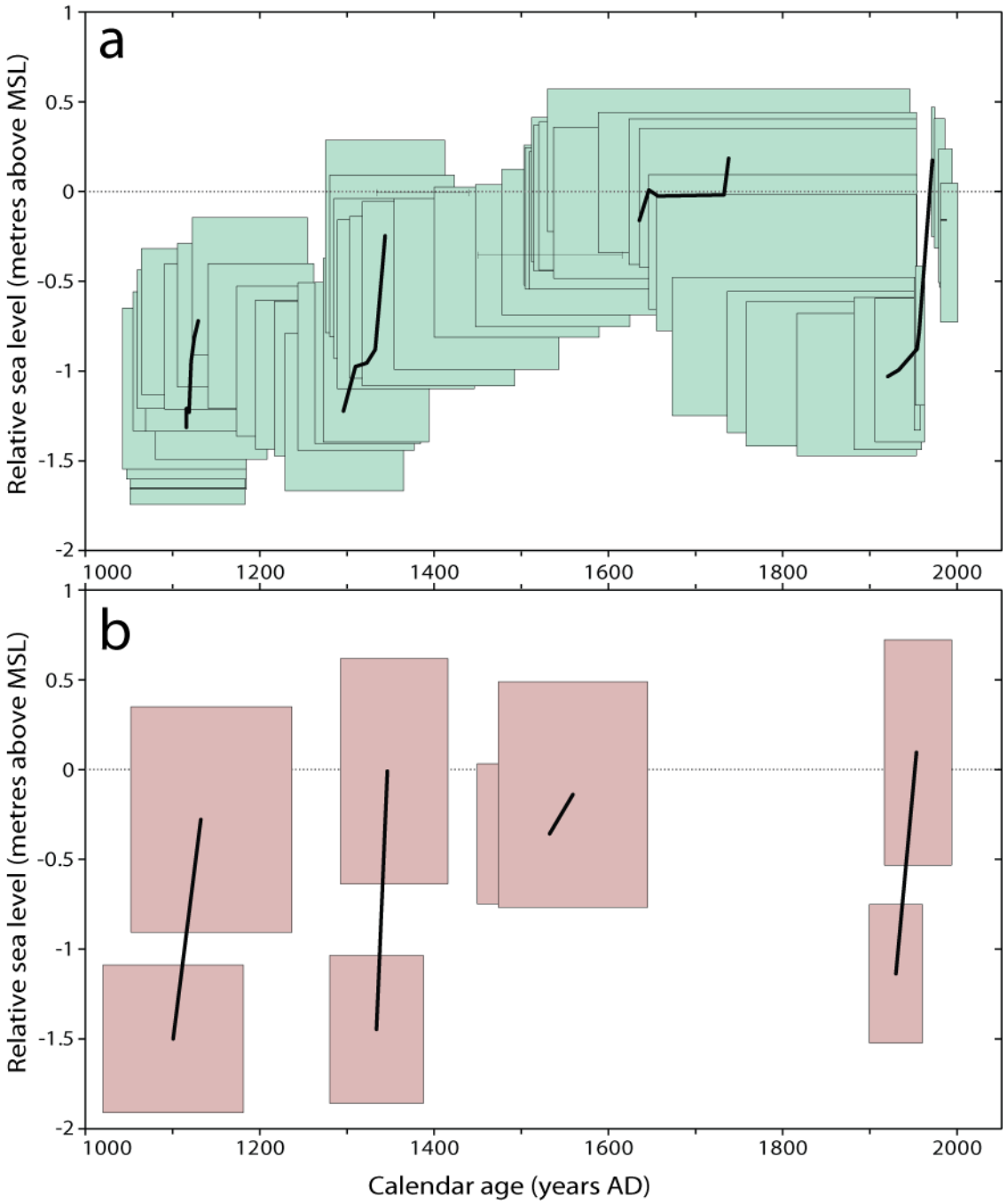

Figure 7.3: One thousand years of relative sea-level change at a. Chucalen and b. Maullín. Coloured boxes reflect age and elevation errors, black lines follow centre points of boxes and indicate the coseismic deformation events. Ages derived from *P_sequence* age modelling (section 6.2.3) for Chucalen and from radiocarbon dates from Cisternas *et al*. (2005) for Maullín. Vertical errors represent the cumulative error associated with sample specific transfer function error, core top elevation and sample depth (section 3.5.6).

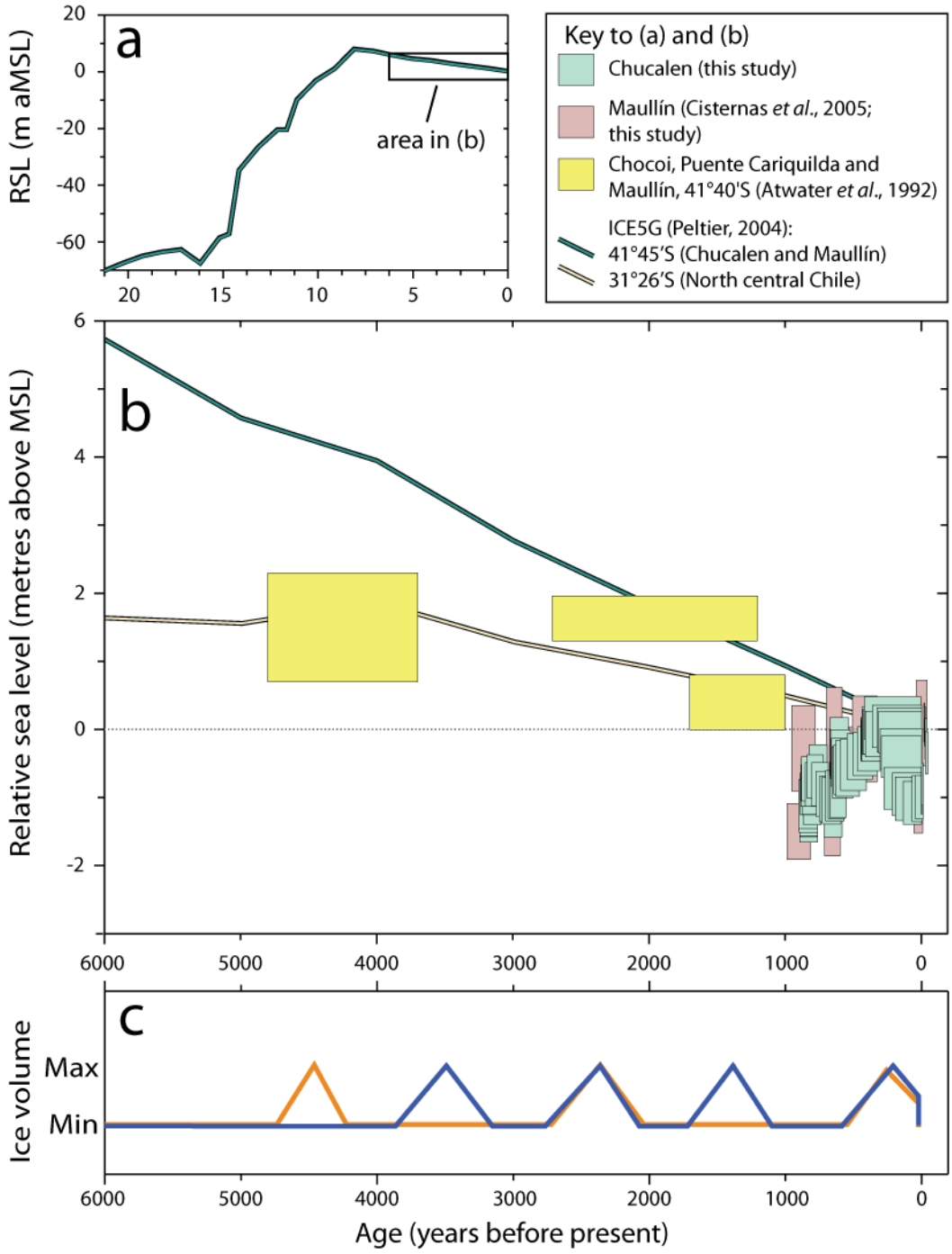

Figure 7.4: Relative sea-level change at Chucalen and Maullín in a mid to late Holocene context. a. ICE5G (VM2) modelled relative sea level change from 21ka BP to present for 73°45'W 41°45'S (Peltier, 2004; data provided by Pippa Whitehouse, pers. com., 2012); b. relative sea level curve for northern Chiloé and the adjacent mainland (Atwater *et al.*, 1992; Cisternas *et al.*, 2005; this study) with ICE5G modelled curves for south central and north central Chile; c. reconstructed Patagonian Neoglacial oscillations using two chronologies proposed by Ivins and James (2002), based in orange on Mercer (1970) and in blue on Aniya (1995).

Appendix 1.1

The following paper has been accepted for publication in *Quaternary Science Reviews* (April 2013).

Reconstructing paleoseismic deformation, 1: modern analogues from the 1960 and 2010 Chilean great earthquakes

E. Garrett [a] , I. Shennan [a *], E.P. Watcham [a, b] and S.A. Woodroffe [a]

[a] Durham University, Sea Level Research Unit, Department of Geography, South Road, Durham, DH1 3LE, UK
[b] Current address: Northumbria University, School of the Built and Natural Environment, Ellison Building, Newcastle-upon-Tyne, NE1 8ST, UK
*Corresponding author: email: edmund.garrett@durham.ac.uk, Tel: +44 (0)191 334 1954

Abstract

The 1960 and 2010 Chilean great earthquakes provide modern analogues for the sedimentary signatures of the largest megathrust events and their accompanying tsunamis. This paper presents lithological and diatom assemblage data from five sites and provides key insights for the development of longer earthquake chronologies, essential for assessing the seismic hazards associated with a subduction zone. We find that the 1960 and 2010 tsunami deposits are fragmentary, variable and have no unique, diagnostic diatom assemblage. Where rapid post-seismic sedimentation occurs, our diatom-based transfer function model gives estimates of coseismic deformation that agree with independent estimates of land-level change. Sedimentary hiatuses at two sites following the 2010 earthquake suggest that the magnitude of coseismic deformation may be underestimated in fossil records. Where sediment accumulation allows, criteria for distinguishing between seismic and non-seismic stratigraphies based on evidence for the largest plate boundary earthquakes are corroborated by the lesser magnitude earthquake of 2010. The key to reconstructing earthquake characteristics, such as rupture magnitude and differences between plate-boundary and upper plate sources, depends on applying explicit stratigraphic assessment criteria at multiple sites in order to identify the spatial pattern of deformation associated with each earthquake.

Keywords: 1960 Valdivia earthquake; 2010 Maule earthquake; earthquake reconstruction; tsunami; diatoms

1. Introduction

The Chilean megathrust creates great earthquakes exceeding moment magnitude (M_w) 8, including the greatest magnitude ever recorded, the 1960 M_w 9.5 rupture of the Valdivia segment, and the M_w 8.8 Maule earthquake of 27th February 2010. These earthquakes are characterised by intense, long duration shaking, significant land surface deformation, generation of near-field tsunamis along the Chilean coast and may spawn destructive trans-Pacific tsunamis. Paleoseismic research at other subduction zones suggests historical and instrumental records may be too short to adequately assess the recurrence of the greatest magnitude seismic hazards, a factor contributing to inadequate anticipation of the 2004 Sumatra-Andaman and 2011 Tohoku megathrust earthquakes (Stein & Okal, 2011). Records kept by Spanish settlers and visiting Europeans indicate four megathrust earthquakes in the Valdivia segment over the last 500 years but current paleoseismic evidence records only some of these. Using evidence from tidal marshes, Cisternas *et al*. (2005) propose a 300-year recurrence interval between the largest ruptures, with the megathrust remaining partly loaded with accumulated plate motion through smaller intervening earthquakes. Differences between the historical and paleoseismic evidence may reflect variations in the size of the rupture zones of megathrust earthquakes; alternatively, interseismic land uplift may lead to low sediment accumulation or erosion of tidal marshes so the sediments record only a partial chronology of great earthquakes. Given the range of processes that may control the preservation of paleoseismic evidence (McCalpin and Carver, 2009), we require correlation of evidence from multiple sites in order to reconstruct the dimensions of land surface deformation and therefore estimate the extent of the segment rupture for each event (Nelson *et al*., 1996; Atwater and Hemphill-Haley, 1997; Atwater *et al*., 2005). Analysis of the sedimentary record of the 1960 and 2010 earthquakes provides potential modern analogues for building century to millennial scale paleoseismic records for different segments of the Chilean megathrust.

Following both the 1960 and 2010 earthquakes, measurements of the displacement of coastal landforms and biotic environments, such as shore platforms and intertidal encrusting molluscs, provided the first quantitative maps of coseismic land uplift and subsidence, essential for constraining models of slip distribution (Plafker and Savage, 1970; Moreno *et al*., 2009; Farías *et al*., 2010; Lorito *et al*., 2011; Vargas *et al*., 2011; Melnick *et al*., 2012). Such records can be fragmentary in both space and time and sedimentary records from tidal marshes can significantly enhance the paleoseismic record of both the coseismic deformation and changes through complete earthquake deformation cycles (Hamilton and Shennan, 2005). In this paper we aim to develop quantitative reconstructions of relative land surface deformation during the 1960 and 2010 earthquakes based on lithostratigraphy and diatom assemblages from five sites. We compare our results with other estimates of coseismic deformation and use our findings to test the applicability of criteria developed in studies of the Cascadia subduction zone to differentiate between sedimentary evidence of relative land- and sea-level changes of seismic and non seismic origins (Nelson *et al*., 1996). The Cascadia studies, from Atwater's (1987) seminal paper onwards, made comparisons with the 1960 Chilean earthquake and the 1964 M_w 9.2 earthquake in Alaska. Nelson *et al*. (1996) suggested their criteria would apply to magnitude 8+ earthquakes and the 2010 Mw 8.8 Maule earthquake provides the opportunity to directly test them. Finally, we assess the application and limitations of stratigraphic and microfossil approaches for developing Holocene records of multiple earthquake deformation cycles in Chile.

2. Study area and methods

In August 2010, six months after the 27th February Maule earthquake, we completed field investigations of tidal marshes at five sites, which we number from north to south for ease of reference (Fig. 1). Sites 1 and 2 lie in the 2010 segment, sites 3 and 4 in the area where the 1960 and 2010 segments overlap, and site 5 is near the centre of the 1960 segment. The spatial pattern of deformation varies longitudinally within each rupture zone, with distance from the trench controlling the zones of coseismic uplift and subsidence (Fig. 1). We targeted tidal marshes as they may preserve evidence of land-level changes and tsunami inundation in their sediment stratigraphy (Atwater, 1987; Cisternas *et al*., 2005; Hamilton and Shennan, 2005). We employed transects of pits and short cores across marshes and adjacent coastal lowlands to assess the type, continuity and extent of 2010 tsunami deposition and the lateral extent and net accretion of sediments laid down since the earthquake. Any sub-surface sand layers were also documented and we use local testimony, comparison with other studies and caesium-137 (^{137}Cs) concentrations to suggest which relate to tsunami deposition following the 1960 earthquake.

We selected cores from each transect for further laboratory analyses, including diatom assemblages and grain size variations, to reconstruct relative sea-level changes and to assess the composition of tsunami deposits. Laboratory preparation of diatoms followed standard methods (Palmer and Abbott, 1986) with a minimum of 250 diatom valves counted per sample. Diatoms live at the sediment surface (epipelic or epipsammic), attached to vegetation (epiphytic) or in the water column (planktonic) and respond to variations in their environment, including salinity and frequency of tidal inundation (e.g. Vos and de Wolf, 1993). Diatoms may provide information on the depositional environment and source of sediments to a coastal area, for example they can be used to distinguish tsunami deposits from other sediments and help identify the source of tsunami lain sand (Dawson *et al.*, 1996; Dawson, 2007; Hemphill-Haley, 1996; Horton *et al.*, 2011).

Diatom assemblages can also provide estimates of coseismic land movement with decimetre precision (e.g. Shennan *et al*., 1996; Hamilton and Shennan, 2005; Zong *et al*., 2003). We estimate coseismic deformation for each site by comparing the diatom assemblages from sediments deposited before and after the earthquake with the modern distribution of diatoms at two tidal marshes in northern Isla de Chiloé, site 5, and data collected by Nelson *et al*. (2009). We use modern diatom samples collected in 2010 from site 5 only as it was not affected by elevation change or tsunami inundation in 2010. To account for variations in tidal ranges between sites, we convert the elevation of each modern sample to a standardized water level index (SWLI), whereby a SWLI value of 100 represents mean sea level and 200 represents mean higher high water (Hamilton and Shennan, 2005). We define:

$$\mathrm{SWLI_n} = \frac{100(\mathrm{h_n} - \mathrm{h_{MSL}})}{\mathrm{h_{MHHW}} - \mathrm{h_{MSL}}} + 100 \qquad (1)$$

Where:
$SWLI_n$ is the standardised water level index for sample n
h_n is the elevation of sample n
h_{MSL} is Mean Sea Level at the site
h_{MHHW} is Mean Higher High Water at the site

We follow the transfer function approach outlined by Hamilton and Shennan (2005), first using detrended canonical correspondence analysis (DCCA) to determine the requirement for a unimodal method, then developing a transfer function model that can produce reconstructions of marsh surface elevations, with error terms, from fossil diatom sequences (Software: C2 version 1.7.2, Juggins, 2011). Estimates of coseismic deformation compare pre- and post-earthquake marsh surface elevations, accounting for the thickness of any tsunami deposit. We define the uncertainty for each estimate of coseismic deformation:

$$\text{CD error} = \sqrt{(\text{E}_{\text{PRE}}\ \text{error})^2 + (\text{E}_{\text{POST}}\ \text{error})^2} \quad (2)$$

Where:
CD error is the 1σ error of the coseismic deformation estimate
E_{PRE} error and E_{POST} error are the sample specific standard errors for samples preceding and following the deformation event respectively.

3. Transfer function model development

The modern training set comprises 96 samples collected in 2010 and 32 collected by Nelson *et al.* (2009) in 1989 (supplementary table A.1). DCCA confirms a unimodal relationship between modern diatom distributions and elevation (environmental gradient >2 standard deviations, Birks, 1995) and we use weighted averaging partial least squares regression (WA-PLS) with bootstrapping cross-validation (ter Braak and Juggins, 1993; Birks, 1995). We chose the three-component model over one and two-component models, as it has the highest r^2 value, a more linear distribution of observed against predicted values and a RMSEP improvement of at least 5 % with the addition of each extra component (Fig. 2). Increased precision can be obtained by reducing the range of sampled elevations; however we currently have no independent measure to select a model using a narrower elevation range, as applied in Alaska where the data set is more than twice the size (Hamilton and Shennan, 2005).

Given the distance between sites and their different environmental conditions, we may not expect the modern training set to fully reflect the range of diatom assemblages and environments that exist in fossil samples, even though the number of samples exceeds the minimum required to give sample-specific error terms in WA-PLS. We use an analogue measure, modern analogue technique (MAT) to quantify the similarity between each fossil sample and the modern training set using a squared chord distance dissimilarity method (Birks, 1995). We use the 5th percentile of the dissimilarity values for the modern samples as the threshold between a 'good' and 'close' modern analogues for each fossil sample and the 20th percentile as the cut-off for a 'poor' modern analogue.

4. Results and reconstructions of deformation

4.1 Site 1: Río Mataquito

The site lies within the 2010 segment and north of the 1960 segment (Fig. 1). The Río Mataquito is deflected northwards by an 8 km long supratidal sand spit at its confluence with the Pacific. The spit was largely submerged following coseismic deformation in 2010 or eroded by the ensuing tsunami which crested 11 m above tide level (Fig. 3; Vargas *et al.*, 2011). Our transect of short

cores from a tidal marsh close to the pre-earthquake river mouth shows the 2010 tsunami deposit to be of variable thickness. The grey sand sheet exceeds 0.4 m in thickness close to the river channel, and thins in a landward direction (Fig. 4). The lower contact is abrupt, with occasional above ground parts of terrestrial plants preserved immediately beneath and within the sand, pointing in the direction of flow as they were flattened by tsunami inundation. The deposit is normally graded and is both coarser grained and less organic than the underlying tidal marsh sediments.

Diatom assemblages from the tsunami deposit are characterised by epipelic and epipsammic taxa, with a significant minority, ~ 30 %, of planktonic forms (Fig. 5). Almost 65 % of the tsunami assemblage is characterised by diatom species identified by the transfer function model as reflecting environments above mean higher high water. A further 25 % of the assemblage consists of species not encountered in the modern tidal marshes, with the remaining 10 % corresponding to species indicative of environments below mean higher high water.

Despite an increase in accommodation space resulting from the reported coseismic subsidence, (Vargas *et al*., 2011; Vigny *et al*., 2011), we do not record any post-tsunami sediment accumulation in the six month interval between the earthquake and field sampling and, therefore, no estimate of coseismic deformation is possible using the diatom-based transfer function.

4.2 Site 2: Río Andalién

The site lies within the 2010 segment and immediately north of the 1960 segment (Fig. 1). Tidal marshes occupy the broad north-facing embayment of the Bahía de Concepción between Talcahuano and Penco. Estimates of coseismic movement in 2010 indicate uplift to the west (Fritz *et al*., 2011) and subsidence to the south (Vigny *et al*., 2011). Watermarks in Talcahuano and Penco indicate 2010 tsunami flow depths of between 4 and 7 m (Fritz *et al*., 2011) and a maximum inundation distance across the low lying tidal marshes of 2.6 km (Morton *et al*., 2011). We investigated two transects from the eastern edge of the embayment, alongside the Río Andalién (Fig. 2).

2010 earthquake and tsunami

The 2010 tsunami deposit is a largely continuous sand sheet with occasional rounded mud rip-up clasts. The normally graded deposit is generally less than 0.1 m thick and both transects exhibit landward thinning (Fig. 4). The lower boundary is abrupt, however vegetation was generally found to have remained in growth position, rather than having been flattened beneath the sand layer. Diatoms that live attached to sediment account for more than 75 % of the 2010 tsunami assemblage (Fig. 5). The summary assemblages (Fig. 6a) show that the tsunami deposit has a greater proportion of species indicative of lower elevations than the underlying tidal marsh sediment, reflecting net sediment transport from the lower intertidal and perhaps subtidal zone during the tsunami.

Six months after the earthquake, postseismic sediment accumulation had reached a maximum of 20 mm. Pre- and post-tsunami diatom assemblages indicate subsidence of 0.75 ± 0.43 m (Fig. 6a), but we note the poor modern analogues and discuss this further in section 5.3.

1960 earthquake and tsunami

A second sand layer occurs approximately 0.2 m below the present ground surface (Fig. 4). Comparison of the colour, grain size and nature of the lower contact with the 2010 tsunami deposit suggests that this lower sand layer was also deposited by a tsunami. Numerous significant tsunamis have struck the coast of central Chile, including major events in 1960, 1835, 1751, 1730, 1657, 1575 and 1570 (Cisternas *et al*., 2005; Lomnitz, 2004). Tide gauge data from Talcahuano indicate that the 1960 tsunami reached heights of 3 m within Bahía de Concepción (Sievers *et al*., 1963). Comparable tide gauge measurements of the 2010 tsunami were approximately 0.65 m lower, suggesting that the 1960 tsunami was also of sufficient size to erode, transport and deposit intertidal sediments within the bay. We find elevated ^{137}Cs concentrations immediately below the sand layer; this indicates deposition no earlier than the beginning of atmospheric nuclear testing in 1952, suggesting that the sand layer was deposited in 1960.

Diatom assemblages from this deposit are highly mixed, with epiphytic species and those that live attached to sediment contributing the majority of the assemblage (Fig. 5). Planktonic species are rare, accounting for less than 5 % of the assemblage. Species indicative of elevation classes above and below mean higher high water occur approximately equally (Fig. 7a), giving no clear indication of predominant sediment source.

Pre- and post-tsunami diatom assemblages are generally similar, with the largest changes in species that are not characterised by our modern assemblage data (Fig. 7a). Quantitative reconstructions indicate uplift of 0.11 ± 0.45 m, again noting the poor modern analogue classifications.

4.3 Site 3: Tubul

Tubul lies in the area where the 2010 and 1960 segments overlap (Fig. 1). The Tubul and Raqui rivers drain a substantial sheltered tidal and freshwater marsh on the northern edge of the Arauco Peninsula (Fig. 1, 3). Estimates of coseismic movement in 2010 indicate uplift of between 1 and 2 m (e.g. Farías *et al*., 2010, Melnick *et al*., 2012). Our coring transects ranged from intertidal mud and sand flat to freshwater marsh above the influence of tides.

2010 earthquake and tsunami

Despite tsunami flow depths estimated at over 5 m (Fritz *et al*., 2011), we did not observe a surficial or subsurface tsunami deposit at any location on our transects. This may reflect local effects of coseismic uplift reducing the potential tsunami inundation distance inland and the position of our sampling area with respect to the open coast.

Although we noted no change in sediment lithology in the field, laboratory analysis of the uppermost 5 mm of the recovered sediment profile shows a significant change in diatom assemblage (Fig. 6b). Our reconstruction indicates coseismic uplift of 0.64 ± 0.67 m, with close modern analogues for the pre-earthquake samples.

4.4 Site 4: Río Tirua

The Río Tirua meanders through a low-lying coastal plain, characterised by tidal and freshwater marsh environments. The site is close to the southern limit of surface deformation in 2010 and

within the 1960 segment (Fig. 1). Intertidal mussels indicate coseismic uplift of between 0.5 and 1 m in 2010 (Melnick *et al*., 2012). Our transect lies ~ 1 km from the open coast (Fig. 3).

2010 earthquake and tsunami

While tsunami runup reached 20 m on the exposed rocky shoreline to the southwest, heights closer to the river mouth were approximately half as large (Bahlburg and Spiske, 2012; Fritz *et al*., 2011; Vargas *et al*., 2011). The 2010 tsunami deposited a grey sand layer which we traced along the incised banks of the Río Tirua. The deposit exceeds 0.1 m in thickness and thins upstream and, more rapidly, away from the river channel (Fig. 4). The lower contact is abrupt, with frequent flattened stems below and encased within the base of the deposit.

The tsunami diatom assemblage is predominately composed of species that live attached to sediment, with some epiphytic forms (Fig. 5). Taxa favouring the lower elevations of the modern transects contribute 25 to 45 % of the assemblage, with species not found in the modern marshes providing a further 30 % (Fig. 6c).

There was no identifiable postseismic sedimentation six months after the 2010 earthquake. Tsunami-lain sand was still visible at the surface in January 2012, almost two years after the earthquake. No estimate of coseismic deformation is possible using the diatom-based transfer function.

1960 earthquake and tsunami

We observed a second sand layer, analogous to that deposited by the 2010 tsunami, at a depth varying between 0.1 and 0.4 m alongside the Río Tirua. The contact with underlying marsh sediments is abrupt. Elevated ^{137}Cs concentrations in the buried marsh surface and the testimony of local residents who experienced the event suggest that this layer relates to the tsunami associated with the 1960 earthquake. Tsunami runup on Isla Mocha, 30 km offshore from the mouth of the Río Tirua, exceeded 15 m (Sievers *et al*., 1963), but the wave height as it approached the mainland in this sector is unknown. By way of comparison, runup during 2010 exceeded 20 m on Isla Mocha (Fritz *et al*., 2011); however the difference may result from the different approach directions of the two tsunamis. The 1960 tsunami deposit is generally thinner and more fragmented than the 2010 deposit (Fig.4), as we also noted for site 2, Río Andalién.

The 1960 sand layer is characterised by a higher proportion of epiphytic and planktonic species than the 2010 deposit, although epipelic and epipsammic species still contribute more than half of the total assemblage (Fig. 5). Species indicative of elevations above mean higher high water are dominant in most of the tsunami samples; however a peak in the abundance of one species results in almost 50 % of one sample consisting of diatoms of unknown elevation preference (Fig. 7b).

Pre- and post-tsunami diatom assemblages are generally similar; however there are no close modern analogues for any of the samples. Our marsh surface reconstructions are indistinguishable from zero, 0.03 ± 0.72 m (Fig 7b).

4.5 Site 5: Chucalen

On the north west of Isla de Chiloé, tidal marshes line the western fringe of Bahía Quetalmahue, sheltered from the Pacific Ocean by the Lacui Peninsula (Fig. 1). This region is close to the centre of the 1960 segment and ~ 400 km south of the 2010 segment. There was no tsunami recorded here in 2010.

1960 earthquake and tsunami

At Chucalen we traced a grey sandy deposit through a 100 m long transect at depths of between 0.1 and 0.35 m below the present marsh surface (Fig. 4). The normally graded deposit decreases in thickness with increasing elevation and distance from the marsh front. The contact with the underlying marsh sediments is abrupt. Through comparison with preliminary investigations by Bartsch-Winkler and Schmoll (1993), ^{137}Cs concentrations and statements from local residents, we correlate this deposit with the 1960 tsunami. Witnesses suggest that a series of three waves resulted in runup exceeding 15 m on exposed headlands on the northern edge of the Lacui Peninsula, with 5 m waves striking Ancud, decreasing to 1.5 m in Bahía Quetalmahue (Sievers *et al*., 1963). Bartsh-Winkler and Schmoll (1993), however, suggested waves of several times this magnitude may have entered the Quetalmahue estuary across the isthmus that joins the Lacui Peninsula, close to our sampling area.

Diatoms that live attached to sediment account for almost three quarters of the tsunami deposit assemblage at Chucalen, with diatoms of unknown life form making up the second largest component (Fig. 5). When classified by modern distribution, the tsunami deposit exhibits a greater proportion of species indicative of lower elevations than those from the underlying tidal marsh sediment (Fig. 7c).

Diatom assemblages in sediments immediately above and below the tsunami deposit show a change from species characteristic of the highest elevations of modern tidal marshes to taxa more tolerant of regular tidal inundation (Fig. 7c). Paleomarsh surface elevation reconstructions indicate land subsidence of 1.12 ± 0.53 m.

5. Discussion

5.1 Tsunami deposition

The tidal marshes investigated here demonstrate a variable and fragmentary record of tsunamis associated with two great earthquakes in 1960 and 2010. We found no 2010 tsunami deposit at one of the four marshes adjacent to the rupture zone. Where present, it is composed of more than 85 % sand and abruptly overlies finer grained, more organic tidal marsh sediments, frequently preserving flattened but still rooted terrestrial plants at their contact. Flattened vegetation assists in determining tsunami flow direction (e.g. Morton *et al*., 2011). The extent and continuity of the deposit is highly variable. At Río Mataquito, site 1, the sand layer reaches a maximum of 0.40 m in thickness, however accumulations of 0.05 to 0.15 m are more common both at this site, and at the other sites investigated. Comparable 2010 tsunami deposit thicknesses are reported by Horton *et al*. (2011) and Morton *et al*. (2011). At our sites the 2010 deposit fines in a landward direction, reflecting decreasing sediment transport as the wave train

moved inland. We attribute further along-transect variability in the thickness of the deposit to variable vegetation cover and pre-tsunami surface topography (Morton *et al*., 2007).

The 1960 tsunami deposit is preserved as a continuous stratigraphic layer only at Chucalen, site 5, in the central part of the rupture segment. Towards the northern limit of the 1960 segment it is absent from site 3, Tubul and fragmented at site 4, Río Tirua. It is present, though fragmented at site 2, Río Andalién, just north of the segment boundary, and we did not encounter any buried sand layers at site 1. Where present, the deposit is similar to the 2010 tsunami layer: sand-rich and abruptly overlying organic tidal marsh sediment. The thin and fragmentary nature of the deposit, despite the significant size of the 1960 tsunami, may indicate postseismic erosion prior to burial and encasement into the sediment record.

Diatom assemblages from tsunami sand layers vary both between different sites for the same tsunami and between different tsunamis at the same site. There is no unique tsunami diatom assemblage. Rather, the assemblage reflects the local sediment source, with mixed assemblages of different salinity preferences, different life forms and different habitats. Diatom assemblages are likely to be mixed as tsunamis inundate inland areas and erode, transport and redeposit marine, inter-tidal and non-marine sediments. Similar mixed assemblages including freshwater, brackish and marine species are observed in tsunami deposits at Pichilemu, central Chile, reported by Horton *et al*. (2011), and are consistent with observations in modern and paleotsunami deposits elsewhere (Hemphill-Haley, 1996; Atwater and Hemphill-Haley, 1997; Tuttle *et al*., 2004; Dawson, 2007; Sawai *et al*., 2008).

5.2 Estimating coseismic land-level change

Transfer function models provide estimates of coseismic land surface deformation for two of the five sites in 2010 and three sites in 1960. The lack of post-earthquake sedimentation or the absence of a 1960 tsunami deposit to guide our sampling approach precludes the quantification of deformation at the remaining sites. Despite our reservations based on the lack of good modern analogues, our reconstructions compare favourably with published estimates of coseismic land-level change (Fig. 8). This confirms the potential of using diatom-based transfer function models to quantify coseismic movement from previous great earthquakes in this region. The apparent offset for the 2010 data (Fig.8) may be the effect of the lack of good modern analogues, but it may also reflect the different measures of coseismic subsidence. The GPS and benchmark relevelling data relate to the vertical movement of rock surfaces, whereas marsh sediments may undergo additional local scale subsidence due to ground shaking and dewatering leading to sediment consolidation. This was observed at numerous locations in Alaska during the 1964 M_w 9.2 earthquake (Plafker, 1969) and the M_w 8.1 and 8.2 earthquakes in 1899 (Plafker and Thatcher, 2008). The estimates by Plafker and Savage (1970) for coseismic motions in 1960 may also incorporate some local sediment consolidation, for example their estimate from close to our site 5 based on comparison of the lower growth limit of pre- and post-earthquake vegetation.

5.3 Limitations and improvement of quantitative reconstructions of relative land- and sea-level change

Although the current modern training set includes samples from four transects in two locations and from modern environments ranging from unvegetated tidal flat below mean sea level to

above the highest limits of tidal inundation, many of the fossil samples do not have a 'good' or 'close' modern analogue. While this is, in part, a result of our selected percentile thresholds that are stricter than those used in some other studies, the apparent dissimilarity between modern and fossil diatom assemblages remains a cause for concern. We highlight this lack of modern analogues as a limitation of the current study and advocate the need for larger training sets, preferably from a wide range of sites. The modern samples are from locations well to the south of sites 1 to 4 and there may be a spatial control on diatom assemblages that we are currently unable to assess. Ongoing postseismic deformation and the lack of significant sedimentation preclude the collection and use of samples from sites within the 2010 rupture zone and further investigations should focus on the northern half of the 1960 rupture zone.

Accurate estimates of the magnitude of coseismic deformation depend on the recommencement of sediment accumulation before significant postseismic deformation has occurred. The four marshes in the 2010 rupture zone showed variable responses six months after the earthquake. At site 1, no postseismic sedimentation followed coseismic subsidence and tsunami deposition. Up to 20 mm of sedimentation followed coseismic subsidence and tsunami deposition at site 2. At site 3, up to 5 mm of sedimentation followed coseismic uplift and no tsunami sedimentation and by early 2012, vegetated marsh was developing on previously unvegetated tidal flat. At site 4, no postseismic sedimentation had occurred almost two years after coseismic uplift and tsunami sedimentation in 2010. These post-seismic accumulation rates are several orders of magnitude less than after the 1964 Alaskan earthquake (Atwater *et al.*, 2001) and closer to estimates from the channels of the Cruces river following the 1960 Chilean earthquake (Reinhardt *et al.*, 2010). Postseismic vertical movements in the six months following the Maule 2010 earthquake were small, estimated from GPS data at < 15 mm at Concepción and < 50 mm elsewhere along the rupture zone (Baez *et al.*, 2010). Consequently, postseismic movements are unlikely to significantly affect estimates of coseismic land motions based on sediment biostratigraphy at sites 2 and 3. At sites with a sedimentary hiatus, coseismic deformation estimates will include both coseismic and some postseismic movements, resulting in potential underestimation of the coseismic movement. In fossil sequences it can be very difficult to identify the duration of any hiatus. Radiocarbon dated samples either side of the stratigraphic boundary will give maximum and minimum ages and may identify a large hiatus (e.g. Carver and Plafker, 2008), while reconstructions for the same episode from multiple locations on the same marsh also help (e.g. Shennan and Hamilton, 2006).

5.4 A test of the criteria to differentiate between sedimentary evidence of seismic and non-seismic relative land- and sea-level changes

Based on observations of sedimentary responses to the largest plate boundary earthquakes and similar stratigraphies found in tectonically stable locations, Nelson *et al*. (1996) propose a series of criteria for differentiating between evidence for seismic and non-seismic relative land- and sea-level changes. Atwater and Hemphill-Haley (1997) apply the same criteria alongside geophysical approaches and structural geology to discuss the differences between plate-boundary and upper-plate sources for the earthquakes, the sizes of the earthquakes, the dimensions of plate-boundary ruptures and the trade-off between size and frequency. Both of these papers point to differences between M_w 7.5 or 8.0 earthquakes and great earthquakes, M_w 8+. The 2010 earthquake provides an opportunity to test the criteria on a smaller plate-boundary rupture than the 1960 Chilean M_w 9.5 and 1964 Alaskan M_w 9.2 earthquakes.

The key criteria outlined by Nelson *et al*. (1996) are: lateral extent of peat-mud couplets with sharp upper contacts, suddenness of subsidence, amount of subsidence, synchroneity of subsidence with other sites and, for some locations, presence of tsunami sediments. Although these criteria were developed for areas undergoing coseismic subsidence, they are equally applicable to identifying coseismic uplift (Shennan *et al*., 2009). Section 5.1, above, demonstrates the variable pattern of tsunami deposition, but confirms that, where present, it is a valuable line of evidence and may occur in either uplifted or subsided locations. Our work on the 2010 earthquake deposits suggests that, in south central Chile, sedimentary hiatuses and low rates of sedimentation may temporarily postpone the formation of the characteristic subsidence stratigraphy (section 5.2), but the burial and preservation of the 1960 deposits shows that any hiatus is brief in the context of multiple earthquake cycles. Our diatom-based reconstructions of relative land/sea-level change are promising, but require a greater range of modern samples in order to provide better modern analogues and greater confidence in the elevation estimates and associated error terms. Nelson *et al*. (1996) and Atwater and Hemphill-Haley (1997) draw attention to a lower limit of resolution for identifying coseismic deformation; approximately 0.5 m. Our estimates, section 5.2, currently do not suggest any finer resolution. Comparison of the marsh sediment sequences for the 2010 and 1960 earthquakes suggests that they produce similar stratigraphic records and that the key to reconstructing earthquake characteristics, such as the rupture magnitude and differences between plate-boundary and upper-plate sources, depends on applying the stratigraphic criteria at multiple sites in order to identify the spatial pattern of deformation associated with each earthquake.

5.5 Implications for reconstructing Holocene megathrust earthquake rupture zones

Precise estimates of coseismic deformation are required from multiple sites to constrain models of the location, dimensions and slip distribution of megathrust earthquakes (Atwater and Hemphill-Haley, 1997; Atwater *et al*., 2005). To date, elastic deformation models of the 1960 and 2010 earthquakes have been constrained by GPS vectors and measurements of displaced coastal landforms and biotic environments (e.g. Plafker and Savage, 1970; Moreno *et al*., 2009; Farías *et al*., 2010; Lorito *et al*., 2011). Further development of the diatom-based transfer function approach detailed here provides an additional viable method for validating models of these earthquakes, with the added benefit of applicability to older ruptures. Databases of coseismic deformation index points, each characterised by a vertical deformation estimate with an associated error term and spatial and chronological attributes, may be used to assist estimation of the magnitude of historical and prehistoric earthquakes. Such databases have already been successfully employed to constrain the magnitude of past great earthquakes in Cascadia (Atwater and Hemphill-Haley, 1997; Leonard *et al*., 2004; 2010; Hawkes *et al*., 2011). The development of this approach along the Chilean subduction zone may allow further investigation of the variability in rupture mode in the 1960 segment (Cisternas *et al*., 2005) and confirm or refute the permanence of the Arauco Peninsula as a segment boundary over multiple seismic cycles.

Differentiation between the closely temporally spaced rupture of two adjacent segments and a single, multi-segment rupture may prove crucial to interpreting evidence for the largest Holocene megathrust earthquakes (Atwater and Hemphill-Haley, 1997; Atwater *et al*., 2005; Shennan, 2009; Shennan *et al*., 2009). While radiocarbon dating alone may be insufficient to distinguish between single and multi-segment ruptures, the work presented here establishes the stratigraphic

separation of two closely timed earthquakes in locations close to a seismic segment boundary. We suggest that detailed marsh surface elevation reconstructions from boundary locations, combined with precise dating approaches, should form an integral part of establishing the long-term history of the seismic hazards associated with the Chilean subduction zone.

6. Conclusions

The 1960 and 2010 Chilean great earthquakes provide critical modern analogues for sedimentary processes during seismic cycles at plate boundaries. The major conclusions of this work are:

1) Deposits from the 1960 and 2010 tsunamis are fragmentary, variable and have no unique, diagnostic diatom assemblage.
2) Our transfer function method provides estimates of coseismic land surface deformation for two sites in 2010 and three sites in 1960. Reconstructions agree with independent estimates, confirming the potential for our approach to be used to quantify coseismic deformation for previous great earthquakes in south central Chile.
3) Sedimentary hiatuses at two sites following the 2010 earthquake indicate that the magnitude of coseismic deformation may be underestimated in fossil records.
4) A lack of close modern analogues for fossil diatom assemblages remains a limitation of the current study and we advocate the need for larger training sets, preferably from a wide range of sites.
5) Where sediment accumulation allows, criteria for distinguishing between seismic and non-seismic stratigraphies developed from evidence for the largest plate boundary earthquakes (Nelson *et al*., 1996; Atwater and Hemphill-Haley, 1997) are corroborated by the lesser magnitude earthquake of 2010.

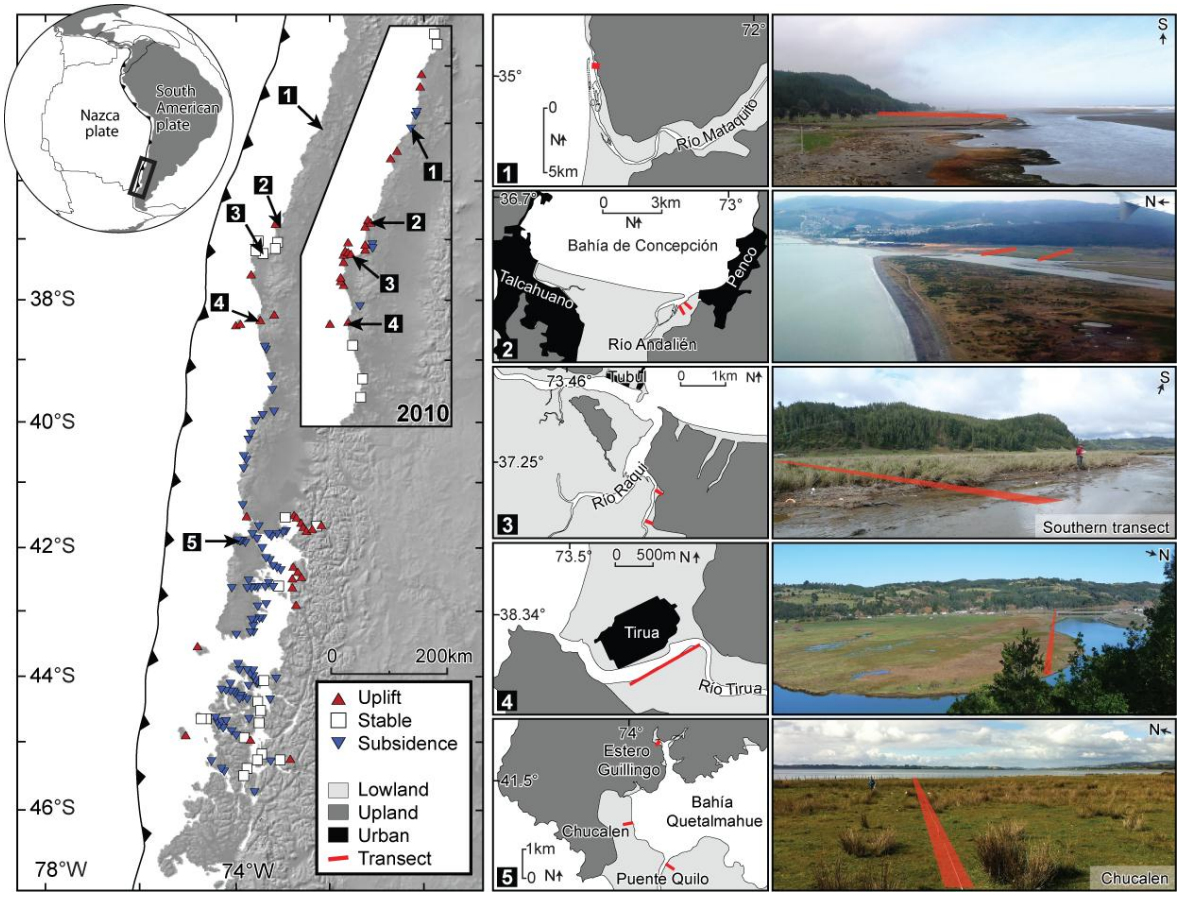

Figure 1: Tectonic setting of the Chilean subduction zone and the location of the field sites in relation to the 2010 and 1960 rupture zones. Vertical land surface deformation in 1960 (main figure) and 2010 (inset) from Plafker and Savage (1970) and Vargas *et al*. (2011) respectively. Site 1: Río Mataquito; site 2: Río Andalién; site 3: Tubul; site 4: Río Tirua; site 5: Northern Isla de Chiloé, including Chucalen and the modern transects at Estero Guillingo and Puente Quilo.

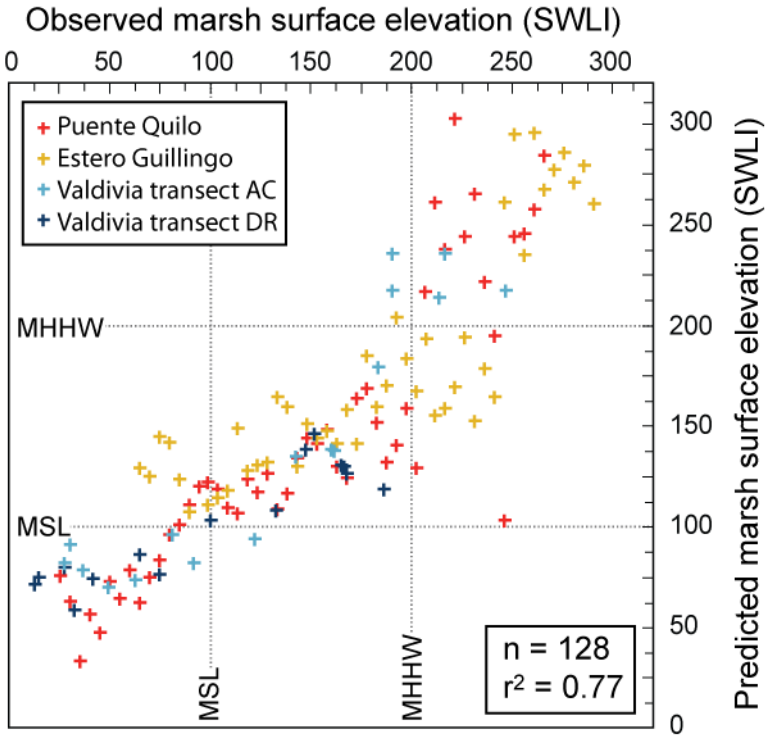

Figure 2: Scatter plot of observed against predicted elevation values for the four transects included in the WA-PLS component 3 transfer function model. Valdivia AC: samples collected from a fan bordering Río Angachilla; Valdivia transect DR: samples collected from Isla del Rey (Nelson *et al.*, 2009).

Figure 3: Comparison of pre and post 2010 Maule earthquake Google Earth imagery for sites 1 – 4. Red lines indicate August 2010 sampling transects.

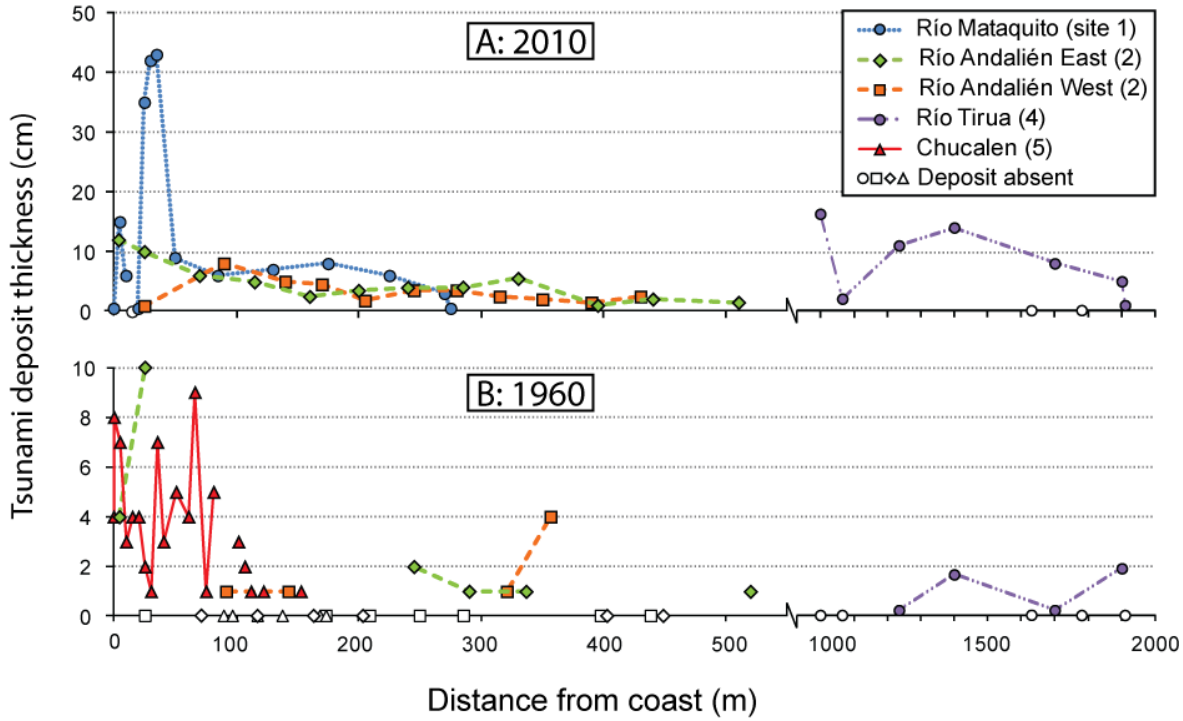

Figure 4: Thickness, extent and continuity of the 2010 and 1960 tsunami deposits at Río Mataquito, Río Andalién, Río Tirua and Chucalen. We could not locate 2010 tsunami deposits at site 3, Tubul, or site 5, Chucalen. The 1960 tsunami deposit was not identified at site 1, Río Mataquito, or site 3, Tubul. Tsunami deposits may extend further inland than the sampled locations; we did not sample to the limit of inundation. Sampling commenced 1 km inland from the coastline at site 4, Río Tirua, due to the location of tidal marshes at this site. Note the change in y-axis scale.

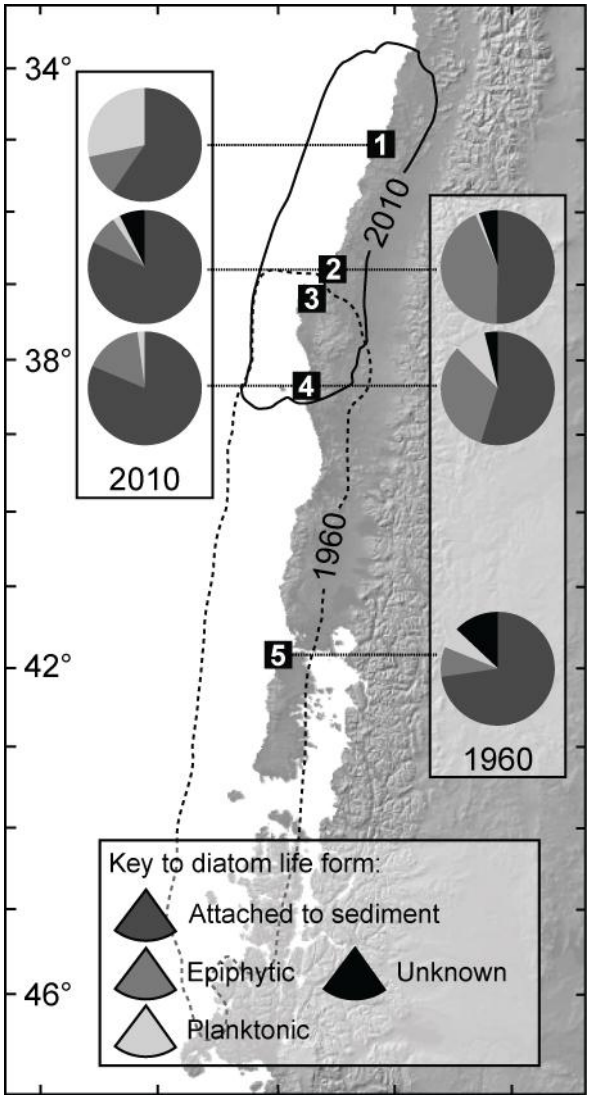

Figure 5: Diatom assemblages of the 2010 and 1960 tsunami deposits, summarised by life form (following Denys, 1991; Stoermer, 1980; Van Dam *et al*., 1994; Vos and de Wolf, 1993, 1988). Epipelic and epipsammic species are grouped as *"attached to sediment*". We do not report any tsunami deposit from site 3, Tubul.

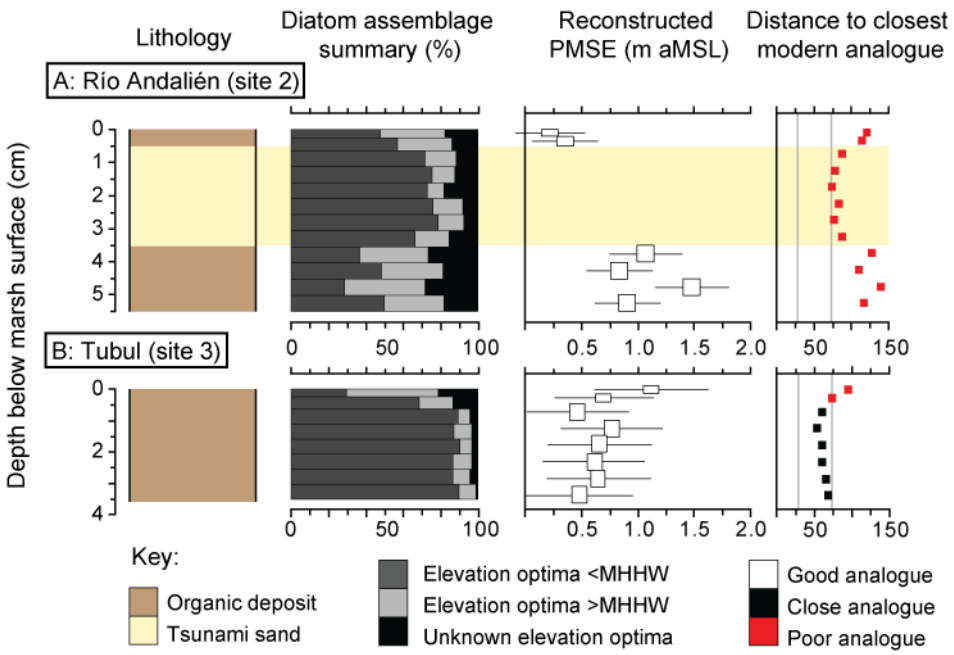

Figure 6: 2010 diatom assemblages and paleomarsh surface elevation reconstructions at A: site 2, Río Andalién and B: site 3, Tubul. Due to a lack of post-earthquake sedimentation, reconstructions are not possible for site 1, Río Mataquito, and site 4, Río Tirua. Assemblage summary based on modern species coefficients derived from the WA-PLS transfer function model. We use the distance to the closest modern analogue from the modern analogue technique in C2 (Juggins, 2011) to assess the similarity between modern and fossil assemblages.

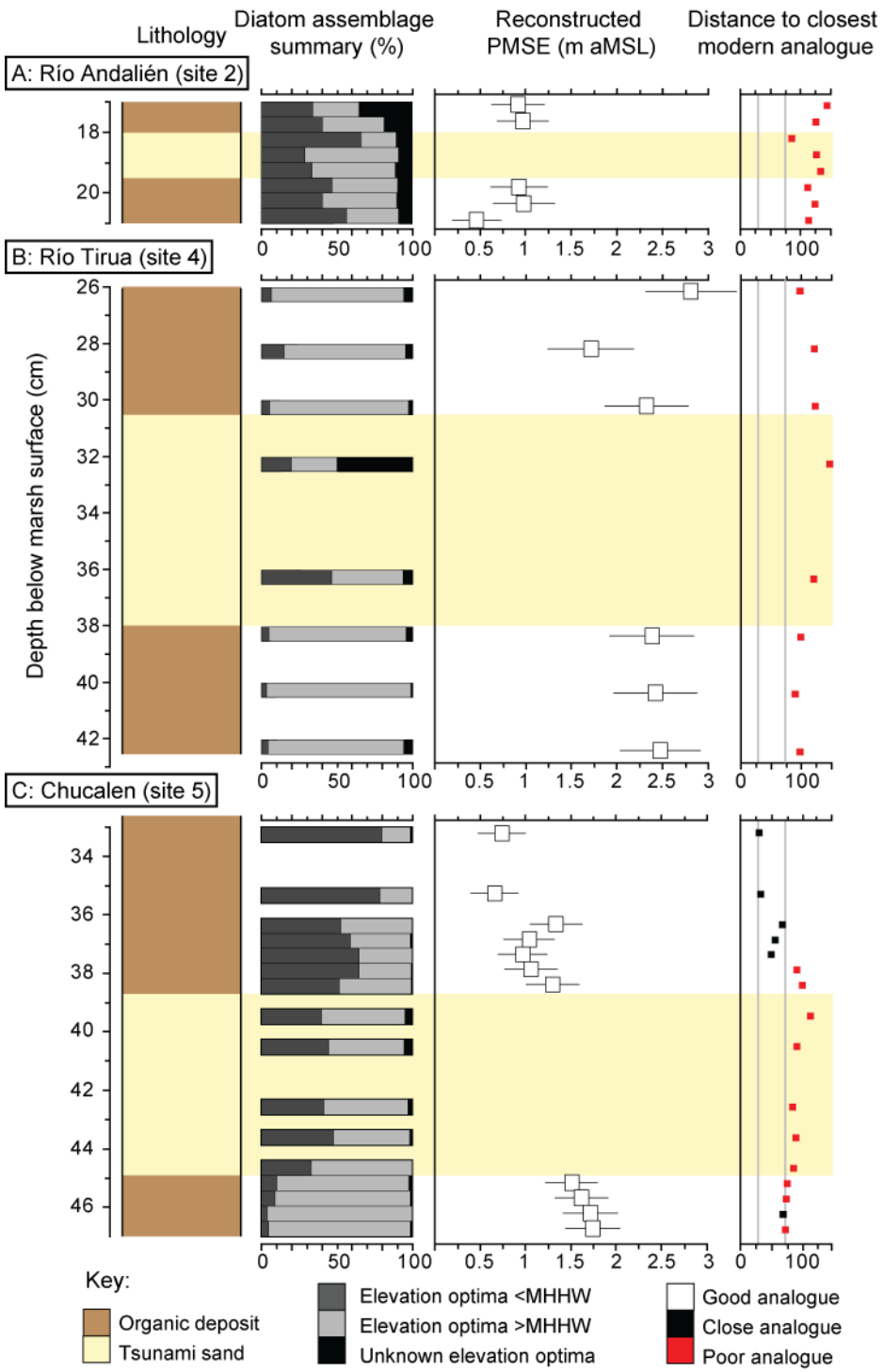

Figure 7: 1960 diatom assemblages and paleomarsh surface elevation reconstructions at A: site 2, Río Andalién; B: site 4, Río Tirua and C: site 5, Chucalen. No pre-2010 tsunami deposits were identified at site 1, Río Mataquito, or site 3, Tubul. Assemblage summary based on modern species coefficients derived from the WA-PLS transfer function model. We use the distance to the closest modern analogue from the modern analogue technique in C2 (Juggins, 2011) to assess the similarity between modern and fossil assemblages.

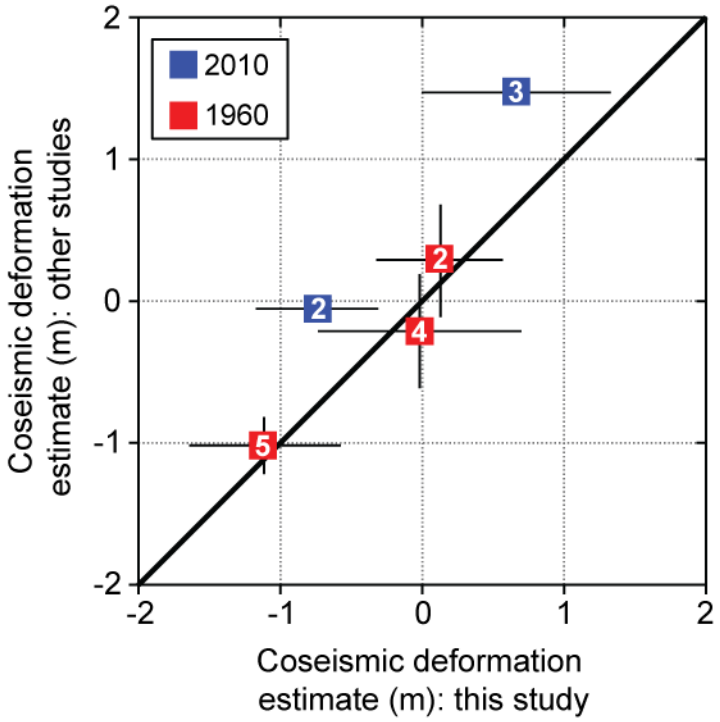

Figure 8: Comparison of transfer function model estimates of coseismic deformation with published estimates of vertical coseismic deformation in 1960 and 2010 at Río Mataquito (2), Tubul (3), Río Tirua (4) and Chucalen (5). Diagonal line is the 1:1 line, not a best-fit regression line. Due to hiatuses or the absence of tsunami deposits, we cannot estimate deformation at sites 1 and 3 for 1960 and at sites 1, 4 and 5 for 2010. For 1960 we compare our estimates with Plafker and Savage's (1970) sampling locations 1, 9 and 45 and for 2010 we compare with the continuous GPS station at Concepción (Vigny *et al*., 2011) and benchmark relevelling at Tubul (Melnick *et al*., 2012).